Journal of Mechanics of Materials and Structures

Volume 1, Nº 4 April 2006

mathematical sciences publishers

JOURNAL OF MECHANICS OF MATERIALS AND STRUCTURES

http://www.jomms.org

mathematical sciences publishers

JOURNAL OF MECHANICS OF MATERIALS AND STRUCTURES
Vol. 1, No. 4, 2006

SPECTRAL ELEMENT MODELING AND ANALYSIS OF AN AXIALLY MOVING THERMOELASTIC BEAM-PLATE

KYUNGSOO KWON AND USIK LEE

Axially moving thin-walled structures exposed to sudden external thermal loads may experience severe vibrations. For accurate predictions of the thermally induced vibrations, this paper develops a spectral element model for the axially moving beam-plates subjected to sudden external thermal loads. The spectral element model is formulated from the frequency-dependent dynamic shape functions which satisfy the governing equations in the frequency domain. Thus, when compared with the conventional finite element model in which simple polynomials are used as the shape functions, the spectral element model provides exact solutions by treating a whole uniform structure member as a single finite element, regardless of its length. Numerical studies are conducted to evaluate the present spectral element model and also to investigate the dynamic characteristics of an axially moving beam-plate subjected to a sudden thermal load on its upper surface.

1. Introduction

A sudden thermal load applied to a structure may induce rapid movements in that structure, causing it to vibrate. These thermally induced vibrations may be encountered, for example, in high-speed modern aircraft subjected to aerodynamic heating, nuclear reactors in extremely high temperature and temperature gradient environments, high-speed propulsion units, and galvanized steel strips passing through a hot zinc tank.

The thermally induced vibration of a beam subjected to a suddenly applied heat flux distributed along its span was studied in [Boley 1956]. Since then many studies have been conducted for various thermoelastic structures such as beams [Boley and Barber 1957; Yu 1969; Manolis and Beskos 1980; Massalas and Kalpakidis 1984; Eslami and Vahedi 1989; Kidawa-Kukla 1997], laminated beams [Al-Huniti 2004], plates [Boley 1956; Kozlov 1972; Takeuti and Furukawa 1981; Massalas et al. 1982; Trajkovski and Čukić 1999; Verma 2001; Arafat et al. 2003; Al-Huniti 2004], laminated plates [Chandrashekhara and Tenneti 1994; Mukherjee and Sinha

Keywords: Thermally induced vibration, beam-plate, axially moving structure, spectral element model, spectral element analysis, dynamic characteristics.

1996], panels [Sharma 2001; Oguamanam et al. 2004], cylinders [Takeuti et al. 1983], and so forth. [Lee 1985] conducted thermoelastic damping analysis for the beams, plates and shells undergoing flexural vibration, and [Kinra and Milligan 1994] considered thermoelastic damping for beams. [Tauchert 1991] presented an extensive review on the subject of thermally induced vibrations of plates, and [Thornton 1992] made a survey of the literature on thermal structures, mostly focusing on aerospace applications. To eliminate the paradox of infinite velocity of heat propagation in the classical theory of thermoelasticity [Biot 1956], some researchers such as [Lord and Shulman 1967] developed the generalized theory of thermoelasticity by introducing thermal relaxation times. However, as the thermal relaxation effect is very small at high temperatures [Lord and Shulman 1967], the classical theory of thermoelasticity will be adopted in this study. In the existing literatures, various solution techniques have been used: they include the Green function method [Kidawa-Kukla 1997], integral transformation method [Massalas et al. 1982; Trajkovski and Čukić 1999; Sharma 2001; Al-Huniti 2004], finite element method [Eslami and Vahedi 1989; Chandrashekhara and Tenneti 1994; Mukherjee and Sinha 1996; Oguamanam et al. 2004], and the modal analysis method [Lee 1985].

Existing studies on thermally induced vibration have focused mostly on stationary (not axially moving) thermoelastic structures. Recently, Al-Huniti [2004] considered the dynamics of a stationary laminated beam under the effect of a moving heat source. However, to our best knowledge, the dynamics of axially moving thermoelastic structures such as the galvanized steel strips passing through a hot zinc tank has not been investigated. Furthermore, the spectral element method (SEM) has not been applied to such axially moving thermoelastic structures. The SEM is an element method, like the finite element method (FEM). The fundamental differences from FEM are:

(1) The SEM uses a spectral element matrix (*exact* dynamic stiffness matrix), which is formulated in the frequency domain by using the dynamic (frequency-dependent) shape functions exactly solved from governing equations.

(2) The FFT algorithm is used to efficiently reconstruct the time domain response from the frequency domain solution. Because no approximation or assumption is made in the course of spectral element formulation, SEM indeed provides exact solutions and thus it is well recognized as an *exact* solution method [Lee and Leung 2000; Lee 2004].

In this paper we develop an SEM for an axially moving thermoelastic beam-plate and conduct a spectral element analysis to investigate the dynamic behavior of an axially moving beam-plate subjected to a sudden temperature change on its surface.

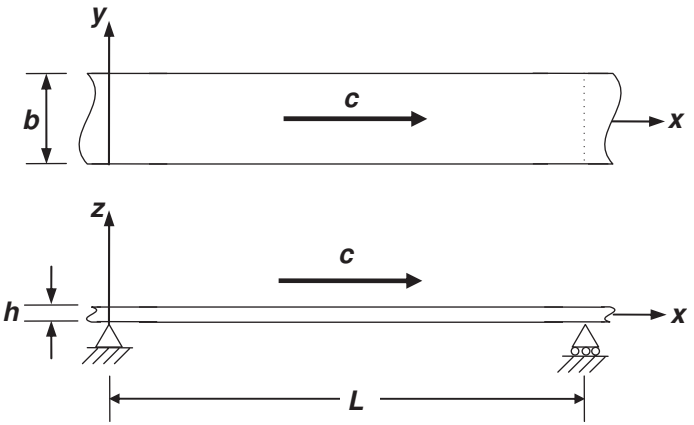

Figure 1. Geometry of an axially moving beam-plate.

2. Derivation of the governing equations

2A. ***Equations of motion.*** Consider a thin beam-plate moving in the x (axial) direction at speed c, as shown in Figure 1. The beam-plate has thickness h and width b. The material properties of the beam-plate are given by Young's modulus E and Poisson's ratio ν. Assume that the beam-plate has a small amplitude vibration and that its displacements don't vary along the width direction as the word 'beam-plate' implies.

Using Kirchhoff's hypothesis, one can write the displacements as

$$\begin{aligned} W(x,t) &= w(x,t), \\ U(x,z,t) &= u(x,t) - zw'(x,t), \end{aligned} \tag{1}$$

where $w(x,t)$ is the displacement of the midplane of the beam-plate in the z direction, $u(x,t)$ the displacement in the x direction, z is the transverse distance from the midplane to the point of interest on the cross-section of the beam-plate, and the prime denotes the derivative with respective to x. From (1), the strain in the x direction can be readily obtained as

$$\varepsilon_{xx} = U'(x,z,t) = u'(x,t) - zw''(x,t). \tag{2}$$

The stress in the x direction, taking into account the thermal stress, is given by [Ugral 1999]

$$\sigma_{xx} = \frac{E}{1-\nu^2}\varepsilon_{xx} - \frac{E\alpha}{1-\nu}\Delta T(x,z,t), \tag{3}$$

where $\Delta T(x, z, t)$ is the difference between the absolute temperature $T(x, z, t)$ and the reference, stress-free absolute temperature T_0 as

$$\Delta T(x, z, t) = T(x, z, t) - T_0.$$

Using (2) and (3) we can derive the strain energy P as

$$P = \frac{1}{2}\int_0^L \int_{-h/2}^{h/2} \sigma_{xx}\varepsilon_{xx} b dz\, dx = \frac{1}{2}\int_0^L (Dw''^2 + \overline{EA}u'^2 + M_T w'' - N_T u')\, dx, \quad (4)$$

where L is the span between two simple supports (see Figure 1), A is the cross-sectional area of the beam-plate, and the following definitions are used:

$$D = \frac{EI}{(1-\nu^2)}, \qquad I = \frac{bh^3}{12}, \qquad \overline{EA} = \frac{EA}{1-\nu^2}. \quad (5)$$

In Equation (4), M_T and N_T are the thermal moment and thermal (axial) force, defined by

$$\begin{aligned} M_T(x, t) &= \frac{E\alpha b}{1-\nu}\int_{-h/2}^{h/2} \Delta T(x, z, t) z\, dz, \\ N_T(x, t) &= \frac{E\alpha b}{1-\nu}\int_{-h/2}^{h/2} \Delta T(x, z, t)\, dz. \end{aligned} \quad (6)$$

Similarly, by using (1), the kinetic energy K can be derived as

$$\begin{aligned} K &= \frac{\rho}{2}\int_0^L \int_{-h/2}^{h/2} \left((c+\dot{U})^2 + (\dot{W} + cW')^2\right) b\, dz\, dx \\ &= \frac{\rho}{2}\int_0^L \left(A(c+\dot{u})^2 + A(\dot{w} + cw')^2 + I\dot{w}'^2\right) dx. \end{aligned} \quad (7)$$

Finally, the virtual work is given by

$$\begin{aligned} \delta W = \int_0^L &\left(p_x(x, t)\delta u(x, t) + p_z(x, t)\delta w(x, t)\right) dx \\ &+ M_1(t)\delta\phi_1(t) + M_2(t)\delta\phi_2(t) + V(t)_1\delta w_1(t) \\ &+ V_2(t)\delta w_2(t) + N_1(t)\delta u_1(t) + N_2(t)\delta u_2(t), \end{aligned} \quad (8)$$

where $p_x(x, t)$ and $p_z(x, t)$ are distributed loads acting on the beam-plate in the x and z directions. M_i, V_i and N_i $(i = 1, 2)$ represent the boundary moments, transverse shear forces and axial forces applied at $x = 0$ and L, respectively. The transverse displacement, axial displacement and slope ($\phi = \partial w/\partial x$) at boundaries

are defined by

$$\begin{aligned} w_1(t) &= w(0,t), & w_2(t) &= w(L,t),\\ \phi_1(t) &= w'(0,t), & \phi_2(t) &= w'(L,t),\\ u_1(t) &= u(0,t), & u_2(t) &= u(L,t). \end{aligned}$$

The equations of motion and the relevant boundary conditions of the beam-plate can be derived from Hamilton's principle:

$$\int_{t_1}^{t_2} (\delta K - \delta P + \delta W)\, dt = 0.$$

Substituting (4), (7), and (8) into this equality and integrating by parts yields

$$\begin{aligned} &\int_{t_1}^{t_2}\int_0^L \left(-Dw'''' - \rho A c^2 w'' - 2\rho A c\dot{w}' - \rho A\ddot{w} + \rho I\ddot{w}'' - \tfrac{1}{2}M_T'' + p_z\right)\delta w\, dx\, dt\\ &+ \int_{t_1}^{t_2}\int_0^L \left(-\rho A\ddot{u} + \overline{EA}u'' - \tfrac{1}{2}N_T' + p_x\right)\delta u\, dx\, dt\\ &+ \int_{t_1}^{t_2} \Big(-M(x,t)\delta\phi\big|_0^L + M_1\delta\phi_1 + M_2\delta\phi_2 - V(x,t)\delta w\big|_0^L + V_1\delta w_1 + V_2\delta w_2\\ &\qquad - N(x,t)\delta u\big|_0^L + N_1\delta u_1 + N_2\delta u_2\Big)\, dt = 0, \end{aligned} \tag{9}$$

where the limits 0 and L refer to the variable x, and where

$$\begin{aligned} M(x,t) &= Dw'' + \tfrac{1}{2}M_T,\\ V(x,t) &= -Dw''' - \rho h c^2 w' - \tfrac{1}{2}M_T' - \rho A c\dot{w} + \rho I\ddot{w}',\\ N(x,t) &= \overline{EA}u' - \tfrac{1}{2}N_T. \end{aligned} \tag{10}$$

From the first two integrals in (9) we obtain the equations of motion:

$$\overline{EA}u'' - \rho A\ddot{u} = -p_x(x,t) + \tfrac{1}{2}N_T', \tag{11}$$

$$Dw'''' + \rho A c^2 w'' + 2\rho A c\dot{w}' - \rho I\ddot{w}'' + \rho A\ddot{w} = \quad p_z(x,t) - \tfrac{1}{2}M_T''. \tag{12}$$

The boundary conditions can be obtained from the last integral of (9) as

$$\begin{aligned} M(0,t) &= -M_1(t) \quad \text{or} \quad \phi(0,t) = \phi_1(t),\\ M(L,t) &= M_2(t) \quad \text{or} \quad \phi(L,t) = \phi_1(t),\\ V(0,t) &= -V_1(t) \quad \text{or} \quad w(0,t) = w_1(t),\\ V(L,t) &= V_2(t) \quad \text{or} \quad w(L,t) = w_2(t),\\ N(0,t) &= -N_1(t) \quad \text{or} \quad u(0,t) = u_1(t),\\ N(L,t) &= N_2(t) \quad \text{or} \quad u(L,t) = u_2(t). \end{aligned} \tag{13}$$

2B. ***Heat conduction equation.*** The temperature field $T(x, z, t)$ or $\Delta T(x, z, t)$ is governed by the heat conduction equation. The heat conduction equation can be derived from the law of energy conservation as [Lee 1985; Özisik 1993]

$$-q_x' - q_z' - \frac{T_0 \alpha E}{1-2\nu} \frac{\partial e}{\partial t} = \rho c_p \frac{\partial T}{\partial t}, \tag{14}$$

where α is the coefficient of thermal expansion and c_p is the specific heat at constant strain. The first two terms in the left of Equation (14) represent the net energy inflow and q_x and q_z are the heat fluxes per unit area in the x and z directions, respectively, defined by

$$\begin{aligned} q_x(x, z, t) &= -kT'(x, z, t) + \rho c_p c \Delta T(x, z, t), \\ q_z(x, z, t) &= -kT^\circ(x, z, t), \end{aligned} \tag{15}$$

where k is the thermal conductivity of the medium. The circle ($^\circ$) symbol denotes the derivative with respective to z and this notation will be used throughout. Notice that the effect of the moving speed c is taken into account in the heat flux q_x [Özisik 1993; Beck and McMasters 2004]. The term on the right in Equation (14) represents the energy stored in the structure. The third term on the left represents the rate of thermal energy generation due to elastic deformation, where $e(x, z, t)$ is the dilatation defined by [Lee 1985; Ugral 1999]

$$e = \varepsilon_{xx} + \varepsilon_{yy} + \varepsilon_{zz} \cong \left(\frac{1-2\nu}{1-\nu}\right)(u' - zw'') + \left(\frac{1+\nu}{1-\nu}\right)\alpha \Delta T \cong \left(\frac{1+\nu}{1-\nu}\right)\alpha \Delta T, \tag{16}$$

where $\varepsilon_{xx}, \varepsilon_{yy}, \varepsilon_{zz}$ are the normal strains in the x, y, z directions. In (16), the strain ε_{yy} is neglected because we are considering a beam-plate. The dilatation due to the pure elastic deformation is also neglected in the last expression of (16) because its effect on the temperature change will be a small, secondary effect.

Substituting (15) and (16) in (14) gives the heat conduction equation as

$$-k(T'' + T^{\circ\circ}) + \rho c_p c T' + (T_0 \alpha^2 E_\nu + \rho c_p)\dot{T} \cong 0, \tag{17}$$

where

$$E_\nu = \frac{1+\nu}{(1-2\nu)(1-\nu)} E. \tag{18}$$

In deriving the heat conduction equation, we have implicitly assumed that the heating of the plate will not exceed the limit where the material's thermal and mechanical properties become temperature-dependent. In addition, we will assume that the beam-plate is subject to the thermal loads applied only on its top or bottom surface and that the thermal loads do not vary along the width direction, y. Because of the geometry of beam-plate and the y-axis independence of thermal loads, the instantaneous temperature variation due to the sudden temperature change on the

top or bottom surface of beam-plate will be more significant in the thickness direction than in the in-plane direction. Accordingly, one may assume the temperature as the function of z and t to simplify (17) as follows:

$$kT^{\circ\circ} - \left(T_0\alpha^2 E_v + \rho c_p\right)\dot{T} = 0. \tag{19}$$

Once the proper thermal boundary conditions are specified for a given problem, one can readily solve Equation (18) for $T(z,t)$ and then apply the solution to Equation (11) to investigate the thermal-induced vibration of a beam-plate. Notice that, because the temperature will be assumed in this study as the function of z and t only, the thermal moment M_T and thermal force N_T defined by Equation (6) will be functions of t only. In this case, the last terms in (11) will vanish and the thermal loads will affect the vibration of beam-plate through the boundary conditions, which can be guessed from Equations (10) and (13).

3. Spectral element formulation

3A. ***Brief review of DFT theory.*** (For more details, see for instance [Newland 1993].) In discrete Fourier transform (DFT) theory, a periodic function of time $x(t)$ with period T can be always expressed by the Fourier series as

$$x(t) = \sum_{n=-\infty}^{\infty} X_n e^{i\omega_n t}, \tag{20}$$

where $i = \sqrt{-1}$, $\omega_n = n(2\pi/T) = n\omega_1$ are the discrete frequencies, and X_n are constant Fourier (or spectral) components given by

$$X_n = \frac{1}{T}\int_0^T x(t)e^{-i\omega_n t}\,dt \quad (n = 0, 1, 2, \ldots, \infty). \tag{21}$$

Equations (20) and (21) are the continuous Fourier transforms pair for a periodic function.

Although $x(t)$ is a continuous function of time t, it is often the case that only sampled values of the function are available, in the form of a discrete time series $\{x(t_r)\}$. If N is the number of samples, all equally spaced with a time interval $\Delta = T/N$, the discrete time series are given by $x_r = x(t_r)$, where $t_r = r\Delta$ and $r = 0, 1, 2, \ldots, N-1$. The integral in Equation (21) can be replaced with the summation as follows:

$$X_n = \sum_{r=0}^{N-1} x(t_r)e^{-i\omega_n t_r} \quad (n = 0, 1, 2, \ldots, N-1), \tag{22}$$

which is the DFT of the discrete time series $\{x_r\}$. Any typical value x_r of the series $\{x_r\}$ can be obtained from the synthesis equation

$$x(t_r) = \frac{1}{N}\sum_{n=0}^{N-1} X_n e^{i\omega_n t_r} \quad (r = 0, 1, 2, \ldots, N-1), \tag{23}$$

which is the inverse discrete Fourier transform (IDFT). Thus Equations (22) and (23) represent the DFT-IDFT pair. Although (22) is an approximation of (20), it allows all discrete time series $\{x_r\}$ to be regained *exactly* [Newland 1993]. The Fourier components X_n in (23) can normally be arranged as

$$X_{N-n} = X_n^* \quad (n = 0, 1, 2, \ldots, N/2),$$

where * denotes complex conjugation. $X_{N/2}$ corresponds to the highest frequency $\omega_{N/2} = (N/2)\omega_1$, the Nyquist frequency.

The fast Fourier transforms (FFT) is an ingenious computer algorithm that performs the synthesis analysis extremely efficiently, in time logarithmic rather than linear in N. While the FFT-based spectral analysis uses a computer, it is not a numerical method in the usual sense, because the analytical descriptions of Equations (22) and (23) are retained.

3B. ***Formulation of the spectral element matrix.*** Based on DFT theory, assume the solutions of Equation (11) in spectral form are

$$u(x,t) = \sum_{n=0}^{N-1} U_n(x) e^{i\omega_n t}, \qquad w(x,t) = \sum_{n=0}^{N-1} W_n(x) e^{i\omega_n t}, \tag{24}$$

where $U_n(x)$ and $W_n(x)$, for $n = 0, 1, \ldots, N-1$, are the spectral components of the dynamic responses $u(x,t)$ and $w(x,t)$. The accuracy of dynamic responses may depend on how many spectral components are taken into account in the FFT-based spectral analysis, for a chosen time window T. Similarly, one can express the external loads and thermal loads in the spectral forms as

$$\begin{aligned} p_x(x,t) &= \sum_{n=0}^{N-1} P_{xn}(x) e^{i\omega_n t}, & p_z(x,t) &= \sum_{n=0}^{N-1} P_{zn}(x) e^{i\omega_n t}, \\ N_T(t) &= \sum_{n=0}^{N-1} N_{Tn} e^{i\omega_n t}, & M_T(t) &= \sum_{n=0}^{N-1} M_{Tn} e^{i\omega_n t}, \end{aligned} \tag{25}$$

where $P_{xn}(x)$, $P_{zn}(x)$, $N_{Tn}(x)$ and $M_{Tn}(x)$, for $n = 0, 1, \ldots, N-1$, are the spectral components of $p_x(x,t)$, $p_y(x,t)$, $N_T(t)$, and $M_T(t)$. The spectral components M_{Tn} and N_{Tn} in Equation (25) are constant, rather than functions of x, because the temperature is assumed to vary only in the thickness (z) direction.

Substituting (24) and (25) into (11), we get

$$\begin{aligned} \overline{EA}U_n'' + \rho A\omega_n^2 U_n &= F_{xn}, \\ DW''''_n + \left(\rho Ac^2 + \rho I\omega_n^2\right)W_n'' + 2i\rho Ac\omega_n W_n' - \rho A\omega_n^2 W_n &= F_{zn}, \end{aligned} \tag{26}$$

where

$$F_{xn}(x) = -P_{xn} + \tfrac{1}{2}N_{Tn}' = -P_{xn}, \qquad F_{zn}(x) = P_{zn} - \tfrac{1}{2}M_{Tn}'' = P_{zn}. \tag{27}$$

Here the thermal force and moment terms do not appear because temperature is assumed to vary only in the thickness direction. In a similar way, the resultant moment, transverse shear force and axial force defined in (10) can be also expressed in spectral form as

$$\begin{aligned} N_n(x) &= \overline{EA}U_n' - \tfrac{1}{2}N_{Tn}, \\ V_n(x) &= -DW_n''' - \left(\rho Ac^2 + \rho I\omega_n^2\right)W_n' - i\rho Ac\omega_n W_n, \\ M_n(x) &= DW_n'' + \tfrac{1}{2}M_{Tn}, \end{aligned} \tag{28}$$

where $N_n(x)$, $V_n(x)$ and $M_n(x)$ are the spectral components of $N(x,t)$, $V(x,t)$ and $M(x,t)$, respectively.

The spectral element formulation begins with the governing equations without external forces [Lee and Leung 2000; Lee 2004]. Therefore, the homogeneous form of governing equations can be deduced from (26) as

$$\begin{aligned} \overline{EA}U_n'' + \rho A\omega_n^2 U_n &= 0, \\ DW''''_n + \left(\rho Ac^2 + \rho I\omega_n^2\right)W_n'' + 2i\rho Ac\omega_n W_n' - \rho A\omega_n^2 W_n &= 0. \end{aligned} \tag{29}$$

The general solutions of (29) can be assumed to be

$$U_n(x) = A_n e^{\kappa_n x}, \qquad W_n(x) = B_n e^{\lambda_n x},$$

where κ_n and λ_n are the wavenumbers for the axial and transverse vibration mode, respectively. Substituting these equalities into (29) yields the dispersion relations

$$\begin{aligned} \overline{EA}k_n^2 + \rho A\omega_n^2 &= 0, \\ D\lambda_n^4 + \left(\rho Ac^2 + \rho I\omega_n^2\right)\lambda_n^2 + 2i\rho Ac\omega_n\lambda_n - \rho A\omega_n^2 &= 0. \end{aligned}$$

From this, two wavenumbers k_{nr} $(r = 1, 2)$ can be obtained for axial vibration modes and four wavenumbers λ_{nr} $(r = 1, 2, 3, 4)$ for the transverse vibration modes. By using the wavenumbers thus computed, the general solutions of the dispersion relations can expressed in summation form as

$$U_n(x) = \sum_{r=1}^{2} A_{nr} e^{k_{nr}x}, \qquad W_n(x) = \sum_{r=1}^{4} B_{nr} e^{\lambda_{nr}x},$$

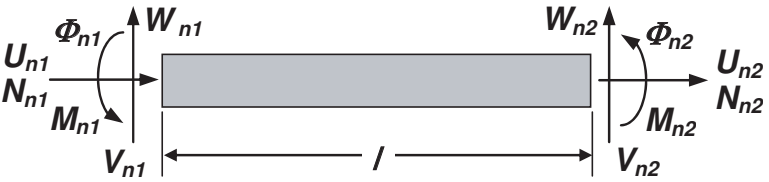

Figure 2. Sign convention for finite beam-plate element.

or in matrix-vector multiplication form as

$$\begin{aligned} U_n(x) &= \left[\boldsymbol{E}_{Un}(x;\omega_n)\right]\{\boldsymbol{C}_n\}, \\ W_n(x) &= \left[\boldsymbol{E}_{Wn}(x;\omega_n)\right]\{\boldsymbol{C}_n\}, \end{aligned} \tag{30}$$

where

$$\begin{aligned} \left[\boldsymbol{E}_{Un}(x;\omega_n)\right] &= \left[e^{k_{n1}x} \;\; 0 \;\; 0 \;\; e^{k_{n2}x} \;\; 0 \;\; 0\right], \\ \left[\boldsymbol{E}_{Wn}(x;\omega_n)\right] &= \left[0 \;\; e^{\lambda_{n1}x} \;\; e^{\lambda_{n2}x} \;\; 0 \;\; e^{\lambda_{n3}x} \;\; e^{\lambda_{n4}x}\right], \\ \{\boldsymbol{C}_n\} &= \left\{A_{n1} \;\; B_{n1} \;\; B_{n2} \;\; A_{n2} \;\; B_{n3} \;\; B_{n4}\right\}^T. \end{aligned}$$

The constant vector $\{\boldsymbol{C}_n\}$ will be determined by the boundary conditions.

Now consider a finite beam-plate element of length l as shown in Figure 2. The corresponding spectral components of the nodal degree of freedom (DOF) are defined by

$$\begin{aligned} U_{n1} &= U_{n1}(0), & W_{n1} &= W_{n1}(0), & \Phi_{n1} &= W'_{n1}(0), \\ U_{n2} &= U_{n2}(l), & W_{n2} &= W_{n2}(l), & \Phi_{n2} &= W'_{n2}(l). \end{aligned}$$

Applying these values to Equation (30) yields a relationship between the spectral nodal DOF vector $\{\boldsymbol{d}_n\}$ and the constant vector $\{\boldsymbol{C}_n\}$:

$$\{\boldsymbol{d}_n\} = \left[\boldsymbol{X}_n(\omega_n)\right]\{\boldsymbol{C}_n\}, \tag{31}$$

where $\{\boldsymbol{d}_n\} = \left\{U_{n1} \;\; W_{n1} \;\; \Phi_{n1} \;\; U_{n2} \;\; W_{n2} \;\; \Phi_{n2}\right\}^T$ and

$$[\boldsymbol{X}_n] = \begin{bmatrix} 1 & 0 & 0 & 1 & 0 & 0 \\ 0 & 1 & 1 & 0 & 1 & 1 \\ 0 & \lambda_{n1} & \lambda_{n2} & 0 & \lambda_{n3} & \lambda_{n4} \\ e^{k_{n1}l} & 0 & 0 & e^{k_{n2}l} & 0 & 0 \\ 0 & e^{\lambda_{n1}l} & e^{\lambda_{n2}l} & 0 & e^{\lambda_{n3}l} & e^{\lambda_{n4}l} \\ 0 & \lambda_{n1}e^{\lambda_{n1}l} & \lambda_{n2}e^{\lambda_{n2}l} & 0 & \lambda_{n3}e^{\lambda_{n3}l} & \lambda_{n4}e^{\lambda_{n4}l} \end{bmatrix}.$$

One can use (31) to eliminate the constant vector $\{\boldsymbol{C}_n\}$ from Equation (30), obtaining

$$\begin{aligned} U_n(x) &= [\boldsymbol{E}_{Un}][\boldsymbol{X}_n]^{-1}\{\boldsymbol{d}_n\} \equiv [\boldsymbol{N}_{Un}(x;\omega_n)]\{\boldsymbol{d}_n\}, \\ W_n(x) &= [\boldsymbol{E}_{Wn}][\boldsymbol{X}_n]^{-1}\{\boldsymbol{d}_n\} \equiv [\boldsymbol{N}_{Wn}(x;\omega_n)]\{\boldsymbol{d}_n\}, \end{aligned} \tag{32}$$

where $[\boldsymbol{N}_{Un}]$ and $[\boldsymbol{N}_{Wn}]$ are the dynamic (frequency-dependent) shape function matrices.

In the following, the well-known variational approach [Reddy 2002] is used to formulate the spectral element matrix by using the displacement fields given by Equation (32) and the temperature field given in the next section. The weak form statements of the governing equations (26) are

$$\int_0^l \left(\overline{EA}U_n'' + \rho A\omega_n^2 U_n + P_{xn}\right)\delta U_n\,dx = 0,$$

$$\int_0^l \left(DW''''_n + (\rho Ac^2 + \rho I\omega_n^2)W_n'' + 2i\rho Ac\omega_n W_n' - \rho A\omega_n^2 W_n - P_{zn}\right)\delta W_n\,dx = 0.$$

Substituting the loading terms from (27) into these equalities and integrating by parts yields

$$\int_0^l \left(\overline{EA}\,U_n'\,\delta U_n' - \rho A\omega_n^2 U_n\,\delta U_n\right)dx - \int_0^l P_{xn}\,\delta U_n\,dx - \tfrac{1}{2}N_{Tn}\,\delta U_n\big|_0^l - N_n\,\delta U_n\big|_0^l = 0,$$

$$\begin{aligned} &\int_0^l \Big(DW_n''\,\delta W_n'' - (\rho Ac^2 + \rho I\omega_n^2)W_n'\,\delta W_n' + i\rho Ac\omega_n(W_n'\,\delta W_n - W_n\,\delta W_n') \\ &\quad - \rho A\omega_n^2 W_n\,\delta W_n\Big)dx - \int_0^l P_{zn}\,\delta W_n\,dx + \tfrac{1}{2}M_{Tn}\,\delta W_n'\big|_0^l - V_n\,\delta W_n\big|_0^l - M_n\,\delta W_n'\big|_0^l = 0, \end{aligned}$$

where Equation (28) has been used and where, as before, the limits 0 and l refer to the variable x.

Substituting (32) into these two equalities yields

$$\{\delta\boldsymbol{d}_n\}^T\left([\boldsymbol{S}_{Un}]\{\boldsymbol{d}_n\} - \{\boldsymbol{f}_{Un}\}\right) = 0, \qquad \{\delta\boldsymbol{d}_n\}^T\left([\boldsymbol{S}_{Wn}]\{\boldsymbol{d}_n\} - \{\boldsymbol{f}_{Wn}\}\right) = 0, \tag{33}$$

where

$$\begin{aligned} [\boldsymbol{S}_{Un}] &= \int_0^l \left(\overline{EA}[\boldsymbol{N}_{Un}']^T[\boldsymbol{N}_{Un}'] - \rho A\omega_n^2[\boldsymbol{N}_{Un}]^T[\boldsymbol{N}_{Un}]\right)dx, \\ [\boldsymbol{S}_{Wn}] &= \int_0^l \Big(D[\boldsymbol{N}_{Wn}'']^T[\boldsymbol{N}_{Wn}''] - (\rho Ac^2 + \rho I\omega_n^2)[\boldsymbol{N}_{Wn}']^T[\boldsymbol{N}_{Wn}'] \\ &\quad + i\rho Ac\omega_n\left([\boldsymbol{N}_{Wn}]^T[\boldsymbol{N}_{Wn}'] - [\boldsymbol{N}_{Wn}']^T[\boldsymbol{N}_{Wn}]\right) - \rho A\omega_n^2[\boldsymbol{N}_{Wn}]^T[\boldsymbol{N}_{Wn}]\Big)dx, \end{aligned} \tag{34}$$

$$\{\boldsymbol{f}_{Un}\}=\{N_{1n}\ 0\ 0\ N_{2n}\ 0\ 0\}^T+\int_0^l P_{xn}(x)[\boldsymbol{N}_{Un}]^T dx-\tfrac{1}{2}N_{Tn}[\boldsymbol{N}_{Un}(l)-\boldsymbol{N}_{Un}(0)]^T,$$

$$\{\boldsymbol{f}_{Wn}\}=\{0\ V_{1n}\ M_{1n}\ 0\ V_{2n}\ M_{2n}\}^T+\int_0^l P_{zn}(x)[\boldsymbol{N}_{Wn}]^T dx + \tfrac{1}{2}M_{Tn}\left[\boldsymbol{N}'_{Wn}(l)-\boldsymbol{N}'_{Wn}(0)\right]^T.$$

The details of the matrices $[\boldsymbol{S}_{Un}]$ and $[\boldsymbol{S}_{Wn}]$ are given in the Appendix.

Since $\{\delta\boldsymbol{d}_n\}$ is arbitrary, the spectral element equation can be deduced from (33):

$$[\boldsymbol{S}_n(\omega)]\{\boldsymbol{d}_n\}=\{\boldsymbol{f}_n\}. \tag{35}$$

Here

$$[\boldsymbol{S}_n(\omega)]=[\boldsymbol{S}_{Un}(\omega)]+[\boldsymbol{S}_{Wn}(\omega)]$$

is the frequency-dependent spectral element matrix and

$$\{\boldsymbol{f}_n\}=\{\boldsymbol{f}_n\}_1+\{\boldsymbol{f}_n\}_2$$

is the spectral nodal force, where

$$\begin{aligned}\{\boldsymbol{f}_n\}_1&=\{N_{1n}\ V_{1n}\ M_{1n}\ N_{2n}\ V_{2n}\ M_{2n}\}^T,\\ \{\boldsymbol{f}_n\}_2&=\int_0^l P_{xn}(x)[\boldsymbol{N}_{Un}]^T dx+\int_0^l P_{zn}(x)[\boldsymbol{N}_{Wn}]^T dx\\ &\quad-\tfrac{1}{2}N_{Tn}[\boldsymbol{N}_{Un}(l)-\boldsymbol{N}_{Un}(0)]^T+\tfrac{1}{2}M_{Tn}[\boldsymbol{N}'_{Wn}(l)-\boldsymbol{N}'_{Wn}(0)]^T.\end{aligned} \tag{36}$$

All spectral elements can be assembled in a completely analogous way to that used in the conventional FEM. Assembling all spectral elements represented by (35) and then applying appropriate boundary conditions yields a global system equation in the form

$$[\boldsymbol{S}_n^G(\omega)]\{\boldsymbol{d}_n^G\}=\{\boldsymbol{f}_n^G\}.$$

The natural frequencies ω_{NAT} can be computed from the condition that the determinant of global spectral stiffness matrix $[\boldsymbol{S}_n^G]$ should vanish at natural frequencies:

$$\det[\boldsymbol{S}_n^G(\omega_{\mathrm{NAT}})]=0.$$

3C. ***Temperature in the frequency domain.*** The approximate temperature field is governed by Equation (18) and the thermal boundary conditions specified on the upper and lower surfaces of the beam-plate. As done in the preceding section for the displacements field, the temperature field can be also represented in the spectral form as

$$T(z,t)=\sum_{n=0}^{N-1}T_n(z)e^{i\omega_n t},$$

where T_n are the spectral components of temperature field $T(z,t)$. Substituting this equality into the heat conduction equation (18) yields

$$T_n^{\circ\circ} - i\omega_n \beta^2 T_n = 0, \tag{37}$$

where

$$\beta^2 = \frac{1}{k}\left(T_0 \alpha^2 E\eta + \rho c_p\right).$$

The general solution of Equation (37) can be readily obtained as

$$T_n(z) = B_{n1} e^{-\tau_n z} + B_{n2} e^{\tau_n z}, \tag{38}$$

where

$$\tau_n = \beta\sqrt{i\omega_n}\beta = (1+i)\beta\sqrt{\frac{\omega_n}{2}}. \tag{39}$$

The constants B_{n1} and B_{n2} are determined by the thermal boundary conditions specified on the upper and lower surfaces of beam-plate. Once the spectral components of temperature T are computed from (38), the corresponding spectral components of thermal moment M_T and thermal force N_T in (36) can be readily computed from (6) and (25).

4. Numerical results and discussion

As an illustrative example, a beam-plate which is axially moving over two simple supports of distance $L = 2$ m is considered. The beam-plate has thickness $h = 5$ mm, width $b = 0.5$ m, Young's modulus $E = 73$ GPa, Poisson's ratio $\nu = 0.33$, mass density $\rho = 2770\,\text{kg/m}^3$, thermal expansion coefficient $\alpha 23.0 \times 10^{-6}/K$, thermal conductivity $k = 177$ W/mK, and specific heat $c_p = 875$ J/kg· K. As shown in Figure 3, the temperature change is applied only to the middle part of the upper surface, while the remaining parts are allowed to remain at room temperature T_0.

First, to show the high accuracy of the present spectral element model, we compare in Table 1 the natural frequencies obtained for the beam-plate using the

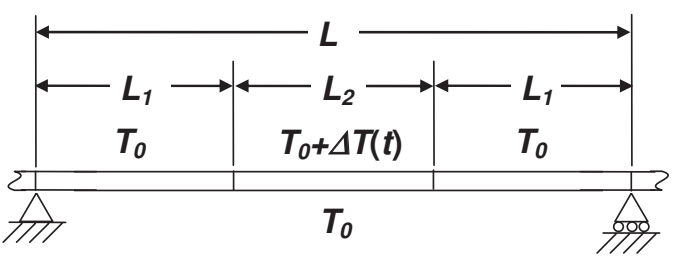

Figure 3. Example problem: thermal boundary conditions on the upper and lower surfaces of the beam-plate which moves axially over two simple supports.

c (m/s)	Method	N	$\omega_1^{(w)}$	$\omega_2^{(w)}$	$\omega_3^{(w)}$	$\omega_4^{(w)}$	$\omega_5^{(w)}$	$\omega_{15}^{(u)}$
0	Exact	–	3.083	12.329	27.743	49.321	77.066	679.78
	SEM	1	3.083	12.329	27.742	49.317	77.057	679.78
	FEM	10	3.083	12.331	27.758	49.403	77.371	680.48
		20	3.083	12.330	27.744	49.327	77.087	679.95
		50	3.083	12.329	27.743	49.322	77.067	679.81
		100	3.083	12.329	27.743	49.322	77.067	679.79
4	SEM	1	2.886	12.197	27.626	49.210	76.955	679.78
	FEM	10	2.886	12.198	27.643	49.298	77.274	680.48
		20	2.886	12.197	27.628	49.220	76.985	679.95
		50	2.886	12.197	27.627	49.215	76.966	679.81
		100	2.886	12.197	27.627	49.215	76.965	679.79
8	SEM	1	2.248	11.790	27.277	48.889	76.649	679.78
	FEM	10	2.248	11.792	27.296	48.983	76.982	680.48
		20	2.248	11.790	27.280	48.899	76.681	679.95
		50	2.248	11.790	27.279	48.893	76.660	679.81
		100	2.248	11.790	27.279	48.893	76.659	679.79
12.33	SEM	1	0.0	11.012	26.631	48.297	76.087	679.78
	FEM	10	0.0	11.015	26.654	48.402	76.446	680.48
		20	0.0	11.012	26.634	48.307	76.120	679.95
		50	0.0	11.012	26.633	48.301	76.098	679.81
		100	0.0	11.012	26.633	48.301	76.097	679.79

Table 1. Natural frequencies (Hz) of a beam-plate obtained by the present SEM, the FEM and the exact theory [Blevins 1979]. N is the number of finite elements used in the analysis, c is the fluid velocity, and the superscripts (w) and (u) stand respectively for the transverse and axial displacement modes.

present spectral element model (SEM), the finite element model (FEM), and the exact theory (only for stationary beam), for various speeds of the beam-plate. The number of finite elements used in the FEM varies from 10 to 100, while only one finite element is used for the SEM. The table shows that the SEM results are almost same as the exact values when $c = 0$, and the FEM values converge to the SEM values when $c \neq 0$ as the number of finite elements used in FEM is increased. This suggests that the present spectral element model is very accurate.

One more thing we can observe from Table 1 is that in general the magnitude of natural frequency (real part of eigenfrequency) decreases as the moving speed of beam-plate is increased. The first natural frequency becomes zero at

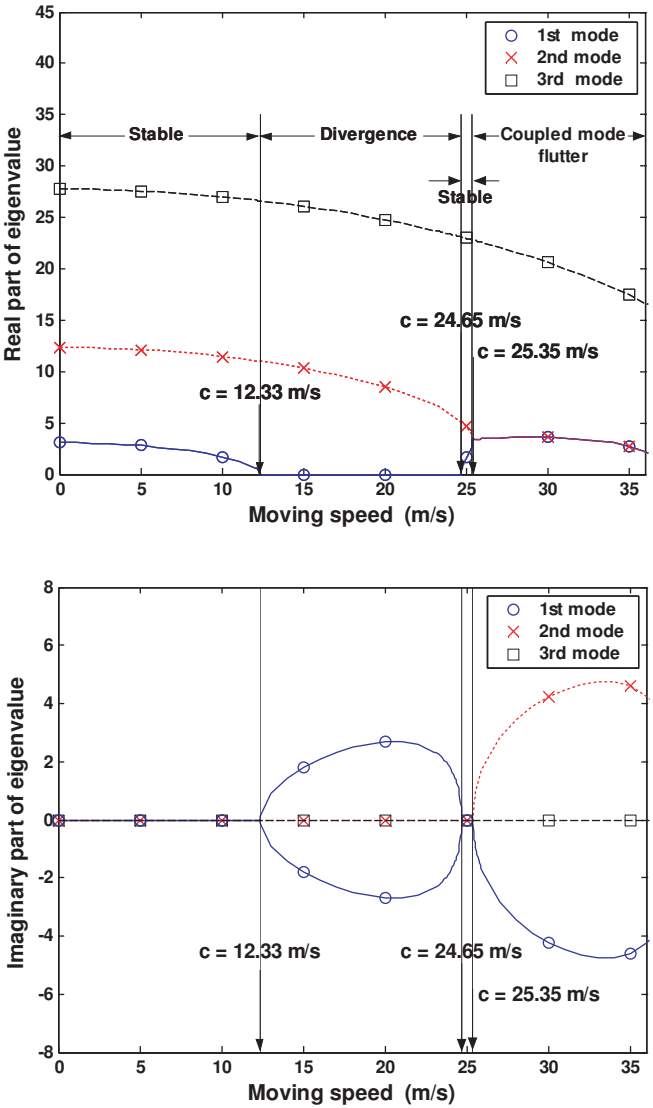

Figure 4. Moving speed dependence of the lowest first three eigenfrequencies of beam-plate.

$c = 12.33$ m/s, which is the divergence speed at which the divergence instability may occur. Figure 4 shows in detail how the eigenfrequency of beam-plate varies as the moving speed of beam-plate is increased. One can see from Figure 4 that the beam-plate will have divergence instability at $c = 12.33$ m/s and coupled-mode flutter instability at $c = 25.35$ m/s.

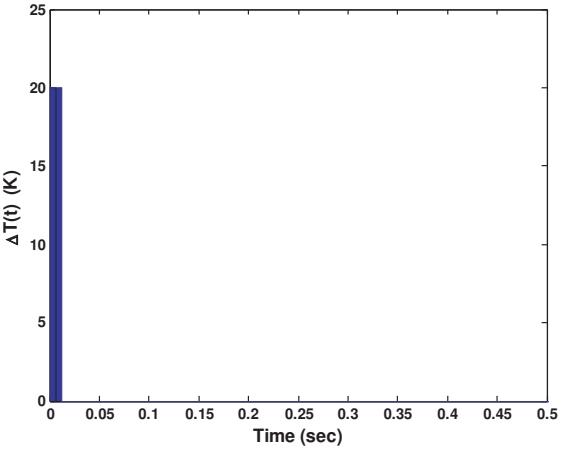

Figure 5. Time history of the thermal load applied on the middle region (L_2) of the upper surface of beam-plate shown in Figure 3.

To investigate the thermally induced vibration of the beam-plate, the temperature on the middle part of the upper surface of the beam-plate is suddenly elevated so that $\Delta T = 20\,\mathrm{K}$ and the elevated temperature is sustained for 0.01 seconds from $t = 0$, as shown in Figure 5. Figure 6 shows the time history of the temperature distribution through the thickness of the beam-plate, and Figure 7

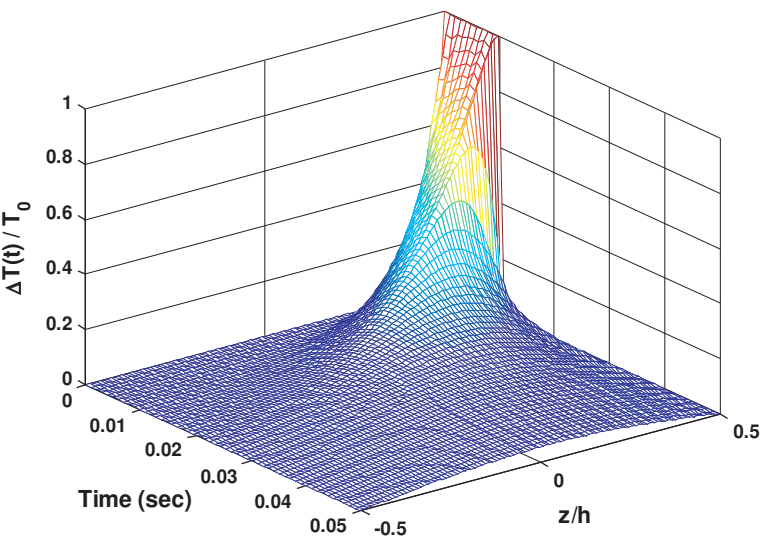

Figure 6. Time history of temperature distribution through the thickness of beam-plate.

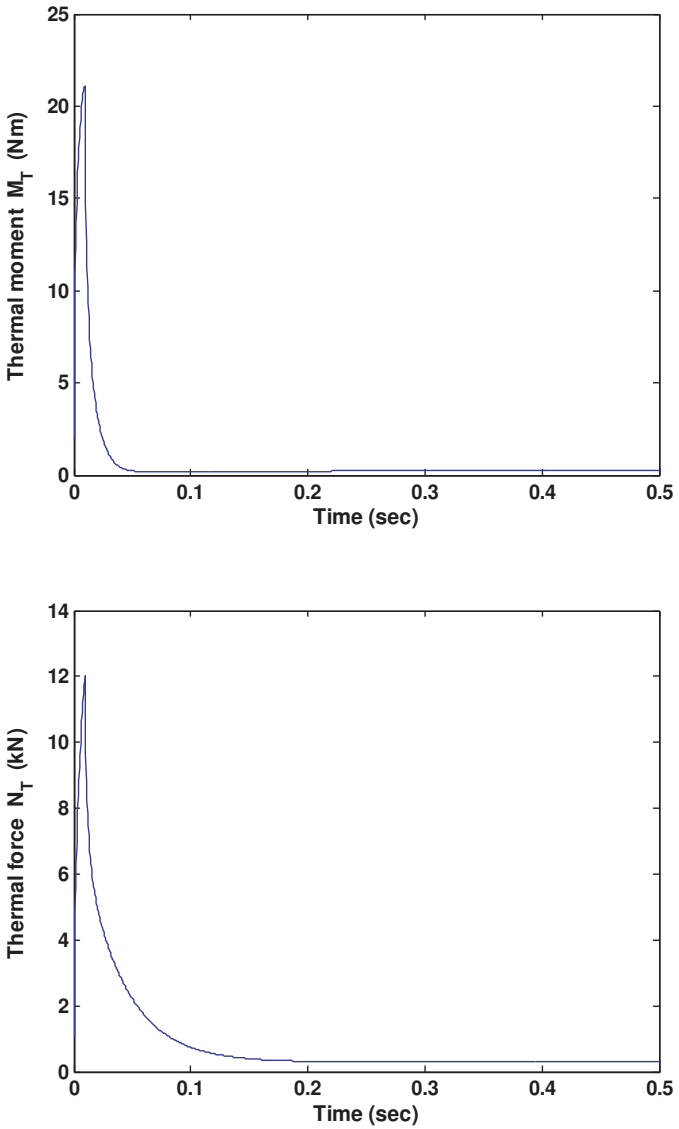

Figure 7. Time histories of the thermal moment M_T and thermal force N_T in the region $L_1 \leq x \leq (L - L_2)$.

shows the corresponding thermal moment M_T and thermal force N_T in the region $L_1 \leq x \leq \quad L - L_2$. Notice that $L_1 = L_3 = 0.8\,\text{m}$ and $L_2 = 0.4\,\text{m}$. Figure 6 shows that the temperature quickly spreads out to become symmetric with respect to the middle plane of the beam-plane. Accordingly the thermal moment M_T disappears after about 0.05 seconds, while the thermal force N_T converges to a small value.

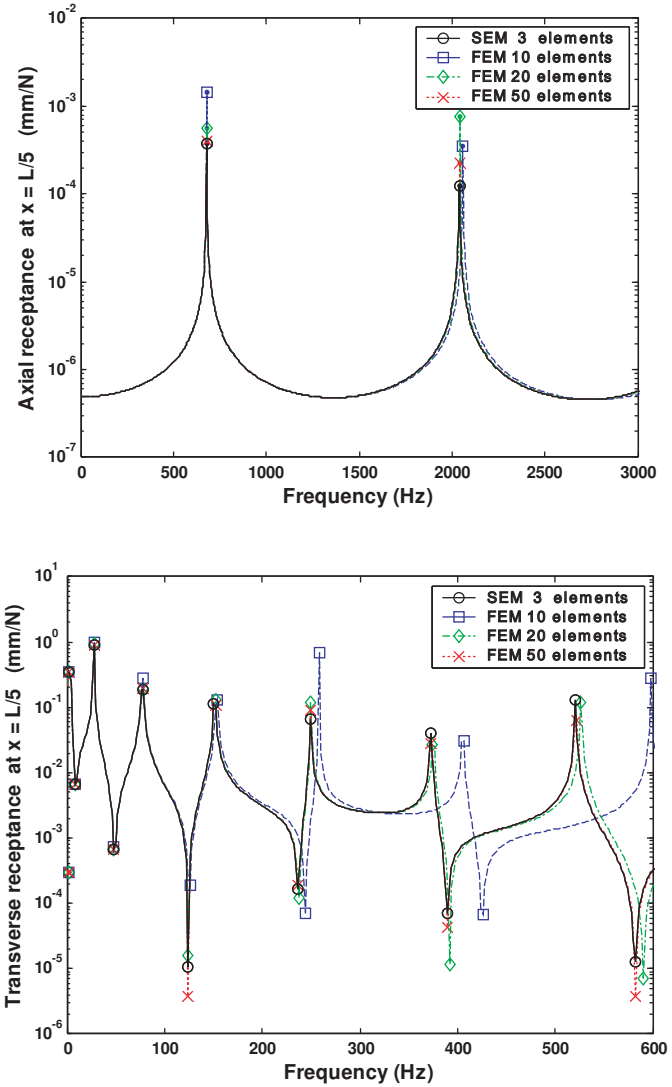

Figure 8. Comparison of the frequency response functions of the axial and transverse displacements obtained by the present SEM and FEM when $c = 4$ m/s and $L_2 = 0.2L$.

Figure 8 compares the frequency response functions obtained by the present SEM and FEM. Similarly Figure 9 compares the corresponding time responses. It is clear from both figures that FEM results converge to SEM results as the number of finite elements used in FEM is increased, which also proves the high accuracy of the present spectral element model. Notice that the minimum number of finite

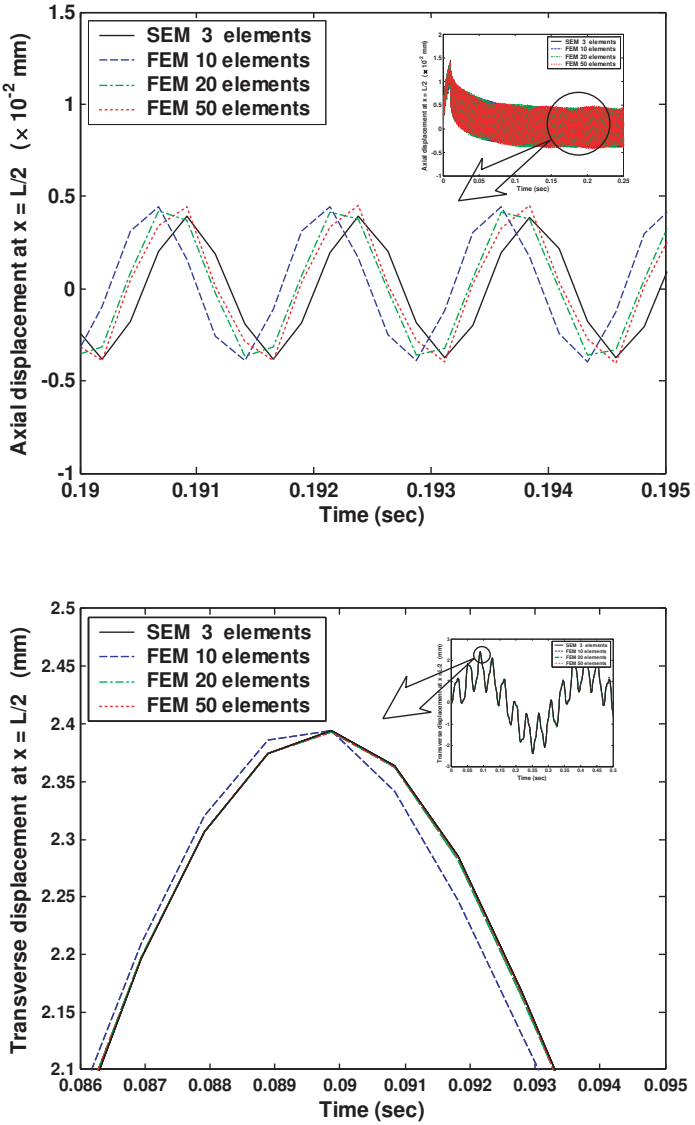

Figure 9. Comparison of the axial and transverse displacements obtained by the present SEM and FEM when $c = 4$ m/s and $L_2 = 0.2L$.

elements used in SEM is three, because the beam-plate has temperature discontinuities at $x = L_1$ and $x = L_1 + L_2$.

Figure 10 shows the time responses of transverse displacement at three different moving speeds of beam-plate. From Figure 10, one can observe that the period of time response increases as the moving speed increases. As previously discussed,

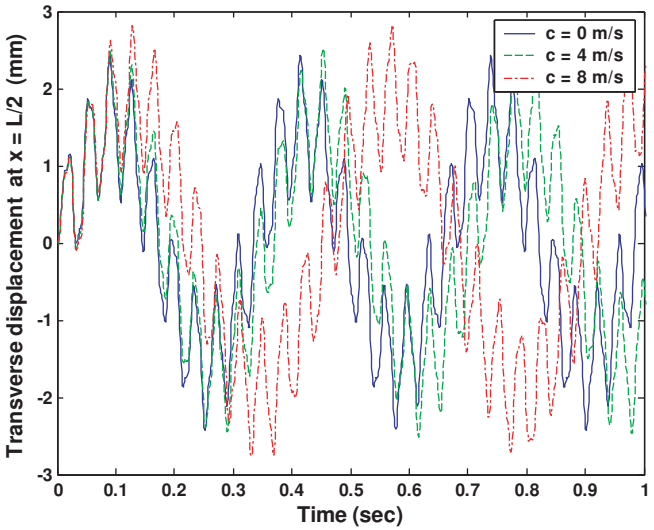

Figure 10. Transverse displacement versus moving speed c when $L_2 = 0.2L$.

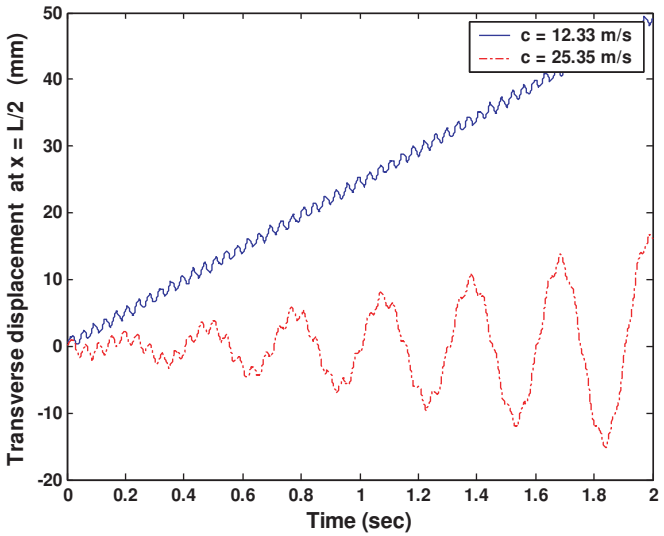

Figure 11. Transverse displacements when $c = 12.33$ m/s (divergence speed) and $c = 25.35$ m/s (flutter speed) when $L_2 = 0.2L$.

this is because the natural frequencies decrease as the moving speed increases. Figure 11 shows the time responses at divergence speed $c = 12.33$ m/s and flutter speed $c = 25.35$ m/s. As expected, the divergence and flutter instabilities indeed occur at the divergence and flutter speeds, respectively.

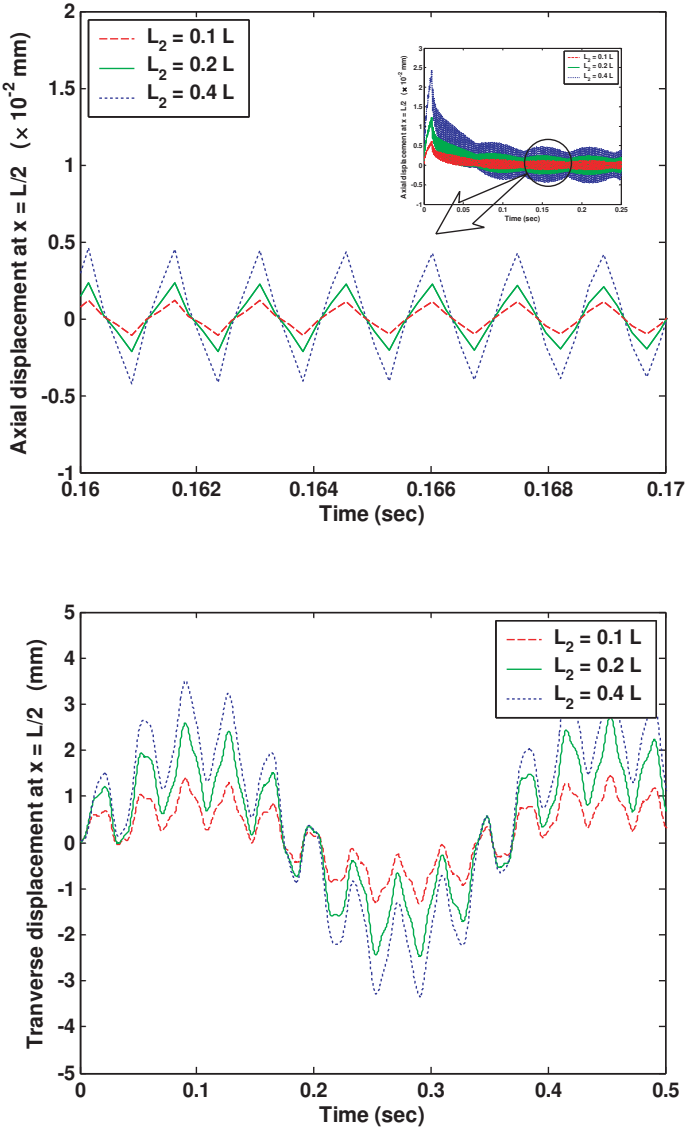

Figure 12. Axial and transverse displacements versus size of L_2 on which thermal load is applied when $c = 4$ m/s.

Figure 12 shows the time responses of axial and transverse displacements depending on the length of middle part (L_2) subjected to the sudden temperature change of Figure 5, when the moving speed of beam-plate is $c = 4$ m/s. The time responses in both axial and transverse displacements tend to increase as the length of middle part becomes larger.

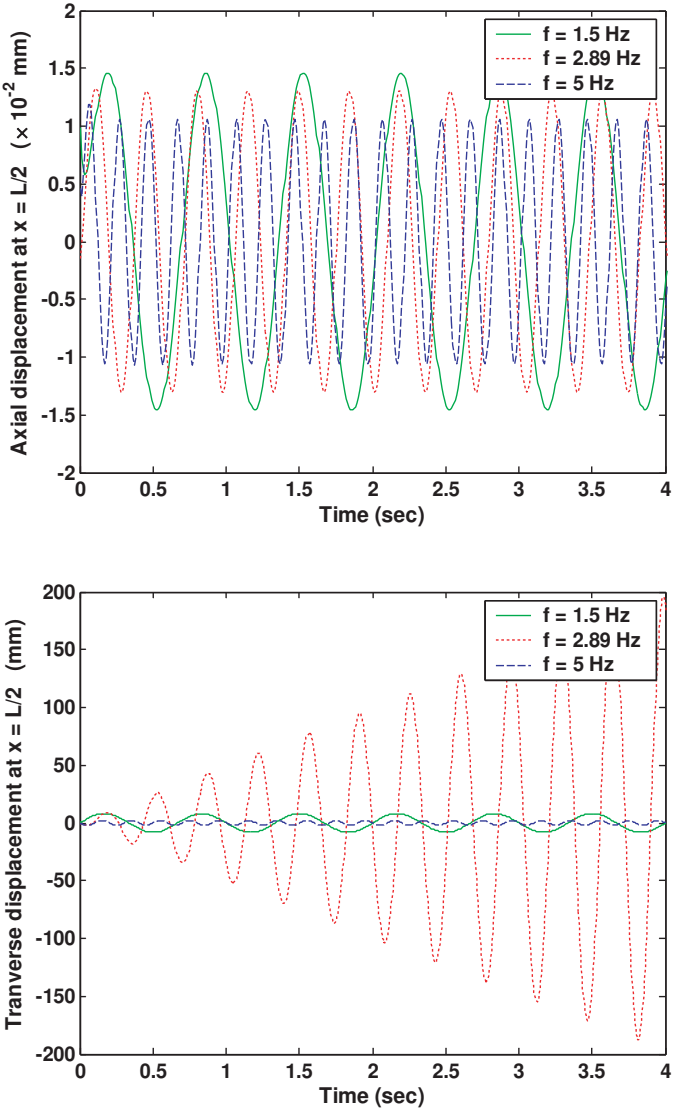

Figure 13. Axial and transverse displacements versus excitation frequency f of the thermal load given by $\Delta T(x,t) = 10\sin(2\pi f t) + 20(K)$ when $c = 4$ m/s and $L_2 = 0.2L$.

Figure 13 compares the axial and transverse displacements excited by a harmonic thermal load defined by $\Delta T(x,t) = 10\sin(2\pi f t) + 20(K)$ when $c = 4$ m/s and $L_2 = 0.2L$. It is obvious from Figure 13 that the resonance in transverse vibration mode occurs when the excitation frequency f is close to the first transverse natural frequency 2.886 Hz (see Table 1).

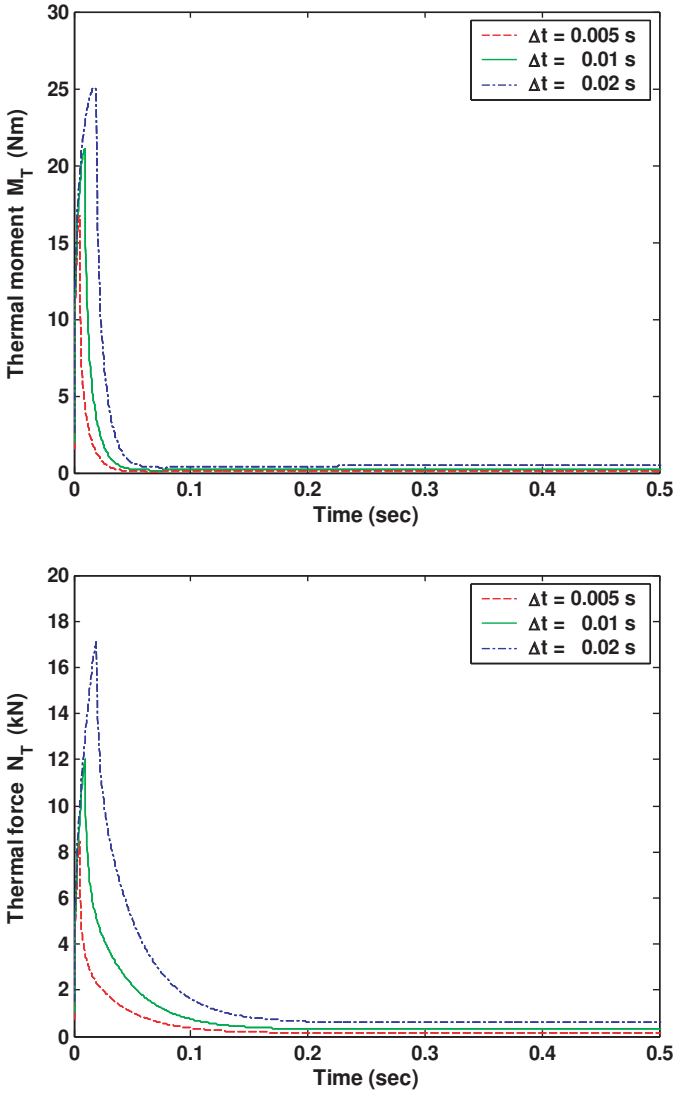

Figure 14. Time histories of the thermal moment M_T and thermal force N_T in the region $L_1 \leq x \leq (L - L_2)$ versus duration of thermal load Δt when $c = 4$ m/s.

Figure 14 shows the time histories of the thermal moments M_T and thermal forces N_T in the region $L_1 \leq x \leq (L - L_2)$ for different durations of thermal load, Δt, and Figure 15 shows the corresponding axial and transverse displacements. In general, it is shown that the amplitudes of vibration become larger as the duration of thermal load becomes larger.

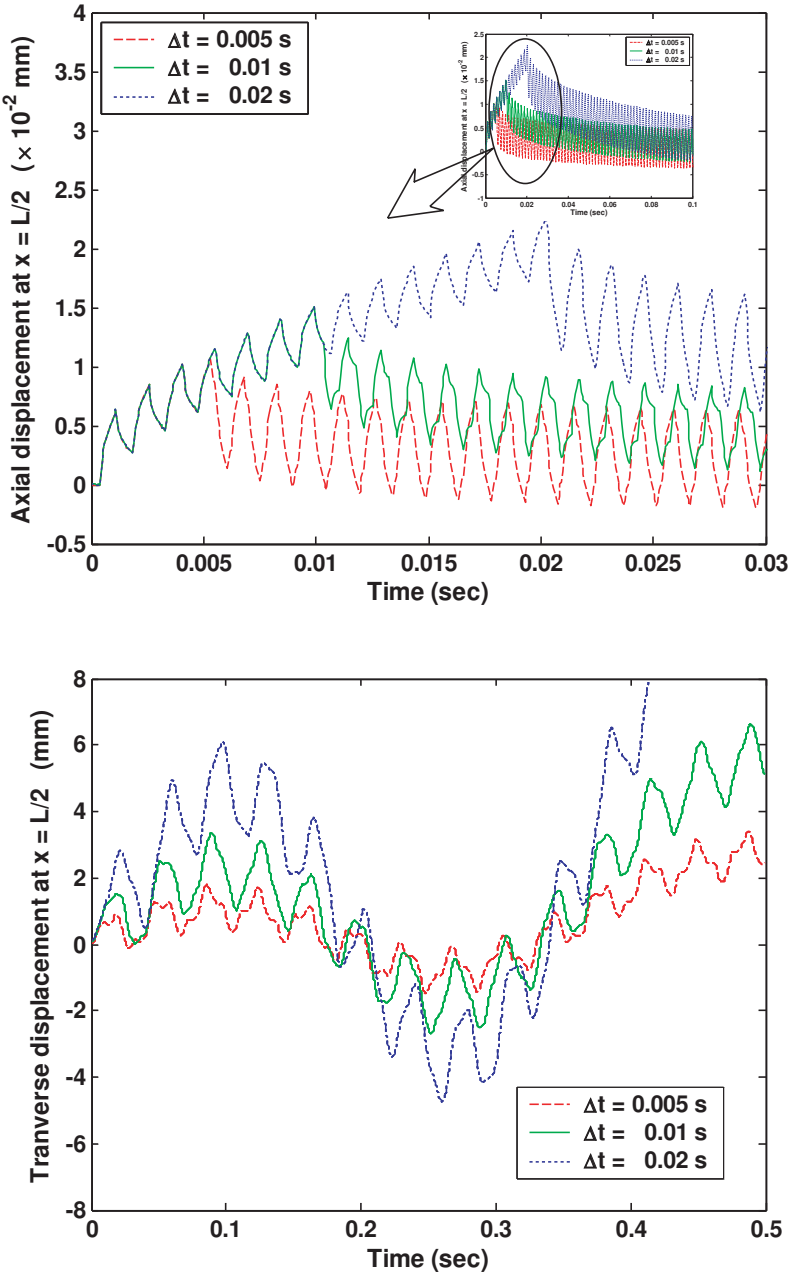

Figure 15. Time responses of axial and transverse displacements versus duration of thermal load Δt when $c = 4$ m/s.

5. Conclusions

We develop a spectral element model for an axially moving beam-plate subjected to external thermal loads. The model is formulated from frequency-dependent dynamic shape functions that are exact frequency-domain solutions of governing equations, and it is evaluated by comparison with the conventional finite element model. Numerical studies show the high accuracy of the present method and allow us to model the thermally induced vibration of an axially moving beam-plate subjected to a sudden temperature change on the upper surface of the beam-plate.

Appendix

Matrices $[\boldsymbol{S_{Un}}]$ ***and*** $[\boldsymbol{S_{Wn}}]$ ***in Equation*** (34)**.**

$$[\boldsymbol{S}_{Un}] = [\boldsymbol{X}_n^{-1}]^T [\boldsymbol{R}_{Un}][\boldsymbol{X}_n^{-1}], \quad \text{where} \quad [\boldsymbol{R}_{Un}] = \begin{bmatrix} Y_{n11} & 0 & 0 & Y_{n14} & 0 & 0 \\ 0 & 0 & 0 & 0 & 0 & 0 \\ 0 & 0 & 0 & 0 & 0 & 0 \\ Y_{n14} & 0 & 0 & Y_{n44} & 0 & 0 \\ 0 & 0 & 0 & 0 & 0 & 0 \\ 0 & 0 & 0 & 0 & 0 & 0 \end{bmatrix} \quad \text{and}$$

$$Y_{nij} = \frac{e^{(k_{ni}+k_{nj})l} - 1}{k_{ni} + k_{nj}} (\overline{EA} k_{ni} k_{nj} - \rho A \omega_n^2).$$

$$[\boldsymbol{S}_{Wn}] = [\boldsymbol{X}_n^{-1}]^T [\boldsymbol{R}_{Wn}][\boldsymbol{X}_n^{-1}], \quad \text{where} \quad [\boldsymbol{R}_{Wn}] = \begin{bmatrix} 0 & 0 & 0 & 0 & 0 & 0 \\ 0 & X_{n11} & X_{n12} & 0 & X_{n13} & X_{n14} \\ 0 & X_{n12} & X_{n22} & 0 & X_{n23} & X_{n24} \\ 0 & 0 & 0 & 0 & 0 & 0 \\ 0 & X_{n13} & X_{n23} & 0 & X_{n33} & X_{n34} \\ 0 & X_{n14} & X_{n24} & 0 & X_{n34} & X_{n44} \end{bmatrix}$$

$$\text{and } X_{nij} = \frac{e^{(\lambda_{ni}+\lambda_{nj})l} - 1}{\lambda_{ni} + \lambda_{nj}} \left(D\lambda_{ni}^2 \lambda_{nj}^2 - R_n \lambda_{ni} \lambda_{nj} + i\rho A c \omega_n (\lambda_{ni} - \lambda_{nj}) - \rho A \omega_n^2 \right).$$

The finite element model

The finite element model used in this study is formulated by assuming the displacement fields within a finite beam-plate element of length l as follows:

$$u(x,t) = [\boldsymbol{N}_U(x)]\{\boldsymbol{d}(t)\}, \qquad w(x,t) = [\boldsymbol{N}_W(x)]\{\boldsymbol{d}(t)\},$$

where $\{\boldsymbol{d}(t)\}$ is the nodal DOF vector defined by

$$\{\boldsymbol{d}(t)\} = \begin{Bmatrix} u_1(t) & w_1(t) & \phi_1(t) & u_2(t) & w_2(t) & \phi_2(t) \end{Bmatrix}^T$$

and $[\boldsymbol{N}_U(t)]$ and $[\boldsymbol{N}_W(t)]$ are the shape function matrices defined by

$$[\boldsymbol{N}_U(x)] = \begin{bmatrix} 1-\xi & 0 & 0 & \xi & 0 & 0 \end{bmatrix} \quad \text{and} \quad [\boldsymbol{N}_W(x)] = \begin{bmatrix} 0 & N_{W1} & N_{W2} & 0 & N_{W3} & N_{W4} \end{bmatrix},$$

where $\xi = x/l$ and

$$N_{W1}=2\xi^3-3\xi^2+1, \quad N_{W2}=l\xi(\xi-1)^2, \quad N_{W3}=-2\xi^3+3\xi^2, \quad N_{W4}=l\xi(\xi^2-\xi).$$

Following the usual procedure [Reddy 2002], the finite element equation can be derived as

$$[\boldsymbol{M}]\{\ddot{\boldsymbol{d}}\}+[\boldsymbol{C}]\{\ddot{\boldsymbol{d}}\}+[\boldsymbol{K}]\{\boldsymbol{d}\}=\{\boldsymbol{f}\},$$

where $\{\boldsymbol{f}\}$ is the nodal force vector defined by

$$\{\boldsymbol{f}\}=\begin{Bmatrix} N_1-N_T/2 & V_1 & M_1+M_T/2 & N_2+N_T/2 & V_2 & M_2-M_T/2 \end{Bmatrix}^T + \int_0^l \left(p_x[\boldsymbol{N}_U]^T + p_z[\boldsymbol{N}_W]^T\right) dx$$

and the finite element matrices $[\boldsymbol{M}]$, $[\boldsymbol{C}]$, and $[\boldsymbol{K}]$ are given by

$$[\boldsymbol{M}] = \int_0^l \left(\rho A[\boldsymbol{N}_U]^T[\boldsymbol{N}_U] + \rho A[\boldsymbol{N}_W]^T[\boldsymbol{N}_W] - \rho I[\boldsymbol{N}'_W]^T[\boldsymbol{N}'_W]\right) dx$$

$$= \frac{\rho Al}{420}\begin{bmatrix} 140 & 0 & 0 & 70 & 0 & 0 \\ 0 & 156 & 22l & 0 & 54 & -13l \\ 0 & 22l & 4l^2 & 0 & 13l & -3l^2 \\ 70 & 0 & 0 & 140 & 0 & 0 \\ 0 & 54 & 13l & 0 & 156 & -22l \\ 0 & -13l & -3l^2 & 0 & -22l & 4l^2 \end{bmatrix} - \frac{\rho I}{30l}\begin{bmatrix} 0 & 0 & 0 & 0 & 0 & 0 \\ 0 & 36 & 3l & 0 & -36 & 3l \\ 0 & 3l & 4l^2 & 0 & -3l & l^2 \\ 0 & 0 & 0 & 0 & 0 & 0 \\ 0 & -36 & -3l & 0 & 36 & -3l \\ 0 & 3l & -l^2 & 0 & -3l & 4l^2 \end{bmatrix}$$

$$[\boldsymbol{C}] = \int_0^l \left(\rho Ac\left([\boldsymbol{N}_W]^T[\boldsymbol{N}'_W] - [\boldsymbol{N}'_W]^T[\boldsymbol{N}_W]\right)\right) dx = \frac{\rho Ac}{30}\begin{bmatrix} 0 & 0 & 0 & 0 & 0 & 0 \\ 0 & 0 & 6l & 0 & 30 & -6l \\ 0 & -6l & 0 & 0 & 6l & -l^2 \\ 0 & 0 & 0 & 0 & 0 & 0 \\ 0 & -30 & -6l & 0 & 0 & 6l \\ 0 & 6l & l^2 & 0 & -6l & 0 \end{bmatrix}$$

$$[\boldsymbol{K}] = \int_0^l \left(\overline{EA}[\boldsymbol{N}'_U]^T[\boldsymbol{N}'_U] + D[\boldsymbol{N}''_W]^T[\boldsymbol{N}''_W] + \rho Ac^2[\boldsymbol{N}'_W]^T[\boldsymbol{N}'_W]\right) dx$$

$$= \frac{\overline{EA}}{l}\begin{bmatrix} 1 & 0 & 0 & -1 & 0 & 0 \\ 0 & 0 & 0 & 0 & 0 & 0 \\ 0 & 0 & 0 & 0 & 0 & 0 \\ -1 & 0 & 0 & 1 & 0 & 0 \\ 0 & 0 & 0 & 0 & 0 & 0 \\ 0 & 0 & 0 & 0 & 0 & 0 \end{bmatrix} + \frac{D}{l^3}\begin{bmatrix} 0 & 0 & 0 & 0 & 0 & 0 \\ 0 & 12 & 6l & 0 & -12 & 6l \\ 0 & 6l & 4l^2 & 0 & -6l & 2l^2 \\ 0 & 0 & 0 & 0 & 0 & 0 \\ 0 & -12 & -6l & 0 & 12 & -6l \\ 0 & 6l & 2l^2 & 0 & -6l & 4l^2 \end{bmatrix} -$$

$$-\frac{\rho A c^2}{30l}\begin{bmatrix} 0 & 0 & 0 & 0 & 0 & 0 \\ 0 & 36 & 3l & 0 & -36 & 3l \\ 0 & 3l & 4l^2 & 0 & -3l & -l^2 \\ 0 & 0 & 0 & 0 & 0 & 0 \\ 0 & -36 & -3l & 0 & 36 & -3l \\ 0 & 3l & -l^2 & 0 & -3l & 4l^2 \end{bmatrix}.$$

References

[Al-Huniti 2004] N. S. Al-Huniti, "Dynamic behavior of a laminated beam under the effect of a moving heat source", *J. Compos. Mater.* **38**:23 (2004), 2143–2160.

[Arafat et al. 2003] H. N. Arafat, W. Faris, and A. H. Nayfeh, "Vibrations and buckling of annular and circular plates subjected to a thermal load", in *44th AIAA/ASME/ASCE/AHS Structures, Structural Dynamics, and Materials Conference* (Norfolk, VA, 2003), AIAA, 2003.

[Beck and McMasters 2004] J. V. Beck and R. L. McMasters, "Solutions for multi-dimensional transient heat conduction with solid body motion", *Int. J. Heat Mass Transf.* **47**:17–18 (2004), 3757–3768.

[Biot 1956] M. Biot, "Thermoelasticity and irreversible thermodynamics", *J. Appl. Phys.* **27** (1956), 240–253.

[Blevins 1979] R. D. Blevins, *Formulas for natural frequency and mode shape*, Van Nostrand Reinhold, New York, 1979.

[Boley 1956] B. A. Boley, "Thermally induced vibrations of beams", *J. Aeronaut. Sci.* **23** (1956), 179–181.

[Boley and Barber 1957] B. A. Boley and A. D. Barber, "Dynamic response of beams and plates to rapid heating", *J. Appl. Mech.* (*Trans. ASME*) **24** (1957), 413–416.

[Chandrashekhara and Tenneti 1994] K. Chandrashekhara and R. Tenneti, "Non-linear static and dynamic analysis of heated laminated plates: a finite element approach", *Compos. Sci. Technol.* **51**:1 (1994), 85–94.

[Eslami and Vahedi 1989] M. R. Eslami and H. Vahedi, "Coupled thermoelasticity beam problems", *AIAA J.* **27**:5 (1989), 662–665.

[Kidawa-Kukla 1997] J. Kidawa-Kukla, "Vibration of a beam induced by harmonic motion of a heat source", *J. Sound Vib.* **205**:2 (1997), 213–222.

[Kinra and Milligan 1994] V. K. Kinra and K. B. Milligan, "A second-law analysis of thermoelastic damping", *J. Appl. Mech.* (*Trans. ASME*) **61** (1994), 71–76.

[Kozlov 1972] V. Kozlov, "Thermoelastic vibrations of a rectangular plate", *Prikl. Mat. Mekh* **8** (1972), 123–127.

[Lee 1985] U. Lee, "Thermoelastic and electromagnetic damping analysis", *AIAA J.* **23**:11 (1985), 1783–1790.

[Lee 2004] U. Lee, *Spectral element method in structural dynamics*, Inha University Press, Incheon, Korea, 2004.

[Lee and Leung 2000] U. Lee and A. Y. T. Leung, "The spectral element method in structural dynamics", *Shock Vibr. Dig.* **32**:6 (2000), 451–465.

[Lord and Shulman 1967] H. Lord and Y. Shulman, "A generalized dynamical theory of thermoelasticty", *J. Mech. Phys. Solids* **15**:5 (1967), 299–309.

[Manolis and Beskos 1980] G. D. Manolis and D. E. Beskos, "Thermally induced vibrations of beam structures", *Comput. Methods Appl. Mech. Eng.* **21**:3 (1980), 337–355.

[Massalas and Kalpakidis 1984] C. V. Massalas and V. K. Kalpakidis, "Coupled thermoelastic vibrations of a Timoshenko beam", *Lett. Appl. Eng. Sci.* **22**:4 (1984), 459–465.

[Massalas et al. 1982] C. V. Massalas, A. Dalamangas, and G. Tzivanidis, "A note on the dynamics of thermoelastic thin plates", *J. Sound Vib.* **81**:2 (1982), 303–306.

[Mukherjee and Sinha 1996] N. Mukherjee and P. K. Sinha, "Thermal shocks in composite plates: a coupled thermoelastic finite element analysis", *Compos. Struct.* **34**:1 (1996), 1–12.

[Newland 1993] D. E. Newland, *Random vibrations, spectral and wavelet analysis*, 3 ed., Longman, New York, 1993.

[Oguamanam et al. 2004] D. C. D. Oguamanam, J. S. Hansen, and G. R. Heppler, "Nonlinear transient response of thermally loaded laminated panels", *J. Appl. Mech.* (*Trans. ASME*) **71**:1 (2004), 49–56.

[Özisik 1993] M. N. Özisik, *Heat conduction*, 2 ed., Wiley, New York, 1993.

[Reddy 2002] J. N. Reddy, *Energy principles and variational methods in applied mechanics*, Wiley, Hoboken, 2002.

[Sharma 2001] J. N. Sharma, "Three-dimensional vibration analysis of a homogeneous transversely isotropic thermoelastic cylindrical panel", *J. Acoust. Soc. Am.* **110**:1 (2001), 254–259.

[Takeuti and Furukawa 1981] Y. Takeuti and T. Furukawa, "Some considerations on thermal shock problems in a plate", *J. Appl. Mech.* (*Trans. ASME*) **48**:2 (1981), 113–118.

[Takeuti et al. 1983] Y. Takeuti, R. Ishida, and Y. Tanigawa, "On an axisymmetric coupled thermal stress problem in a finite circular cylinder", *J. Appl. Mech.* (*Trans. ASME*) **50** (1983), 116–121.

[Tauchert 1991] T. R. Tauchert, "Thermally induced flexure, buckling, and vibration of plates", *Appl. Mech. Rev.* **44**:8 (1991), 347–360.

[Thornton 1992] E. A. Thornton, "Thermal structures: four decades of progress", *J. Aircr.* **29**:3 (1992), 485–498.

[Trajkovski and Čukić 1999] D. Trajkovski and R. Čukić, "A coupled problem of thermoelastic vibrations of a circular plate with exact boundary conditions", *Mech. Res. Commun.* **26**:2 (1999), 217–224.

[Ugral 1999] A. C. Ugral, *Stresses in plates and shells*, McGraw-Hill, New York, 1999.

[Verma 2001] K. L. Verma, "Thermoelastic vibrations of a transversely isotropic plate with thermal relaxations", *Int. J. Solids Struct.* **38**:46–47 (2001), 8529–8546.

[Yu 1969] Y. Y. Yu, "Thermally induced vibration and flutter of a flexible boom", *J. Spacecr. Rockets* **6**:8 (1969), 902–910.

Received 28 Sep 2005.

KYUNGSOO KWON: g2041021@inhaian.net
Department of Mechanical Engineering, Inha University, 253 Yonghyun-Dong, Nam-Ku, Incheon 402-751, Korea

USIK LEE: ulee@inha.ac.kr
Department of Mechanical Engineering, Inha University, 253 Yonghyun-Dong, Nam-Ku, Incheon 402-751, Korea

JOURNAL OF MECHANICS OF MATERIALS AND STRUCTURES
Vol. 1, No. 4, 2006

AN ATOMISTIC INSTABILITY CONDITION AND APPLICATIONS

JIA LU AND LIANG ZHANG

We present an atomic-level criterion for material stability in an atomic system. The criterion draws on the strong ellipticity condition in continuum elasticity theory; however, it is formulated directly in terms of atomic potential without resorting to the continuum concepts. Since the criterion is based on local energetics at an atomic site, we expect it to be applicable to pre-defected systems, provided that the site energy can be reasonably defined. The kinetic implication of the stability condition is also discussed. The application in nanotubes shows that the criterion can capture the tensile limit strain of both perfect and defective nanotubes, and the predictions agree well with the atomistic simulations reported in the literature.

1. Introduction

The loss of elastic stability in an atomic lattice is often a precursor to defect nucleation. For a nonhomogeneous system, lattice instability typically occurs first at "weak spots" where the local deformation has exceeded the stability limit. If loaded further, the lattice may respond by irreversible deformations such as bond breaking, defect nucleation or topological transformation. Thus, local instability provides fundamental information about elastic limit and ultimately the strength of an atomic structure. Present atomistic simulations such as molecular dynamics can provide invaluable details of the mechanical motion of atomic systems. However, to extract physical insight into the system behavior especially the onset of local irreversible motion requires the identification of indicators that characterize the critical state at which the transition occurs.

To motivate the stability condition presented in this work, it is instructive to review relevant concepts in elastic stability at continuum scale. The stability of a finitely deforming elastic body under quasistatic load is typically characterized by the positiveness of the increment of the free energy in reconfigurations from an equilibrium state [Truesdell and Noll 1965]. Stability conditions may be divided into two categories: one is for *structural stability* that characterizes the stability of the entire system including possibly the energetic contribution from the external load;

Keywords: Strong ellipticity condition, acoustic tensor, lattice stability, carbon nanotube.

the other is for *material stability* that concerns the stability of an isolated material element. In nonlinear elasticity, the material stability is characterized by the strong ellipticity condition [Ogden 1997; Ciarlet 1988]. Van Hove [1947] showed that the strong ellipticity condition guarantees the uniqueness of solution for Dirichlet boundary value problems. In the context of stability, the condition precludes the existence of any nonzero reconfiguration that does not alter its boundary. The loss of strong ellipticity, on the other hand, indicates that the stationary acceleration wave [Hill 1962] or locally supported discontinuous bifurcation [Rice 1976] becomes admissible in an initially homogeneous deformation field. The stability governed by the strong ellipticity condition, therefore, corresponds to Gibbs' notion of internal stability that requires a system be stable under arbitrary reconfigurations that leave the boundary unaltered [Gibbs 1993]. The condition is intrinsic to the material since the energetic influence from the external environment is excluded.

The local stability considered in this work can be intuitively understood as material stability in atomic systems. Numerous studies have reported on the elastic stability of crystal lattice. Born and Huang [1954] and others [Hill and Milstein 1977; Wang and Yip 1993; Wang et al. 1995; Morris and Krenn 2000] treated a unit cell as an elastic system, and derived stability conditions for perfect crystals. These criteria are formulated in terms of the local stress and the elasticity tensor; however, they are derived under the assumption that the unit cell deforms homogeneously, which is valid only for simple lattice. The analysis of material stability can be further complicated by the presence of defects. Presently, there is no unified method for local stability in defective systems. Kitamura et al. [2004a; 2004b] proposed to detect the instability by the singularity of the *global* tangent stiffness matrix. The method applies to general systems; however, it is for structural stability and the detected unstable motions include global modes such as elastic buckling. Dmitriev et al. [2004] proposed a scheme of local analysis that considers only atoms in a small region of interest. The method, strictly speaking, is not of material stability analysis. Yashiro and Tomita [2001] used Wang's criteria [Wang and Yip 1993; Wang et al. 1995], which are for defect-free simple lattice, to predict the material stability in defective system. The results showed a reasonable correlation with molecular dynamics simulations, however, the theoretical basis remains unclear.

In a series of papers, Li and others [Li et al. 2002; Van Vliet et al. 2003; Zhu et al. 2004; Li et al. 2004] have proposed a local condition (called Λ criterion therein) for detecting the nucleation of point defect in perfect crystals. The criterion is based on the strong ellipticity condition, but evaluated using the stress and elasticity tensor derived from the atomic description. Li and others [Li et al. 2002; Van Vliet et al. 2003] speculated that the loss of strong ellipticity indicates the admissibility of nonhomogeneous bifurcation modes, which could occur at atomic spacing and result in a single dislocation or microcrack. While the exact nature

of the localized singularity remains debatable, this line of thinking suggests that the atomistic displacement singularity and the continuum scale strain localization may be analyzed in the same theoretical framework. A similar approach has been applied to predict the strain-localization and crack initiation in atomic-informed continuum models [Klein and Gao 1998; Gao and Klein 1998].

In this contribution, we further explore this line of thinking and propose an alternative form of atomic material stability condition. The condition is based on the local energy landscape and is formulated directly in atomistic description without resorting to continuum concepts and homogenization. We also discuss the kinetic implication of the condition, and show that the condition corresponds to a monotonicity condition in a properly defined atomic stress. The critical state signifies the stationary point in the response of "atomic traction". We utilize the criterion to analyze the stability of carbon nanotubes (CNT). The application improves a recent work by the same authors [Lu and Zhang 2006] where they used the strong ellipticity condition based on a continuum elasticity model to predict the failure strain of CNTs. The tensile failure strains in [Lu and Zhang 2006] compare well with the stability limits obtained from crystal elasticity models [Zhang et al. 2002a] as well as early molecular dynamics simulations [Yakobson et al. 1997]; however, they appear higher than those reported in recent publications [Troya et al. 2003; Zhang et al. 2005; Mielke et al. 2004]. In the present work, the analysis is performed directly in the discrete setting and comparable results are obtained. In addition, the method in [Lu and Zhang 2006] is limited to perfect tubes. Here, both perfect and defective tubes are considered.

2. Atomistic material instability condition

As discussed above, the strong ellipticity condition characterizes material stability in an finitely deforming elastic body. With reference to the strain energy function $W = W(\boldsymbol{F})$ where $\boldsymbol{F}$ is the deformation gradient, the strong ellipticity condition is given by

$$A_{iIkK}\, b_i b_k N_I N_K > 0 \quad \text{with } A_{iIkK} = \frac{\partial^2 W}{\partial F_{iI}\, \partial F_{kK}}$$

for all arbitrary nonzero vectors $\boldsymbol{b}$ and $\boldsymbol{N}$. A_{iIkK} is the (Cartesian) component of the fourth-order elasticity tensor, F_{iI} is the component of the deformation gradient, and (b_i, N_I) are the components of the vectors $\boldsymbol{b}$ and $\boldsymbol{N}$. The summation convention applies to repeated indices unless stated otherwise. Introducing $\boldsymbol{n} = \boldsymbol{F}^{-T}\boldsymbol{N}$, the condition can be written in spatial form, as

$$(C_{ijkl} + \delta_{ik}\tau_{jl})\, b_i b_k n_j n_l > 0, \tag{1}$$

where $C_{ijkl} = (\det \boldsymbol{F})^{-1} A_{iIkK} F_{jI} F_{lK}$ is the spatial elasticity tensor and τ_{jl} is the component of the Cauchy stress. This condition is often stated alternatively in

terms of the positive-definiteness of the acoustic tensor

$$Q_{ik}(\boldsymbol{n}) = (C_{ijkl} + \delta_{ik}\tau_{jl})n_j n_l. \tag{2}$$

If the energy function is sufficiently smooth, the strong ellipticity condition is equivalent to the rank-one convexity of the energy function, which can written

$$\frac{\partial^2}{\partial \varepsilon^2}\Big|_{\varepsilon=0} W(\boldsymbol{F} + \varepsilon \boldsymbol{b} \otimes \boldsymbol{N}) > 0 \tag{3}$$

for arbitrary nonzero vectors $\boldsymbol{b}$ and $\boldsymbol{N}$, see [Ciarlet 1988, Section 5.10]. In this paper, the operator $\otimes$ means the standard tensor product.

There are several justifications for the strong ellipticity condition. At continuum scale, the strong ellipticity condition guarantees the uniqueness of solution for Dirichlet boundary value problems [Van Hove 1947]. In the context of stability, the condition precludes any nonzero incremental motion that leaves the boundary unaltered. The loss of strong ellipticity condition indicates that the energy surface is locally concave, and a particular form of local discontinuous bifurcation become admissible even if the material element is subjected to all round displacement boundary conditions [Hill 1962; Rice 1976]. In [Li et al. 2002; Van Vliet et al. 2003; Zhu et al. 2004; Li et al. 2004], the condition (1) is utilized in atomic system, with the continuum stress and elasticity tensor being evaluated using the Ray sum [Ray et al. 1986; Lutsko 1988].

Here, we propose a direct atomic level stability condition without resorting to the concepts of stress and elasticity tensor. We focus on models in which the system potential can be expressed as a sum of bond potentials. For such systems one can define the energy of an atomic site and partition the total potential into contributions from the site potentials. Consider such a system at an equilibrium state (temperature $T = 0$). Let $\boldsymbol{r}_a$ be the position of atom a and let $\boldsymbol{r}_{ab} := \boldsymbol{r}_b - \boldsymbol{r}_a$ be the bond vector. The potential of bond ab is

$$V_{ab} = V_{ab}(\boldsymbol{r}_{pq}).$$

For many-body interaction, the potential V_{ab} depends not only on bond $\boldsymbol{r}_{ab}$, but also on other bonds in the potential range. The potential of an atom site can be defined by

$$W_a = \tfrac{1}{2}\sum_b V_{ab}(\boldsymbol{r}_{pq}). \tag{4}$$

The summation runs over all bonds connecting to atom a.

Motivated by the strong ellipticity condition, we postulate that for an atomic site to be locally stable, the equilibrium state must satisfy the condition

$$\boldsymbol{b} \cdot \boldsymbol{Q}_a(\boldsymbol{n})\boldsymbol{b} > 0 \tag{5}$$

for arbitrary nonzero vectors $\boldsymbol{n}$ and $\boldsymbol{b}$. Here,

$$\boldsymbol{Q}_a(\boldsymbol{n}) = \frac{1}{2}\sum_b \sum_{p,q} \sum_{s,t} (\boldsymbol{r}_{pq}\cdot\boldsymbol{n}) \frac{\partial^2 V_{ab}}{\partial \boldsymbol{r}_{pq}\partial \boldsymbol{r}_{st}} (\boldsymbol{r}_{st}\cdot\boldsymbol{n}) \tag{6}$$

is the atomistic counterpart of the acoustic tensor, which depends quadratically on $\boldsymbol{n}$. The condition (5) is equivalent to the positive-definiteness of the atomistic acoustic tensor $\boldsymbol{Q}_a$.

The condition can be stated alternatively as a convexity condition for W_a. If the site energy W_a is at least twice differentiable, the condition (5) is equivalent to

$$\frac{\partial^2}{\partial \varepsilon^2}\Big|_{\varepsilon=0} W_a\big(\boldsymbol{r}_{pq} + \varepsilon \boldsymbol{b}(\boldsymbol{r}_{pq}\cdot\boldsymbol{n})\big) > 0 \tag{7}$$

for arbitrary nonzero vectors $\boldsymbol{b}$ and $\boldsymbol{n}$. The equivalence can be directly verified. This representation corresponds directly to the rank-one convexity condition (3). The rank-one deformation gradient increment, in a discrete setting, corresponds to the atomic displacement increment

$$\delta \boldsymbol{r}_{ab} = \boldsymbol{b}(\boldsymbol{r}_{ab}\cdot\boldsymbol{n}). \tag{8}$$

We refer to (7) as a *mono-mode convexity condition*.

Several remarks on the condition (5) or (7) are in order. First, the stability condition is postulated based on the premise that the stability of a site is determined by the local energy landscape. If the condition (5) is violated for certain vectors $\boldsymbol{b}$ and $\boldsymbol{n}$, the energy surface is locally concave, and bifurcation into lower energy modes becomes possible. The displacement mode (8) is chosen to test the convexity as it naturally corresponds to the rank-one deformation gradient in the continuum theory. In simple crystals $\boldsymbol{b}$ and $\boldsymbol{n}$ retain the physical explanation as wave vectors [Li et al. 2002; Van Vliet et al. 2003]. Second, as will be discussed in Section 3, the condition is related to the monotonicity of a properly defined atomic stress that characterizes the average intensity of interaction between an atom and the surrounding atoms. In particular, the singularity in $\boldsymbol{Q}$ signifies the state where the traction is momentarily stationary in a mono-mode incremental displacements. Thirdly, the condition coincides with Li's criterion for simple crystals (see Appendix). However, they may differ in complex lattices depending on how the atomic stress and elasticity tensor are evaluated in Li's approach. The atomistic form (6) has the advantage of being free from continuum concepts. More importantly, since the condition is based on the local property of the energy function, we expect it to be applicable to defective systems provided that the site energy can be reasonably defined.

3. Kinetic implications

The condition (5) can be further examined from the standpoint of atomic stress, which provides information about the local kinetics in some average sense. For systems that admit the site energy of the form (4), the static atomic stress at site a can be defined as

$$\boldsymbol{\sigma}_a = \frac{1}{2\omega} \sum_b \sum_{p,q} \frac{\partial V_{ab}}{\partial \boldsymbol{r}_{pq}} \otimes \boldsymbol{r}_{pq},$$

where ω is the volume of atomic site a. This expression of stress can be derived from an energetic argument by considering the mechanical power in a superposed affine incremental motion. The quantity represents the average intensity of interaction between the atom a and the surrounding atoms. The stress so defined is symmetric, and the symmetry follows from the invariant requirement $V_{ab}(\boldsymbol{r}_{pq}) = V_{ab}(\boldsymbol{R}\boldsymbol{r}_{pq})$ for any rotation tensor $\boldsymbol{R}$. Intuitively, if the atomic system is mechanically stable, one expects the stress to satisfy the *monotonicity condition*

$$\delta\boldsymbol{\sigma}_a \cdot \delta\boldsymbol{\epsilon} > 0$$

for properly defined strain increment $\delta\boldsymbol{\epsilon}$.

The stress increment under incremental atomic displacements $\delta\boldsymbol{r}_{pq}$ is given by

$$\delta\boldsymbol{\sigma}_a = \frac{1}{2\omega} \sum_b \sum_{p,q} \sum_{s,t} \Big(\frac{\partial^2 V_{ab}}{\partial \boldsymbol{r}_{pq} \partial \boldsymbol{r}_{st}} \delta\boldsymbol{r}_{st} \Big) \otimes \boldsymbol{r}_{pq} + \frac{1}{2\omega} \sum_b \sum_{p,q} \frac{\partial V_{ab}}{\partial \boldsymbol{r}_{pq}} \otimes \delta\boldsymbol{r}_{pq} - \frac{\delta\omega}{2\omega^2} \sum_b \sum_{p,q} \frac{\partial V_{ab}}{\partial \boldsymbol{r}_{pq}} \otimes \boldsymbol{r}_{pq}. \quad (9)$$

Consider the mono-mode displacement increment (8). Since this incremental displacement field is affine, we can define the corresponding strain increment, as

$$\delta\boldsymbol{\epsilon} = \tfrac{1}{2}(\boldsymbol{b} \otimes \boldsymbol{n} + \boldsymbol{n} \otimes \boldsymbol{b}). \quad (10)$$

Regardless of how the atomic volume ω is defined, the volume increment is given by the formula $\delta\omega = \omega(\operatorname{tr} \delta\boldsymbol{\epsilon})$, which yield

$$\delta\omega = \omega(\boldsymbol{b} \cdot \boldsymbol{n}). \quad (11)$$

Substituting (8) into (9), and invoking equations (10), (11), a straight forward calculation yields

$$\delta\boldsymbol{\sigma}_a \cdot \delta\boldsymbol{\epsilon} = \tfrac{1}{\omega}\, \boldsymbol{b} \cdot \boldsymbol{Q}_a(\boldsymbol{n})\, \boldsymbol{b}.$$

Hence, the positiveness of $\boldsymbol{Q}_a$ ensures that the atomic stress is at least monotonic in the incremental mode (8).

Alternatively, the definition of stress motivates the introduction of atomic traction in an imaginary plane of normal $\boldsymbol{n}$:

$$\boldsymbol{t}_a^{\boldsymbol{n}} := \boldsymbol{\sigma}_a \boldsymbol{n} = \frac{1}{2\omega} \sum_b \sum_{p,q} \frac{\partial V_{ab}}{\partial \boldsymbol{r}_{pq}} (\boldsymbol{r}_{pq} \cdot \boldsymbol{n}). \tag{12}$$

This quantity represents the contribution of the atom a to the macroscopic traction in the direction $\boldsymbol{n}$. Similarly to (9), the increment under incremental atomic displacements $\delta \boldsymbol{r}_{ab}$ is

$$\delta \boldsymbol{t}_a^{\boldsymbol{n}} = \frac{1}{2\omega} \sum_b \sum_{p,q} \sum_{s,t} (\boldsymbol{r}_{pq} \cdot \boldsymbol{n}) \frac{\partial^2 V_{ab}}{\partial \boldsymbol{r}_{pq} \partial \boldsymbol{r}_{st}} \delta \boldsymbol{r}_{st} + \frac{1}{2\omega} \sum_b \sum_{p,q} \frac{\partial V_{ab}}{\partial \boldsymbol{r}_{pq}} (\delta \boldsymbol{r}_{pq} \cdot \boldsymbol{n}) - \frac{\delta \omega}{2\omega^2} \sum_b \sum_{p,q} \frac{\partial V_{ab}}{\partial \boldsymbol{r}_{pq}} (\boldsymbol{r}_{pq} \cdot \boldsymbol{n}). \tag{13}$$

Again, consider the mono-mode (8). Recalling (11), the last two terms in equation (13) cancel each other and the traction increment (13) takes the form

$$\delta \boldsymbol{t}_a^{\boldsymbol{n}} = \tfrac{1}{\omega} \boldsymbol{Q}_a(\boldsymbol{n}) \boldsymbol{b}. \tag{14}$$

If at a point along a loading path the acoustic tensor becomes singular, namely $\boldsymbol{Q}_a(\boldsymbol{n})\boldsymbol{b} = \boldsymbol{0}$ for a pair of direction vectors $(\boldsymbol{b}, \boldsymbol{n})$, then, according to equation (14), the atomic traction is momentarily stationary. This is another important indicator for the onset of instability in atomic systems, since the stationary point in atomic force often marks the incipiency of softening response.

4. Application in carbon nanotubes

The validity of the stability condition is assessed with application in carbon nanotubes. The criterion is utilized to identify the critical load of elastic instability in defective carbon nanotubes under tension. In this study, we are concerned with the stability of CNT at lower temperatures where the system is in quasistatic state, and its stability is determined primarily by the mechanical characteristics of the interatomic potential. The atomic coordinates are computed using molecular mechanics (MM). The analysis does not consider thermal effects, however, we expect that at low temperatures the influence of thermal contribution to the local stability of CNT is negligibly small. The first generation Tersoff–Brenner potential [Brenner 1990; 1992] is used to model CNT bond energy. The parameters listed as potential-I in [Brenner 1990] are utilized in the computation, as in [Zhang et al. 2002a; 2002b]. This empirical potential has been widely used in studying carbon nanotubes and is found to be able to accurately describe the bond energy, elastic modulus and even defect nucleation. With Brenner's potential the interatomic energy between atom

a and b is expressed by the function

$$V(r_{ab}) = V_R(r_{ab}) - \bar{B}V_A(r_{ab}),$$

where r_{ab} is the length of the covalent bond, V_R and V_A are the repulsive and attractive terms depending on the bond length, and $\bar{B}$ models the multibody coupling between bond ab and its environment, which depends on angles between ab and adjacent bonds. At an atomic site of a CNT, one can distinguish the three bond vectors in the unit cell of the honeycomb lattice of graphene by bond vectors $\boldsymbol{r}_\alpha$, $\alpha = 1, 2, 3$ which makes three angles, labeled such that $\theta_{\alpha\beta}$ is the angle between bond α and β. The site energy is

$$W_a = \tfrac{1}{2}\sum_{\alpha=1}^{3}\left(V_R(r_\alpha) - \bar{B}(\cos\theta_{\alpha\beta}, \cos\theta_{\alpha\gamma})V_A(r_\alpha)\right) \qquad (\beta \neq \gamma).$$

It has been observed that the cutoff function in Brenner's bond-order potential produces unphysical results [Shenderova et al. 2000; Belytschko et al. 2002]. Recent studies [Troya et al. 2003; Zhang et al. 2005; Mielke et al. 2004] have used a modification originally suggested in [Shenderova et al. 2000], which removes the cutoff function but retains the interactions only for atoms initially within a 2 Å cutoff distance. The present work also follows this approach. The summation over the bonds pq and st in (6) is truncated accordingly. Nevertheless, the resulting stress and acoustic tensor include the contributions from the derivatives of the bond order function $\bar{B}(\theta_{\alpha\beta}, \theta_{\alpha\gamma})$. These contributions can not be omitted because π bond characterized by the function $\bar{B}$ plays an important role in strengthening the cohesive interaction between carbon atoms.

To simulate uniaxial tension, the atoms at the two ends are subjected to prescribed displacement increments while the coordinates of the interior atoms are computed using molecular mechanics. The convexity condition (5) is monitored by the smallest eigenvalue of $\boldsymbol{Q}_a(\boldsymbol{n})$. To find the minimum eigenvalue at a given atomic configuration, the vector $\boldsymbol{n}$ is swept through the admissible range with a pre-set increment and a bi-section process is used to locate the critical direction, as in [Lu and Zhang 2006]. The procedure is performed at every atom site and at every load increment. Although the process can be computationally intensive, it is a mere postprocessing of the molecular mechanics data and therefore doesn't interfere with MM solution process.

We begin by considering pristine tubes. Figure 1 shows the values of the smallest eigenvalue of $\boldsymbol{Q}_a$ at different elongation in an armchair [10, 10] and a zigzag [17, 0] tube. Black circles indicates unstable atoms at which the smallest eigenvalue becomes negative. Stable atom sites are denoted by grey or hollow circles, where the grey scale is obtained by scaling the (positive) eigenvalue of $\boldsymbol{Q}_a$ from 0 to 1, with increasing grayness for decreasing eigenvalues. Our analysis finds that the pristine

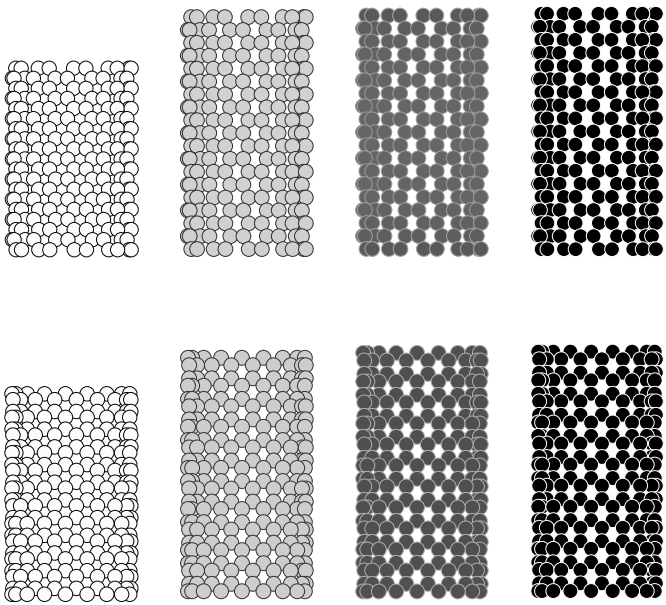

Figure 1. Stability of perfect armchair [10, 10] (upper row) and zigzag [17, 0] tubes (lower row) under various tensile strains. Black circles indicate the unstable sites where the smallest eigenvalue of the acoustic tensor is negative. The grey scale is obtained by scaling the (positive) eigenvalues inversely against the largest positive value in the loading process.

tubes lose stability uniformly when stretched to a critical strain. Particularly, the armchair [10, 10] becomes unstable at 29.8%. In comparison, numerous studies reported the critical tensile strain values close to 30% [Yakobson et al. 1997; Marques et al. 2004; Mielke et al. 2004; Zhang et al. 2005]. The critical strain for the zigzag tube [17, 0] is found to be 19.1%, again the value is consistent with the reported range of 16–20% [Dumitrica et al. 2003; Mielke et al. 2004; Zhang et al. 2005]. See Table 1. The molecular dynamics simulations by Yakobson et al. [1997] and recently by Marques et al. [2004] showed that the deformation is initially homogeneous till the critical strain is reached. Upon further stretching, a largely distorted neck appears and the tube quickly breaks into segments. As in [Lu and Zhang 2006], the critical directions $\boldsymbol{b}$ and $\boldsymbol{n}$ are found to be parallel to the tube axis, indicating that the unstable model corresponds to an incipient mode-I crack.

The same analysis is conducted for nanotubes embedded with a single Stone-Wales (SW) defect [Stone and Wales 1986]. Existing studies suggest that the

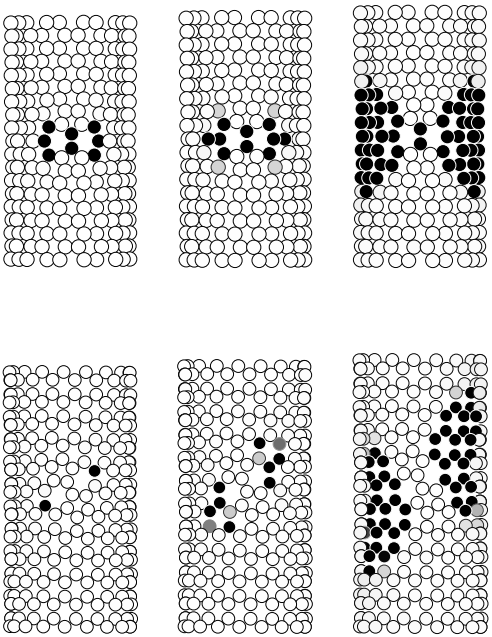

Figure 2. Evolution of unstable zone in CNTs with Stone-Wales defect. Upper row: [10, 10] armchair tube. Lower row: [17, 0] zigzag.

5/7/7/5 ring may behave as a dislocation core and weakens the strength moderately [Buongiorno Nardelli et al. 1998; Yakobson 1998; Mielke et al. 2004; Troya et al. 2003]. Figure 2 shows the evolution of instability zone during stretching. Unlike the pristine tubes which lose stability uniformly, here the unstable sites appear first at the SW ring; when loaded further the unstable zone quickly spreads out and results in global instability (MM computation fails to converge). For the [10, 10] armchair, the initial instability is found to occur at 21% strain, and the tube loses global stability at 26% strain. As shown in Table 1, the lower limit compares well with the reported yield strain obtained from molecular and quantum mechanics simulations. The upper limit 26% also corresponds nicely with break strain of SW defective tubes reported by Marques et al. [2004]. For the zigzag tube [17, 0], the initial instability is found to be 14%. In comparison, other studies [Mielke et al. 2004; Troya et al. 2003] found the critical strains of zigzag tubes to be close to 14%.

Recent simulations have reported that vacancy defects can significantly reduce the strength of CNTs. Mielke et al. [2004] predicted the limit strain of 11–15% for [5, 5] armchair tubes with one-atom vacancy, and 9–13% limit strain for [10, 0] tubes with the same defect. Zhang et al. [2005] reported moderately lower limit

Critical Tensile Strains of SWCNTs				
Tube type	Defect	$\varepsilon_{crit}(\%)$	Method	Reference
[17, 0]	pristine	19.1	MM (TB-G1)	present work
[10, 0]	pristine	16.0	QM-AM1	[Dumitrica et al. 2003]
[10, 0]	pristine	20.0	QM-PM3	[Mielke et al. 2004]
[10, 0]	pristine	18.1	MM (MTB-G2)	[Zhang et al. 2005]
[10, 10]	pristine	29.8	MM (TB-G1)	present work
[5, 5]	pristine	27.9	QM-MSINDO	[Troya et al. 2003]
[5, 5]	pristine	30.0	QM-DFT	[Mielke et al. 2004]
[5, 5]	pristine	29.7	MM (MTB-G2)	[Zhang et al. 2005]
[17, 0]	SW	14.1	MM (TB-G1)	present work
[10, 0]	SW	13.9	QM-PM3	[Mielke et al. 2004]
[10, 10]	SW	21.3	MM (TB-G1)	present work
[5, 5]	SW	24.4	QM-MSINDO	[Troya et al. 2003]
[5, 5]	SW	22.0	QM-PM3	[Mielke et al. 2004]
[17, 0]	vacancy	13.0	MM (TB-G1)	present work
[10, 0]	vacancy	13.0	QM-PM3	[Mielke et al. 2004]
[10, 10]	vacancy	12.8	MM (TB-G1)	present work
[5, 5]	vacancy	15.3	QM-PM3	[Mielke et al. 2004]
[5, 5]	vacancy	11.4	MM (MTB-G2)	[Zhang et al. 2005]

Table 1. Tensile failure strain of CNTs and comparison with predictions of molecular mechanics (MM), molecular dynamics (MD) and quantum mechanics (QM) simulations. TB-G1 and MTB-G2 stand for the first- and modified second-generation Tersoff-Brenner potentials.

strain for the zigzag tubes. We consider the [17, 0] zigzag tube with a symmetric, reconstructed one-atom vacancy. The initial instability is found to occur at 13.0% strain. When loaded further, the unstable zone spreads and the tube loss global stability at about 17% strain. Figure 3 shows the distribution of unstable sites at various strains. We also consider the [10, 10] armchair tube with an asymmetric one-atom vacancy. The onset of unstable atoms is captured at 12.8% strain, and the tube quickly loss global stability when loaded slightly further. The limit strains for both the armchair and the zigzag tubes compare reasonally well with Mielke's predictions. The armchair result also agrees with the range reported in [Zhang et al. 2005].

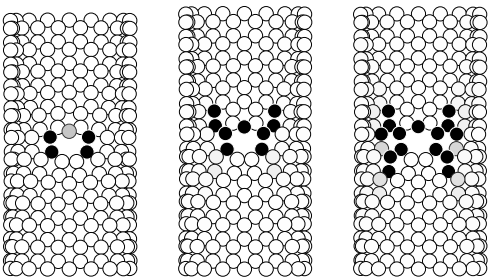

Figure 3. Evolution of unstable zone in the [17, 0] tube with a symmetric one-atom vacancy.

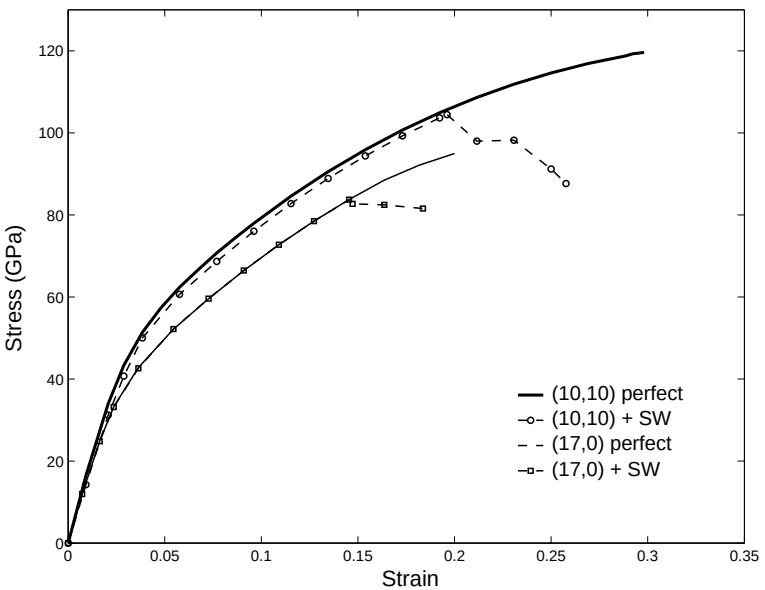

Figure 4. Stress versus strain in perfect and SW defective tubes. The instability points detected by the stability criterion correlate directly to the sudden stress drop in the response.

Figure 4 shows the (engineering) tensile stress as a function of strain for the pristine and SW defective tubes. The limit strains correlate nicely to the sudden loss of stress in the response. The stress is computed by dividing the resultant end reaction force by the tube's original circumference and the shell thickness of 0.34 nanometer.

5. Summary

An atomic level stability condition has been presented for predicting the local elastic instability of an atomic system. The criterion corresponds to the strong ellipticity condition in continuum elasticity, but is formulated directly in terms of atomic quantities without explicit reference to continuum stress and elasticity tensor. Being essentially a generalization of the continuum condition for material stability, the criterion is expected to capture the onset of local failure in atomic systems. Also, since the criterion is directly based on the site potential, we expect it to be applicable in complex lattices and defective systems provided that the site energy can be reasonably defined.

Preliminary applications in tensile CNTs has shown promising results. For pristine tubes, the predicted limit strains are in excellent agreement with the reported values from molecular and quantum mechanics simulations. For SW defective tubes, the lower limits (at the onset of unstable sites) agree very well with the reported failure strains. A single one-atom vacancy in the [10, 10] is found to reduce the limit strain significantly, consistently with the findings in recent publications. The spatial distribution of the stability indicator also provides useful information about the unstable zone and its evolution during a loading course.

Appendix

In this appendix we provide an explicit expression for the acoustic tensor $\boldsymbol{Q}_a$ in the context of pairwise potentials and show that in this case the condition coincides with the criterion in [Li et al. 2002; Van Vliet et al. 2003]. Fir a pairwise potential, the bond energy V_{ab} depends only on the bond length $r_{ab} = \sqrt{\boldsymbol{r}_{ab} \cdot \boldsymbol{r}_{ab}}$, namely $V_{ab} = V(r_{ab})$. The site energy therefore is $W_a = \sum_b V(r_{ab})$. Using the chain rule and invoking the identity $\partial r_{ab}/\partial \boldsymbol{r}_{ab} = \boldsymbol{r}_{ab}/r_{ab}$, we find

$$\frac{\partial V}{\partial \boldsymbol{r}_{ab}} = \frac{\partial V}{\partial r_{ab}} \frac{\boldsymbol{r}_{ab}}{r_{ab}}.$$

Furthermore,

$$\frac{\partial^2 V}{\partial \boldsymbol{r}_{ab} \partial \boldsymbol{r}_{ab}} = \frac{1}{r_{ab}^2} \frac{\partial^2 V}{\partial r_{ab}^2} \boldsymbol{r}_{ab} \otimes \boldsymbol{r}_{ab} + \frac{1}{r_{ab}} \frac{\partial V}{\partial r_{ab}} \left(\boldsymbol{I} - \frac{1}{r_{ab}^2} \boldsymbol{r}_{ab} \otimes \boldsymbol{r}_{ab} \right),$$

where $\boldsymbol{I}$ is the second order identity tensor. It follows that, for this system the atomistic acoustic tensor (6) takes the form

$$\boldsymbol{Q}_a = \frac{1}{2} \sum_b \left(\frac{1}{r_{ab}^2} \left(\frac{\partial^2 V}{\partial r_{ab}^2} - \frac{1}{r_{ab}} \frac{\partial V}{\partial r_{ab}} \right) (\boldsymbol{r}_{ab} \cdot \boldsymbol{n})^2 \boldsymbol{r}_{ab} \otimes \boldsymbol{r}_{ab} + \frac{1}{r_{ab}} \frac{\partial V}{\partial r_{ab}} (\boldsymbol{r}_{ab} \cdot \boldsymbol{n})^2 \boldsymbol{I} \right). \quad (15)$$

The summation runs over all bonds emanating from atom a.

According to the recipe of Li and others [Li et al. 2002; Van Vliet et al. 2003], the stability condition is evaluated using the continuum acoustic tensor (2) in conjunction with derived atomic stress and elasticity tensor. For this system, the static Virial stress [Irving and Kirkwood 1950; Cheung and Yip 1991; Shen and Atluri 2004] or BDT stress [Basinski et al. 1971; Shen and Atluri 2004] is given by

$$\boldsymbol{\sigma} := \frac{1}{2\omega}\sum_b \frac{\partial V}{\partial \boldsymbol{r}_{ab}} \otimes \boldsymbol{r}_{ab} = \frac{1}{r_{ab}}\frac{\partial V}{\partial r_{ab}} \boldsymbol{r}_{ab} \otimes \boldsymbol{r}_{ab}, \tag{16}$$

where ω is the volume of atomic site a. The isothermal elastic tensor at $T = 0$ can be obtained from the Ray sum [Ray et al. 1986; Lutsko 1988], as

$$\mathbb{C} = \frac{1}{2\omega}\sum_b \frac{1}{r_{ab}^2}\left(\frac{\partial^2 V}{\partial r_{ab}^2} - \frac{1}{r_{ab}}\frac{\partial V}{\partial r_{ab}}\right) \boldsymbol{r}_{ab} \otimes \boldsymbol{r}_{ab} \otimes \boldsymbol{r}_{ab} \otimes \boldsymbol{r}_{ab}. \tag{17}$$

Li's procedure results in an expression identical to (15) modulo a volume factor, as can be readily checked by substituting (16) and (17) into (2). The two criteria coincide in this special case.

Acknowledgments

The work was partially supported by a Scientific Research Initiative Grant from the University of Iowa.

References

[Basinski et al. 1971] Z. S. Basinski, M. S. Duesberry, and R. Taylor, "Influence of shear stress on screw dislocations in a model sodium lattice", *Can. J. Phys.* **49** (1971), 2160–2180.

[Belytschko et al. 2002] T. Belytschko, S. P. Xiao, G. C. Schatz, and R. S. Ruoff, "Atomistic simulations of nanotube fracture", *Phys. Rev. B* **65**:23 (2002), 235430.

[Born and Huang 1954] M. Born and K. Huang, *Dynamical theory of crystal lattices*, Oxford University Press, Oxford, 1954.

[Brenner 1990] D. W. Brenner, "Empirical potential for hydrocarbons for use in simulating the chemical vapor deposition of diamond films", *Phys. Rev. B* **42**:15 (1990), 9458–9471.

[Brenner 1992] D. W. Brenner, "Erratum: Empirical potential for hydrocarbons for use in simulating the chemical vapor deposition of diamond films", *Phys. Rev. B* **46**:3 (1992), 1948.

[Buongiorno Nardelli et al. 1998] M. Buongiorno Nardelli, B. I. Yakobson, and J. Bernholc, "Brittle and ductile behavior in carbon nanotubes", *Phys. Rev. Lett.* **81**:21 (1998), 4656–4659.

[Cheung and Yip 1991] K. S. Cheung and S. Yip, "Atomic-level stress in an inhomogeneous system", *J. Appl. Phys.* **70**:10 (1991), 5688–5690.

[Ciarlet 1988] P. G. Ciarlet, *Mathematical elasticity, I: Three-dimensional elasticity*, North-Holland, Amsterdan, 1988.

[Dmitriev et al. 2004] S. V. Dmitriev, J. Li, N. Yoshikawa, Y. Tanaka, Y. Kagawa, T. Kitamura, and S. Yip, "Breaking atomic bonds through vibrational mode localization", *Defect Diffus. Forum* **233-234** (2004), 49–59.

[Dumitrica et al. 2003] T. Dumitrica, T. Belytschko, and B. I. Yakobson, "Bond-breaking bifurcation states in carbon nanotube fracture", *J. Chem. Phys.* **118**:21 (2003), 9485–9488.

[Gao and Klein 1998] H. Gao and P. Klein, "Numerical simulation of crack growth in an isotropic solid with randomized internal cohesive bonds", *J. Mech. Phys. Solids* **46**:2 (1998), 187–218.

[Gibbs 1993] J. W. Gibbs, *The scientific papers of J. Willard Gibbs, 1: Thermodynamics*, Ox Bow Press, Woodbridge, Connecticut, 1993.

[Hill 1962] R. Hill, "Acceleration waves in solids", *J. Mech. Phys. Solids* **10**:1 (1962), 1–16.

[Hill and Milstein 1977] R. Hill and F. Milstein, "Principles of stability analysis of ideal crystals", *Phys. Rev. B* **15**:6 (1977), 3087–3096.

[Irving and Kirkwood 1950] J. H. Irving and J. G. Kirkwood, "The statistical mechanical theory of transport processes, IV: The equations of hydrodynamics", *J. Chem. Phys.* **18**:6 (1950), 817–829.

[Kitamura et al. 2004a] T. Kitamura, Y. Umeno, and R. Fushino, "Instability criterion of inhomogeneous atomic system", *Mat. Sci. Eng. A* **379**:1–2 (2004), 229–233.

[Kitamura et al. 2004b] T. Kitamura, Y. Umeno, and N. Tsuji, "Analytical evaluation of unstable deformation criterion of atomic structure and its application to nanostructure", *Comput. Mater. Sci.* **29**:4 (2004), 499–510.

[Klein and Gao 1998] P. Klein and H. Gao, "Crack nucleation and growth as strain localization in a virtual-bond continuum", *Eng. Fract. Mech.* **61**:1 (1998), 21–48.

[Li et al. 2002] J. Li, K. J. Van Vliet, T. Zhu, S. Yip, and S. Suresh, "Atomistic mechanisms governing elastic limit and incipient plasticity in crystals", *Nature* **418** (2002), 303–310.

[Li et al. 2004] J. Li, T. Zhu, S. Yip, K. J. Van Vliet, and S. Suresh, "Elastic criterion for dislocation nucleation", *Mat. Sci. Eng. A* **365**:1–2 (2004), 25–30.

[Lu and Zhang 2006] J. Lu and L. Zhang, "Analysis of localized failure of single-wall carbon nanotubes", *Comput. Mater. Sci.* **35**:4 (2006), 432–441.

[Lutsko 1988] J. F. Lutsko, "Stress and elastic constants in aniostropic solids: Molecular dynamics techniques", *J. Appl. Phys.* **64**:3 (1988), 1152–1154.

[Marques et al. 2004] M. A. L. Marques, H. E. Troiani, M. Miki-Yoshida, M. Jose-Yacaman, and A. Rubio, "On the breaking of carbon nanotubes under tension", *Nano Letters* **4**:5 (2004), 811–815.

[Mielke et al. 2004] S. L. Mielke, D. Troya, S. L. Zhang, J. L. Li, S. Xiao, R. Car, R. S. Ruoff, G. C. Schatz, and T. Belytschko, "The role of vacancy defects and holes in the fracture of carbon nanotubes", *Chem. Phys. Lett.* **390**:4–6 (2004), 413–420.

[Morris and Krenn 2000] J. W. Morris, Jr. and C. R. Krenn, "The internal stability of an elastic solid", *Philos. Mag. A* **80**:12 (2000), 2827–2840.

[Ogden 1997] R. W. Ogden, *Non-linear elastic deformations*, Dover Publications, New York, 1997.

[Ray et al. 1986] J. R. Ray, M. C. Moody, and A. Rahman, "Calculation of elastic constants using isothermal molecular dynamics", *Phys. Rev. B* **33**:2 (1986), 895–899.

[Rice 1976] J. R. Rice, "The localization of plastic deformation", pp. 207–220 in *Theoretical and applied mechanics*, edited by W. T. Koiter, North-Holland Publishing Company, 1976.

[Shen and Atluri 2004] S. P. Shen and S. N. Atluri, "Atomic-level stress calculation and continuum-molecular system equivalence", *Comput. Model. Eng. Sci.* **6**:1 (2004), 91–104.

[Shenderova et al. 2000] O. A. Shenderova, D. W. Brenner, A. Omeltchenko, and X. Su, "Atomistic modeling of the fracture of polycrystalline diamond", *Phys. Rev. B* **61**:6 (2000), 3877–3888.

[Stone and Wales 1986] A. J. Stone and D. J. Wales, "Theoretical studies of icosahedral C_{60} and some related species", *Chem. Phys. Lett.* **128**:5–6 (1986), 501–503.

[Troya et al. 2003] D. Troya, S. L. Mielke, and G. C. Schatz, "Carbon nanotube fracture – differences between quantum mechanical mechanisms and those of empirical potentials", *Chem. Phys. Lett.* **382**:1–2 (2003), 133–141.

[Truesdell and Noll 1965] C. Truesdell and W. Noll, "The non-linear field theories of mechanics", pp. 1–602 in *Handbuch der Physik, Band III/3*, edited by S. Flugge, Springer-Verlag, Berlin, 1965. MR 33 #2030

[Van Hove 1947] L. Van Hove, "Sur l'extension de la condition de Legendre du calcul des variations aux integrales multiples a plusieurs fonctions inconnues", *K. Ned. Akad. Van Wet.* **50** (1947), 18–23.

[Van Vliet et al. 2003] K. J. Van Vliet, J. Li, T. Zhu, S. Yip, and S. Suresh, "Quantifying the early stages of plasticity through nanoscale experiments and simulations", *Phys. Rev. B* **67**:10 (2003), 104105.

[Wang and Yip 1993] J. H. Wang and S. Yip, "Crystal instabilities at finite strain", *Phys. Rev. Lett.* **71**:25 (1993), 4182–4185.

[Wang et al. 1995] J. Wang, J. Li, S. Yip, S. Phillpot, and D. Wolf, "Mechanical instabilities of homogeneous crystals", *Phys. Rev. B* **52**:17 (1995), 12627–12635.

[Yakobson 1998] B. I. Yakobson, "Mechanical relaxation and "intramolecular plasticity" in carbon nanotubes", *Appl. Phys. Lett.* **72**:8 (1998), 918–920.

[Yakobson et al. 1997] B. I. Yakobson, M. P. Campbell, C. J. Brabec, and J. Bernholc, "High strain rate fracture and C-chain unraveling in carbon", *Comput. Mater. Sci.* **8**:4 (1997), 341–348.

[Yashiro and Tomita 2001] K. Yashiro and Y. Tomita, "Local lattice instability at a dislocation nucleation and motion", *J. Phys. (France) IV* **11**:Pr5 (2001), 3–10. Proceedings.

[Zhang et al. 2002a] P. Zhang, Y. Huang, H. Gao, and K. C. Hwang, "Fracture nucleation in single-wall carbon nanotubes under tension: A continuum analysis incorporating interatomic potentials", *J. Appl. Mech. (ASME)* **69**:4 (2002), 454–458.

[Zhang et al. 2002b] P. Zhang, Y. Huang, P. H. Geubelle, P. A. Klein, and K. C. Hwang, "The elastic modulus of single-wall carbon nanotubes: a continuum analysis incorporating interatomic potentials", *Int. J. Solids Struct.* **39**:13–14 (2002), 3893–3906.

[Zhang et al. 2005] S. L. Zhang, S. L. Mielke, R. Khare, D. Troya, R. S. Ruoff, G. C. Schatz, and T. Belytschko, "Mechanics of defects in carbon nanotubes: Atomistic and multiscale simulations", *Phys. Rev. B* **71** (2005), 115403.

[Zhu et al. 2004] T. Zhu, J. Li, K. J. Van Vliet, S. Ogata, S. Yip, and S. Suresh, "Predictive modeling of nanoindentation-induced homogeneous dislocation nucleation in copper", *J. Mech. Phys. Solids* **52**:3 (2004), 691–724.

Received 29 Sep 2005.

JIA LU: jia-lu@uiowa.edu
Department of Mechanical Engineering, University of Iowa, 2137 Seamans Center, Iowa City, IA 52242, United States

LIANG ZHANG: lianzhan@engineering.uiowa.edu
Department of Mechanical Engineering, University of Iowa, 2137 Seamans Center, Iowa City, IA 52242, United States

JOURNAL OF MECHANICS OF MATERIALS AND STRUCTURES
Vol. 1, No. 4, 2006

A MODE III MOVING CRACK BETWEEN A FUNCTIONALLY GRADED COATING AND A HOMOGENEOUS SUBSTRATE

BAO-LIN WANG AND JIE-CAI HAN

This paper considers an anti-plane moving crack between a functionally graded coating and a homogeneous substrate. The shear modulus and the mass density of the FGM coating are considered for a class of functional forms for which the equilibrium equation has an analytical solution. The problem is solved by means of singular integral equation technique. Results are plotted to show the effect of material nonhomogeneity and crack moving velocity on the crack tip field. The angular variation of the near-tip stress field is of particular interest, and the crack bifurcation behaviour is also discussed. It is shown that choice of an appropriate fracture criterion is essential for studying the stability of a moving crack in FGMs. Different fracture criteria could give opposite predictions for crack stability. It seems that the maximum cleavage stress near the crack tips is a reasonable failure criterion for a moving crack in FGMs.

1. Introduction

In functionally graded materials, the compositions and microstructures vary continuously in the thickness direction and the mismatch of material properties at the coating/substrate interface is eliminated. The problem of cracks in functionally graded materials has been studied extensively. In particular, some authors have studied dynamic fracture problems of FGMs. Marur and Tippur [1998] computed the magnitude and phase of complex stress intensity factors in FGMs for static and dynamic loading. Rousseau and Tippur [2001] studied the effect of different elastic gradient profiles on the fracture behavior of dynamically loaded functionally graded materials with cracks parallel to the elastic gradient. They used finite-element analyses of FGM and homogeneous beams to examine crack tip responses to low velocity and symmetric impact loading on the uncracked edge of the beams. Wu et al. [2002] proposed an extended dynamic J integral for functional graded materials. Zhang et al. [2003] used a boundary integral equation method to investigate the dynamic response of FGM crack problems. Chen et al. [2003] investigated the dynamic fracture of a crack in a functionally graded piezoelectric interface. Guo et al. [2005] considered the dynamic response of an edge crack in a functionally

Keywords: functionally graded materials, coatings, fracture mechanics, moving crack.

graded orthotropic strip. Zhou et al. [2004] investigated the dynamic behavior of a finite crack in functionally graded materials using the Schmidt method. The dynamic propagations of anti-plane shear cracks in functionally graded piezoelectric strips have been investigated by Kwon [2004] and Shin et al. [2004]. Recently, Sladek et al. [2005] used a meshless local boundary integral equation method for dynamic anti-plane shear crack problems in functionally graded materials.

All these papers considered the time dependence of the crack tip field in FGMs. Solutions to problems of moving cracks in FGMs are important since they can assist in the understanding of how FGMs can best be constructed to arrest running cracks. Some earlier investigations [Jin et al. 2003; Bi et al. 2003; Jin and Zhong 2002; Li and Weng 2002; Ma et al. 2005] have considered moving cracks in FGMs with exponentially distributed material properties.

In this paper, we study a crack moving at the interface between an FGM layer and a homogeneous substrate. The properties of the FGM are considered for a class of continuous functions of the coordinate perpendicular to the crack plane. The Yoffe model [1951] of a running crack is adopted. The crack is assumed to propagate at a constant velocity. The results show that crack growth behavior is strongly affected by the material nonhomogeneity and the crack moving velocity. Different fracture criteria may lead to different, indeed opposite, crack growth predictions. This suggests that the selection of a fracture criterion is essential for moving cracks in FGMs. Based on the maximum cleavage stress criterion, the dependence of crack bifurcation angle and the critical crack speed (at which bifurcation occurs) on the stress intensity factor are found to be identical for functionally graded materials and homogeneous materials. Stress intensity factors, however, have a strong dependence on material nonhomogeneity and crack moving velocity.

2. Formulation of the crack problem

From the viewpoint of applications, anti-plane crack problems often provide a useful analog to the more interesting in-plane fracture problems. Therefore, we investigate an anti-plane crack problem in an FGM/substrate structure. The properties of the FGM vary along the y-axis, as shown in Figure 1. There is a plane crack of length $2a$ lying at the interface between the FGM and the substrate. The crack advances with a constant length in the material having shear modulus $\mu(Y)$ and mass density $\rho(Y)$. Crack motion is maintained at a constant velocity V by the uniform anti-plane shear stress $-\tau_0(x)$ applied to the crack faces.

We call XY the fixed coordinate system and xy the coordinates attached to the moving crack. Under anti-plane deformation, the constitutive equations are

$$\tau_{xz} = \mu(Y)\frac{\partial w}{\partial X}, \qquad \tau_{yz} = \mu(Y)\frac{\partial w}{\partial Y}, \tag{1}$$

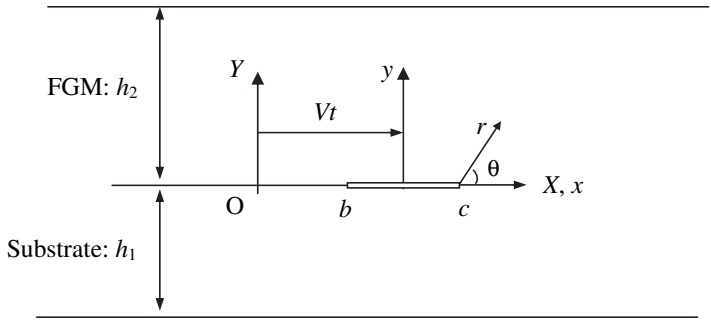

Figure 1. Geometry of the crack problem.

where $\mu(Y)$ is the shear modulus, which is a constant for $y < 0$. From the equilibrium equation

$$\frac{\partial \tau_{xz}}{\partial X} + \frac{\partial \tau_{yz}}{\partial Y} = \rho \frac{\partial^2 w}{\partial t^2}$$

and the constitutive equations, we obtain

$$\mu(Y)\left(\frac{\partial^2 w}{\partial X^2} + \frac{\partial^2 w}{\partial Y^2}\right) + \frac{d\mu(Y)}{dY}\frac{\partial w}{\partial Y} = \rho(Y)\frac{\partial^2 w}{\partial t^2}.$$

To simplify this equation, we apply the coordinate change $x = X - Vt$, obtaining

$$\mu(y)\left(\frac{\partial^2 w}{\partial x^2} + \frac{\partial^2 w}{\partial y^2}\right) + \frac{d\mu(y)}{dy}\frac{\partial w}{\partial y} - V^2\rho(y)\frac{\partial^2 w}{\partial x^2} = 0. \tag{2}$$

Let the solution of (2) be given by

$$w(x, y) = \frac{1}{2\pi}\int_{-\infty}^{\infty} F(y, s)e^{-isx}\, ds \tag{3}$$

(see [Erdogan and Ozturk 1992]), where the function F is to be determined. It follows from (2) and (3) that

$$\frac{d^2F}{dy^2} + p(y)\frac{dF}{dy} - \left(1 - \frac{V^2\rho(y)}{\mu(y)}\right)s^2F = 0, \tag{4}$$

where

$$p(y) = \frac{\mu'(y)}{\mu(y)}.$$

To overcome the complexity of mathematics involved, we will focus in this study on a special class of FGMs in which the properties vary proportionally, that is,

$$\mu(y) = \mu_0 f(y) \quad \text{and} \quad \rho(y) = \rho_0 f(y) \tag{5}$$

for some function $f(y)$, where μ_0 and ρ_0 are material properties of the homogeneous substrate. From equations (4) and (5), we obtain

$$\frac{d^2F}{dy^2} + p(y)\frac{dF}{dy} - \omega^2 s^2 F = 0, \tag{6}$$

where

$$\omega = \sqrt{1-(V/c)^2} \quad \text{with} \quad c = \sqrt{\mu_0/\rho_0}$$

is the lowest bulk wave speed for plane wave propagation along the x direction. Introduce the function

$$H(y,s) = F(y,s)f(y)^{1/2}. \tag{7}$$

Then Equation (6) becomes

$$\frac{d^2H}{dy^2} - \frac{1}{4}\Big(p^2 + 2\frac{dp}{dy} + 4s^2\omega^2\Big)H = 0. \tag{8}$$

We will now look for a particular class of functions for which this equation has an analytical solution. The simplest class of such functions is obtained by assuming that

$$p^2 + 2\frac{dp}{dy} = 4\ell_0,$$

where ℓ_0 is a constant. We consider three classes of functions satisfying this equation (see [Erdogan and Ozturk 1992; Wang et al. 2003]):

(a) With $\ell_0 > 0$ and $\beta = \sqrt{\ell_0}$:

$$\begin{aligned} &p(y) = \mp 2\beta, && f(y) = \exp(\mp 2\beta y),\\ &p(y) = 2\beta\coth(\beta y + 0.8814), && f(y) = \sinh^2(\beta y + 0.8814),\\ &p(y) = 2\beta\tanh(\beta y), && f(y) = \cosh^2(\beta y). \end{aligned} \tag{9}$$

(b) With $\ell_0 < 0$ and $\beta = \sqrt{-\ell_0}$:

$$p(y) = -2\beta\tan(\beta y), \qquad f(y) = \cos^2(\beta y). \tag{10}$$

(c) With $\ell_0 = 0$ and β arbitrary:

$$\begin{aligned} &p(y) = 2\beta/(\beta y + 1), && f(y) = (\beta y + 1)^2,\\ &p(y) = 0, && f(y) = 1. \end{aligned} \tag{11}$$

The material properties are continuous at the interface between the coating and the substrate if the coating property gradient is described by any of these equations. The case $p = 0$, $f = 1$ describes a homogeneous coating.

3. The solutions

For the choices of $p(y)$ and $f(y)$ just listed, Equation (8) can be solved in analytic form:

$$H = A(s)\exp(|s|\gamma y) + B(s)\exp(-|s|\gamma y), \qquad \gamma = \sqrt{\omega^2 + \ell_0/s^2}, \tag{12}$$

where A and B are arbitrary constants. It follows from (12), (7) and (3) that

$$\begin{aligned} w(x, y) &= \frac{1}{2\pi}\int_{-\infty}^{\infty} \big(f_{1a}(y)A_1(s) + f_{1b}(y)B_1(s)\big)e^{-isx}\,ds, \quad -h_1 < y < 0, \\ w(x, y) &= \frac{1}{2\pi}\int_{-\infty}^{\infty} \big(f_{2a}(y)A_2(s) + f_{2b}(y)B_2(s)\big)e^{-isx}\,ds, \qquad h_2 > y > 0, \end{aligned} \tag{13}$$

where $A_1(s)$, $B_1(s)$, $A_2(s)$ and $B_2(s)$ are unknown functions and

$$\begin{aligned} f_{1a}(y) &= e^{|s|\omega y}, & f_{1b}(y) &= e^{-|s|\omega y}, \\ f_{2a}(y) &= f(y)^{-1/2}e^{|s|\gamma y}, & f_{2b}(y) &= f(y)^{-1/2}e^{-|s|\gamma y}. \end{aligned} \tag{14}$$

In formulating those boundary conditions, the crack problem has been treated using the superposition technique; that is, the problem without any cracks has been solved and the equal and opposite values of the stresses have been used as the applied loads on the crack surfaces. Therefore, the boundary and continuity conditions are as follows (see Figure 1):

$$\tau_{yz}(x, -h_1) = 0 = \tau_{yz}(x, h_2) \quad \text{for} x \in (-\infty, \infty), \tag{15}$$

$$\tau_{yz}(x, +0) = \tau_{yz}(x, -0) \quad \text{for} x \in (-\infty, \infty), \tag{16}$$

$$w(x, +0) = w(x, -0) \quad \text{for} x \notin (b, c), \tag{17}$$

$$\tau_{yz}(x, +0) = \tau_{yz}(x, -0) = \tau_0(x) \quad \text{for} x \in (b, c). \tag{18}$$

Those conditions can be used to determine the unknown constants $A_1(s)$, $B_1(s)$, $A_2(s)$ and $B_2(s)$.

3.1. ***The singular integral equation.*** The three homogeneous boundary conditions shown in Equations (15) and (16) can be used to eliminate three of the four unknown functions. The mixed boundary conditions (17)–(18) then give a system of dual integral equations to determine the remaining one. By defining a new unknown function

$$g(x) = \frac{\partial w(x, +0) - \partial w(x, -0)}{\partial x}, \tag{19}$$

the problem can be reduced to an integral equation in g; then it is seen that (17) is equivalent to

$$g(x) = 0 \text{ for } x \notin (b, c) \qquad \int_b^c g(x)\,dx = 0,$$

and (18) gives the desired integral equation.

By substituting the values from Equations (13) via Hooke's law into the boundary conditions (15) and continuity conditions (16), and by using Equation (19), we can determine $A_1(s)$, $B_1(s)$, $A_2(s)$ and $B_2(s)$ in terms of the Fourier transforms of g. Noting that g is zero for $x \notin (b, c)$, the expressions found for $A_1(s)$, $B_1(s)$, $A_2(s)$ and $B_2(s)$ are

$$A_1(s) = \frac{1}{\Delta(s)}\left(f'_{2a}(0) - f'_{2b}(0)\frac{f'_{2a}(h_2)}{f'_{2b}(h_2)}\right)\frac{i}{s}\int_b^c g(t)e^{ist}dt,$$

$$B_1(s) = \exp(-2|s|\omega h_1)A_1(s),$$

$$A_2(s) = \frac{1}{\Delta(s)}\left(f'_{1a}(0) - f'_{1b}(0)\frac{f'_{1a}(-h_1)}{f'_{1b}(-h_1)}\right)\frac{i}{s}\int_b^c g(t)e^{ist}dt,$$

$$B_2(s) = -\frac{f'_a(h_2)}{f'_b(h_2)}A_2(s),$$

where

$$f'_a(y) = \partial f_a(y)/\partial y, \qquad f'_b(y) = \partial f_b(y)/\partial y,$$

and

$$\Delta(s) = \left(1 - \frac{f'_{2a}(h_2)}{f'_{2b}(h_2)}\right)\left(f'_{1a}(0) - f'_{1b}(0)\frac{f'_{1a}(-h_1)}{f'_{1b}(-h_1)}\right) - \left(1 - \frac{f'_{1a}(-h_1)}{f'_{1b}(-h_1)}\right)\left(f'_{2a}(0) - f'_{2b}(0)\frac{f'_{2a}(h_2)}{f'_{2b}(h_2)}\right).$$

Substituting Equations (1) and (13) into the remaining boundary condition (18), we obtain:

$$\frac{1}{\pi}\int_b^c g(t)K(x,t)\,dt = \tau_0(x)/\mu_0, \tag{20}$$

where

$$K(x,t) = \frac{i}{2}\int_{-\infty}^{\infty} k(s)e^{is(t-x)}ds, \tag{21}$$

$$k(s) = \frac{1}{s\Delta(s)}\left(f'_{1a}(0) - f'_{1b}(0)\frac{f'_{1a}(-h_1)}{f'_{1b}(-h_1)}\right)\left(f'_{2a}(0) - f'_{2b}(0)\frac{f'_{2a}(h_2)}{f'_{2b}(h_2)}\right). \tag{22}$$

Therefore, the integral kernel k can be obtained by inserting the property distributions (9)–(11) into Equations (14) and then into (22).

To determine the singular behavior of (20) we must examine the behavior of the kernel k. For this, it is sufficient to determine and separate those leading terms in the asymptotic expansion of k as $|s| \to \infty$ that would lead to unbounded integrals. From the expression of k in (22) it can be shown that in the asymptotic expansions for $|s| \to \infty$ the only terms that would give unbounded integrals are

$$k(\pm\infty) = -\operatorname{sgn}(s)\, \tfrac{1}{2}\omega.$$

By adding and substituting this asymptotic value to and from k in (21), and by evaluating the integrals involving the leading terms, we obtain

$$K(x,t) = \tfrac{1}{2}\omega \frac{1}{t-x} + \frac{i}{2}\int_{-\infty}^{\infty} \Lambda(s) e^{is(t-x)}\, ds,$$

where

$$\Lambda(s) = k(s) + \tfrac{1}{2}\operatorname{sgn}(s)\,\omega.$$

Thus, Equation (20) becomes

$$\frac{\omega}{2\pi}\int_b^c \frac{1}{t-x} g(t)\, dt + \frac{1}{\pi}\int_b^c K_1(x,t) g(t)\, dt = \frac{\tau_0(x)}{\mu_0}, \tag{23}$$

where

$$K_1(x,t) = \frac{i}{2}\int_{-\infty}^{\infty} \Lambda(s) e^{is(t-x)} ds = -\int_0^{\infty} \Lambda(s) \sin\big(s(t-x)\big)\, ds$$

is a known bounded function.

3.2. ***The crack tip field.*** Equation (23) contains a Cauchy-type kernel. Consequently, the crack tip behavior can be characterized by a standard square-root singularity. The solution of the singular integral equation (23) has the form

$$g(x) = \frac{G(x)}{\sqrt{(x-b)(c-x)}}, \tag{24}$$

where G is a bounded function. After normalizing the interval (b, c), equation (23) can be solved numerically by using a Gaussian quadrature formula. The mode III stress intensity factor at, for example, at the crack tip $x = b$ is defined by

$$k_3(b) = \lim_{x \to b-0} \sqrt{2(x-b)}\, \tau_{yz}(x, 0).$$

Observing that Equation (23) gives the stress component $\tau_{yz}(x, 0)$ on the plane of the crack for $x \in (b, c)$ as well as $x \notin (b, c)$, and substituting from (24) into (23), a simple asymptotic analysis shows that

$$k_3(b) = \frac{\mu_0}{2}\omega\frac{G(b)}{\sqrt{a}}, \qquad k_3(c) = -\frac{\mu_0}{2}\omega\frac{G(c)}{\sqrt{a}}.$$

Of practical interest is the stress status near the crack tip. From the above results we can obtain the asymptotic fields near the moving crack tips in terms of the stress intensity factor in the moving coordinate system. The results at the right crack tip are

$$\tau_{yz} = \frac{k_3(c)}{\sqrt{2\pi\hat{r}}}\cos\frac{\hat{\theta}}{2}, \qquad \tau_{xz} = -\frac{k_3(c)}{\omega\sqrt{2\pi\hat{r}}}\sin\frac{\hat{\theta}}{2}, \tag{25}$$

where

$$\hat{r} = \sqrt{(x-a)^2 + (\omega y)^2}, \qquad \hat{\theta} = \tan^{-1}\frac{\omega y}{x-a}. \tag{26}$$

4. Infinite functionally graded medium

The foregoing analysis can be easily extended to the case of an infinite functionally graded medium ($h_1 \to \infty$ and $h_2 \to \infty$). Suppose by using superposition technique, the solution has been reduced to a perturbation problem where the only applied loads are the anti-plane shear stresses on the crack surfaces. To satisfy the regularity conditions at infinity, the constants B_1 and A_2 in Equations (13) must equal zero. Following a similar analysis procedure in Section 3, we obtain the remaining unknown constants B_2 and A_1 as

$$A_1(s) = \frac{f'_{2b}(0)}{f'_{1a}(0) - f'_{2b}(0)}\frac{i}{s}\int_b^c g(t)e^{ist}dt,$$

$$B_2(s) = \frac{f'_{1a}(0)}{f'_{1a}(0) - f'_{2b}(0)}\frac{i}{s}\int_b^c g(t)e^{ist}dt.$$

The integral equation (20) remains unchanged, provided that the integral kernel $k(s)$ in (21) be replaced by

$$k(s) = \frac{f'_{1a}(0)f'_{2b}(0)}{s[f'_{1a}(0) - f'_{2b}(0)]}.$$

The rest of the analysis and the equation system are the same as those in the previous section.

5. Results and discussion

We have considered an infinite medium ($h_1 \to \infty$, $h_2 \to \infty$) with proportional material properties $f(y)$ and $p(y)$ varying according to one of several functions, namely, $f(y) = \exp(\beta y)$, $f(y) = \sinh^2(\beta y + 0.8814)$, and $f(y) = \exp(-\beta y)$. The latter represents a soft coating (the stiffness of the coating is less than that of the substrate). The values of the stress intensity factors for a single crack are given in Figure 2, where $a = (c-b)/2$ is the half-crack length. As expected, the value of k_3 for a homogeneous medium ($\beta = 0$) is 1 for any crack velocity. For

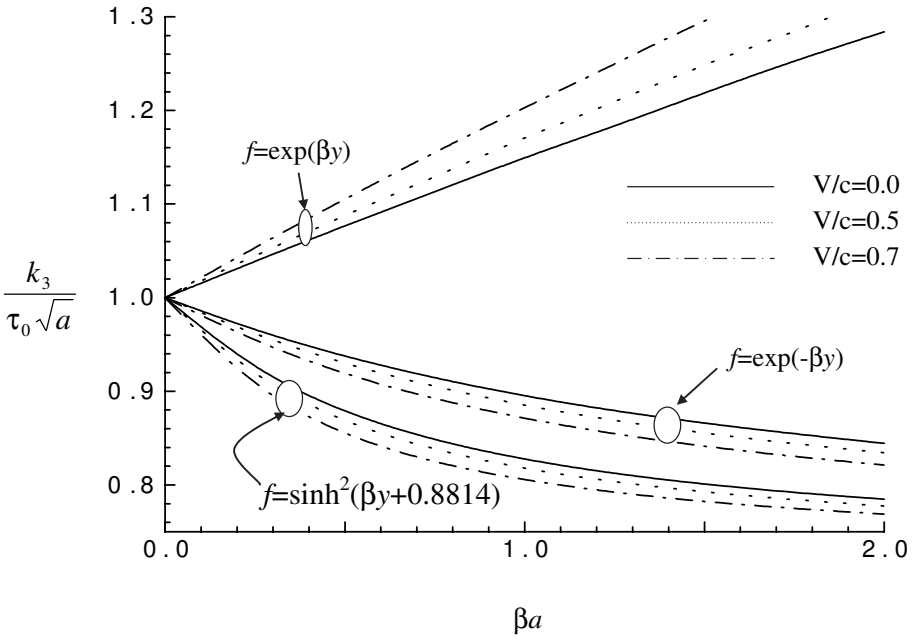

Figure 2. Stress intensity factors for a crack at different velocities.

the property distribution $f(y) = \exp(\beta y)$, the values of the stress intensity factor k_3 increase with the material nonhomogeneity β and the crack moving velocity V. Oppositely, for the property distributions $f(y) = \exp(-\beta y)$ and $f(y) = \sinh^2(\beta y + 0.8814)$, the values of k_3 decrease with the material nonhomogeneity and the crack moving velocity. The results indicate further that for a nonhomogeneous material with property distributions $f(y) = \exp(-\beta y)$ and $f(y) = \sinh^2(\beta y + 0.8814)$ the stress intensity factor k_3 is smaller than the corresponding value for a homogeneous material.

The fact that the values of k_3 can increase or decrease with crack moving velocities suggests that, if the stress intensity factor criterion is used to predict the unstable fracture initiation, then the critical applied loads can increase or decrease with crack velocities, depending on the type of the material nonhomogeneity (gradient). For example, unstable fracture is more likely to take place, for a lower crack moving velocity, for material gradient $f(y) = \sinh^2(\beta y + 0.8814)$, and for a higher crack moving velocity, for material gradient $f(y) = \exp(\beta y)$.

For a quick assessment of a possible unstable crack growth initiation, it is generally sufficient to examine the amplitude and the direction of the maximum cleavage stress $\tau_{\theta z}(r, \theta)$ at the crack tips. The cleavage stress $\tau_{\theta z}(r, \theta)$ can be expressed as

$$\tau_{\theta z}(r, \theta) = \tau_{yz} \cos\theta - \tau_{xz} \sin\theta, \tag{27}$$

where (r, θ) are the polar coordinates at the crack tip and θ is measured from the positive x-axis (see Figure 1). Figure 3 gives the variation of cleavage shear stress $\tau_{\theta z}(r, \theta)$ with the angle for different crack velocities. It is seen that the stresses depend significantly on the crack velocities. Unlike the static solution, the maximum value of $\tau_{\theta z}(r, \theta)$ does not always occur along the axis coincident with the crack ($\theta = 0$). For small velocities, the shear stress decreases monotonously with the angle. As the velocity increases, $\tau_{\theta z}(r, \theta)$ in each curve attains a maximum

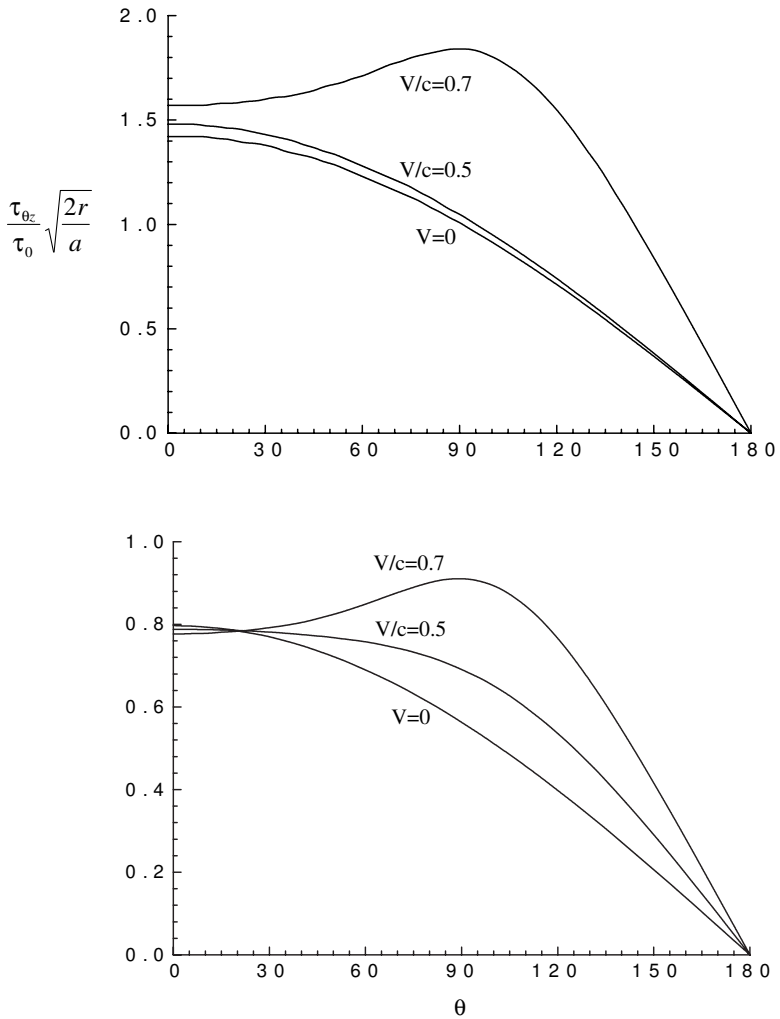

Figure 3. Angular distribution of stress $\tau_{\theta z}$ with polar angle for a crack moving at different velocities. Top: $f = \exp(\beta y)$, $\beta a = 3$. Bottom: $f = \sinh^2(\beta y + 0.8814)$, $\beta a = 1.5$.

value at an angle different from $\theta = 0$. This suggests that crack bifurcation may occur at a sufficient higher crack moving velocity.

Further consideration of the results in Figure 3 shows that the peak values of the cleavage stress $\tau_{\theta z}(r, \theta)$ increase with the crack moving velocity, both for the gradient $f(y) = \exp(\beta y)$ and for the gradient $f(y) = \sinh^2(\beta y + 0.8814)$. Hence, it is more reasonable to use the maximum cleavage stress $\tau_{\theta z}(r, \theta)$ as a fracture criterion, since it can predict that the fracture is more likely to take place for a higher crack moving velocity, no matter what kind of material nonhomogeneity the medium has.

As mentioned above, the crack may bifurcate at a sufficient high moving velocity. Referring to Figure 3, the bifurcation angle θ_c and the critical crack speed at which bifurcation initiation can be found from:

$$\frac{\partial \tau_{\theta z}(r, \theta_c)}{\partial \theta_c} = 0, \qquad \frac{\partial^2 \tau_{\theta z}(r, \theta_c)}{\partial \theta_c^2} < 0. \tag{28}$$

From Equations (25), (26), (27) and (28) we see that the value of θ_c is only a function of crack moving velocities and does not depend on the material gradient. Therefore, the bifurcation angle θ_c and the critical crack speed at which bifurcation occurs are the same as for an ordinary homogeneous isotropic solid.

6. Conclusions

The fracture problem for a functionally graded material under anti-plane shear loads is investigated for a class of property distributions. The paper aims at determining the crack tip stress field, evaluating simultaneously the effects of the crack velocity and material varying properties. Also discussed are the stability of crack growth, crack bifurcation and failure criteria to be adopted. The following conclusions can be drawn:

- Unlike the case of a a homogeneous coating, crack motion affects the stress intensity factors for an FGM coating.
- Stress intensity factors depend on the crack velocity as well as material nonhomogeneity. They can increase or decrease with material nonhomogeneities and crack velocities, depending on the type of the material property distribution.
- For a stationary crack, the angular distribution of the stress field near the crack tips is the same as for a homogeneous material. But for a moving crack the singular stress field near the crack tips is altered considerably by crack velocity.
- It is more convenient to use the maximum cleavage stress $\tau_{\theta z}(r, \theta)$ as a fracture criterion for a moving crack in FGMs, since it can explain the fact that the

fracture is more likely to take place for a higher moving velocity, for any of the kinds of material nonhomogeneity (gradients) considered in this paper. Oppositely, if the stress intensity factor criterion is used, the crack growth could be enhanced or retarded by crack moving velocity, depending on the material nonhomogeneity.

Acknowledgements

Comments from two anonymous reviewers on the original manuscript were especially useful for the improvement of the presentation and quality of the paper.

References

[Bi et al. 2003] X. S. Bi, J. Cheng, and X. L. Chen, "Moving crack for functionally grated material in an infinite length strip under antiplane shear", *Theor. Appl. Fract. Mech.* **39**:1 (2003), 89–97.

[Chen et al. 2003] J. Chen, Z. Liu, and Z. Zou, "Dynamic response of a crack in a functionally graded interface of two dissimilar piezoelectric half-planes", *Arch. Appl. Mech.* **72**:9 (2003), 686–696.

[Erdogan and Ozturk 1992] F. Erdogan and M. Ozturk, "Diffusion problems in bonded nonhomogeneous materials with an interface cut", *Int. J. Eng. Sci.* **30**:10 (1992), 1507–1523.

[Guo et al. 2005] L. C. Guo, L. Z. Wu, and T. Zeng, "The dynamic response of an edge crack in a functionally graded orthotropic strip", *Mech. Res. Commun.* **32**:4 (2005), 385–400.

[Jin and Zhong 2002] B. Jin and Z. Zhong, "A moving mode-III crack in functionally graded piezoelectric material: permeable problem", *Mech. Res. Commun.* **29**:4 (2002), 217–224.

[Jin et al. 2003] B. Jin, A. K. Soh, and Z. Zhong, "Propagation of an anti-plane moving crack in a functionally graded piezoelectric strip", *Arch. Appl. Mech.* **73**:3–4 (2003), 252–260.

[Kwon 2004] S. M. Kwon, "On the dynamic propagation of an anti-plane shear crack in a functionally graded piezoelectric strip", *Acta Mech.* **167**:1–2 (2004), 73–89.

[Li and Weng 2002] C. Y. Li and G. J. Weng, "Yoffe-type moving crack in a functionally graded piezoelectric material", *P. Roy. Soc. Lond. A Mat.* **458**:2018 (2002), 381–399.

[Ma et al. 2005] L. Ma, L. Z. Wu, L. C. Guo, and Z. G. Zhou, "On the moving Griffith crack in a non-homogeneous orthotropic medium", *Eur. J. Mech. A: Solids* **24**:3 (2005), 393–405.

[Marur and Tippur 1998] P. R. Marur and H. V. Tippur, "Evaluation of mechanical properties of functionally graded materials", *J. Test. Eval.* **26**:6 (1998), 539–545.

[Rousseau and Tippur 2001] C.-E. Rousseau and H. V. Tippur, "Influence of elastic gradient profiles on dynamically loaded functionally graded materials: cracks along the gradient", *Int. J. Solids Struct.* **38**:44–45 (2001), 7839–7856.

[Shin et al. 2004] J. W. Shin, T. U. Kim, and S. C. Kim, "Dynamic characteristics of an eccentric crack in a functionally graded piezoelectric ceramic strip", *Korean Soc. Mech. Eng. Int. J.* **18**:9 (2004), 1582–1589.

[Sladek et al. 2005] J. Sladek, V. Sladek, and C. Z. Zhang, "A meshless local boundary integral equation method for dynamic anti-plane shear crack problem in functionally graded materials", *Eng. Anal. Bound. Elem.* **29**:4 (2005), 334–342.

[Wang et al. 2003] B. L. Wang, Y. W. Mai, and Y. G. Sun, "Anti-plane fracture of a functionally graded material strip", *Eur. J. Mech. A: Solids* **22**:3 (2003), 357–368.

[Wu et al. 2002] C. Wu, P. He, and Z. Li, "Extension of J integral to dynamic fracture of functional graded material and numerical analysis", *Comput. Struct.* **80**:5–6 (2002), 411–416.

[Yoffe 1951] E. H. Yoffe, "The moving Griffith crack", *Philos. Mag.* **42**:7 (1951), 739–750.

[Zhang et al. 2003] C. Zhang, A. Savaidis, G. Savaidis, and H. Zhu, "Transient dynamic analysis of a cracked functionally graded material by a BIEM.", *Comput. Mater. Sci.* **26** (2003), 167–174.

[Zhou et al. 2004] Z. G. Zhou, B. Wang, and Y. G. Sun, "Investigation of the dynamic behavior of a finite crack in the functionally graded materials by use of the Schmidt method", *Wave Motion* **39**:3 (2004), 213–225.

Received 2 Dec 2005.

BAO-LIN WANG: wangbl2001@hotmail.com
Centre for Advanced Materials Technology (CAMT), School of Aerospace, Mechanical and Mechatronic Engineering, The University of Sydney, Sydney, NSW 2006, Australia

JIE-CAI HAN: hanjc@hit.edu.cn
Center for Composite Materials, Harbin Institute of Technology, Harbin 150001, P.R. China

JOURNAL OF MECHANICS OF MATERIALS AND STRUCTURES
Vol. 1, No. 4, 2006

NONLOCAL CONTINUUM MODELS FOR CARBON NANOTUBES SUBJECTED TO STATIC LOADING

QUAN WANG AND YASUHIDE SHINDO

Static and buckling analyses of carbon nanotubes (CNTs) are carried out with newly developed nonlocal continuum models. Small-scale effects are explicitly derived for bending deformation solutions for CNTs subjected to general flexural loading first. Solutions via nonlocal continuum models are expressed by simple terms related to scale coefficients in addition to remaining terms via local continuum models in which the simplicity of the nonlocal continuum models is clearly observed. Discussions on various derivations of Young's modulus for CNTs from existing experimental work in the literature are provided, revealing the applicability of the nonlocal continuum models. In addition, a simple equation for the buckling load of CNTs with various general boundary conditions subject to axial loading via the nonlocal elastic beam model is explicitly derived for instability analysis. The results of this research provide benchmark solutions for the response of CNTs subject to general static loading, with small-scale effects modeled and revealed. Thus, the work has great potential in studying mechanical properties of CNTs of various sizes.

1. Introduction

Carbon nanotubes (CNTs) have been the focus of extensive research [Ball 2001; Baughman et al. 2002; Harris 1999; Treacy et al. 1996] since they were discovered by Iijima [1991], because of their potential to lead to new applications, such as frictionless nanoactuators, nanomotors, nanobearings, and nanosprings [Lau 2003].

Two major analytical approaches are used in studies of CNTs. The first is atomic modeling, and includes techniques such as classical molecular dynamics (MD) [Iijima et al. 1996; Yakobson et al. 1997], tight binding molecular dynamics (TBMD) [Hernandez et al. 1998] and density functional theory (DFT) [Sanchez-Portal et al. 1999]. Its use is limited to the study of systems having a relatively small number of atoms.

The second approach, continuum modeling, is more practical in analyzing carbon nanotubes of large-scale systems. Continuum modeling includes elastic beam

Keywords: Nonlocal continuum models, carbon nanotubes, single-walled carbon nanotubes, elastic beam model, stability analysis.

The authors thank the reviewers for their constructive comments.

and shell models, which have been applied in analyzing static response, stability and vibration of CNTs. Yakobson et al. [1996] studied unique features of fullerenes and developed a continuum shell model to study instability patterns of a CNT under different compressive loads. Ru [2000a; 2000b] proposed the buckling analysis of CNTs with shell models. Parnes and Chiskis [2002] investigated elastic buckling of nanofiber reinforced composites with elastic beam theory. Wang and coworkers [Wang and Varadan 2005; Wang 2005; Wang et al. 2005b] have investigated global and local instability or kinks of CNTs with elastic beam models. In these continuum models, stress at a reference point is defined and considered traditionally to be a functional of the strain field at the exact point in the body; hence the models are usually called *classical* or *local* continuum models. A pioneering work [Zhang et al. 2002] established a nanoscale continuum theory to incorporate interatomic potentials into a continuum analysis in studying the linear modulus of a single-wall CNT. The Young's modulus predicted by that work agreed well with prior experimental results and atomic studies. The simplicity of these continuum models has inspired a great deal of work on CNT mechanical behavior, and this research has shown that continuum mechanics is easy to handle and accurate in predicting much this behavior.

Local continuum models do not admit intrinsic size dependence in elastic solutions of inclusions and inhomogeneities. At nanolength scales, however, size effects often become prominent, and in view of the increasing interest in nanotechnology, they need to be addressed [Sharma et al. 2003]. Wang et al. [2005a] used the Tersoff–Brenner potential and *ab initio* calculations to find the size dependence of CNTs in a thin-shell model. Sun and Zhang [2003] pointed out the limitations of the applicability of classical continuum models in nanotechnology. They indicated the importance of semicontinuum models in analyzing nanomaterials with plate-like geometry. Their results contrast with those obtained from classical continuum models; the values of material properties were found to depend heavily on the thickness of the plate structure. The modeling of such a size-dependent phenomenon has become an active researcher subject [Sheehan and Lieber 1996; Yakobson and Smalley 1997]. One concludes from these works that the applicability of the classical continuum models at small scales may be questionable. At such scales the microstructure of the material, such as the lattice spacing between individual atoms, becomes increasingly important and the discrete structure of the material can no longer be homogenized into a continuum. Therefore, more appropriate continuum models rather than classical or local elastic beam and shell theories are needed in studying the small-scale effect in nanomaterials.

Nonlocal elasticity was first proposed by Eringen [1976; 1983] to account for the scale effect in elasticity, by assuming the stress at a reference point to be a functional of the strain field at *every point* in the body. In this way, the internal size scale

could be considered in the constitutive equations simply as a material parameter. Recently, Pugno and Ruoff [2004] modified continuum fracture mechanics and proposed their fracture quantized mechanics to predict fractures of tiny systems with a given geometry and type of loading occurred at quantized stress.

The application of nonlocal elasticity models to nanomaterials has received attention from the nanotechnology community only recently. Peddieson et al. [2003] proposed a version of nonlocal elasticity for the formulation of an Euler–Bernoulli beam theory. They concluded that nonlocal continuum mechanics could potentially play a useful role in the analysis of phenomena related to nanotechnology applications. Sudak [2003] studied infinitesimal column buckling of CNTs, incorporating van der Waals forces and small-scale effects, and showed that the critical axial strain decreases, compared to the results with classical continuum beam model, where the small length scale increases in magnitude. Zhang et al. [2004] proposed a nonlocal multishell model for the axial buckling of CNTs under axial compression. Their results showed that the effect of the small-scale on axial buckling strain is related to the buckling mode and the length of tubes. Wang [2005] studied the dispersion relations for CNTs considering small-scale effects. A qualitative validation study showed that results based on the nonlocal continuum mechanics are in agreement with the published experimental reports in this field.

These studies of the use of nonlocal continuum mechanics in the mechanical analysis of CNTs have shown that nonlocal continuum mechanics is not significantly harder to apply than local continuum mechanics. In existing buckling and vibration analyses of CNTs, the results can all be expressed concisely; only a few terms related to scale coefficients need be included in addition to those based on local continuum models. The simplicity of nonlocal continuum mechanics implies that these proposed nonlocal elastic models, such as nonlocal elastic beam and shell models, have great potential in the study of scale effects, in cases where such effects have to be taken into account (which cannot be done via local continuum mechanics).

In this article we focus on the static and buckling analysis of CNTs using nonlocal continuum models. We first derive explicitly the small-scale effect in the bending analysis of single-walled CNTs subjected to general loading; one clearly observes a difference in response between the local and nonlocal continuum models for this problem. To our knowledge, no experimental data based on CNT static measurements are available yet that would to reflect scale effects. Wang [2005] studied the validity and applicability of nonlocal continuum models using experimental data for *vibrating* CNTs only.

To qualitatively show the scope of the proposed research, we show how to derive the Young's modulus of a CNT from experiments, using the force-displacement relation, in such a way that small-scale effects, in particular systems studied in

the literature, can be identified and estimated from published measurements of the Young's modulus.

We next derive solutions for the buckling load of a CNT subjected to axial loading with various boundary conditions, using the nonlocal continuum model, relating these solutions to those obtained with local continuum models. In all simulations, the results of static and buckling analyses are expressed in simple terms related to scale coefficients, in addition to the terms corresponding to local continuum models. This shows the simplicity of the nonlocal continuum models. It is hoped that this work will help provide benchmark solutions for the analysis of CNTs via continuum models.

2. Elastic nonlocal beam models for CNT analysis

According to the theory of nonlocal elasticity [Eringen 1976], the stress at a reference point x is considered to be a functional of the strain field at every point in the body. This observation is in accordance with the atomic theory of lattice dynamics and experimental observations on phonon dispersion. In the limit when the effects of strains at points other than x is neglected, one obtains the classical (local) theory of elasticity. The basic equations for linear, homogeneous, isotropic, nonlocal elastic solid with zero body force are given by

$$\begin{aligned} \sigma_{ij,j} &= 0, \\ \sigma_{ij}(x) &= \int \alpha\big(|x-x'|, \tau\big) C_{ijkl}\varepsilon_{kl}(x')\, dV(x') \text{for } x \in V, \\ \varepsilon_{ij} &= \tfrac{1}{2}(u_{i,j} + u_{j,i}), \end{aligned}$$

where C_{ijkl} is the elastic module tensor of classical isotropic elasticity, σ_{ij} and ε_{ij} are the stress and strain tensors, and u_i is displacement vector.

Next,

$$\alpha\big(|x-x'|, \tau\big)$$

is the *nonlocal modulus* or attenuation function, which serves to incorporate into the constitutive equations the nonlocal effects at the reference point x produced by local strain at the source x'. Here $\big|x-x'\big|$ is the Euclidean distance and τ is the quotient $e_0 a/l$ [Peddieson et al. 2003], where l is the external characteristic length (crack length, wavelength, etc.), a is an internal characteristic length, which we choose as 0.142 nm, the length of a C-C bond, as in [Sudak 2003]; and e_0 is an adjustable parameter, given as 0.39 in [Eringen 1983], although Sudak [2003] proposed a value in the order of hundreds. Our work suggests that Eringen's value is close to the mark, but it needs to be further verified through experiments or through matching dispersion curves of plane waves with those of atomic lattice dynamics for CNTs.

Wang [2005] made a rough estimate of the scale coefficient e_0a from the available highest frequency of a single-walled CNT in the literature, based on vibration analysis using the nonlocal elastic Timoshenko beam model. The asymptotic frequency was derived there as $\overline{\omega} = 21456/(e_0a)$ if the mass density is $\rho = 2.3\,\text{g/cm}^3$ and the thickness of the nanotube is $t = 0.34\,\text{nm}$. Hence, a conservative evaluation of the scale coefficient is given by the equation above as $e_0a < 2.1\,\text{nm}$ for a single-walled CNT, if the measured frequency value is greater than 10 THz. This value, like the frequency, is radius-dependent.

Eringen [1983] reduced the integral-partial differential equations for this linear nonlocal elasticity problem to singular partial differential equations of a special class of physically admissible kernel. In addition, Hooke's law for a uniaxial stress state can be determined by

$$\sigma(x) - (e_0a)^2 \frac{d^2\sigma(x)}{dx^2} = E\varepsilon(x), \tag{1}$$

where E is the Young's modulus of the material.

We now apply Euler–Bernoulli beam theory based on the nonlocal continuum elasticity. The free body diagram of an infinitesimal element of a beam structure subjected to both an axial compression force F and a flexural distributed force $q(x)$ is shown in Figure 1. The equilibrium equation for the vertical force component is easily seen to be

$$\frac{dV}{dx} + q(x) = 0,$$

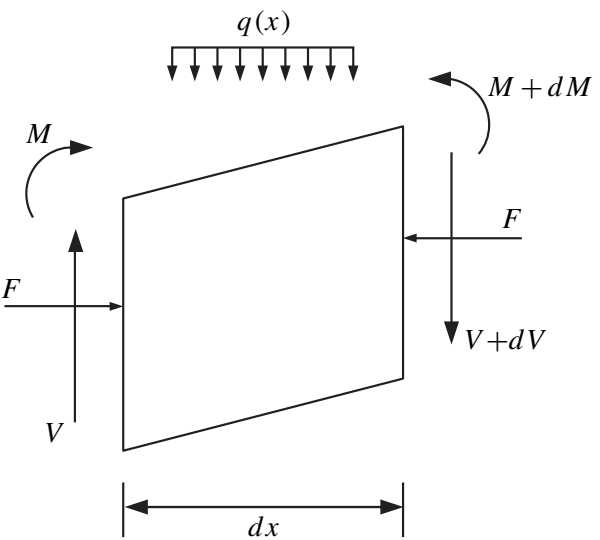

Figure 1. Free body diagram of a beam element.

and that for the moment on the one-dimensional structure is

$$V - \frac{dM}{dx} + F\frac{dw(x)}{dx} = 0, \tag{2}$$

where $V(x,t)$ and $M(x,t)$ are the resultant shear force and bending moment on the beam, and $w(x)$ is the flexural deflection of the beam.

Differentiating the latter equation and substituting into the former one gets

$$\frac{d^2M}{dx^2} = F\frac{dw^2(x)}{dx^2} - q(x). \tag{3}$$

Consider the definitions of the resultant bending moment and the kinematics relation in a beam structure:

$$M = \int_A y\,\sigma\,dA \qquad \text{and} \qquad \varepsilon = -y\frac{d^2w}{dx^2},$$

where y is the coordinate measured from the mid-plane in the height direction of the beam.

Substituting this into the nonlocal constitutive relation Equation (1) leads to

$$M - (e_0a)^2\frac{d^2M}{dx^2} = -\,\mathrm{EI}\,\frac{d^2w}{dx^2},$$

where EI is the bending rigidity of the beam structure. Further considering Equation (3) and Equation (2), the expressions for moment and shear force are derived as

$$\begin{aligned} M(x) &= -\left(\mathrm{EI} - F(e_0a)^2\right)\frac{d^2w(x)}{dx^2} - q(e_0a)^2, \\ V(x) &= -\,\mathrm{EI}\,\frac{d^3w(x)}{dx^3} - F\frac{d}{dx}\left(w(x) - \left(e_0a\right)^2\frac{d^2w(x)}{dx^2}\right) - (e_0a)^2\frac{dq(x)}{dx}. \end{aligned} \tag{4}$$

Substitution of the second of these equations into (2) yields the nonlocal elastic beam model for CNTs subjected to static flexural and axial loadings:

$$\mathrm{EI}\,\frac{d^4w(x)}{dx^4} + F\frac{d^2}{dx^2}\left(w(x) - (e_0a)^2\frac{d^2w(x)}{dx^2}\right) - q(x)\left(1 - (e_0a)^2\frac{d^2q(x)}{dx^2}\right) = 0. \tag{5}$$

It is easily seen from the derivation that the local Euler–Bernoulli beam model is recovered when the parameter e_0 is identically zero.

3. Flexural bending analysis of CNTs

To investigate the bending analysis of CNTs subjected to static flexural loading, the governing equation for CNTs can be derived from (5) as

$$\mathrm{EI}\,\frac{d^4w(x)}{dx^4} = q(x) - (e_0a)^2\,\frac{d^2q(x)}{dx^2}.$$

Hence the model for a CNT subject to a distributed force $q(x)$, concentrated forces P_i at $x = a_i$ $(i = 1 \ldots m)$, and bending moment M_j at $x = b_j$ $(j = 1 \ldots n)$ has the form

$$\mathrm{EI}\,\frac{d^4w(x)}{dx^4} = q(x) - (e_0a)^2\frac{d^2q(x)}{dx^2} + \sum_{i=1}^{m} P_i\big(\delta(x-a_i) - (e_0a)^2\delta''(x-a_i)\big) - \sum_{j=1}^{n} M_j\big(\delta'(x-b_j) - (e_0a)^2\delta'''(x-b_j)\big), \quad (6)$$

where δ is the Dirac delta function, and $'$ denotes differentiation with respect to x.

By integrating both sides of (6), one obtains expressions for the beam deformation and its three derivatives as follows:

$$w'''(x) = \frac{1}{\mathrm{EI}}\int_0^x q(x_1)\,dx_1 - (e_0a)^2\,\frac{dq(x)}{dx} + C_1 + \sum_{i=1}^{m} P_i\big(H(x-a_i) - (e_0a)^2\delta'(x-a_i)\big) - \sum_{j=1}^{n} M_j\big(\delta(x-b_j) - (e_0a)^2\delta''(x-b_j)\big), \quad (7)$$

$$w''(x) = \frac{1}{\mathrm{EI}}\int_0^x (x-x_1)q(x_1)\,dx_1 - (e_0a)^2q(x) + C_1x + C_2 + \sum_{i=1}^{m} P_i\big((x-a_i)H(x-a_i) - (e_0a)^2\delta(x-a_i)\big) - \sum_{j=1}^{n} M_j\big(H(x-b_j) - (e_0a)^2\delta'(x-b_j)\big), \quad (8)$$

$$w'(x) = \frac{1}{\mathrm{EI}}\frac{1}{2}\int_0^x (x-x_1)^2q(x_1)\,dx_1 - (e_0a)^2\int_0^x q(x_1)\,dx_1 + \frac{C_1}{2}x^2 + C_2x + C_3 + \sum_{i=1}^{m} P_i\big((x-a_i)^2H(x-a_i)/2 - (e_0a)^2H(x-a_i)\big) - \sum_{j=1}^{n} M_j\big((x-b_j)H(x-b_j) - (e_0a)^2\delta(x-b_j)\big), \quad (9)$$

$$w(x) = \frac{1}{\mathrm{EI}}\frac{1}{6}\int_0^x (x-x_1)^3 q(x_1)\,dx_1 - (e_0a)^2\int_0^x (x-x_1)q(x_1)\,dx_1 + \frac{C_1}{6}x^3 + \frac{C_2}{2}x^2 + C_3x + C_4 + \sum_{i=1}^{m} P_i\big((x-a_i)^3 H(x-a_i)/6 - (e_0a)^2(x-a_i)H(x-a_i)\big) - \sum_{j=1}^{n} M_j\big((x-b_j)^2 H(x-b_j)/2 - (e_0a)^2 H(x-b_j)\big). \quad (10)$$

3.1. ***Cantilevered CNT.*** Next we discuss small-scale effects on the response of a CNT under different boundary conditions.

We first study a cantilevered CNT of length L subjected to a concentrated force P at $x = l$. This system has been used by Wong et al. [1997] to measure the Young's modulus. According to (10), the response of the CNT under a point force P is

$$w(x) = \frac{1}{\mathrm{EI}}\big(\tfrac{1}{6}C_1x^3 + \tfrac{1}{2}C_2x^2 + C_3x + C_4 + \tfrac{1}{6}P(x-l)^3H(x-l) - P(x-l)H(x-l)\big).$$

The boundary conditions at the left end, $w(0) = w'(0) = 0$, lead to the solutions having $C_3 = C_4 = 0$. The boundary conditions at the right end, $M(L) = V(L) = 0$, together with Equations (4), lead to

$$\begin{aligned} -\mathrm{EI}\left.\frac{d^2w(x)}{dx^2}\right|_{x=L} - P\delta(L-l)(e_0a)^2 = 0, \quad \text{that is,} \quad \left.\frac{d^2w(x)}{dx^2}\right|_{x=L} = 0, \\ -\mathrm{EI}\left.\frac{d^3w(x)}{dx^3}\right|_{x=L} - (e_0a)^2P\delta'(L-l) = 0, \quad \text{that is,} \quad \left.\frac{d^3w(x)}{dx^3}\right|_{x=L} = 0. \end{aligned} \quad (11)$$

Hence C_1 and C_2 can be derived by substituting (7) and (8) into (11):

$$C_1 = -P \qquad \text{and} \qquad C_2 = Pl.$$

The response of the CNT is therefore

$$w(x) = \frac{1}{\mathrm{EI}}\left(\frac{P(x-l)^3}{6}H(x-l) - P\big(e_0a\big)^2(x-l)H(x-l) - \frac{Px^3}{6} + \frac{Plx^2}{2}\right).$$

From this we find that the small-scale term, $P(e_0a)^2(x-l)H(x-l)$, will affect the response of the CNT only in the domain $x > a$. The response at $x = l$ is

$$w(l) = \frac{Pl^3}{3\mathrm{EI}}. \quad (12)$$

It is important to determine whether the small-scale term has any effect on the derived Young's modulus in experimental investigations. In the investigations of

mechanical properties of CNTs by Wong et al. [1997] and Poncharal et al. [1999], the response of a cantilevered CNT at the position of the concentrated force was employed to evaluate Young's modulus of CNTs. According to Equation (12), it is clear that the derived Young's modulus can be viewed as an "accurate" evaluation, since the measurement is independent of the small-scale effect.

Wong et al. [1997] also considered the beam subjected to surface friction force in their modeling of the cantilevered CNT. The friction force can be modeled as a uniform distributed force f applied on the beam. From Equation (10), the response of the CNT can be written as

$$w(x) = \frac{1}{\mathrm{EI}}\left(\frac{fx^4}{24} - \frac{fx^2}{2}(e_0a)^2 + C_1x^3/6 + C_2x^2/2 + C_3x + C_4\right).$$

The fixed left end again leads to $C_3 = C_4 = 0$. Zero moment and shear force at the right end lead to $C_1 = -fL$ and $C_2 = fL^2/2$, by (4), leading to the solution

$$\mathrm{EI}w''(L) + (e_0a)^2 f = 0 \qquad \text{and} \qquad \mathrm{EI}w'''(L) = 0.$$

Therefore, the response of the CNT under uniform distributed force is

$$w(x) = \frac{1}{\mathrm{EI}}\left(\frac{fx^4}{24} - \frac{fLx^3}{6} + \frac{fL^2x^2}{4} - \frac{fx^2}{2}(e_0a)^2\right).$$

It can be seen that the small-scale term has an effect on the measurement of mechanical properties for a cantilevered CNT subjected to uniformly distributed force. This effect has to be considered if an independent value for the Young's modulus or any other material properties is to be evaluated properly. The small-scale effect on the deformation of the CNT is studied numerically in terms of the location of the deformation and the length of the CNT by studying the ratio of the response for the nonlocal versus the local continuum models, at $x = l$. In the simulations we take $e_0a = 2\,\mathrm{nm}$, as suggested in [Wang 2005]. In the top half of Figure 2 we see a plot of this ratio versus the nondimensional location (l/L), for a CNT having length $L = 10\,\mathrm{nm}$. We see that the small-scale effect is more obvious for the response at the point near the free end. The small-scale effect decreases the response, indicating that its neglect may lead to an overestimation of the Young's modulus from the measurements. In [Wong et al. 1997], an increasing variation of the Young's modulus was found by using the classical beam model when the measurement was towards the free end of the cantilever CNT, with both distributed friction and point loading modeled in their experiment. These authors' findings on the increasing variation of the Young's modulus are in agreement with the result shown in the figure for the nonlocal beam model, in which a decreasing variation of the bending deformation is observed as one moves toward the free end. The effect of the length of the CNT on the ratio is seen in Figure 2, bottom, where

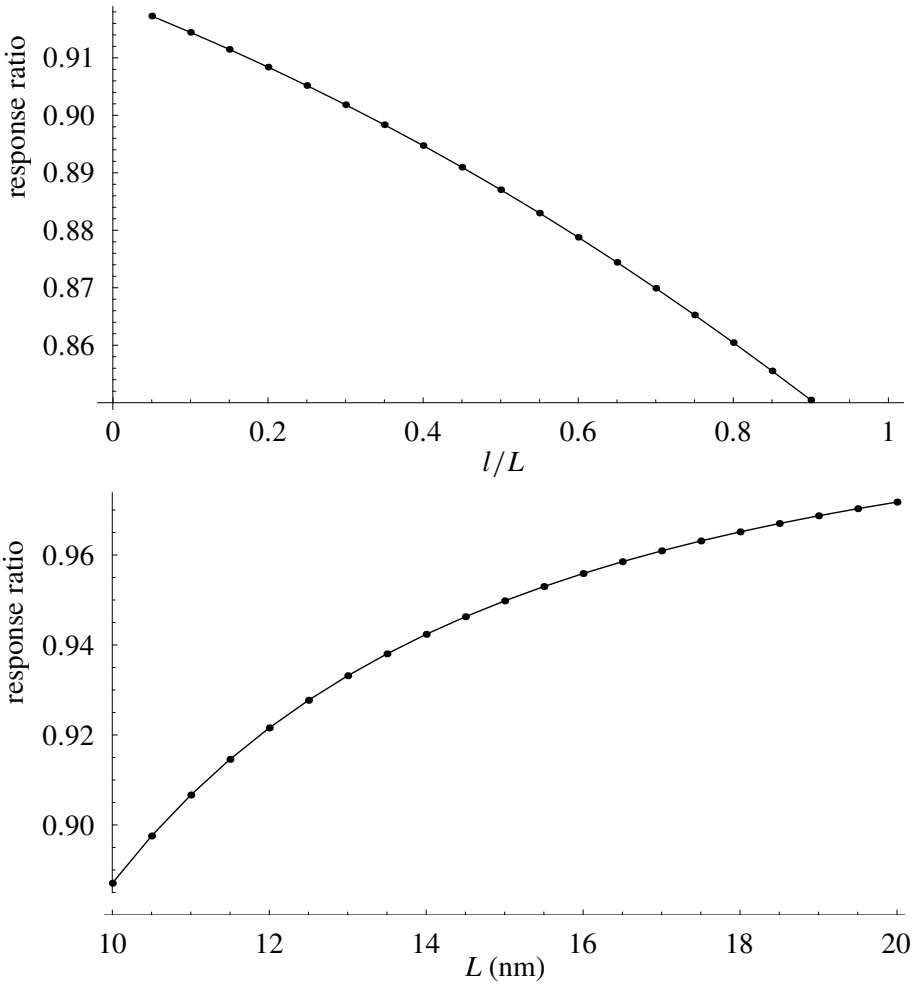

Figure 2. Small-scale effect versus location of the measurement (top) and length of CNT (bottom) for the model of a cantilevered CNT under distributed force.

we take $l/L = 0.5$. It is expected that the small-scale effect is higher for shorter CNTs, and this can be seen in the figure. Thus a local continuum model becomes appropriate for modeling large CNTs.

3.2. ***Simply supported CNT.*** Next, the response of a simply supported CNT subjected to a concentrated force P at $x = l$ will be discussed to show the small-scale effect. The governing equation for the CNT can be obtained from (10) as

$$w(x) = \frac{1}{EI}\left(\frac{P(x-l)^3}{6}H(x-l) - P(x-l)H(x-l)(e_0a)^2 + \frac{C_1x^3}{6} + \frac{C_2x^2}{2} + C_3x + C_4\right). \quad (13)$$

The boundary conditions on the two sides of the CNT, $w(0) = w(L) = M(0) = M(L) = 0$, lead to the solution for the four coefficients, C_1, C_2, C_3 and C_4, and thus the response of the CNT can finally be obtained as:

$$w(x) = \frac{1}{EI}\left(\frac{P(x-l)^3}{6}H(x-l) - P(x-l)H(x-l)\left(e_0a\right)^2 - \frac{P\left(L-l\right)x^3}{6L} + \frac{P(L-l)(-l^2+2Ll)x}{6L} + \frac{P(L-l)\left(e_0a\right)^2x}{L}\right).$$

The response of the CNT at the force location, $x = l$, is thus derived as:

$$w(l) = \frac{1}{EI}\left(-\frac{P\left(L-l\right)l^3}{6L} + \frac{P(L-l)(-l^2+2Ll)l}{6L} + \frac{P(L-l)\left(e_0a\right)^2l}{L}\right).$$

Especially when $l = L/2$, one can obtain,

$$w\left(\frac{L}{2}\right) = \frac{L^3}{48EI}\left(1 + 12\left(\frac{e_0a}{L}\right)^2\right).$$

The study of the small-scale effect on the simply supported CNT is illustrated in Figure 3. The top half of the figure plots the ratio of the response from the local and nonlocal continuum model versus the nondimensional location (l/L) for a CNT with $L = 10$ nm. It is observed that the small-scale effect is more obvious for the response at the two ends of the beam. The effect leads to the value of the ratio up to 2.4. The small-scale effect makes the response of the CNT larger indicating that an under-estimated Young's modulus might be obtained from the measurement of deformation of a simply supported CNT. The effect of the length of the CNT on the ratio is shown in the bottom half of the figure, for $l/L = 0.5$. It is again within our understanding that the small-scale has higher effect for shorter simply supported CNTs.

3.3. ***Fixed-fixed CNT.*** Salvetat et al. [1999] investigated the elastic and shear modulus of CNTs by measuring the displacement of a fixed-fixed CNT subjected to a concentrated force. Thus, it is of significance to understand and evaluate the small-scale effect on the results of the moduli by measuring the response of fixed-fixed CNTs. The general expression for the deformation result of a fixed-fixed CNT subjected to a concentrated force P at $x = l$ is same as Equation (13). Considering the boundary conditions at the two ends of the beam, $w(0) = w'(0) = w(L) =$

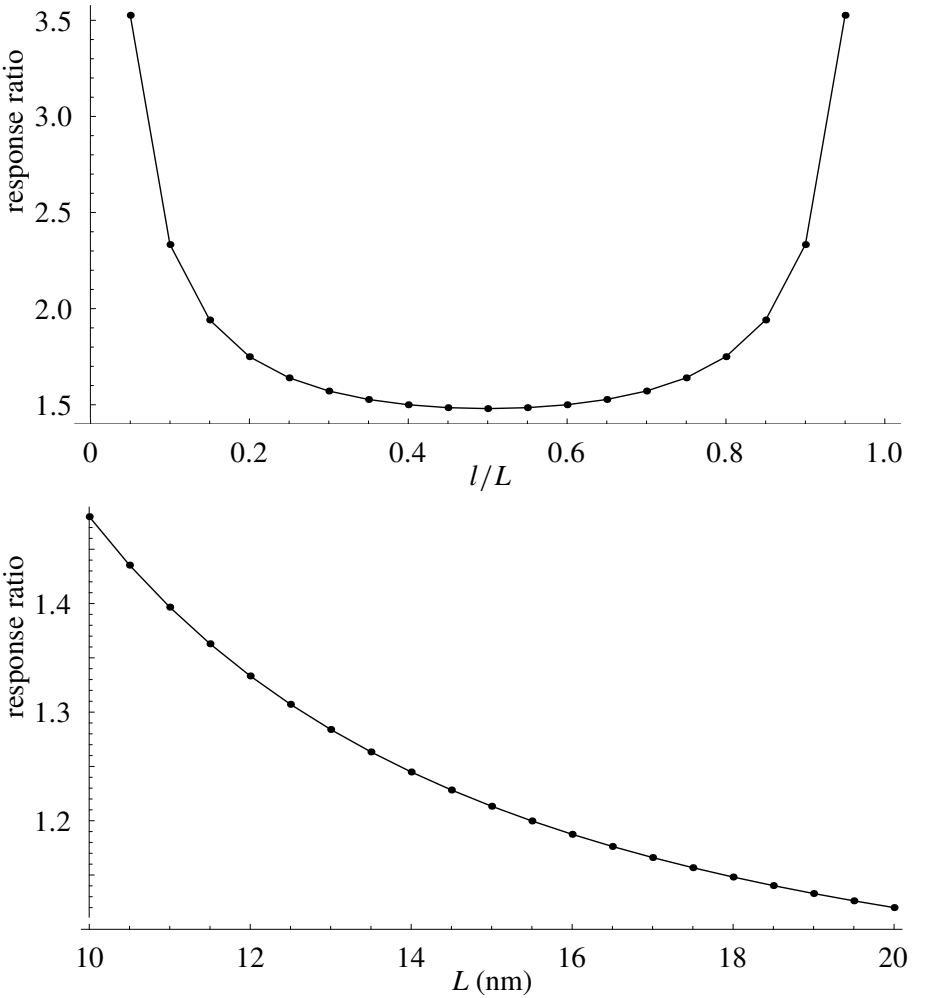

Figure 3. Small-scale effect versus location of the measurement (top) and length of CNT (bottom) for a singly supported CNT.

$w'(L) = 0$, one can obtained the values for the four coefficients, C_1, C_2, C_3 and C_4, and hence, the response of the beam shown as

$$w(x) = \frac{1}{\mathrm{EI}}\left(\frac{P(x-l)^3}{6}H(x-l) - P(x-l)H(x-l)(e_0a)^2 + \left(\frac{P(e_0a)^2}{L^2}\left(\frac{2l}{L}-1\right) - \frac{P(L-l)^2}{6L^2}\left(1+\frac{2l}{L}\right)\right)x^3 + \left(\frac{P\left(e_0a\right)^2}{L^2}\left(2L-3l\right) + \frac{P(L-l)^2 l}{2L^2}\right)x^2\right).$$

The expression for the response at $x = l$ is thus given as:

$$w(x) = \frac{1}{\mathrm{EI}}\left(\left(\frac{P(e_0a)^2}{L^2}\left(\frac{2l}{L}-1\right) - \frac{P(L-l)^2}{6L^2}\left(1+\frac{2l}{L}\right)\right)x^3 + \left(\frac{P(e_0a)^2}{L^2}(2L-3l) + \frac{P(L-l)^2 l}{2L^2}\right)x^2\right).$$

Furthermore, the result for $l = L/2$ is given as:

$$w\left(\frac{L}{2}\right) = \frac{PL^3}{192}\left(1+24\left(\frac{e_0a}{L}\right)^2\right).$$

Figure 4, top, shows the ratio of the response from the local and nonlocal continuum model versus the nondimensional location (l/L), for $L = 10$ nm. It is seen clearly that the ratio reaches 3.7 when the measurement is taken near fixed ends and 1.96 for measurement at the center of the beam. This observation indicates that the Young's modulus may be underestimated by a factor of at least two in the fixed-fixed CNT. The bottom half of the figure again shows the effect of the length of the CNT on the estimation of the response, if the measurement point is taken at the middle of the CNT. It is seen that the small-scale effect is still obvious for a CNT with $L = 15$ nm although this effect becomes smaller with longer CNTs.

From the numerical simulation on three types of CNTs, it is found that the small-scale effects are more obvious for stiffer CNTs, i.e. fixed-fixed CNTs, and less obvious for softer CNTs, i.e. cantilevered CNTs. Since the experimental results in [Salvetat et al. 1999] are inconsistent, the verification for the nonlocal beam model cannot be implemented at the moment, but will be conducted when consistent data are available. However, the scale effect was truly observed in [Salvetat et al. 1999].

4. Buckling analysis of CNTs

Buckling is one type of instability exhibited by structures subjected to compressive loading. Sudak [2003] derived the buckling load of simply supported CNTs via the nonlocal continuum model. To establish the relationship between the buckling load of CNTs considering small-effect from nonlocal continuum models and that without taking into account of small-effect from local continuum models is the main objective in this section.

The governing equation for a CNT subjected to a compressive loading, F, is given as follows according to Equation (5):

$$\mathrm{EI}\frac{d^4w(x)}{dx^4} + F\frac{d^2}{dx^2}\left(w(x) - (e_0a)^2\frac{d^2w(x)}{dx^2}\right) = 0. \tag{14}$$

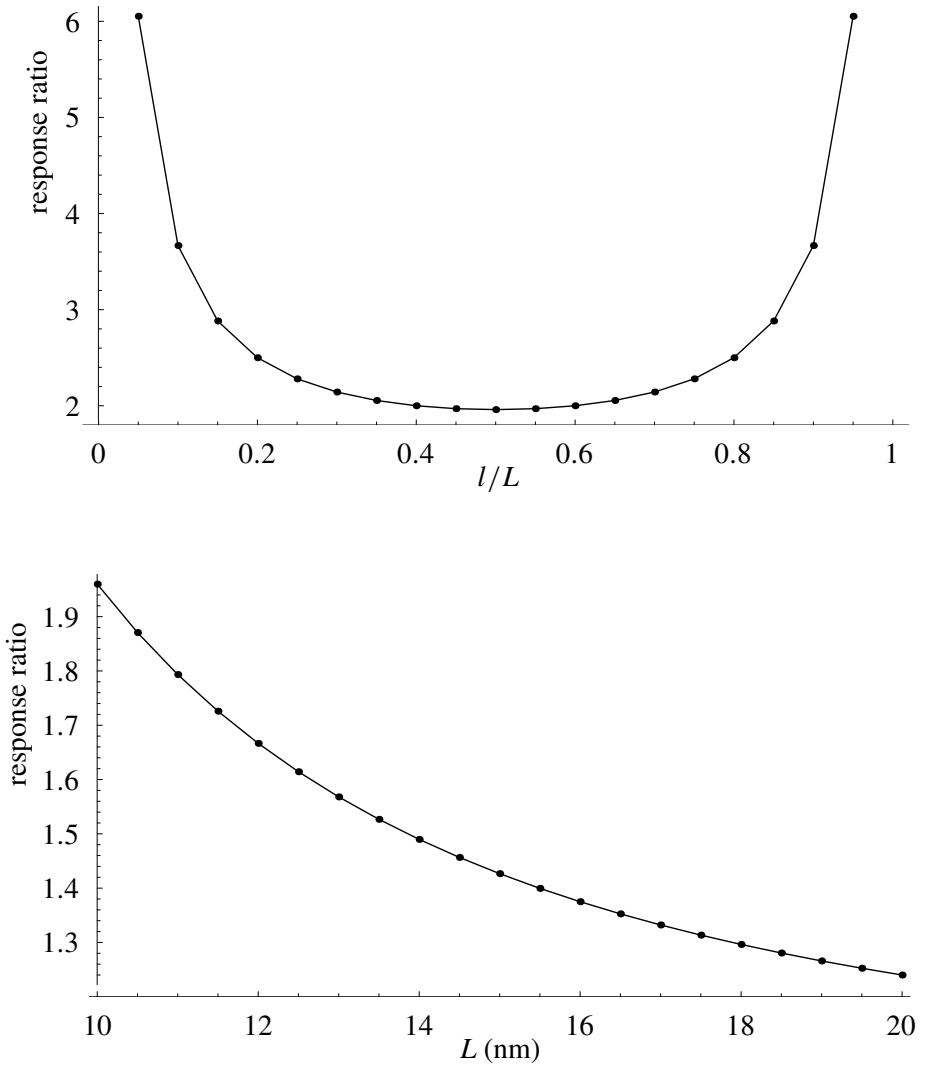

Figure 4. Small-scale effect versus location of the measurement (top) and length of CNT (bottom) for a fixed-fixed CNT.

The general solution for Equation (14) can be easily derived as:

$$w(x) = A_1 \cos \alpha\, x + A_2 \sin \alpha\, x + A_3 x + A_4, \tag{15}$$

where $\alpha = \sqrt{\frac{F}{\mathrm{EI} - F(e_0 a)^2}}$.

The buckling load can be derived from an eigenvalue problem to find nontrivial solution for $w(x)$ by substituting Equation (15) into four boundary conditions at

the ends of beams. The fundamental value of α for the first buckling mode is derived as follows [Timoshenko and Gere 1963]:

$$\alpha = \frac{\beta\pi}{L}, \tag{16}$$

where β has different value for beams with different boundary conditions, i.e. $\beta = 1$ for simply supported beams; $\beta = 0.5$ for cantilevered beams; $\beta = 2$ for fixed-fixed beams. From Equation (16), the buckling load for CNTs with the nonlocal continuum model can thus be obtained as

$$F = \frac{\mathrm{EI}\left(\frac{\beta\pi}{L}\right)^2}{1 + (e_0 a)^2\left(\frac{\beta\pi}{L}\right)^2}. \tag{17}$$

It can be seen clearly that the buckling load becomes smaller with a factor

$$\left(1 + (e_0 a)^2\left(\frac{\beta\pi}{L}\right)^2\right)^{-1} \tag{18}$$

from the nonlocal elastic beam theory compared to that from local continuum model. Equation (17) provides a general solution for the buckling load with the nonlocal continuum model. For example, the solution for buckling load at $\beta = 1$ for a simply supported CNT was provided by Sudak [2003]. From the solution shown in (17), it can be concluded that the small-scale effect is more obvious for shorter, or smaller L, and stiffer CNT, or higher β. Yakobson et al. [1996] studied the instability behavior of CNTs by using molecular dynamics. In their results on the instability patterns, they found a beam-like buckling mode with two half wavenumber in tube length direction at the axial compression strain $\varepsilon = 0.09$ for a CNT with length 6 nm and diameter 1 nm. However, according to the continuous elastic beam model [Wang and Varadan 2005], the CNT may have its beam-like buckling for a two-half wavenumber mode only at compression strain $\varepsilon = 0.137$. Such discrepancy of the derived buckling strain may be due to the scale effect. From the currently developed nonlocal theory, it can be easily found that the over-estimated buckling strain can be modulated to match the result from the molecular dynamics calculations in [Yakobson et al. 1996] if the scale coefficient is set to be $e_0 a = 1.2$ nm. It is also noted that the nonlocal beam model cannot capture the radius-dependent scale effect since in beam model, a uniform radial deformation assumption is endorsed. The possible radius-dependent scale effect found in [Wang et al. 2005a] could only be evaluated from a nonlocal shell model which will be developed and studied later.

5. Conclusions

Small-scale effects on both the bending analysis of CNTs subjected to static flexural loading and the buckling load of CNTs subjected to compressive loading are explicitly studied with the nonlocal continuum beam theory. It is found that there is no such effect on the static response of a cantilevered CNT at the location where the beam is subjected to a concentrated force, and hence the experimental work on the measurement of Young's modulus of CNTs on a cantilevered CNT subjected to concentrated force is relatively reliable since the small-scale effect of CNTs is not involved in the measurement of the response. On the other hand, the small-scale effects are explicitly derived on the response of cantilevered CNT subjected to distributed force at all locations, simply supported CNTs and fixed-fixed CNTs at the location where the CNT is subjected to concentrated force. The effect becomes more obvious with smaller size of CNTs. In addition, the effect is dependent on the location where the response is taken. For example, the effect is higher on the responses, where the force is applied at the two ends of both simply supported and fixed-fixed CNTs. But the effect is higher at the free end of a cantilevered CNT subjected to a uniformly distributed force. The results also reveals that the small-scale effects are more obvious for stiffer CNTs, i.e. fixed-fixed CNTs, and less obvious for softer CNTs, i.e. cantilevered CNTs. The results on buckling instability of CNTs show that the buckling load becomes smaller when small-scale effect is considered by the nonlocal continuum model. The ratio of the result from nonlocal model to that via local model is explicitly derived for CNTs with any general boundary conditions. Furthermore, the small-scale effect is found to be more obvious for shorter and stiffer CNT in buckling analysis. Further studies may focus on the corresponding analysis of multi-walled CNTs. In all simulations, the results for CNTs static and buckling analyses are all expressed by simple terms related to scale coefficients in addition to terms by local continuum models. Thus, the simplicity of the nonlocal continuum mechanics is well seen and the applicability of the theory is promising.

References

[Ball 2001] P. Ball, "Roll up for the revolution", *Nature* **414**:6860 (2001), 142–144.

[Baughman et al. 2002] R. H. Baughman, A. A. Zakhidov, and W. A. de Heer, "Carbon nanotubes – the route toward applications", *Science* **297**:5582 (2002), 787–792.

[Eringen 1976] A. C. Eringen, *Nonlocal polar field models*, Academic Press, New York, 1976.

[Eringen 1983] A. C. Eringen, "On differential equations of nonlocal elasticity and solutions of screw dislocation and surface waves", *J. Appl. Phys.* **54**:9 (1983), 4703–4710.

[Harris 1999] P. J. F. Harris, *Carbon nanotubes and related structures*, Cambridge University Press, Cambridge, 1999.

[Hernandez et al. 1998] E. Hernandez, C. Goze, P. Bernier, and A. Rubio, "Elastic properties of C and $B_xC_yN_z$ composite nanotubes", *Phys. Rev. Lett.* **80**:20 (1998), 4502–4505.

[Iijima 1991] S. Iijima, "Helical microtubules of graphitic carbon", *Nature* **354**:6348 (1991), 56–58.

[Iijima et al. 1996] S. Iijima, C. Brabec, A. Maiti, and J. Bernholc, "Structural flexibility of carbon nanotubes", *J. Chem. Phys.* **104**:5 (1996), 2089–2092.

[Lau 2003] K. T. Lau, "Interfacial bonding characteristics of nanotube/polymer composites", *Chem. Phys. Lett.* **370**:3–4 (2003), 399–405.

[Parnes and Chiskis 2002] R. Parnes and A. Chiskis, "Buckling of nano-fibre reinforced composites: a reexamination of elastic buckling", *J. Mech. Phys. Solids* **50**:4 (2002), 855–879.

[Peddieson et al. 2003] J. Peddieson, G. R. Buchanan, and R. P. McNitt, "Application of nonlocal continuum models to nanotechnology", *Int. J. Eng. Sci.* **41**:3–5 (2003), 305–312.

[Poncharal et al. 1999] P. Poncharal, Z. L. Wang, D. Ugarte, and W. de Heer, "Electrostatic deflections and electromechanical resonances of carbon nanotubes", *Science* **283**:5407 (1999), 1513–1516.

[Pugno and Ruoff 2004] N. Pugno and R. Ruoff, "Quantized fracture mechanics", *Philos. Mag.* **84**:27 (2004), 2829–2845.

[Ru 2000a] C. Q. Ru, "Effective bending stiffness of carbon nanotubes", *Phys. Rev.* **B62**:15 (2000), 9973–9976.

[Ru 2000b] C. Q. Ru, "Elastic buckling of single-walled carbon nanotubes ropes under high pressure", *Phys. Rev.* **B62**:15 (2000), 10405–10408.

[Salvetat et al. 1999] J. P. Salvetat, G. A. Briggs, J. M. Bonard, R. R. Bacsa, A. J. Kulik, T. Stockli, N. A. Burnham, and L. Forro, "Elastic and shear moduli of single-walled carbon nanotube ropes", *Phys. Rev. Lett.* **82**:5 (1999), 944–947.

[Sanchez-Portal et al. 1999] D. Sanchez-Portal, E. A. and. J. M. Soler, A. Rubio, and P. Ordejon, "Ab initio structural, elastic, and vibrational properties of carbon nanotubes", *Phys. Rev.* **B59**:19 (1999), 12678–12688.

[Sharma et al. 2003] P. Sharma, S. Ganti, and N. Bhate, "Effect of surfaces on the size-dependent elastic state of nano-inhomogeneities", *Appl. Phys. Lett.* **82**:4 (2003), 535–537.

[Sheehan and Lieber 1996] P. E. Sheehan and C. M. Lieber, "Nanotribology and nanofabrication of MoO3 structures by atomic force microscopy", *Science* **272**:5265 (1996), 1158–1161.

[Sudak 2003] L. J. Sudak, "Column buckling of multiwalled carbon nanotubes using nonlocal continuum mechanics", *J. Appl. Phys.* **94**:11 (2003), 7281–7287.

[Sun and Zhang 2003] C. T. Sun and H. Zhang, "Size-dependent elastic moduli platelike nanomaterials", *J. Appl. Phys.* **93**:2 (2003), 1212–1218.

[Timoshenko and Gere 1963] S. P. Timoshenko and J. M. Gere, *Theory of elastic stability*, McGraw-Hill, New York, 1963.

[Treacy et al. 1996] M. M. J. Treacy, T. W. Ebbesen, and J. M. Gibson, "Exceptionally high Young's modulus observed for individual carbon nanotubes", *Nature* **381**:6584 (1996), 678–680.

[Wang 2005] Q. Wang, "Wave propagation in carbon nanotubes via nonlocal continuum mechanics", *J. Appl. Phys.* **98** (2005), 124301.

[Wang and Varadan 2005] Q. Wang and V. K. Varadan, "Stability analysis of carbon nanotubes via continuum models", *Smart Mater. Struct.* **14** (2005), 281–286.

[Wang et al. 2005a] L. Wang, Q. Zheng, J. Liu, and Q. Jiang, "Size dependence of the thin-shell model for carbon nanotubes", *Phys. Rev. Lett.* **95** (2005), 105501.

[Wang et al. 2005b] Q. Wang, T. Hu, G. Chen, and Q. Jiang, "Bending instability characteristics of double-walled carbon nanotubes", *Phys. Rev.* **B71** (2005), 045403.

[Wong et al. 1997] E. W. Wong, P. E. Sheehan, and C. M. Lieber, "Nanobeam mechanics: elasticity, strength, and toughness of nanorods and nanotubes", *Science* **277**:5334 (1997), 1971–1975.

[Yakobson and Smalley 1997] B. I. Yakobson and R. Smalley, "Fullerene nanotubes: $C_{1,000,000}$ and beyond", *Am. Sci.* **85** (1997), 324–337.

[Yakobson et al. 1996] B. I. Yakobson, C. J. Brabec, and J. Bernholc, "Nanomechanics of carbon tubes: instabilities beyond linear response", *Phys. Rev. Lett.* **76**:14 (1996), 2511–2514.

[Yakobson et al. 1997] B. I. Yakobson, M. P. Campbell, C. J. Brabec, and J. Bernholc, "High strain rate fracture and C-chain unraveling in carbon nanotubes", *Comput. Mater. Sci.* **8**:4 (1997), 341–348.

[Zhang et al. 2002] P. Zhang, Y. Huang, P. H. Geubelle, P. A. Klein, and K. C. Hwang, "The elastic modulus of single-wall carbon nanotubes: a continuum analysis incorporating interatomic potentials", *Int. J. Solids Struct.* **39**:13–14 (2002), 3893–3906.

[Zhang et al. 2004] Y. Q. Zhang, G. R. Liu, and J. S. Wang, "Small scale effects on buckling of multiwalled carbon nanotubes under axial compression", *Phys. Rev.* **B70** (2004), 205430.

Received 2 Dec 2005.

QUAN WANG: qzwang@mail.ucf.edu
Department of Mechanical and Manufacturing Engineering, University of Manitoba, Winnipeg, Manitoba R3T 5V6, Canada

YASUHIDE SHINDO: shindo@msws.material.tohoku.ac.jp
Department of Materials Processing, Graduate School of Engineering, Tohoku University, Sendai 980-8579, Japan

JOURNAL OF MECHANICS OF MATERIALS AND STRUCTURES
Vol. 1, No. 4, 2006

CONSERVATION LAWS AT NANO/MICRO SCALES

YOUPING CHEN AND JAMES LEE

This paper aims to find a field description of local conservation laws at nano/micro scales. Atomistic definitions and field representations of fundamental physical quantities are presented. By decomposing atomic deformation into homogeneous lattice deformation and inhomogeneous relative atomic deformation, and also decomposing momentum flux and heat flux into homogeneous and inhomogeneous parts, the field representations of conservation laws at atomic scale have been formulated, which follow exactly the time evolution laws that exist in atomistic simulations, where the atomic motion is fully described, the inhomogeneous internal motion is not ignored, and the smallest particles considered are atoms.

1. Introduction

The atomic view of a crystal is as a periodic arrangement of local atomic bonding units. Each lattice point defines the location of the center of a unit. The space lattice is macroscopically homogeneous. Embedded in each lattice point is a group of bonded atoms, the smallest structural unit of the crystal. The structure of the unit together with the network of lattice points determines the crystal structure and hence the physical properties of the material.

For crystals that have more than one atom in the unit cell, elastic distortions give rise to wave propagation of two types: acoustic and optic. In the acoustic type, all atoms in the unit cell move essentially in the same phase, resulting in deformation of the lattice. In the optical type, atoms move within the unit cell, leave the lattice unchanged, and give rise to internal deformations. In real material response, atomic vibrations usually include simultaneous lattice deformation and internal deformation. The displacement of the α-th atom in the k-th unit cell, $\boldsymbol{u}(k,\alpha)$ is in fact a sum of the lattice displacement $\boldsymbol{u}(k)$ and the internal displacement $\boldsymbol{\xi}(k,\alpha)$, that is,

$$\boldsymbol{u}(k,\alpha) = \boldsymbol{u}(k) + \boldsymbol{\xi}(k,\alpha). \tag{1–1}$$

Keywords: local conservation laws, lattice deformation.
Support for this work by the National Science Foundation under Awards Number CMS-0301539 and CMS-0428419 is gratefully acknowledged.

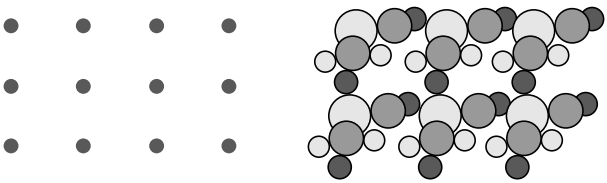

Figure 1. Atomic view of crystal structure: left, space lattice; right, crystal structure.

Analysis of phonon dispersion relations can show that, for a unit cell with ν atoms, there will be 3 acoustic and $3(\nu-1)$ optical vibrational modes, and hence 3 lattice displacements and $3(\nu-1)$ internal displacement patterns. There are two length/time scales associated with the atomic displacement in Equation (1–1). The lattice deformation $\boldsymbol{u}(k)$ is homogeneous up to the point of structural instability (phase transformation). It is in the low and audible frequency region, and its length scale can be from sub-nano to macroscopic. The internal displacement $\boldsymbol{\xi}(k,\alpha)$ measures the displacement of atoms relative to the lattice, and contributes to the inhomogeneous deformation. It is in the high frequency region, typically in the infrared, and its length scale is less than a nanometer.

From the viewpoint of molecular dynamics simulation, an ordered single crystal is considered to have n unit cells; each unit cell is composed of ν atoms with mass m^α, position $\boldsymbol{R}^{k\alpha}$ and velocity $\boldsymbol{V}^{k\alpha}$, where $\alpha = 1, 2, \ldots, \nu$ and $k = 1, 2, \ldots, n$. The mass m, coordinate $\boldsymbol{R}^k$ and velocity $\boldsymbol{V}^k$ at the center of the unit cell can be obtained as

$$m = \sum_{\alpha=1}^{\nu} m^\alpha, \qquad \boldsymbol{R}^k = \frac{1}{m}\sum_{\alpha=1}^{\nu} m^\alpha \boldsymbol{R}^{k\alpha}, \qquad \boldsymbol{V}^k = \frac{1}{m}\sum_{\alpha=1}^{\nu} m^\alpha \boldsymbol{V}^{k\alpha}. \tag{1–2}$$

The relative positions and velocities between atoms and the center of the unit cell are

$$\Delta\boldsymbol{r}^{k\alpha} = \boldsymbol{R}^{k\alpha} - \boldsymbol{R}^k, \qquad \Delta\boldsymbol{v}^{k\alpha} = \boldsymbol{V}^{k\alpha} - \boldsymbol{V}^k. \tag{1–3}$$

It follows that

$$\boldsymbol{u}(k,\alpha) = \boldsymbol{u}(k) + \boldsymbol{\xi}(k,\alpha). \tag{1–4}$$

This again shows that the total atomic displacement $\boldsymbol{u}(k,\alpha)$ is a sum of a homogeneous lattice deformation $\boldsymbol{u}(k)$ and an inhomogeneous internal deformation $\boldsymbol{\xi}(k,\alpha)$, as is obtained in Equation (1–1) from a crystal dynamics viewpoint. Note that the inhomogeneous internal deformations will be averaged out upon cell-averages, and are ignored in classical macroscopic theories.

This paper aims to formulate a field representation of the conservation laws for multielement systems. Unlike the approach in statistical mechanics, here the

atomic motion and deformation are decomposed into homogeneous and inhomogeneous parts and the conservation equations are to be valid at atomic scale. Atomistic definitions of physical quantities are derived in Section 2; general dynamic equations (time evolution) of instantaneous and averaged physical quantities are introduced in Section 3; and the balance laws at atomic scale are formulated in Section 4. A summary and discussions are presented in Section 5. Standard dyadic notations are adopted in this paper.

2. Atomistic definitions of physical quantities

2.1. ***Instantaneous physical quantities.*** Macroscopic quantities are generally described by continuous (or piecewise-continuous) functions of physical space coordinates $\boldsymbol{x}$ and of time t. They are fields in physical space-time. Microscopic dynamic quantities, on the other hand, are functions of phase-space coordinates $(\boldsymbol{r}, \boldsymbol{p})$, that is, the positions and momenta of atoms (see Equations (1–2) and (1–3)):

$$\boldsymbol{r} = \left\{ \boldsymbol{R}^{k\alpha} = \boldsymbol{R}^k + \Delta\boldsymbol{r}^{k\alpha} \;\middle|\; k = 1, 2, \ldots, n; \alpha = 1, 2, \ldots, \nu \right\},$$
$$\boldsymbol{p} = \left\{ m^\alpha \boldsymbol{V}^{k\alpha} = m^\alpha \boldsymbol{V}^k + m^\alpha \Delta\boldsymbol{v}^{k\alpha} \;\middle|\; k = 1, 2, \ldots, n; \alpha = 1, 2, \ldots, \nu \right\},$$

where the superscript $k\alpha$ refers to the α-th atom in the k-th unit cell. Consider a one-particle dynamic function $a(\boldsymbol{R}^{k\alpha}, \boldsymbol{V}^{k\alpha})$. The corresponding local density at a given point $\boldsymbol{x}$ in physical space can be represented by

$$A(\boldsymbol{R}^{k\alpha}, \boldsymbol{V}^{k\alpha}; \boldsymbol{x}) = a(\boldsymbol{R}^{k\alpha}, \boldsymbol{V}^{k\alpha})\,\delta(\boldsymbol{R}^{k\alpha} - \boldsymbol{x}).$$

Here the δ-function, $\delta(\boldsymbol{R}^{k\alpha} - \boldsymbol{x})$, is a localization function and provides the link between phase space and physical space descriptions. It can be a Dirac δ-function or a distribution function. For a Dirac δ-function [Irving and Kirkwood 1950], one has

$$\delta(\boldsymbol{x} - \boldsymbol{R}^{k\alpha}) = \begin{cases} \infty, & \boldsymbol{x} = \boldsymbol{R}^{k\alpha}, \\ 0, & \boldsymbol{x} \neq \boldsymbol{R}^{k\alpha}. \end{cases}$$

This means that, in a discontinuous atomic description, there can be a contribution to this function only if an atom happens to be located at $\boldsymbol{x}$, that is, if $\boldsymbol{R}^{k\alpha} = \boldsymbol{x}$.

In the distribution or weighting function approach, the localization function is a nonnegative function that has a finite size and finite value [Hardy 1963; 1982; Ranninger 1965], peaks at $\boldsymbol{x} = \boldsymbol{R}^{k\alpha}$ and tends to zero as $|\boldsymbol{x} - \boldsymbol{R}^{k\alpha}|$ becomes large. For example, one can use the Gaussian distribution function

$$\delta(\boldsymbol{x} - \boldsymbol{R}^{k\alpha}) = \frac{1}{\pi^{3/2} l^3} \exp\left(-|\boldsymbol{x} - \boldsymbol{R}^{k\alpha}|^2 / l^2\right),$$

where l characterizes the length of the region of a lattice point or of an atom. Both the Dirac δ-function and the distribution function shall satisfy

$$\int_V \delta(\boldsymbol{x} - \boldsymbol{R}^{k\alpha})\, d^3x = 1.$$

This is a standard treatment in statistical mechanics for defining a *mapping of phase space into physical space*.

We intend here to employ a different field description that specifies the positions of the unit cell and of the atom relative to the unit cell, similar to the MD model representation in Figure 2 of a multielement crystal. Unlike the standard treatment in statistical mechanics, we employ $\boldsymbol{x}$ throughout the rest of this paper to represent continuous collections of lattice points, corresponding to the phase space coordinates, $\boldsymbol{R}^k$ and $\boldsymbol{y}^\alpha$ to represent the α-th atomic position relative to the lattice point $\boldsymbol{x}$, corresponding to $\Delta\boldsymbol{r}^{k\alpha}$; see Figures 2 and 3. Therefore, this localization function

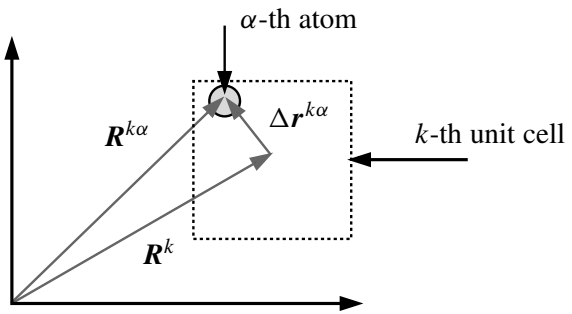

Figure 2. Atomic coordinate in terms of the positions of the unit cell and of the atom relative to the unit cell.

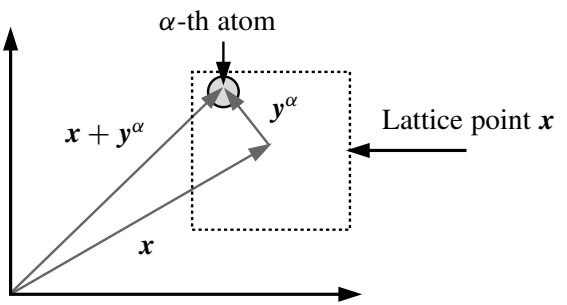

Figure 3. Field representation of the positions of the unit cell and of the atoms relative to the unit cell.

that defines the *mapping of phase space into physical space* has the form

$$\delta(\boldsymbol{R}^k + \Delta\boldsymbol{r}^{k\alpha} - \boldsymbol{x} - \boldsymbol{y}^\alpha) = \delta(\boldsymbol{R}^k - \boldsymbol{x})\,\delta(\Delta\boldsymbol{r}^{k\alpha} - \boldsymbol{y}^\alpha),$$

with which the correspondence between a lattice point $\boldsymbol{x}$ in physical space to the position of the center of the k-th unit cell in phase space, $\boldsymbol{R}^k$, is then established, and the position of the α-th atom associated with lattice point $\boldsymbol{x}$, $\boldsymbol{y}^\alpha$, shall be in one-to-one correspondence with $\Delta\boldsymbol{r}^{k\alpha}$, the relative position of the α-th atom in the unit cell k. That is, for any given physical point $\boldsymbol{x}$ at an instantaneous time, a unit cell can be found whose center $\boldsymbol{R}^k$ is located at this point, and a physical space description of the relative position of the α-th atom, $\boldsymbol{y}^\alpha$, can be determined.

The local density of any measurable phase-space function $A(\boldsymbol{r}, \boldsymbol{p})$ can then be defined as

$$\boldsymbol{A}(\boldsymbol{x}, \boldsymbol{y}^\alpha) = \sum_{k=1}^{n} A(\boldsymbol{r}, \boldsymbol{p})\,\delta(\boldsymbol{R}^k - \boldsymbol{x})\,\delta(\Delta\boldsymbol{r}^{k\alpha} - \boldsymbol{y}^\alpha) \equiv \boldsymbol{A}^\alpha(\boldsymbol{x}),$$

with normalization conditions

$$\int_V \delta(\boldsymbol{R}^k - \boldsymbol{x})\, d^3x = 1 \quad \text{for all } k, \tag{2–1}$$

where V is the volume of the whole system. Equation (2–1) implies that over the entire physical space all the unit cells ($k = 1, 2, \ldots, n$) can be found. Then, for each unit cell k, the second δ-function, $\delta(\Delta\boldsymbol{r}^{k\alpha} - \boldsymbol{y}^\alpha)$, identifies $\boldsymbol{y}^\alpha$ to be $\Delta\boldsymbol{r}^{k\alpha}$:

$$\delta(\Delta\boldsymbol{r}^{k\xi} - \boldsymbol{y}^\alpha) = \begin{cases} 1 & \text{if } \xi = \alpha \quad \text{and} \quad \Delta\boldsymbol{r}^{k\xi} = \boldsymbol{y}^\alpha, \\ 0 & \text{if } \xi \neq \alpha \quad \text{or} \quad \Delta\boldsymbol{r}^{k\xi} \neq \boldsymbol{y}^\alpha. \end{cases}$$

It follows that

$$\delta(\Delta\boldsymbol{r}^{k\alpha} - \boldsymbol{y}^\alpha) = \sum_{\xi=1}^{\nu} \delta(\Delta\boldsymbol{r}^{k\xi} - \boldsymbol{y}^\alpha),$$

and

$$\int_V \delta(\boldsymbol{R}^k - \boldsymbol{x})\,\delta(\Delta\boldsymbol{r}^{k\alpha} - \boldsymbol{y}^\alpha)\, d^3\boldsymbol{x} = 1 \quad \text{for all } k, \alpha.$$

2.2. ***Averaged field variables.*** To obtain an observable quantity in a MD simulation, one must first be able to express this observable as a function of the positions and momenta of the particles in the system. However, a measured value of A, called A_m, is not obtained from an experiment performed at an instant; rather the experiment requires a finite duration. During that measuring period individual atoms evolve through many values of positions and momenta. Therefore, the measured

value A_m is generally the phase function $A(\boldsymbol{r}, \boldsymbol{p})$ averaged over a time interval Δt:

$$A_m(t) = \frac{1}{\Delta t} \int_0^{\Delta t} A\big(\boldsymbol{r}(t+\tau), \boldsymbol{p}(t+\tau)\big)\, d\tau.$$

In equilibrium MD it is assumed that this time-interval average reliably approximates the time average $\langle A \rangle = \lim_{t\to\infty} \frac{1}{t} \int_0^t A(\boldsymbol{r}(\tau), \boldsymbol{p}(\tau))\, d\tau$, which would be obtained from a measurement performed over an essentially infinite duration:

$$A_m = \langle A \rangle. \tag{2–2}$$

In statistical mechanics a macroscopic quantity is defined as the ensemble average of an instantaneous dynamical function:

$$\langle A \rangle \equiv \int_{\boldsymbol{p}} \int_{\boldsymbol{r}} A(\boldsymbol{r}, \boldsymbol{p})\, f(\boldsymbol{r}, \boldsymbol{p}, t)\, d\boldsymbol{r}\, d\boldsymbol{p},$$

where f is the normalized probability density function $\big(\big(\int f(\boldsymbol{r}, \boldsymbol{p}, t)\, d\boldsymbol{r}\, d\boldsymbol{p} = 1\big)\big)$. Equation (2–2) distinguishes molecular dynamics from statistical mechanics. Statistical mechanics replaces the time average with an ensemble average by invoking the ergodic hypothesis, which is motivated by the inability to compute the phase-space trajectory of a real system containing huge numbers of molecules. When one departs from equilibrium, very little theoretical guidance is available from statistical mechanics, and MD begins to play the role of an experimental tool.

Most current MD applications involve systems that are either in equilibrium or in some time-independent stationary state; where individual results are subject to fluctuation, it is the well-defined averages over sufficiently long time intervals that are of interest. Extending MD to open systems, where coupling to the external world is of a more general kind, introduces many new problems. Not only are open systems out of thermodynamic equilibrium, but also in many cases they are spatially inhomogeneous and time-dependent. To smooth out the results and to obtain results close to experiments, measurements of physical quantities are need to be collected and averaged over a finite time duration. *Therefore, in deriving the field descriptions of atomic quantities and balance equations, it is the time-interval averaged quantities that will be used*, and the local density function, averaged over an interval Δt around time t, reads

$$\begin{aligned}\bar{A}^\alpha(\boldsymbol{x}, t) &= \langle A^\alpha \rangle \equiv A^\alpha_m \\ &= \frac{1}{\Delta t} \int_0^{\Delta t} \sum_{k=1}^{n} A\big(\boldsymbol{r}(t+\tau), \boldsymbol{p}(t+\tau)\big)\, \delta(\boldsymbol{R}^k - \boldsymbol{x})\, \delta(\Delta \boldsymbol{r}^{k\alpha} - \boldsymbol{y}^\alpha)\, d\tau.\end{aligned}$$

The fundamental physical quantities considered in this paper are mass, momentum, atomic force, momentum flux, total and internal energy, heat flux and temperature.

2.3. ***Mass density.*** Define the local mass density of the α-th atom as a time-interval averaged quantity

$$\bar{\rho}^{\alpha}(\boldsymbol{x},t)=\bar{\rho}(\boldsymbol{x},\boldsymbol{y}^{\alpha},t)=\left\langle\sum_{k=1}^{n}m^{\alpha}\delta(\boldsymbol{R}^{k}-\boldsymbol{x})\delta(\Delta\boldsymbol{r}^{k\alpha}-\boldsymbol{y}^{\alpha})\right\rangle.$$

The total mass of the system is then given by

$$\begin{aligned}M&=\int_{V}\left(\sum_{\alpha=1}^{v}\bar{\rho}^{\alpha}(\boldsymbol{x},t)\right)d^{3}x\\&=\left\langle\int_{V}\left(\sum_{k=1}^{n}\sum_{\alpha=1}^{v}m^{\alpha}\delta(\boldsymbol{R}^{k}-\boldsymbol{x})\delta(\Delta\boldsymbol{r}^{k\alpha}-\boldsymbol{y}^{\alpha})\right)d^{3}x\right\rangle=n\sum_{\alpha=1}^{v}m^{\alpha}=nm.\end{aligned}$$

Here, the definition of mass densities is similar to that of Kreuzer [1981], who defined the total mass density of a system involving ν different components, each with mass density ρ^{α}, as

$$\bar{\rho}=\sum_{\alpha=1}^{v}\bar{\rho}^{\alpha}.$$

2.4. ***Linear momentum density.*** The linear momentum measures the flow of mass. The link between the atomic measure of the flow of mass and the field description of momentum density is achieved through the localization function and time interval averaging:

$$\bar{\rho}^{\alpha}(\bar{\boldsymbol{v}}+\Delta\bar{\boldsymbol{v}}^{\alpha})=\left\langle\sum_{k=1}^{n}m^{\alpha}(\boldsymbol{V}^{k}+\Delta\boldsymbol{v}^{k\alpha})\delta(\boldsymbol{R}^{k}-\boldsymbol{x})\delta(\Delta\boldsymbol{r}^{k\alpha}-\boldsymbol{y}^{\alpha})\right\rangle,$$

where $\bar{\boldsymbol{v}}=\dot{\boldsymbol{x}}$ and $\Delta\bar{\boldsymbol{v}}^{\alpha}=\dot{\boldsymbol{y}}^{\alpha}$ are the time-interval averaged velocity of the mass center of a unit cell and the velocity of the α-th atom relative to the center of the unit cell, respectively.

2.5. ***Atomic forces.*** It is assumed that the interatomic force can be derived from interatomic potential. Whether the interaction is through two or three-body potential, one always has the force acting on the atom i as

$$\boldsymbol{f}^{i}=-\frac{\partial U}{\partial\boldsymbol{R}^{i}},\tag{2–3}$$

and the mutual interaction force between atom i and atom j can be obtained as

$$\boldsymbol{f}^{ij}=-\frac{\partial U}{\partial(\boldsymbol{R}^{i}-\boldsymbol{R}^{j})}=\frac{\partial U}{\partial(\boldsymbol{R}^{j}-\boldsymbol{R}^{i})}=-\boldsymbol{f}^{ji},\tag{2–4}$$

where U is the total potential energy of the system, $\boldsymbol{f}^{ij}$ the interatomic force, and $\boldsymbol{R}^{i}-\boldsymbol{R}^{j}$ the relative separation vector between the two atoms i and j.

For multielement systems, forces acting on an atom can be divided into three kinds:

(1) $\boldsymbol{f}_1^{\substack{k\alpha \\ l\beta}}$: interatomic force between (k,α) and (l,β) atoms in two different unit cells, and $\boldsymbol{f}_1^{\substack{k\alpha \\ l\beta}} = -\boldsymbol{f}_1^{\substack{l\beta \\ k\alpha}}$;

(2) $\boldsymbol{f}_2^{k_\beta^\alpha}$: interatomic force between (k,α) and (k,β) atoms in the same unit cell, and $\boldsymbol{f}_2^{k_\beta^\alpha} = -\boldsymbol{f}_2^{k_\alpha^\beta}$;

(3) $f_3^{k\alpha}$: body force on atom (k,α) due to the external fields.

The total force acting on an atom (k,α) can be written as

$$\boldsymbol{F}^{k\alpha} = \sum_{l=1}^{n}\sum_{\beta=1}^{\nu} \boldsymbol{f}_1^{\substack{k\alpha \\ l\beta}} + \sum_{\beta=1}^{\nu} \boldsymbol{f}_2^{k_\beta^\alpha} + \boldsymbol{f}_3^{k\alpha}. \tag{2–5}$$

The body force density due to an external field is

$$\bar{\boldsymbol{f}}^{\alpha} \equiv \left\langle \sum_{k=1}^{n} \boldsymbol{f}_3^{k\alpha}\delta(\boldsymbol{R}^k - \boldsymbol{x})\delta(\Delta\boldsymbol{r}^{k\alpha} - \boldsymbol{y}^{\alpha}) \right\rangle,$$

and body couple density is

$$\boldsymbol{L}^{\alpha} = \left\langle \sum_{k=1}^{n} \boldsymbol{f}_3^{k\alpha} \otimes (\boldsymbol{R}^k + \Delta\boldsymbol{r}^{k\alpha})\delta(\boldsymbol{R}^k - \boldsymbol{x})\delta(\Delta\boldsymbol{r}^{k\alpha} - \boldsymbol{y}^{\alpha}) \right\rangle = \bar{\boldsymbol{f}}^{\alpha} \otimes \boldsymbol{x} + \bar{\boldsymbol{l}}^{\alpha},$$

where $\bar{\boldsymbol{l}}^{\alpha} = \langle \sum_{k=1}^{n} \boldsymbol{f}_3^{k\alpha} \otimes \Delta\boldsymbol{r}^{k\alpha}\delta(\boldsymbol{R}^k - \boldsymbol{x})\delta(\Delta\boldsymbol{r}^{k\alpha} - \boldsymbol{y}^{\alpha})\rangle$.

Assuming that the total internal potential energy is U_{int} and using the force-potential function relationship (2–3)–(2–4), the internal force density due to atomic interaction can be expressed as

$$\begin{aligned}
\bar{\boldsymbol{f}}_{\text{int}}^{\alpha}(\boldsymbol{x}) &\equiv \left\langle \sum_{k=1}^{n} \left(\sum_{l=1}^{n}\sum_{\beta=1}^{\nu} \boldsymbol{f}_1^{\substack{k\alpha \\ l\beta}} + \sum_{\beta=1}^{\nu} \boldsymbol{f}_2^{k_\beta^\alpha} \right) \delta(\boldsymbol{R}^k - \boldsymbol{x})\delta(\Delta\boldsymbol{r}^{k\alpha} - \boldsymbol{y}^{\alpha}) \right\rangle \\
&= -\left\langle \sum_{k,l=1}^{n}\sum_{\xi,\eta=1}^{\nu} \frac{\partial U_{\text{int}}}{\partial(\boldsymbol{R}^{k\xi} - \boldsymbol{R}^{l\eta})} \delta(\boldsymbol{R}^k - \boldsymbol{x})\delta(\Delta\boldsymbol{r}^{k\xi} - \boldsymbol{y}^{\alpha}) \right\rangle \\
&\quad -\left\langle \sum_{k=1}^{n}\sum_{\xi,\eta=1}^{\nu} \frac{\partial U_{\text{int}}}{\partial(\boldsymbol{R}^{k\xi} - \boldsymbol{R}^{k\eta})} \delta(\boldsymbol{R}^k - \boldsymbol{x})\delta(\Delta\boldsymbol{r}^{k\xi} - \boldsymbol{y}^{\alpha}) \right\rangle.
\end{aligned}$$

From Equation (2–4) we have $\boldsymbol{f}_1^{\substack{k\xi \\ l\eta}} = -\boldsymbol{f}_1^{\substack{l\eta \\ k\xi}}$ and $\boldsymbol{f}_2^{k_\eta^\xi} = -\boldsymbol{f}_2^{k_\xi^\eta}$. Interchanging the

indices $k\xi$ and $l\eta$, we see that

$$\bar{\boldsymbol{f}}^{\alpha}_{\text{int}}(\boldsymbol{x}) = \frac{1}{2}\left\langle \sum_{k,l=1}^{n} \sum_{\xi,\eta=1}^{v} \boldsymbol{f}_1^{l\eta,k\xi} \left(\delta(\boldsymbol{R}^k - \boldsymbol{x})\,\delta(\Delta\boldsymbol{r}^{k\xi} - \boldsymbol{y}^{\alpha}) - \delta(\boldsymbol{R}^l - \boldsymbol{x})\,\delta(\Delta\boldsymbol{r}^{l\eta} - \boldsymbol{y}^{\alpha})\right)\right\rangle$$
$$+ \frac{1}{2}\left\langle \sum_{k=1}^{n} \sum_{\xi,\eta=1}^{v} \boldsymbol{f}_2^{k\xi,k\eta}\,\delta(\boldsymbol{R}^k - \boldsymbol{x})\left(\delta(\Delta\boldsymbol{r}^{k\xi} - \boldsymbol{y}^{\alpha}) - \delta(\Delta\boldsymbol{r}^{k\eta} - \boldsymbol{y}^{\alpha})\right)\right\rangle, \quad (2\text{–}6)$$

Since the formulation involves many-body interactions, it is understood that the summation over k and l does not include the case $k = l$ and similarly the summation over α and β does not include the case $\alpha = \beta$. In this article, velocity-dependent interactions such as interaction with magnetic fields are not considered, and hence the forces depend only on atomic positions. However, the results can be generalized to include such cases.

2.6. ***Momentum flux density.*** It is well accepted that the momentum flux in an N-body dynamics system can be divided into two parts: kinetic and potential parts [Hoover 1986; 1991; Chen and Lee 2003a; 2003b; Chen et al. 2003]. The kinetic part of the momentum flux is the flow of momentum due to atomic motion, which, in the co-moving coordinate system, is

$$\boldsymbol{s}_{\text{kin}} = -\boldsymbol{p} \otimes \boldsymbol{p}/m.$$

By virtue of the possible macroscopic motion of the material body, the velocity that contributes to momentum flux is the difference between the instantaneous velocity and the stream velocity (the ensemble or time average of the velocity):

$$\tilde{\boldsymbol{V}}^{k\alpha} = \boldsymbol{V}^{k\alpha} - \langle \boldsymbol{V}^{k\alpha} \rangle = \boldsymbol{V}^{k\alpha} - (\bar{\boldsymbol{v}} + \Delta\bar{\boldsymbol{v}}^{\alpha}).$$

This velocity difference $\tilde{\boldsymbol{V}}^{k\alpha}$ measures the fluctuations of atoms relative to the local equilibrium and is related to the thermal motion of atoms. In the field representation, the kinetic part of local density of momentum flux at the α-th atomic position embedded in lattice point $\boldsymbol{x}$ is

$$\bar{\boldsymbol{s}}^{\alpha}_{\text{kin}} = -\left\langle \sum_{k=1}^{n} m^{\alpha}\,\tilde{\boldsymbol{V}}^{k\alpha} \otimes \tilde{\boldsymbol{V}}^{k\alpha}\,\delta(\boldsymbol{R}^k - \boldsymbol{x})\,\delta(\Delta\boldsymbol{r}^{k\alpha} - \boldsymbol{y}^{\alpha}) \right\rangle.$$

The potential flow of momentum occurs through the mechanism of the interparticle forces (Figure 4). For a pair of particles α and β that lie on different sides of a surface that intersects the line connecting the two particles at $\boldsymbol{x} + \boldsymbol{y}^{\alpha}$, the pair force

$$\boldsymbol{f}^{k\xi,l\eta} = -\boldsymbol{f}^{l\eta,k\xi}$$

gives the rate at which momentum is transported from particle $k\xi$ to particle $l\eta$. For each such pair the direction of this transport is along the direction of $\boldsymbol{R}^{k\xi} - \boldsymbol{R}^{l\eta}$. So, the potential contribution to the momentum flux is

$$\boldsymbol{s}_{\text{pot}} = -(\boldsymbol{R}^{k\xi} - \boldsymbol{R}^{l\eta}) \otimes \overset{k\xi}{\boldsymbol{f}}{}^{l\eta},$$

which is continuous along the line connecting the two particles. Notice that

$$\begin{aligned}\delta(\boldsymbol{R}^k - \boldsymbol{x})\delta(\Delta\boldsymbol{r}^{k\xi} - \boldsymbol{y}^\alpha) - \delta(\boldsymbol{R}^l - \boldsymbol{x})\delta(\Delta\boldsymbol{r}^{l\eta} - \boldsymbol{y}^\alpha)\\ = \int_0^1 \frac{d}{d\lambda}\big(\delta(\boldsymbol{R}^k\lambda + \boldsymbol{R}^l(1-\lambda) - \boldsymbol{x})\delta(\Delta\boldsymbol{r}^{k\xi}\lambda + \Delta\boldsymbol{r}^{l\eta}(1-\lambda) - \boldsymbol{y}^\alpha)\big)\, d\lambda.\end{aligned}$$

With the consideration of all interatomic forces that pass through the atomic site $(\boldsymbol{x}, \boldsymbol{y}^\alpha)$, the local density of the momentum transport at $(\boldsymbol{x}, \boldsymbol{y}^\alpha)$ due to atomic interaction is thus expressed as

$$\begin{aligned}\bar{\boldsymbol{s}}^\alpha_{\text{pot}} = &-\left\langle \frac{1}{2}\int_0^1 d\lambda \sum_{k,l=1}^{n}\sum_{\xi,\eta=1}^{\nu} (\boldsymbol{R}^{k\xi} - \boldsymbol{R}^{l\eta}) \otimes \overset{k\xi}{\boldsymbol{f}}{}^{l\eta}_1 \delta\big(\boldsymbol{R}^k\lambda + \boldsymbol{R}^l(1-\lambda) - \boldsymbol{x}\big)\right.\\ &\left.\delta\big(\Delta\boldsymbol{r}^{k\xi}\lambda + \Delta\boldsymbol{r}^{l\eta}(1-\lambda) - \boldsymbol{y}^\alpha\big)\right\rangle\\ &-\left\langle \frac{1}{2}\int_0^1 d\lambda \sum_{k=1}^{n}\sum_{\xi,\eta=1}^{\nu} (\boldsymbol{R}^{k\xi} - \boldsymbol{R}^{k\eta}) \otimes \boldsymbol{f}^{k\xi}_{2\,k\eta} \delta(\boldsymbol{R}^k - \boldsymbol{x})\right.\\ &\left.\delta\big(\Delta\boldsymbol{r}^{k\xi}\lambda + \Delta\boldsymbol{r}^{k\eta}(1-\lambda) - \boldsymbol{y}^\alpha\big)\right\rangle.\end{aligned}$$

The continuum counterpart of momentum flux density is the stress tensor. However, the mathematical infinitesimal volume that does not violate the continuum assumption is the volume ΔV defining the density of lattice points, which is the volume of a unit cell. The vector sum of all the atomic forces within this volume may not pass through the mass center of the ΔV. The continuum definition of stress is, therefore, not the momentum flux density; for a crystal with more than one atom in the unit cell, the continuum stress is only the homogeneous part of the momentum flux summing over a volume of at least one unit cell, and it may not be symmetric.

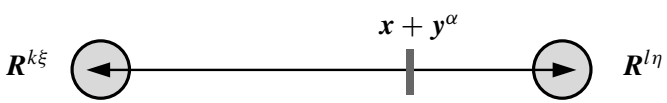

Figure 4. Flow of momentum due to interatomic force.

The total momentum flux is, therefore, better represented upon decomposition of a homogeneous part, caused by lattice motion and deformation and related to continuum stress, and an inhomogeneous part, caused by internal (relative) atomic motion and deformation. The homogeneous kinetic, inhomogeneous kinetic, homogeneous potential and inhomogeneous potential parts are given by, respectively,

$$\bar{\boldsymbol{t}}^{\alpha}_{\text{kin}} = -\left\langle \sum_{k=1}^{n} m^{\alpha} \tilde{\boldsymbol{V}}^{k} \otimes \tilde{\boldsymbol{V}}^{k\alpha} \delta(\boldsymbol{R}^{k} - \boldsymbol{x}) \delta(\Delta \boldsymbol{r}^{k\alpha} - \boldsymbol{y}^{\alpha}) \right\rangle, \tag{2–7}$$

$$\bar{\boldsymbol{\tau}}^{\alpha}_{\text{kin}} = -\left\langle \sum_{k=1}^{n} m^{\alpha} \Delta \tilde{\boldsymbol{v}}^{k\alpha} \otimes \tilde{\boldsymbol{V}}^{k\alpha} \delta\big(\boldsymbol{R}^{k} - \boldsymbol{x}\big) \delta(\Delta \boldsymbol{r}^{k\alpha} - \boldsymbol{y}^{\alpha}) \right\rangle,$$

$$\bar{\boldsymbol{t}}^{\alpha}_{\text{pot}} = -\left\langle \frac{1}{2} \int_{0}^{1} d\lambda \sum_{k,l=1}^{n} \sum_{\xi,\eta=1}^{\nu} (\boldsymbol{R}^{k} - \boldsymbol{R}^{l}) \otimes \overset{k\xi}{\boldsymbol{f}}{}^{l\eta}_{1} \delta(\boldsymbol{R}^{k}\lambda + \boldsymbol{R}^{l}(1-\lambda) - \boldsymbol{x}) \times \delta(\Delta \boldsymbol{r}^{k\xi}\lambda + \Delta \boldsymbol{r}^{l\eta}(1-\lambda) - \boldsymbol{y}^{\alpha}) \right\rangle,$$

$$\bar{\boldsymbol{\tau}}^{\alpha}_{\text{pot}} = -\left\langle \frac{1}{2} \int_{0}^{1} d\lambda \sum_{k,l=1}^{n} \sum_{\xi,\eta=1}^{\nu} (\Delta \boldsymbol{r}^{k\xi} - \Delta \boldsymbol{r}^{l\eta}) \otimes \overset{k\xi}{\boldsymbol{f}}{}^{l\eta}_{1} \delta\big(\boldsymbol{R}^{k}\lambda + \boldsymbol{R}^{l}(1-\lambda) - \boldsymbol{x}\big) \times \delta\big(\Delta \boldsymbol{r}^{k\xi}\lambda + \Delta \boldsymbol{r}^{l\eta}(1-\lambda) - \boldsymbol{y}^{\alpha}\big) \right\rangle$$

$$-\left\langle \frac{1}{2} \int_{0}^{1} d\lambda \sum_{k=1}^{n} \sum_{\xi,\eta=1}^{\nu} (\Delta \boldsymbol{r}^{k\xi} - \Delta \boldsymbol{r}^{k\eta}) \otimes \overset{k\xi}{\boldsymbol{f}}{}^{k\eta}_{2} \delta(\boldsymbol{R}^{k} - \boldsymbol{x}) \times \delta\big(\Delta \boldsymbol{r}^{k\xi}\lambda + \Delta \boldsymbol{r}^{k\eta}(1-\lambda) - \boldsymbol{y}^{\alpha}\big) \right\rangle,$$

where $\tilde{\boldsymbol{V}}^{k} = \boldsymbol{V}^{k} - \langle \boldsymbol{V}^{k} \rangle = \boldsymbol{V}^{k} - \bar{\boldsymbol{v}}$, $\Delta \tilde{\boldsymbol{v}}^{k\alpha} = \Delta \boldsymbol{v}^{k\alpha} - \langle \Delta \boldsymbol{v}^{k\alpha} \rangle = \Delta \boldsymbol{v}^{k\alpha} - \Delta \bar{\boldsymbol{v}}^{\alpha}$.

Using

$$\frac{d}{d\lambda}\big(\delta\big(\boldsymbol{R}^{k}\lambda + \boldsymbol{R}^{l}(1-\lambda) - \boldsymbol{x}\big)\delta\big(\Delta \boldsymbol{r}^{k\xi}\lambda + \Delta \boldsymbol{r}^{l\eta}(1-\lambda) - \boldsymbol{y}^{\alpha}\big)\big)$$
$$= -\nabla_{\boldsymbol{x}} \cdot \Big((\boldsymbol{R}^{k} - \boldsymbol{R}^{l})\delta\big(\boldsymbol{R}^{k}\lambda + \boldsymbol{R}^{l}(1-\lambda) - \boldsymbol{x}\big)\delta\big(\Delta \boldsymbol{r}^{k\xi}\lambda + \Delta \boldsymbol{r}^{l\eta}(1-\lambda) - \boldsymbol{y}^{\alpha}\big)\Big)$$
$$-\nabla_{\boldsymbol{y}^{\alpha}} \cdot \Big((\Delta \boldsymbol{r}^{k\xi} - \Delta \boldsymbol{r}^{l\eta})\delta\big(\boldsymbol{R}^{k}\lambda + \boldsymbol{R}^{l}(1-\lambda) - \boldsymbol{x}\big)\delta\big(\Delta \boldsymbol{r}^{k\xi}\lambda + \Delta \boldsymbol{r}^{l\eta}(1-\lambda) - \boldsymbol{y}^{\alpha}\big)\Big),$$

we see from Equation (2–6), and the last two equations of (2–7), that the divergences of the potential momentum fluxes are related to the internal forces by

$$\nabla_{\boldsymbol{x}} \cdot \bar{\boldsymbol{t}}^{\alpha}_{\text{pot}} + \nabla_{\boldsymbol{y}^{\alpha}} \cdot \bar{\boldsymbol{\tau}}^{\alpha}_{\text{pot}} = \bar{\boldsymbol{f}}^{\alpha}_{\text{int}} = \left\langle \sum_{k=1}^{n} \sum_{\eta=1}^{\nu} \left(\sum_{l=1}^{n} \overset{k\alpha}{\boldsymbol{f}}{}^{l\eta}_{1} + \boldsymbol{f}_{2}^{k^{\alpha}_{\eta}} \right) \delta(\boldsymbol{R}^{k} - \boldsymbol{x}) \delta(\Delta \boldsymbol{r}^{k\alpha} - \boldsymbol{y}^{\alpha}) \right\rangle. \tag{2–8}$$

2.7. ***Total energy density and internal energy density.*** The total energy of atom α in a microscopic N-body dynamics system is the sum of kinetic and potential energies. In continuum theory, the local energy density is usually defined as energy per unit mass. This implies

$$\bar{\rho}^{\alpha}\bar{E}^{\alpha} = \left\langle \sum_{k=1}^{n} \left(\tfrac{1}{2}m^{\alpha}(\boldsymbol{V}^{k\alpha})^2 + U^{k\alpha}\right)\delta(\boldsymbol{R}^k - \boldsymbol{x})\,\delta(\Delta\boldsymbol{r}^{k\alpha} - \boldsymbol{y}^{\alpha}) \right\rangle.$$

The local density of internal energy, which is the state function of thermodynamics, can be expressed as the sum of thermal energy and potential energy:

$$\bar{\rho}^{\alpha}\bar{\varepsilon}^{\alpha} = \left\langle \sum_{k=1}^{n} \left(\tfrac{1}{2}m^{\alpha}(\tilde{\boldsymbol{V}}^{k\alpha})^2 + U^{k\alpha}\right)\delta(\boldsymbol{R}^k - \boldsymbol{x})\,\delta(\Delta\boldsymbol{r}^{k\alpha} - \boldsymbol{y}^{\alpha}) \right\rangle.$$

Rewriting the total energy density as

$$\bar{\rho}^{\alpha}\bar{E}^{\alpha} = \left\langle \sum_{k=1}^{n} \left(\tfrac{1}{2}m^{\alpha}\left\{(\tilde{\boldsymbol{V}}^{k\alpha})^2 + 2\tilde{\boldsymbol{V}}^{k\alpha}\cdot(\bar{\boldsymbol{v}} + \Delta\bar{\boldsymbol{v}}^{\alpha}) + (\bar{\boldsymbol{v}} + \Delta\bar{\boldsymbol{v}}^{\alpha})^2\right\} + U^{k\alpha}\right) \times \delta(\boldsymbol{R}^k - \boldsymbol{x})\,\delta(\Delta\boldsymbol{r}^{k\alpha} - \boldsymbol{y}^{\alpha}) \right\rangle,$$

there results the macroscopic relation of densities of the total energy, the internal energy and the kinetic energy as

$$\langle \rho^{\alpha}E^{\alpha}\rangle = \langle \rho^{\alpha}\varepsilon^{\alpha}\rangle + \tfrac{1}{2}\bar{\rho}^{\alpha}(\bar{\boldsymbol{v}} + \Delta\bar{\boldsymbol{v}}^{\alpha})^2.$$

2.8. ***Heat flux.*** The flow of energy by atomic motion, for all particles in the volume ΔV, gives the kinetic contribution to the energy flux. It comes from the rate at which the local energy E^i of atom i moves with local atomic velocity $\boldsymbol{p}^i/m^i$,

$$\boldsymbol{Q}^i_{\text{kin}} = -\frac{\boldsymbol{p}^i}{m^i}E^i.$$

The potential contribution to the energy flow occurs whenever two moving particles interact in such a way that one particle transfers a part of their joint energy to the other. It comes from the rate at which energy is transported through the action of interparticle forces: atom i is doing work on atom j, multiplied by the distance $\boldsymbol{R}^i - \boldsymbol{R}^j$ over which this energy is transferred:

$$\boldsymbol{Q}_{\text{pot}} = -\frac{1}{2}(\boldsymbol{R}^i - \boldsymbol{R}^j)\left(\frac{\boldsymbol{p}^i}{2m^i} + \frac{\boldsymbol{p}^j}{2m^j}\right)\cdot \boldsymbol{f}^{ij}.$$

Noting that heat flux is the conductive flow of internal energy per unit time and area [Huang 1967; Cochran 1973], the local density functions of kinetic and

potential heat fluxes, therefore, are expressed as

$$\bar{\boldsymbol{Q}}^{\alpha}_{\text{kin}} = -\left\langle \sum_{k=1}^{n} \tilde{\boldsymbol{V}}^{k\alpha}\left[\tfrac{1}{2}m^{\alpha}(\tilde{\boldsymbol{V}}^{\boldsymbol{k}\alpha})^2 + U^{k\alpha}\right]\delta(\boldsymbol{R}^k - \boldsymbol{x})\,\delta(\Delta\boldsymbol{r}^{k\alpha} - \boldsymbol{y}^{\alpha})\right\rangle,$$

$$\begin{aligned}\bar{\boldsymbol{Q}}^{\alpha}_{\text{pot}} = &-\left\langle \frac{1}{2}\int_0^1 d\lambda \sum_{k,l=1}^{n}\sum_{\xi,\eta=1}^{\nu} (\boldsymbol{R}^{k\xi} - \boldsymbol{R}^{l\eta})\tilde{\boldsymbol{V}}^{k\xi} \right.\\ &\qquad \left. \times \boldsymbol{f}_1^{k\xi\,l\eta}\,\delta\big(\boldsymbol{R}^k\lambda + \boldsymbol{R}^l(1-\lambda) - \boldsymbol{x}\big)\delta\big(\Delta\boldsymbol{r}^{k\xi}\lambda + \Delta\boldsymbol{r}^{l\eta}(1-\lambda) - \boldsymbol{y}^{\alpha}\big)\right\rangle\\ &-\left\langle \frac{1}{2}\int_0^1 d\lambda \sum_{k=1}^{n}\sum_{\xi,\eta=1}^{\nu} (\boldsymbol{R}^{k\xi} - \boldsymbol{R}^{k\eta})\tilde{\boldsymbol{V}}^{k\xi} \right.\\ &\qquad \left. \times \boldsymbol{f}_2^{k\xi\,k\eta}\,\delta(\boldsymbol{R}^k - \boldsymbol{x})\,\delta\big(\Delta\boldsymbol{r}^{k\xi}\lambda + \Delta\boldsymbol{r}^{k\eta}(1-\lambda) - \boldsymbol{y}^{\alpha}\big)\right\rangle.\end{aligned}$$

Clearly there are homogeneous and inhomogeneous parts. Similar to the decomposition of momentum flux density, let the heat flux density be decomposed into four parts: the homogeneous kinetic, inhomogeneous kinetic, homogeneous potential and inhomogeneous potential part of heat flux, all of which are given by, respectively,

$$\bar{\boldsymbol{q}}^{\alpha}_{\text{kin}} = -\left\langle \sum_{k=1}^{n} \tilde{\boldsymbol{V}}^{k}\left[\tfrac{1}{2}m^{\alpha}(\tilde{\boldsymbol{V}}^{k\alpha})^2 + U^{k\alpha}\right]\delta(\boldsymbol{R}^k - \boldsymbol{x})\,\delta(\Delta\boldsymbol{r}^{k\alpha} - \boldsymbol{y}^{\alpha})\right\rangle,$$

$$\bar{\boldsymbol{j}}^{\alpha}_{\text{kin}} = -\left\langle \sum_{k=1}^{n} \Delta\tilde{\boldsymbol{v}}^{k\alpha}\left[\tfrac{1}{2}m^{\alpha}(\tilde{\boldsymbol{V}}^{k\alpha})^2 + U^{k\alpha}\right]\delta(\boldsymbol{R}^k - \boldsymbol{x})\,\delta(\Delta\boldsymbol{r}^{k\alpha} - \boldsymbol{y}^{\alpha})\right\rangle,$$

$$\begin{aligned}\bar{\boldsymbol{q}}^{\alpha}_{\text{pot}} = &-\left\langle \frac{1}{2}\int_0^1 d\lambda \sum_{k,l=1}^{n}\sum_{\xi,\eta=1}^{\nu} (\boldsymbol{R}^{k} - \boldsymbol{R}^{l})\tilde{\boldsymbol{V}}^{k\xi} \right.\\ &\qquad \left. \times \boldsymbol{f}_1^{k\xi\,l\eta}\,\delta\big(\boldsymbol{R}^k\lambda + \boldsymbol{R}^l(1-\lambda) - \boldsymbol{x}\big)\delta\big(\Delta\boldsymbol{r}^{k\xi}\lambda + \Delta\boldsymbol{r}^{l\eta}(1-\lambda) - \boldsymbol{y}^{\alpha}\big)\right\rangle,\end{aligned}$$

$$\begin{aligned}\bar{\boldsymbol{j}}^{\alpha}_{\text{pot}} = &-\left\langle \frac{1}{2}\int_0^1 d\lambda \sum_{k,l=1}^{n}\sum_{\xi,\eta=1}^{\nu} (\Delta\boldsymbol{r}^{k\xi} - \Delta\boldsymbol{r}^{l\eta})\tilde{\boldsymbol{V}}^{k\xi} \right.\\ &\qquad \left. \times \boldsymbol{f}_1^{k\xi\,l\eta}\,\delta\big(\boldsymbol{R}^k\lambda + \boldsymbol{R}^l(1-\lambda) - \boldsymbol{x}\big)\delta\big(\Delta\boldsymbol{r}^{k\xi}\lambda + \Delta\boldsymbol{r}^{l\eta}(1-\lambda) - \boldsymbol{y}^{\alpha}\big)\right\rangle\\ &-\left\langle \frac{1}{2}\int_0^1 d\lambda \sum_{k=1}^{n}\sum_{\xi,\eta=1}^{\nu} (\Delta\boldsymbol{r}^{k\xi} - \Delta\boldsymbol{r}^{k\eta})\tilde{\boldsymbol{V}}^{k\xi} \right.\\ &\qquad \left. \times \boldsymbol{f}_2^{k\xi\,k\eta}\,\delta(\boldsymbol{R}^k - \boldsymbol{x})\,\delta\big(\Delta\boldsymbol{r}^{k\xi}\lambda + \Delta\boldsymbol{r}^{k\eta}(1-\lambda) - \boldsymbol{y}^{\alpha}\big)\right\rangle.\end{aligned}$$

We see that the inhomogeneous heat flux is closely associated with the inhomogeneous stress and may represent the thermal currents that flow back and forth during vibration between stress inhomogeneities. With the definition of the potential parts of momentum fluxes and the identity of δ function, it is straightforward to prove that the divergences of potential heat fluxes have the following characteristics:

$$\begin{aligned}\nabla_{\boldsymbol{x}} \cdot \left(\bar{\boldsymbol{q}}^{\alpha}_{\text{pot}} + \bar{\boldsymbol{t}}^{\alpha}_{\text{pot}} \cdot (\bar{\boldsymbol{v}} + \Delta\bar{\boldsymbol{v}}^{\alpha})\right) + \nabla_{\boldsymbol{y}^{\alpha}} \cdot \left(\bar{\boldsymbol{j}}^{\alpha}_{\text{pot}} + \bar{\boldsymbol{\tau}}^{\alpha}_{pot} \cdot (\bar{\boldsymbol{v}} + \Delta\bar{\boldsymbol{v}}^{\alpha})\right)\\ = \left\langle \frac{1}{2} \sum_{k,l=1}^{n} \sum_{\eta=1}^{\nu} (\boldsymbol{V}^{k\alpha} + \boldsymbol{V}^{l\eta}) \cdot \boldsymbol{f}_1^{l\eta}{}^{k\alpha} \delta(\boldsymbol{R}^k - \boldsymbol{x}) \delta(\Delta\boldsymbol{r}^{k\alpha} - \boldsymbol{y}^{\alpha}) \right\rangle\\ + \left\langle \frac{1}{2} \sum_{k=1}^{n} \sum_{\eta=1}^{\nu} (\boldsymbol{V}^{k\alpha} + \boldsymbol{V}^{k\eta}) \cdot \boldsymbol{f}_2^{k\eta}{}^{k\alpha} \delta(\boldsymbol{R}^k - \boldsymbol{x}) \delta(\Delta\boldsymbol{r}^{k\alpha} - \boldsymbol{y}^{\alpha}) \right\rangle. \quad (2\text{–}9)\end{aligned}$$

2.9. ***Temperature.*** The temperature T for the microscopic N-body system is also an average quantity. It can be most simply expressed in terms of thermal energy by the mean-squared velocity relative to the local stream velocity [Hoover 1991], as

$$\begin{aligned}T^{\alpha}(\boldsymbol{x}) &= \left\langle \frac{\Delta V}{3k_B} \sum_{k=1}^{n} m^{\alpha} (\tilde{\boldsymbol{V}}^{k\alpha})^2 \delta(\boldsymbol{R}^k - \boldsymbol{x}) \delta(\Delta\boldsymbol{r}^{k\alpha} - \boldsymbol{y}^{\alpha}) \right\rangle\\ &= \left\langle \frac{\Delta V}{3k_B} \sum_{k=1}^{n} m^{\alpha} (\boldsymbol{V}^{k\alpha})^2 \delta(\boldsymbol{R}^k - \boldsymbol{x}) \delta(\Delta\boldsymbol{r}^{k\alpha} - \boldsymbol{y}^{\alpha}) \right\rangle - \frac{m^{\alpha}}{3k_B} (\bar{\boldsymbol{v}} + \Delta\bar{\boldsymbol{v}}^{\alpha})^2,\end{aligned}$$

where k_B is Boltzmann constant, $\tilde{\boldsymbol{V}}^{k\alpha}$ are the velocity differences or the fluctuations of atoms, and ΔV is the volume that defines the density of lattice points, that is, the volume of a unit cell.

3. Time evolution of physical quantities

As mentioned above, an observable quantity in a MD simulation is supposed to be a function of the positions and momenta of the particles in the system:

$$A(\boldsymbol{x}, \boldsymbol{y}^{\alpha}) = \sum_{k=1}^{n} A(\boldsymbol{r}, \boldsymbol{p}) \delta(\boldsymbol{R}^k - \boldsymbol{x}) \delta(\Delta\boldsymbol{r}^{k\alpha} - \boldsymbol{y}^{\alpha}) \equiv A^{\alpha}(\boldsymbol{x}).$$

With

$$\begin{aligned}\nabla_{\boldsymbol{R}^k} \delta(\boldsymbol{R}^k - \boldsymbol{x}) &= -\nabla_{\boldsymbol{x}} \delta(\boldsymbol{R}^k - \boldsymbol{x}),\\ \nabla_{\Delta\boldsymbol{r}^{k\alpha}} \delta(\Delta\boldsymbol{r}^{k\alpha} - \boldsymbol{y}^{\alpha}) &= -\nabla_{\boldsymbol{y}^{\alpha}} \delta(\Delta\boldsymbol{r}^{k\alpha} - \boldsymbol{y}^{\alpha}),\end{aligned}$$

and in the general case that the phase space function A does not involve field quantities, the time evolution of its local density function can be expressed as

$$\left.\frac{\partial \boldsymbol{A}^{\alpha}}{\partial t}\right|_{\boldsymbol{x},\boldsymbol{y}^{\alpha}} = \sum_{k=1}^{n} \dot{\boldsymbol{A}}\delta(\boldsymbol{R}^{k}-\boldsymbol{x})\,\delta(\Delta\boldsymbol{r}^{k\alpha}-\boldsymbol{y}^{\alpha}) - \nabla_{\boldsymbol{x}}\cdot\left(\sum_{k=1}^{n}\boldsymbol{V}^{k}\otimes\boldsymbol{A}\delta(\boldsymbol{R}^{k}-\boldsymbol{x})\,\delta(\Delta\boldsymbol{r}^{k\alpha}-\boldsymbol{y}^{\alpha})\right) - \nabla_{\boldsymbol{y}^{\alpha}}\cdot\left(\sum_{k=1}^{n}\Delta\boldsymbol{v}^{k\alpha}\otimes\boldsymbol{A}\delta(\boldsymbol{R}^{k}-\boldsymbol{x})\,\delta(\Delta\boldsymbol{r}^{k\alpha}-\boldsymbol{y}^{\alpha})\right). \quad (3\text{–}1)$$

For the time-interval averaged (at time t in the interval Δt) field quantity $\bar{\boldsymbol{A}}^{\alpha}$,

$$\bar{\boldsymbol{A}}^{\alpha}(\boldsymbol{x},t) = \langle \boldsymbol{A}^{\alpha}\rangle \equiv \boldsymbol{A}^{\alpha}_{m} = \frac{1}{\Delta t}\int_{0}^{\Delta t}\boldsymbol{A}(\boldsymbol{r}(t+\tau),\boldsymbol{p}(t+\tau),\boldsymbol{x},\boldsymbol{y}^{\alpha})\,d\tau,$$

one has

$$\left.\frac{\partial \bar{\boldsymbol{A}}^{\alpha}}{\partial t}\right|_{x,y^{\alpha}} = \left\langle \sum_{k,l=1}^{n}\sum_{\gamma=1}^{v}\delta(\boldsymbol{R}^{k}-\boldsymbol{x})\,\delta(\Delta\boldsymbol{r}^{k\alpha}-\boldsymbol{y}^{\alpha})\left(\boldsymbol{V}^{l\gamma}\cdot\nabla_{\boldsymbol{R}^{l\gamma}}+\frac{1}{m^{\gamma}}\mathbf{F}^{l\gamma}\cdot\nabla_{\boldsymbol{V}^{l\gamma}}\right)\boldsymbol{A}\right\rangle - \nabla_{\boldsymbol{x}}\cdot\left\langle\sum_{k=1}^{n}\boldsymbol{V}^{k}\otimes\boldsymbol{A}\delta(\boldsymbol{R}^{k}-\boldsymbol{x})\,\delta(\Delta\boldsymbol{r}^{k\alpha}-\boldsymbol{y}^{\alpha})\right\rangle - \nabla^{\alpha}_{y}\cdot\left\langle\sum_{k=1}^{n}\Delta\boldsymbol{v}^{k\alpha}\otimes\boldsymbol{A}\delta(\boldsymbol{R}^{k}-\boldsymbol{x})\,\delta(\Delta\boldsymbol{r}^{k\alpha}-\boldsymbol{y}^{\alpha})\right\rangle. \quad (3\text{–}2)$$

Equations (3–1) and (3–2) are the time evolution laws for instantaneous quantity $\boldsymbol{A}^{\alpha}$ and averaged field quantity $\bar{\boldsymbol{A}}^{\alpha}$, respectively. When $\boldsymbol{A}^{\alpha}$ is a conserved property, it results in the local conservation laws that govern the time evolution of $\boldsymbol{A}^{\alpha}$ and $\bar{\boldsymbol{A}}^{\alpha}$, respectively.

4. Formulation of the balance laws

A thermodynamic theory of irreversible processes starts with a set of general balance equations that govern the time evolution of the system. It is the objective of this paper to establish differential balance equations for a thermodynamic system on the same foundation of molecular dynamics: the classical N-body dynamics. Those balance equations will follow exactly the time evolution laws that exist in a molecular dynamics simulation, where the atomic motion is fully described, the inhomogeneous internal motion is not ignored, and the smallest particles are atoms.

4.1. ***Conservation of mass.*** With $\bar{\rho}^\alpha = \langle \sum_{k=1}^n m^\alpha \delta(\boldsymbol{R}^k - \boldsymbol{x})\delta(\Delta \boldsymbol{r}^{k\alpha} - \boldsymbol{y}^\alpha)\rangle$, the time evolution of mass density can be obtained as

$$\frac{\partial \bar{\rho}^\alpha}{\partial t} = -\nabla_{\boldsymbol{x}} \cdot \left\langle \sum_{k=1}^n m^\alpha \boldsymbol{V}^k \delta(\boldsymbol{R}^k - \boldsymbol{x})\delta(\Delta \boldsymbol{r}^{k\alpha} - \boldsymbol{y}^\alpha) \right\rangle - \nabla_{\boldsymbol{y}^\alpha} \cdot \left\langle \sum_{k=1}^n m^\alpha \Delta \boldsymbol{v}^{k\alpha} \delta(\boldsymbol{R}^k - \boldsymbol{x})\delta(\Delta \boldsymbol{r}^{k\alpha} - \boldsymbol{y}^\alpha) \right\rangle.$$

From the definition of linear momentum, one immediately finds

$$\frac{\partial \bar{\rho}^\alpha}{\partial t} + \nabla_{\boldsymbol{x}} \cdot (\bar{\rho}^\alpha \bar{\boldsymbol{v}}) + \nabla_{\boldsymbol{y}^\alpha} \cdot (\bar{\rho}^\alpha \Delta \bar{\boldsymbol{v}}^\alpha) = 0 \qquad \text{or} \qquad \frac{d\bar{\rho}^\alpha}{dt} + \bar{\rho}^\alpha (\nabla_{\boldsymbol{x}} \cdot \bar{\boldsymbol{v}} + \nabla_{\boldsymbol{y}^\alpha} \cdot \Delta \bar{\boldsymbol{v}}^\alpha) = 0.$$

For cell-average mass density $\bar{\rho} = \langle \sum_{k=1}^n m\delta(\boldsymbol{R}^k - \boldsymbol{x})\rangle$, we readily see that

$$\frac{\partial \bar{\rho}}{\partial t} + \nabla_{\boldsymbol{x}} \cdot (\bar{\rho}\bar{\boldsymbol{v}}) = 0 \qquad \text{or} \qquad \frac{d\bar{\rho}}{dt} + \bar{\rho}\nabla_{\boldsymbol{x}} \cdot \bar{\boldsymbol{v}} = 0.$$

This is identical to the continuity equation in macroscopic physics.

4.2. ***Balance of linear momentum.*** Recall the field representation of local linear momentum density as

$$\bar{\rho}^\alpha (\bar{\boldsymbol{v}} + \Delta \bar{\boldsymbol{v}}^\alpha) \equiv \left\langle \sum_{k=1}^n m^\alpha \boldsymbol{V}^{k\alpha} \delta(\boldsymbol{R}^k - \boldsymbol{x})\delta(\Delta \boldsymbol{r}^{k\alpha} - \boldsymbol{y}^\alpha) \right\rangle.$$

Substituting it into Equation (3–2), it follows that

$$\begin{aligned} \frac{\partial \bar{\rho}^\alpha (\bar{\boldsymbol{v}} + \Delta \bar{\boldsymbol{v}}^\alpha)}{\partial t} = &\left\langle \sum_{k,l=1}^n \sum_{\gamma=1}^v \delta(\boldsymbol{R}^k - \boldsymbol{x})\delta(\Delta \boldsymbol{r}^{k\alpha} - \boldsymbol{y}^\alpha) \frac{\boldsymbol{F}^{l\gamma}}{m^\gamma} \cdot \nabla_{\boldsymbol{V}^{l\gamma}} (m^\alpha \boldsymbol{V}^{k\alpha}) \right\rangle \\ &- \nabla_{\boldsymbol{x}} \cdot \left\langle \sum_{k=1}^n m^\alpha \boldsymbol{V}^k \otimes \boldsymbol{V}^{k\alpha} \delta(\boldsymbol{R}^k - \boldsymbol{x})\delta(\Delta \boldsymbol{r}^{k\alpha} - \boldsymbol{y}^\alpha) \right\rangle \\ &- \nabla_{\boldsymbol{y}^\alpha} \cdot \left\langle \sum_{k=1}^n m^\alpha \Delta \boldsymbol{v}^{k\alpha} \otimes \boldsymbol{V}^{k\alpha} \delta(\boldsymbol{R}^k - \boldsymbol{x})\delta(\Delta \boldsymbol{r}^{k\alpha} - \boldsymbol{y}^\alpha) \right\rangle. \end{aligned}$$

With the divergence of momentum flux, Equation (2–8), one has

$$\left\langle \sum_{k=1}^n \boldsymbol{F}^{k\alpha} \delta(\boldsymbol{R}^k - \boldsymbol{x})\delta(\Delta \boldsymbol{r}^{k\alpha} - \boldsymbol{y}^\alpha) \right\rangle = \nabla_{\boldsymbol{x}} \cdot \bar{\boldsymbol{t}}^\alpha_{\text{pot}} + \nabla_{\boldsymbol{y}^\alpha} \cdot \bar{\boldsymbol{\tau}}^\alpha_{\text{pot}} + \bar{\boldsymbol{f}}^\alpha. \tag{4–1}$$

Since

$$\left\langle \sum_{k=1}^n m^\alpha \tilde{\boldsymbol{V}}^k \delta(\boldsymbol{R}^k - \boldsymbol{x})\delta(\Delta \boldsymbol{r}^{k\alpha} - \boldsymbol{y}^\alpha) \right\rangle = \left\langle \sum_{k=1}^n m^\alpha \Delta \tilde{\boldsymbol{v}}^{k\alpha} \delta(\boldsymbol{R}^k - \boldsymbol{x})\delta(\Delta \boldsymbol{r}^{k\alpha} - \boldsymbol{y}^\alpha) \right\rangle = 0,$$

this gives

$$\begin{aligned}
&\nabla_{\boldsymbol{x}} \cdot \left\langle \sum_{k=1}^{n} m^{\alpha} \boldsymbol{V}^{k} \otimes \boldsymbol{V}^{k\alpha} \delta(\boldsymbol{R}^{k} - \boldsymbol{x}) \delta(\Delta \boldsymbol{r}^{k\alpha} - \boldsymbol{y}^{\alpha}) \right\rangle \\
&\quad = \nabla_{\boldsymbol{x}} \cdot \left\langle \sum_{k=1}^{n} m^{\alpha} \big(\tilde{\boldsymbol{V}}^{k} \otimes \tilde{\boldsymbol{V}}^{k\alpha} + \bar{\boldsymbol{v}} \otimes (\bar{\boldsymbol{v}} + \Delta \bar{\boldsymbol{v}}^{\alpha}) \big) \delta(\boldsymbol{R}^{k} - \boldsymbol{x}) \delta(\Delta \boldsymbol{r}^{k\alpha} - \boldsymbol{y}^{\alpha}) \right\rangle \\
&\quad = \nabla_{\boldsymbol{x}} \cdot \big(-\bar{\boldsymbol{t}}_{\mathrm{kin}^{\alpha}} + \bar{\rho}^{\alpha} \bar{\boldsymbol{v}} \otimes (\bar{\boldsymbol{v}} + \Delta \bar{\boldsymbol{v}}^{\alpha}) \big), \qquad (4\text{–}2)
\end{aligned}$$

$$\begin{aligned}
&\nabla_{\boldsymbol{y}^{\alpha}} \cdot \left\langle \sum_{k=1}^{n} m^{\alpha} \Delta \boldsymbol{v}^{k\alpha} \otimes \boldsymbol{V}^{k\alpha} \delta(\boldsymbol{R}^{k} - \boldsymbol{x}) \delta(\Delta \boldsymbol{r}^{k\alpha} - \boldsymbol{y}^{\alpha}) \right\rangle \\
&\quad = \nabla_{\boldsymbol{y}^{\alpha}} \cdot \left\langle \sum_{k=1}^{n} m^{\alpha} \big(\Delta \tilde{\boldsymbol{v}}^{k\alpha} \otimes \tilde{\boldsymbol{V}}^{k\alpha} + \Delta \bar{\boldsymbol{v}}^{\alpha} \otimes (\bar{\boldsymbol{v}} + \Delta \bar{\boldsymbol{v}}^{\alpha}) \big) \delta(\boldsymbol{R}^{k} - \boldsymbol{x}) \delta(\Delta \boldsymbol{r}^{k\alpha} - \boldsymbol{y}^{\alpha}) \right\rangle \\
&\quad = \nabla_{\boldsymbol{y}^{\alpha}} \cdot \big(-\bar{\boldsymbol{\tau}}^{\alpha}_{\mathrm{kin}} + \bar{\rho}^{\alpha} \Delta \bar{\boldsymbol{v}}^{\alpha} \otimes (\bar{\boldsymbol{v}} + \Delta \bar{\boldsymbol{v}}^{\alpha}) \big). \qquad (4\text{–}3)
\end{aligned}$$

Combining Equations (4–1)–(4–3) with $\bar{\boldsymbol{t}}^{\alpha} = \bar{\boldsymbol{t}}^{\alpha}_{\mathrm{kin}} + \bar{\boldsymbol{t}}^{\alpha}_{\mathrm{pot}}$ and $\bar{\boldsymbol{\tau}}^{\alpha} = \bar{\boldsymbol{\tau}}^{\alpha}_{\mathrm{kin}} + \bar{\boldsymbol{\tau}}^{\alpha}_{\mathrm{pot}}$, the time evolution of linear momentum is obtained as

$$\begin{aligned}
&\frac{\partial}{\partial t} \big(\bar{\rho}^{\alpha} (\bar{\boldsymbol{v}} + \Delta \bar{\boldsymbol{v}}^{\alpha}) \big) \\
&\qquad = \nabla_{\boldsymbol{x}} \cdot \big(\bar{\boldsymbol{t}}^{\alpha} - \bar{\rho}^{\alpha} \bar{\boldsymbol{v}} \otimes (\bar{\boldsymbol{v}} + \Delta \bar{\boldsymbol{v}}^{\alpha}) \big) + \nabla_{\boldsymbol{y}^{\alpha}} \cdot \big(\bar{\boldsymbol{\tau}}^{\alpha} - \bar{\rho}^{\alpha} \Delta \bar{\boldsymbol{v}}^{\alpha} \otimes (\bar{\boldsymbol{v}} + \Delta \bar{\boldsymbol{v}}^{\alpha}) \big) + \bar{\boldsymbol{f}}^{\alpha},
\end{aligned}$$

or

$$\bar{\rho}^{\alpha} \frac{d}{dt} (\bar{\boldsymbol{v}} + \Delta \bar{\boldsymbol{v}}^{\alpha}) = \nabla_{\boldsymbol{x}} \cdot \bar{\boldsymbol{t}}^{\alpha} + \nabla_{\boldsymbol{y}^{\alpha}} \cdot \bar{\boldsymbol{\tau}}^{\alpha} + \bar{\boldsymbol{f}}^{\alpha}.$$

For cell-average linear momentum density, $\bar{\rho} \bar{\boldsymbol{v}} \equiv \langle \sum_{k=1}^{n} m \boldsymbol{V}^{k} \delta(\boldsymbol{R}^{k} - \boldsymbol{x}) \rangle$, the time evolution is obtained as

$$\frac{\partial}{\partial t} (\bar{\rho} \bar{\boldsymbol{v}}) = \nabla_{\boldsymbol{x}} \cdot \big[\bar{\boldsymbol{t}} - \rho \bar{\boldsymbol{v}} \otimes \bar{\boldsymbol{v}} \big] + \bar{\boldsymbol{f}} \qquad \text{or} \qquad \bar{\rho} \frac{d}{dt} \bar{\boldsymbol{v}} = \nabla_{\boldsymbol{x}} \cdot \bar{\boldsymbol{t}} + \bar{\boldsymbol{f}}, \qquad (4\text{–}4)$$

where $\bar{\boldsymbol{t}} = \sum_{\alpha=1}^{\nu} \bar{\boldsymbol{t}}^{\alpha}$ and $\bar{\boldsymbol{f}} = \sum_{\alpha=1}^{\nu} \bar{\boldsymbol{f}}^{\alpha}$ are the cell averages of homogeneous momentum flux density and body force density, respectively. Equation (4–4) is identical with the conservation law of linear momentum in macroscopic continuum mechanics. However, the latter no longer holds at atomic scale.

4.3. ***Balance of angular momentum.*** The angular momentum density can be defined as

$$\bar{\rho}^{\alpha} \bar{\boldsymbol{\psi}}^{\alpha} \equiv \left\langle \sum_{k=1}^{n} m^{\alpha} \boldsymbol{V}^{k\alpha} \times \boldsymbol{R}^{k\alpha} \delta(\boldsymbol{R}^{k} - \boldsymbol{x}) \delta(\Delta \boldsymbol{r}^{k\alpha} - \boldsymbol{y}^{\alpha}) \right\rangle = \bar{\rho}^{\alpha} (\bar{\boldsymbol{v}} + \Delta \bar{\boldsymbol{v}}^{\alpha}) \times (\boldsymbol{x} + \boldsymbol{y}^{\alpha}).$$

Substituting it into Equation (3–2), there results

$$\frac{\partial}{\partial t}(\bar{\rho}^{\alpha}\bar{\boldsymbol{\psi}}^{\alpha}) = \left\langle \sum_{k=1}^{n} m^{\alpha}\boldsymbol{V}^{k\alpha}\cdot\boldsymbol{V}^{k\alpha}\delta(\boldsymbol{R}^{k}-\boldsymbol{x})\delta(\Delta\boldsymbol{r}^{k\alpha}-\boldsymbol{y}^{\alpha})\right\rangle$$
$$+\left\langle \sum_{k=1}^{n}\boldsymbol{F}^{k\alpha}\cdot\boldsymbol{R}^{k\alpha}\delta(\boldsymbol{R}^{k}-\boldsymbol{x})\delta(\Delta\boldsymbol{r}^{k\alpha}-\boldsymbol{y}^{\alpha})\right\rangle$$
$$-\nabla_{\boldsymbol{x}}\cdot\left\langle \sum_{k=1}^{n}(\tilde{\boldsymbol{V}}^{k}+\bar{\boldsymbol{v}})\otimes m^{\alpha}(\tilde{\boldsymbol{V}}^{k\alpha}+\bar{\boldsymbol{v}}+\Delta\bar{\boldsymbol{v}}^{\alpha})\times\boldsymbol{R}^{k\alpha}\delta(\boldsymbol{R}^{k}-\boldsymbol{x})\delta(\Delta\boldsymbol{r}^{k\alpha}-\boldsymbol{y}^{\alpha})\right\rangle$$
$$-\nabla_{y^{\alpha}}\cdot\left\langle \sum_{k=1}^{n}(\Delta\tilde{\boldsymbol{v}}^{k\alpha}+\Delta\bar{\boldsymbol{v}}^{\alpha})\otimes m^{\alpha}(\tilde{\boldsymbol{V}}^{k\alpha}+\bar{\boldsymbol{v}}+\Delta\bar{\boldsymbol{v}}^{\alpha})\times\boldsymbol{R}^{k\alpha}\delta(\boldsymbol{R}^{k}-\boldsymbol{x})\delta(\Delta\boldsymbol{r}^{k\alpha}-\boldsymbol{y}^{\alpha})\right\rangle$$
$$\equiv A+B+C+D,$$

where

$$A=\left\langle \sum_{k=1}^{n}(m^{\alpha}\boldsymbol{V}^{ka}\times\boldsymbol{V}^{ka})\delta(\boldsymbol{R}^{k}-\boldsymbol{x})\delta(\Delta\boldsymbol{r}^{k\alpha}-\boldsymbol{y}^{\alpha})\right\rangle=0,$$

$$B=\left\langle \sum_{k=1}^{n}\left(\sum_{l=1}^{n}\sum_{\eta=1}^{\nu}\boldsymbol{f}_{1}^{\substack{k\alpha\\ l\eta}}\times\boldsymbol{R}^{k\alpha}+\sum_{\eta=1}^{\nu}\boldsymbol{f}_{2}^{k_{\eta}^{\alpha}}\times\boldsymbol{R}^{k\alpha}\right)\times\delta(\boldsymbol{R}^{k}-\boldsymbol{x})\delta(\Delta\boldsymbol{r}^{k\alpha}-\boldsymbol{y}^{\alpha})\right\rangle+\bar{\boldsymbol{L}}^{\alpha}$$
$$=\left\langle \sum_{k=1}^{n}\left(\sum_{l=1}^{n}\sum_{\eta=1}^{\nu}\boldsymbol{f}_{1}^{\substack{k\alpha\\ l\eta}}+\sum_{\eta=1}^{\nu}\boldsymbol{f}_{2}^{k_{\eta}^{\alpha}}\right)\delta(\boldsymbol{R}^{k}-\boldsymbol{x})\delta(\Delta\boldsymbol{r}^{k\alpha}-\boldsymbol{y}^{\alpha})\right\rangle\times(\boldsymbol{x}+\boldsymbol{y}^{\alpha})+\bar{\boldsymbol{L}}^{\alpha}$$
$$=(\nabla_{\boldsymbol{x}}\cdot\bar{\boldsymbol{t}}_{\mathrm{pot}}^{\alpha}+\nabla_{y^{\alpha}}\cdot\bar{\boldsymbol{\tau}}_{\mathrm{pot}}^{\alpha})\times(\boldsymbol{x}+\boldsymbol{y}^{\alpha})+\bar{\mathbf{L}}^{\alpha},$$

$$C=-\nabla_{\boldsymbol{x}}\cdot\left(\left\langle \sum_{k=1}^{n}m^{\alpha}\tilde{\boldsymbol{V}}^{k}(\boldsymbol{R}^{k}-\boldsymbol{x})\delta(\Delta\boldsymbol{r}^{k\alpha}-\boldsymbol{y}^{\alpha})\right\rangle\times(\boldsymbol{x}+\boldsymbol{y}^{\alpha})\right)-\nabla_{\boldsymbol{x}}\cdot(\bar{\boldsymbol{v}}\otimes\bar{\rho}^{\alpha}\bar{\boldsymbol{\psi}}^{\alpha})$$
$$=-\nabla_{\boldsymbol{x}}\cdot\left(\bar{\boldsymbol{v}}\otimes\bar{\rho}^{\alpha}\bar{\boldsymbol{\psi}}^{\alpha}-\bar{\boldsymbol{t}}_{\mathrm{kin}}^{\alpha}\times(\boldsymbol{x}+\boldsymbol{y}^{\alpha})\right),$$

$$D=-\nabla_{y^{\alpha}}\cdot\left(\Delta\bar{\boldsymbol{v}}^{\alpha}\otimes\bar{\rho}^{\alpha}\bar{\boldsymbol{\psi}}^{\alpha}+\left\langle \sum_{k=1}^{n}\Delta\tilde{\boldsymbol{v}}^{k\alpha}\otimes m^{\alpha}\boldsymbol{V}^{k\alpha}\times\boldsymbol{R}^{k\alpha}\delta(\boldsymbol{R}^{k}-\boldsymbol{x})\times\delta(\Delta\boldsymbol{r}^{k\alpha}-\boldsymbol{y}^{\alpha})\right\rangle\right)$$
$$=-\nabla_{y^{\alpha}}\cdot(\Delta\bar{\boldsymbol{v}}^{\alpha}\otimes\bar{\rho}^{\alpha}\bar{\boldsymbol{\psi}}^{\alpha})$$
$$-\nabla_{y^{\alpha}}\cdot\left(\left\langle \sum_{k=1}^{n}\Delta\tilde{\boldsymbol{v}}^{\boldsymbol{k}}\alpha\otimes m^{\alpha}(\tilde{\boldsymbol{V}}^{\boldsymbol{k}}\alpha+\bar{\boldsymbol{v}}+\Delta\bar{\boldsymbol{v}}^{\alpha})\delta(\boldsymbol{R}^{k}-\boldsymbol{x})\delta(\Delta\boldsymbol{r}^{k\alpha}-\boldsymbol{y}^{\alpha})\right\rangle\times(\boldsymbol{x}+\boldsymbol{y}^{\alpha})\right)$$
$$=-\nabla_{y^{\alpha}}\cdot\left(\Delta\bar{\boldsymbol{v}}^{\alpha}\otimes\bar{\rho}^{\alpha}\bar{\boldsymbol{\psi}}^{\alpha}-\bar{\boldsymbol{\tau}}_{\mathrm{kin}}^{\alpha}\times(\boldsymbol{x}+\boldsymbol{y}^{\alpha})\right).$$

Combining A, B, C, and D gives

$$\frac{\partial}{\partial t}(\bar{\rho}^\alpha \bar{\boldsymbol{\psi}}^\alpha) = -\nabla_{\boldsymbol{x}} \cdot \left(\bar{\boldsymbol{v}} \otimes \bar{\rho}^\alpha \bar{\boldsymbol{\psi}}^\alpha - \bar{\boldsymbol{t}}^\alpha_{\text{kin}} \times (\boldsymbol{x} + \boldsymbol{y}^\alpha)\right) - \nabla_{\boldsymbol{y}^\alpha} \cdot \left(\Delta \bar{\boldsymbol{v}}^\alpha \otimes \bar{\rho}^\alpha \bar{\boldsymbol{\psi}}^\alpha - \bar{\boldsymbol{\tau}}^\alpha_{\text{kin}} \times (\boldsymbol{x} + \boldsymbol{y}^\alpha)\right) + (\nabla_{\boldsymbol{x}} \cdot \bar{\boldsymbol{t}}^\alpha_{\text{pot}} + \nabla_{\boldsymbol{y}^\alpha} \cdot \bar{\boldsymbol{\tau}}^\alpha_{\text{pot}}) \times (\boldsymbol{x} + \boldsymbol{y}^\alpha) + \bar{\boldsymbol{L}}^\alpha,$$

or

$$\bar{\rho}^\alpha \frac{d\bar{\boldsymbol{\psi}}^\alpha}{dt} = \nabla_{\boldsymbol{x}} \cdot \left(\bar{\boldsymbol{t}}^\alpha_{\text{kin}} \times (\boldsymbol{x} + \boldsymbol{y}^\alpha)\right) + \nabla_{\boldsymbol{y}^\alpha} \cdot \left(\bar{\boldsymbol{\tau}}^\alpha_{\text{kin}} \times (\boldsymbol{x} + \boldsymbol{y}^\alpha)\right) + (\nabla_{\boldsymbol{x}} \cdot \bar{\boldsymbol{t}}^\alpha_{\text{pot}} + \nabla_{\boldsymbol{y}^\alpha} \cdot \bar{\boldsymbol{\tau}}^\alpha_{\text{pot}}) \times (\boldsymbol{x} + \boldsymbol{y}^\alpha) + \bar{\boldsymbol{L}}^\alpha.$$

Notice that the time evolution of angular momentum can also be expressed from its field definition as

$$\bar{\rho}^\alpha \frac{d\bar{\boldsymbol{\psi}}^\alpha}{dt} = \bar{\rho}^\alpha \frac{d(\bar{\boldsymbol{v}} + \Delta \bar{\boldsymbol{v}}^\alpha)}{dt} \times (\boldsymbol{x} + \boldsymbol{y}^\alpha) = (\nabla_{\boldsymbol{x}} \cdot \bar{\boldsymbol{t}}^\alpha + \nabla_{\boldsymbol{y}^\alpha} \cdot \bar{\boldsymbol{\tau}}^\alpha + \bar{\boldsymbol{f}}^\alpha) \times (\boldsymbol{x} + \boldsymbol{y}^\alpha).$$

Since $\bar{\boldsymbol{t}}^\alpha + \bar{\boldsymbol{\tau}}^\alpha$ is symmetric (see Equations (2–7) and $\boldsymbol{x}$ and $\boldsymbol{y}^\alpha$ are mutually independent within any unit cell, the balance law of angular momentum is shown to be identically satisfied.

4.4. ***Conservation of energy.*** With the definition of local total energy density

$$\bar{\rho}^\alpha \bar{E}^\alpha = \left\langle \sum_{k=1}^{n} \left(\tfrac{1}{2} m^\alpha (\boldsymbol{V}^{k\alpha})^2 + U^{k\alpha}\right) \delta(\boldsymbol{R}^k - \boldsymbol{x}) \, \delta(\Delta \boldsymbol{r}^{k\alpha} - \boldsymbol{y}^\alpha) \right\rangle,$$

Equation (3–2) results in

$$\begin{aligned}
\frac{\partial}{\partial t}(\rho^\alpha \bar{E}^\alpha) = & -\nabla_{\boldsymbol{x}} \cdot \left\langle \sum_{k=1}^{n} \boldsymbol{V}^k \left(\tfrac{1}{2} m^\alpha (\boldsymbol{V}^{k\alpha})^2 + U^{k\alpha}\right) \delta(\boldsymbol{R}^k - \boldsymbol{x}) \delta(\Delta \boldsymbol{r}^{k\alpha} - \boldsymbol{y}^\alpha) \right\rangle \\
& - \nabla_{\boldsymbol{y}^\alpha} \cdot \left\langle \sum_{k=1}^{n} \Delta \boldsymbol{v}^{k\alpha} \left(\tfrac{1}{2} m^\alpha (\boldsymbol{V}^{k\alpha})^2 + U^{k\alpha}\right) \delta(\boldsymbol{R}^k - \boldsymbol{x}) \, \delta(\Delta \boldsymbol{r}^{k\alpha} - \boldsymbol{y}^\alpha) \right\rangle \\
& + \left\langle \sum_{k=1}^{n} \boldsymbol{F}^{k\alpha} \cdot \boldsymbol{V}^{k\alpha} \delta(\boldsymbol{R}^k - \boldsymbol{x}) \, \delta(\Delta \boldsymbol{r}^{k\alpha} - \boldsymbol{y}^\alpha) \right\rangle \\
& + \left\langle \sum_{k,m=1}^{n} \sum_{\gamma=1}^{\nu} (\boldsymbol{V}^{m\gamma} \cdot \nabla_{\boldsymbol{R}^{m\gamma}}) U^{k\alpha} \delta(\boldsymbol{R}^k - \boldsymbol{x}) \, \delta(\Delta \boldsymbol{r}^{k\alpha} - \boldsymbol{y}^\alpha) \right\rangle \\
\equiv & \, A + B + C + D.
\end{aligned}$$

A, B, C and D can be further derived as

$$\begin{aligned}
A =& -\nabla_{\boldsymbol{x}}\cdot\Big\langle\sum_{k=1}^{n}(\boldsymbol{V}^{k}-\bar{\boldsymbol{v}}+\bar{v})\big(\tfrac{1}{2}m^{\alpha}(\tilde{\boldsymbol{V}}^{k\alpha})^{2}+\tilde{\boldsymbol{V}}^{k\alpha}\cdot(\bar{\boldsymbol{v}}+\Delta\bar{\boldsymbol{v}}^{\alpha})\\
&\qquad+\tfrac{1}{2}m^{\alpha}(\bar{\boldsymbol{v}}+\Delta\bar{\boldsymbol{v}}^{\alpha})^{2}+U^{k\alpha}\big)\delta(\boldsymbol{R}^{k}-\boldsymbol{x})\delta(\Delta\boldsymbol{r}^{k\alpha}-\boldsymbol{y}^{\alpha})\Big\rangle\\
=& -\nabla_{\boldsymbol{x}}\cdot\big(-\bar{\boldsymbol{q}}^{\alpha}_{\mathrm{kin}}-\bar{\boldsymbol{t}}^{\alpha}_{\mathrm{kin}}\cdot(\bar{\boldsymbol{v}}+\Delta\bar{\boldsymbol{v}}^{\alpha})+\bar{\boldsymbol{v}}\big(\bar{\rho}^{\alpha}\bar{\varepsilon}^{\alpha}+\tfrac{1}{2}\bar{\rho}^{\alpha}(\bar{\boldsymbol{v}}+\Delta\bar{\boldsymbol{v}}^{\alpha})^{2}\big)\big),\\
B =& -\nabla^{\alpha}_{\boldsymbol{y}}\cdot\Big\langle\sum_{k=1}^{n}(\Delta\boldsymbol{v}^{k\alpha}-\Delta\bar{\boldsymbol{v}}^{\alpha}+\Delta\bar{\boldsymbol{v}}^{\alpha})\big(\tfrac{1}{2}m^{\alpha}(\tilde{\boldsymbol{V}}^{ka})^{2}+\tilde{\boldsymbol{V}}^{ka}\cdot(\bar{\boldsymbol{v}}+\Delta\bar{\boldsymbol{v}}^{\alpha})\\
&\qquad+\tfrac{1}{2}m^{\alpha}(\bar{\boldsymbol{v}}+\Delta\bar{\boldsymbol{v}}^{\alpha})^{2}+U^{k\alpha}\big)\delta(\boldsymbol{R}^{k}-\boldsymbol{x})\delta(\Delta\boldsymbol{r}^{ka}-\boldsymbol{y}^{\alpha})\Big\rangle\\
=& -\nabla_{\boldsymbol{y}^{\alpha}}\cdot\big(-\bar{\boldsymbol{j}}^{\alpha}_{\mathrm{kin}}-\bar{\boldsymbol{\tau}}^{\alpha}_{\mathrm{kin}}\cdot(\bar{\boldsymbol{v}}+\Delta\bar{\boldsymbol{v}}^{\alpha})+\Delta\bar{\boldsymbol{v}}^{\alpha}\big(\bar{\rho}^{\alpha}\bar{\varepsilon}^{\alpha}+\tfrac{1}{2}\bar{\rho}^{\alpha}(\bar{\boldsymbol{v}}+\Delta\bar{\boldsymbol{v}}^{\alpha})^{2}\big)\big),
\end{aligned}$$

$$\begin{aligned}
C =& \Big\langle\sum_{k=1}^{n}\sum_{\beta=1}^{v}\boldsymbol{V}^{k\alpha}\cdot\Big(\sum_{l=1}^{n}\boldsymbol{f}_{1}^{k\alpha\,l\eta}+\boldsymbol{f}_{2}^{k^{\alpha}_{\beta}}\Big)\delta(\boldsymbol{R}^{k}-\boldsymbol{x})\delta(\Delta\boldsymbol{r}^{k\alpha}-\boldsymbol{y}^{\alpha})\Big\rangle\\
&+\Big\langle\sum_{k=1}^{n}\boldsymbol{V}^{k\alpha}\cdot\boldsymbol{f}_{3}\delta(\boldsymbol{R}^{k}-\boldsymbol{x})\delta(\Delta\boldsymbol{r}^{k\alpha}-\boldsymbol{y}^{\alpha})\Big\rangle,\\
D =& \frac{1}{2}\Big\langle\sum_{k=1}^{n}\sum_{l=1}^{n}\sum_{\gamma=1}^{v}(\boldsymbol{V}^{l\gamma}\cdot\nabla_{\boldsymbol{R}^{l\gamma}})U^{k\alpha}\delta(\boldsymbol{R}^{k}-\boldsymbol{x})\delta(\Delta\boldsymbol{r}^{k\alpha}-\boldsymbol{y}^{\alpha})\Big\rangle\\
=& -\frac{1}{2}\Big\langle\sum_{k=1}^{n}\sum_{l=1}^{n}\sum_{\gamma=1}^{v}(\boldsymbol{V}^{k\alpha}-\boldsymbol{V}^{l\gamma})\cdot\boldsymbol{f}_{1}^{k\alpha\,l\gamma}\delta(\boldsymbol{R}^{k}-\boldsymbol{x})\delta(\Delta\boldsymbol{r}^{k\alpha}-\boldsymbol{y}^{\alpha})\Big\rangle\\
&-\frac{1}{2}\Big\langle\sum_{k=1}^{n}\sum_{\gamma=1}^{v}(\boldsymbol{V}^{k\alpha}-\boldsymbol{V}^{k\gamma})\cdot\boldsymbol{f}_{2}^{k^{\alpha}_{\gamma}}\delta(\boldsymbol{R}^{k}-\boldsymbol{x})\delta(\Delta\boldsymbol{r}^{k\alpha}-\boldsymbol{y}^{\alpha})\Big\rangle.
\end{aligned}$$

With the divergence of heat flux (Equation (2–9)), we see that

$$\begin{aligned}
C+D =& \Big\langle\frac{1}{2}\sum_{k,l=1}^{n}\sum_{\eta=1}^{v}(\boldsymbol{V}^{k\alpha}+\boldsymbol{V}^{l\eta})\cdot\boldsymbol{f}_{1}^{k\alpha\,l\eta}\delta(\boldsymbol{R}^{k}-\boldsymbol{x})\delta(\Delta\boldsymbol{r}^{k\alpha}-\boldsymbol{y}^{\alpha})\Big\rangle\\
&+\Big\langle\frac{1}{2}\sum_{k=1}^{n}\sum_{\eta=1}^{v}(\boldsymbol{V}^{k\alpha}+\boldsymbol{V}^{k\eta})\cdot\boldsymbol{f}_{2}^{k^{\alpha}_{\eta}}\delta(\boldsymbol{R}^{k}-\boldsymbol{x})\delta(\Delta\boldsymbol{r}^{k\alpha}-\boldsymbol{y}^{\alpha})\Big\rangle\\
=& \nabla_{\boldsymbol{x}}\cdot\big(\bar{\boldsymbol{q}}^{\alpha}_{\mathrm{pot}}+\bar{\boldsymbol{t}}^{\alpha}_{\mathrm{pot}}\cdot(\bar{\boldsymbol{v}}+\Delta\bar{\boldsymbol{v}}^{\alpha})\big)+\nabla_{\boldsymbol{y}^{\alpha}}\cdot\big(\bar{\boldsymbol{j}}^{\alpha}_{\mathrm{pot}}+\bar{\boldsymbol{\tau}}^{\alpha}_{\mathrm{pot}}\cdot(\bar{\boldsymbol{v}}+\Delta\bar{\boldsymbol{v}}^{\alpha})\big)\\
&+\Big\langle\sum_{k=1}^{n}(\boldsymbol{V}^{k\alpha}-\bar{\boldsymbol{v}}-\Delta\bar{\boldsymbol{v}}^{\alpha})\cdot\boldsymbol{f}_{3}\delta(\boldsymbol{R}^{k}-\boldsymbol{x})\delta(\Delta\boldsymbol{r}^{k\alpha}-\boldsymbol{y}^{\alpha})/\Delta V^{\alpha}\Big\rangle\\
&+(\bar{\boldsymbol{v}}+\Delta\bar{\boldsymbol{v}}^{\alpha})\cdot\bar{\boldsymbol{f}}^{\alpha}.
\end{aligned}$$

If the external field is not velocity-dependent, the sum of A, B, C, and D reads

$$\begin{aligned}&\frac{\partial(\bar{\rho}^\alpha \bar{E}^\alpha)}{\partial t}\\&= \nabla_{\boldsymbol{x}} \cdot \left(\bar{\boldsymbol{q}}^\alpha - \bar{\boldsymbol{v}}\bar{\rho}^\alpha \bar{\varepsilon}^\alpha + \bar{\boldsymbol{t}}^\alpha \cdot (\bar{\boldsymbol{v}} + \Delta\bar{\boldsymbol{v}}^\alpha)\right) + \nabla_{\boldsymbol{y}^\alpha} \cdot \left(\bar{\boldsymbol{j}}^\alpha - \Delta\bar{\boldsymbol{v}}^\alpha \bar{\rho}^\alpha \bar{\varepsilon}^\alpha + \bar{\boldsymbol{\tau}}^\alpha \cdot (\bar{\boldsymbol{v}} + \Delta\bar{\boldsymbol{v}}^\alpha)\right)\\&\quad - \nabla_{\boldsymbol{x}} \cdot \left\{\tfrac{1}{2}\bar{\rho}^\alpha \bar{\boldsymbol{v}}(\bar{\boldsymbol{v}} + \Delta\bar{\boldsymbol{v}}^\alpha)^2\right\} - \nabla_{\boldsymbol{y}^\alpha} \cdot \left\{\tfrac{1}{2}\bar{\rho}^\alpha \Delta\bar{\boldsymbol{v}}^\alpha (\bar{\boldsymbol{v}} + \Delta\bar{\boldsymbol{v}}^\alpha)^2\right\} + (\bar{\boldsymbol{v}} + \Delta\bar{\boldsymbol{v}}^\alpha) \cdot \bar{\boldsymbol{f}}^\alpha.\end{aligned}$$

From the conservation equation of mass and the balance equation of linear momentum, the total energy equation can be rewritten in terms of internal energy as

$$\begin{aligned}\frac{\partial}{\partial t}(\bar{\rho}^\alpha \bar{E}^\alpha) &= \frac{\partial}{\partial t}\left(\bar{\rho}^\alpha \bar{\varepsilon}^\alpha + \tfrac{1}{2}\bar{\rho}^\alpha (\bar{\boldsymbol{v}} + \Delta\bar{\boldsymbol{v}}^\alpha)^2\right)\\&= \frac{\partial}{\partial t}(\bar{\rho}^\alpha \bar{\varepsilon}^\alpha) - \nabla_{\boldsymbol{x}} \cdot \left(\tfrac{1}{2}\bar{\rho}^\alpha \bar{\boldsymbol{v}}(\bar{\boldsymbol{v}} + \Delta\bar{\boldsymbol{v}}^\alpha)^2\right) - \nabla_{\boldsymbol{y}^\alpha} \cdot \left(\tfrac{1}{2}\bar{\rho}^\alpha \Delta\bar{\boldsymbol{v}}^\alpha (\bar{\boldsymbol{v}} + \Delta\bar{\boldsymbol{v}}^\alpha)^2\right)\\&\quad + (\bar{\boldsymbol{v}} + \Delta\bar{\boldsymbol{v}}^\alpha) \cdot (\nabla_{\boldsymbol{x}} \cdot \bar{\boldsymbol{t}}^\alpha + \nabla \boldsymbol{y}^\alpha \cdot \bar{\boldsymbol{\tau}}^\alpha + \bar{\boldsymbol{f}}^\alpha).\end{aligned}$$

Finally, the time evolution of internal energy is obtained as

$$\begin{aligned}&\frac{\partial}{\partial t}(\bar{\rho}^\alpha \bar{\varepsilon}^\alpha) + \nabla_x \cdot (-\bar{\boldsymbol{q}}^\alpha + \bar{\boldsymbol{v}}\bar{\rho}^\alpha \bar{\varepsilon}^\alpha) + \nabla_{\boldsymbol{y}^\alpha} \cdot (-\bar{\boldsymbol{j}}^\alpha + \Delta\bar{\boldsymbol{v}}^\alpha \bar{\rho}^\alpha \bar{\varepsilon}^\alpha)\\&\qquad = \bar{\boldsymbol{t}}^\alpha : \nabla_{\boldsymbol{x}}(\bar{\boldsymbol{v}} + \Delta\bar{\boldsymbol{v}}^\alpha) + \bar{\boldsymbol{\tau}}^\alpha : \nabla_{\boldsymbol{y}^\alpha}(\bar{\boldsymbol{v}} + \Delta\bar{\boldsymbol{v}}^\alpha),\end{aligned}$$

or

$$\bar{\rho}^\alpha \frac{d\bar{\varepsilon}^\alpha}{dt} = \nabla_{\boldsymbol{x}} \cdot \bar{\boldsymbol{q}}^\alpha + \nabla_{\boldsymbol{y}^\alpha} \cdot \bar{\boldsymbol{j}}^\alpha + \bar{\boldsymbol{t}}^\alpha : \nabla_{\boldsymbol{x}}(\bar{\boldsymbol{v}} + \Delta\bar{\boldsymbol{v}}^\alpha) + \bar{\boldsymbol{\tau}}^\alpha : \nabla_{\boldsymbol{y}^\alpha}(\bar{\boldsymbol{v}} + \Delta\bar{\boldsymbol{v}}^\alpha),$$

where

$$\bar{\boldsymbol{t}}^\alpha : \nabla_{\boldsymbol{x}}(\bar{\boldsymbol{v}} + \Delta\bar{\boldsymbol{v}}^\alpha) \equiv \bar{t}_{ij}^\alpha \frac{\partial(\bar{v}_j + \Delta\bar{v}_j^\alpha)}{\partial x_i},$$

$$\bar{\boldsymbol{\tau}}^\alpha : \nabla_{\boldsymbol{y}^\alpha}(\bar{\boldsymbol{v}} + \Delta\bar{\boldsymbol{v}}^\alpha) \equiv \bar{\tau}_{ij}^\alpha \frac{\partial(\bar{v}_j + \Delta\bar{v}_j^\alpha)}{\partial y_i^\alpha}.$$

One can find that the time evolution law of cell-averaged energy is different from the macroscopic equation of conservation of energy. This indicates that the macroscopic form of the conservation of energy equation no longer holds even at cell level; the energy density of a unit cell is not a homogeneous quantity; and the contribution of the internal motion and deformation of atoms to the evolution of energy density cannot be ignored.

5. Summary and discussion

By decomposing atomic displacements, momentum and heat fluxes into homogeneous and inhomogeneous parts, we have formulated a field representation of

conservation laws at an atomic scale. The mathematical representations for conservation of mass, balance of linear momentum and conservation of energy are

$$\frac{d\bar{\rho}^{\alpha}}{dt} + \bar{\rho}^{\alpha}(\nabla_{\boldsymbol{x}} \cdot \bar{\boldsymbol{v}} + \nabla_{\boldsymbol{y}^{\alpha}} \cdot \Delta\bar{\boldsymbol{v}}^{\alpha}) = 0,$$

$$\bar{\rho}^{\alpha}\frac{d}{dt}(\bar{\boldsymbol{v}} + \Delta\bar{\boldsymbol{v}}^{\alpha}) = \nabla_{\boldsymbol{x}} \cdot \bar{\boldsymbol{t}}^{\alpha} + \nabla_{\boldsymbol{y}^{\alpha}} \cdot \bar{\boldsymbol{\tau}}^{\alpha} + \bar{\boldsymbol{f}}^{\alpha},$$

$$\bar{\rho}^{\alpha}\frac{d\bar{\varepsilon}^{\alpha}}{dt} = \nabla_{\boldsymbol{x}} \cdot \bar{\boldsymbol{q}}^{\alpha} + \nabla_{\boldsymbol{y}^{\alpha}} \cdot \bar{\boldsymbol{j}}^{\alpha} + \bar{\boldsymbol{t}}^{\alpha} : \nabla_{\boldsymbol{x}}(\bar{\boldsymbol{v}} + \Delta\bar{\boldsymbol{v}}^{\alpha}) + \bar{\boldsymbol{\tau}}^{\alpha} : \nabla_{\boldsymbol{y}^{\alpha}}(\bar{\boldsymbol{v}} + \Delta\bar{\boldsymbol{v}}^{\alpha}),$$

and the balance law of angular momentum at atomic scale is identically satisfied. Here are some conclusions:

(1) The field representations of conservation equations were formulated within the framework of atomic N-body dynamics. They are the exact time evolution laws of conserved quantities in MD simulations.

(2) Recall that in micromorphic theory [Eringen and Suhubi 1964; Eringen 1999], the balance laws for mass, linear momentum, generalized spin, and energy were obtained as

$$\frac{d\bar{\rho}}{dt} = -\bar{\rho}\nabla_{\boldsymbol{x}} \cdot \bar{\boldsymbol{v}}$$

$$\bar{\rho}\frac{d\bar{\boldsymbol{v}}}{dt} = \nabla_{\boldsymbol{x}} \cdot \bar{\boldsymbol{t}} + \bar{\boldsymbol{f}},$$

$$\bar{\rho}\frac{d\bar{\boldsymbol{\phi}}}{dt} = \nabla_{\boldsymbol{x}} \cdot \bar{\boldsymbol{m}} + \bar{\boldsymbol{\omega}} \cdot \overline{\rho\boldsymbol{i}} \cdot \bar{\boldsymbol{\omega}}^{T} + (\bar{\boldsymbol{t}} - \bar{\boldsymbol{s}})^{T} + \bar{\boldsymbol{l}},$$

$$\bar{\rho}\frac{d\bar{\varepsilon}}{dt} = \bar{\boldsymbol{t}} : \nabla\bar{\boldsymbol{v}} + \bar{\boldsymbol{m}} \vdots \nabla\bar{\boldsymbol{\omega}} + \bar{\boldsymbol{\omega}} : (\bar{\boldsymbol{s}} - \bar{\boldsymbol{t}})^{T} + \nabla \cdot \bar{\boldsymbol{q}},$$

where φ is generalized spin, ω the gyration tensor and l the external couple. Assuming that the inner atomic structure is a continuum and thus $\Delta\boldsymbol{v}^{k\alpha} = \boldsymbol{\omega} \cdot \Delta\boldsymbol{r}^{k\alpha}$, one will find that the obtained balance laws in this paper can be reduced to the balance laws in micromorphic theory upon such continuum assumption and cell averaging [Chen and Lee 2003a; 2003b; Chen et al. 2003]. Note that because the atomic motion and deformation as well as momentum and heat fluxes are decomposed into homogeneous and inhomogeneous parts, the higher order moment stress is avoided in this paper. Also, if the structural unit of the crystal is considered as a point mass, ignoring the atomic structure of the primitive unit cell and relative motion and deformation within this cell, the balance equations we obtain can be reduced to those of continuum mechanics.

(3) For a single component system the obtained balance laws are identical with those obtained by Irving and Kirkwood [1950].

(4) The averaged quantities are time-interval averages. If one uses ensemble averages, it is straightforward to prove that Liouville's theorem would result in the same form as in Equation (3–2) for the time evolutions in equilibrium statistical mechanics; the Boltzmann transport equation as well as BBGKY theory would also yield the same for conserved properties in nonequilibrium statistical mechanics [Chen and Lee 2003a; 2003b; Chen et al. 2003; Kreuzer 1981].

(5) The formulation in this paper has proved that for multielement systems the local conservation equations at atomic scale differ from that at macroscopic scale, and the contribution of the internal motion and deformation of atoms cannot be ignored.

(6) While in molecular dynamics simulations, some physical phenomena may depend on the initial condition, the time-interval Δt, and the choice of the localization function δ, it is noticed that the obtained mathematical representation of the conservation laws is fully in terms of field variables, and is independent of the initial conditions, the time interval and the choice of the localization function.

References

[Chen and Lee 2003a] Y. Chen and J. D. Lee, "Connecting molecular dynamics to micromorphic theory, I: Instantaneous mechanical variables", *Physica A* **322** (2003), 359–376.

[Chen and Lee 2003b] Y. Chen and J. D. Lee, "Connecting molecular dynamics to micromorphic theory, II: Balance laws", *Physica A* **322** (2003), 377–392.

[Chen et al. 2003] Y. Chen, J. D. Lee, and A. Eskandarian, "Atomistic counterpart of micromorphic theory", *Acta Mech.* **161**:1–2 (2003), 81–102.

[Cochran 1973] W. Cochran, *The dynamics of atoms in crystals*, Edward Arnold Limited, London, 1973.

[Eringen 1999] A. C. Eringen, *Microcontinuum field theories, I: Foundations and solids*, Springer, New York, 1999. MR 2000i:74007

[Eringen and Suhubi 1964] A. C. Eringen and E. S. Suhubi, "Nonlinear theory of simple microelastic solids, I", *Int. J. Eng. Sci.* **2**:2 (1964), 189–203.

[Hardy 1963] R. J. Hardy, "Energy-flux operator for a lattice", *Phys. Rev.* **132**:1 (1963), 168–177. MR 28 #948

[Hardy 1982] R. J. Hardy, "Formulas for determining local properties in molecular-dynamics simulations: Shock waves", *J. Chem. Phys.* **76**:1 (1982), 622–628.

[Hoover 1986] W. G. Hoover, *Molecular dynamics*, Springer, Berlin, 1986.

[Hoover 1991] W. G. Hoover, *Computational statistical mechanics*, Elsevier, Amsterdam, 1991.

[Huang 1967] K. Huang, *Statistical mechanics*, Willey, New York, 1967.

[Irving and Kirkwood 1950] J. H. Irving and J. G. Kirkwood, "The statistical mechanical theory of transport processes, IV: The equations of hydrodynamics", *J. Chem. Phys.* **18**:6 (1950), 817–829. MR 12,230d

[Kreuzer 1981] H. J. Kreuzer, *Nonequilibrium thermodynamics and its statistical foundations*, Oxford University Press, London, 1981. MR 82d:82001

[Ranninger 1965] J. Ranninger, "Lattice thermal conductivity", *Phys. Rev.* **140**:6A (1965), A2031–A2046.

Received 4 Dec 2005.

YOUPING CHEN: ypchen2@gwu.edu
School of Engineering and Applied Science, The George Washington University, Academic Center T739, 801 22nd Street NW, Washington, DC 20052, United States

JAMES LEE: jdlee@gwu.edu
School of Engineering and Applied Science, The George Washington University, Academic Center T739, 801 22nd Street NW, Washington, DC 20052, United States

JOURNAL OF MECHANICS OF MATERIALS AND STRUCTURES
Vol. 1, No. 4, 2006

STRESSES AND STRAINS AT NANO/MICRO SCALES

YOUPING CHEN, JAMES LEE AND LIMING XIONG

This paper is concerned with stress and strain fields at atomic scale. Unlike other formulations of atomistic expression of macroscopic stress fields or homogeneous systems, this paper aims at field descriptions of atomic stresses and strains for multi-element crystalline materials. By decomposing atomic deformation into homogeneous lattice deformation and inhomogeneous relative atomic deformation, a field representation of momentum flux is formulated within the framework of atomic many-body dynamics, and the connection to a macroscopic definition of stress is obtained. The atomic strain measures and the atomic stress-strain relations are derived. Phonon dispersion relations are calculated and presented.

1. Introduction

Stress is an important concept in characterizing the states of condensed matter, and has been extensively studied from both macroscopic and microscopic points of view. Quantum mechanics theory of stress may be traced back to the earliest years of the development of quantum mechanics [Born et al. 1926]. Through atomistic simulations of momentum flux in classical many-body dynamics, the study of stress response to external disturbance has played an important role in understanding mechanical properties of materials [Horstemeyer and Baskes 1999]. One of the fundamental properties in classical continuum mechanics is stress. Extensions of macroscopic continuum theory to microcontinuum theories are mainly due to the deficiency of stress descriptions – we thus have theories incorporating moment stress, microstress average, couple stress, etc. [Eringen and Suhubi 1964; Mindlin 1964; Eringen 1967; Cosserat and Cosserat 1909; Toupin 1962; Green and Rivlin 1964]. While the underlying physics is same, the descriptions from different viewpoints are thoroughly different.

Atomistic view of a crystal is as a periodic arrangement of local atomic bonding units. Each lattice point defines the location of the center of the unit that forms the smallest structural unit of the crystal. The structure of the unit together with

Keywords: stress, strain, atomic scale, many-body dynamics.
The support to this work by National Science Foundation under Award Numbers CMS-0301539 and CMS-0428419 is gratefully acknowledged.

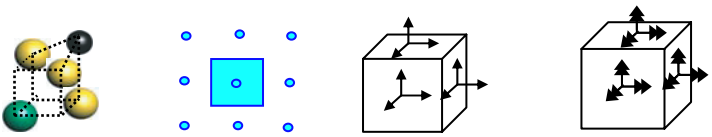

Figure 1. Stresses in ABO_3 ferroelectrics: (a) The ABO_3 structural unit; (b) Lattice points and the unit cell (2D illustration); (c) stress evaluated at lattice position with the volume of a unit cell; (d) moment stress resulting from the resultant moment of interatomic forces.

the network of lattice points determines the crystal structure and hence the physical properties of the material. Classical continuum mechanics, on the other hand, views a crystal as a homogeneous and continuous medium. The basic structural unit of the crystal is idealized as point mass, and the internal motion and deformation of atoms within the unit are ignored.

Consider ABO_3 ferroelectrics as an example. There are five atoms in a unit cell, the smallest structural unit (Figure 1a). This unit cell (a mass point in classical continuum theory) gives the smallest allowable volume in which the continuum hypothesis is not violated (Figure 1b). However, at ferroelectric phase, for this mathematical infinitesimal, the vector sum of all interatomic forces will not pass through the mass center. This will result in a surface couple on the surface of this infinitesimal volume, and hence a higher order moment stress, $\boldsymbol{m}$, (as shown in Figure 1d) in addition to the stress in the traditional continuum definition (Figure 1c). Such higher order stress has been employed in many micro-continuum theories to account for the effect of microstructure. Among those well-established, there are micromorphic theory [Eringen and Suhubi 1964; Eringen 1999], microstructure theory [Mindlin 1964], micropolar theory [Eringen 1967], and Cosserat theory [Cosserat and Cosserat 1909]. As a consequence of the higher order stresses, there are higher order strains to be the corresponding thermodynamic conjugates.

However, it is very difficult, if not impossible, for these micro-continuum theories to describe the dynamics feature of atoms in complex crystals at nano/micro scales. Material properties or behavior related to atomic motion and interaction cannot be modeled accurately by the existing micro-continuum theories. Moreover, the stresses and strains defined in classical or micro-continuum theories may not be consistent with the atomistic definitions in microscopic modeling and simulations.

This paper aims at field descriptions of stress and strain at atomic scale for multi-element crystals. In Section 2 the momentum flux density in the classical N-body dynamics will be introduced. A field representation of momentum flux will be derived in Section 3, atomic stress-strain relation as well as the atomistic measures

of strain will be derived in Section 4, a few numerical examples will be presented in Section 5, and a summary and discussions will be presented in Section 6. Standard dyadic and tensor notations are employed in this paper.

2. Momentum flux in classical N-body dynamics

2.1. ***Atomic forces.*** In an atomic N-body system, if one defines the force between atom i and atom j as

$$\boldsymbol{f}^{ij} = -\left\langle \frac{\partial U_{\text{int}}}{\partial(\boldsymbol{R}^i - \boldsymbol{R}^j)} \right\rangle = \left\langle \frac{\partial U_{\text{int}}}{\partial(\boldsymbol{R}^j - \boldsymbol{R}^i)} \right\rangle = -\boldsymbol{f}^{ji}, \tag{2–1}$$

one then has

$$\boldsymbol{f}^i = \sum_{j=1}^{n} \boldsymbol{f}^{ij},$$

where $\boldsymbol{f}^{ij}$ is the interatomic force and $\boldsymbol{R}^i - \boldsymbol{R}^j$ the relative separation vector between the two atoms i and j.

Now consider a multi-element crystal with n unit cell and ν atoms in each primitive unit cell. Generally, forces acting on an atom (k, α), where $k = 1, 2, \ldots n$ and $\alpha = 1, 2, \ldots \nu$, can be divided into three kinds:

1. $\boldsymbol{f}_1^{k\alpha}{}_{l\beta}$: interatomic force between (k, α) and (l, β) atoms in two different unit cells k and l, with
$$\boldsymbol{f}_1^{k\alpha}{}_{l\beta} = -\boldsymbol{f}_1^{l\beta}{}_{k\alpha}.$$
2. $\boldsymbol{f}_2^{k}{}_{\beta}^{\alpha}$: interatomic force between (k, α) and (k, β) atoms in the same unit cell k, with
$$\boldsymbol{f}_2^{k}{}_{\beta}^{\alpha} = -\boldsymbol{f}_2^{k}{}_{\alpha}^{\beta}.$$
3. $\boldsymbol{f}_3^{k\alpha}$: body force on atom (k, α) due to the external fields.

The total force acting on an atom (k, α) can be written as

$$\boldsymbol{F}^{k\alpha} = \sum_{l=1}^{n} \sum_{\beta=1}^{\nu} \boldsymbol{f}_1^{k\alpha}{}_{l\beta} + \sum_{\beta=1}^{\nu} \boldsymbol{f}_2^{k}{}_{\beta}^{\alpha} + \boldsymbol{f}_3^{k\alpha}.$$

2.2. ***Momentum flux.*** The quantum mechanical theorem of stress by Born et al. [1926] and Nielsen and Martin [1985] can result in exactly the same form as the momentum flux in classical many-body dynamics [Hoover 1986; 1991; Chen and Lee 2003a; 2003b]. On a microscopic basis of atomic many-body dynamics, there are two kinds of contributions to the momentum flux: kinetic and potential.

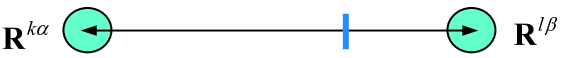

Figure 2. Flow of momentum due to inter-particle force.

Suppose a particle α carries a momentum $\boldsymbol{p}$. During a small time interval dt this momentum is transported a distance $(\boldsymbol{p}/m^{\alpha})dt$. The resulting "kinetic" contribution to the momentum flux, in the co-moving coordinate system, is

$$\boldsymbol{s}^{\alpha}_{\text{kin}} = -\boldsymbol{p} \otimes \boldsymbol{p}/m^{\alpha}. \tag{2–2}$$

By virtue of the possible macroscopic motion of the material body, the velocity that contributes to momentum flux is the difference between the instantaneous velocity and the stream velocity (the ensemble or time-interval average of the velocity),

$$\tilde{\boldsymbol{V}}^{k\alpha} = \boldsymbol{V}^{k\alpha} - \left\langle \boldsymbol{V}^{k\alpha} \right\rangle = \boldsymbol{V}^{k\alpha} - (\bar{\boldsymbol{v}} + \Delta\bar{\boldsymbol{v}}^{\alpha}). \tag{2–3}$$

This velocity difference, $\tilde{\boldsymbol{V}}^{k\alpha}$, measures the fluctuations of atoms relative to the local equilibrium and is related to the thermal motion of atoms.

The "potential" flow of momentum occurs through the mechanism of the inter-particle forces. For a pair of particles $k\alpha$ and $l\beta$ that lie on different sides of a surface, the pair force

$$\boldsymbol{f}^{k\alpha}_{l\beta} = -\boldsymbol{f}^{l\beta}_{k\alpha}$$

gives the rate at which momentum is transported from particle $k\alpha$ to particle $l\beta$. For each such pair the direction of this transport is along the line parallel to $\boldsymbol{R}^{k\alpha} - \boldsymbol{R}^{l\beta}$, and the potential contribution to the momentum flux is

$$\boldsymbol{s}_{\text{pot}} = -\boldsymbol{R}^{k\alpha} \otimes \boldsymbol{f}^{k\alpha}_{l\beta} - \boldsymbol{R}^{l\beta} \otimes \boldsymbol{f}^{l\beta}_{k\alpha} = -(\boldsymbol{R}^{k\alpha} - \boldsymbol{R}^{l\beta}) \otimes \boldsymbol{f}^{k\alpha}_{l\beta}. \tag{2–4}$$

This momentum transfer can be visualized as a direct connection between two interacting particles (Figure 2), which is continuous through the line linking them.

3. Field representation of momentum flux

3.1. ***Field representation of the atomic system.*** An ordered atomic system can be viewed as a periodic arrangement of local atomic bonding units. Each lattice point defines the location of the center of the unit. The space lattice is macroscopically homogeneous, and the deformation of lattice is homogeneous up to the point of structural instability (phase transformation). Therefore, the network of lattice point is continuous, and the deformation gives rise to a field function $\boldsymbol{u}(\boldsymbol{x})$, where each point $\boldsymbol{x}$ in the physical space corresponds to a lattice point $\boldsymbol{R}^{k}$ in the phase space;

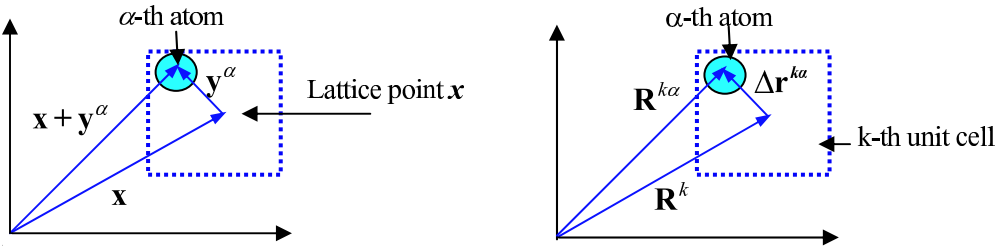

Figure 3. Physical space and phase space descriptions of an atomic position.

embedded within each point $\boldsymbol{x}$ is a group of ν discrete atoms ($\Delta\boldsymbol{r}^{k\alpha}$) (Figure 3). With a localization function

$$\delta(\boldsymbol{R}^{k}+\Delta\boldsymbol{r}^{k\alpha}-\boldsymbol{x}-\boldsymbol{y}^{\alpha})=\delta(\boldsymbol{R}^{k}-\boldsymbol{x})\delta(\Delta\boldsymbol{r}^{k\alpha}-\boldsymbol{y}^{\alpha}),$$

the local density of any measurable phase-space function $A(\boldsymbol{r},\,\boldsymbol{p})$, where

$$A(\boldsymbol{r},\,\boldsymbol{p})=A\big(\boldsymbol{r}(t),\,\boldsymbol{p}(t)\big),$$

can be expressed as [Chen and Lee 2006]

$$\bar{A}^{\alpha}(\boldsymbol{x},t)=\left\langle A^{\alpha}\right\rangle\equiv A_{m}^{\alpha}=\frac{1}{\Delta t}\int_{0}^{\Delta t}\sum_{k=1}^{n}A(\boldsymbol{r},\,\boldsymbol{p})\delta(\boldsymbol{R}^{k}-\boldsymbol{x})\delta(\Delta\boldsymbol{r}^{k\alpha}-\boldsymbol{y}^{\alpha})\,d\tau,$$

Here, quantities in physical space are expressed in terms of time-interval averages, as in experimental observations, which are performed over a finite duration. The localization function, a Dirac δ-function or a distribution function, links the expressions of a dynamic function in phase space to the local density function in physical space. The displacement of lattice point $\boldsymbol{x}$, $\boldsymbol{u}(\boldsymbol{x})$, gives rise to the homogeneous and continuous lattice deformation with length scale from nano to macroscopic. The relative displacements of the a-th atom, $\xi(\boldsymbol{x},\alpha)$, result in relative atomic deformation within the inner structure and describe the inhomogeneous and non-continuum atomic behavior whose length scale is less than a nanometer. The total atomic displacement is $\boldsymbol{u}(\boldsymbol{x})+\xi(\boldsymbol{x},\alpha)$ in physical space, corresponding to the $\boldsymbol{u}(k)+\xi(k,\alpha)$ in phase space, with the time scale of $\boldsymbol{u}(\boldsymbol{x})$ at audible frequency region and $\xi(\boldsymbol{x},\alpha)$ at inferred.

3.2. ***Field descriptions of forces and momentum flux.*** The field representation of total force acting on a an atom α can be expressed as

$$\boldsymbol{F}^{\alpha}(\boldsymbol{x})\equiv\left\langle\sum_{k=1}^{n}\left(\sum_{l=1}^{n}\sum_{\beta=1}^{\nu}\boldsymbol{f}_{1}^{\substack{k\alpha\\ l\beta}}+\sum_{\beta=1}^{\nu}\boldsymbol{f}_{2}^{k\alpha}_{\beta}+\boldsymbol{f}_{3}^{k\alpha}\right)\delta(\boldsymbol{R}^{k}-\boldsymbol{x})\delta(\Delta\boldsymbol{r}^{k\alpha}-\boldsymbol{y}^{\alpha})\right\rangle,$$

where the external body force density $\bar{\boldsymbol{f}}^{\alpha}$ is given by

$$\bar{\boldsymbol{f}}^{\alpha}(\boldsymbol{x}) \equiv \left\langle \sum_{k=1}^{n} \boldsymbol{f}_3^{k\alpha} \delta(\boldsymbol{R}^k - \boldsymbol{x}) \delta(\Delta \boldsymbol{r}^{k\alpha} - \boldsymbol{y}^{\alpha}) \right\rangle,$$

and the internal force density is (see Equation (2–1))

$$\bar{\boldsymbol{f}}^{\alpha}_{\text{int}}(\boldsymbol{x}) = \left\langle \sum_{k=1}^{n} \left(\sum_{l=1}^{n} \sum_{\xi,\eta=1}^{v} \boldsymbol{f}_1^{l\eta\,k\xi} + \sum_{\xi,\eta=1}^{v} \boldsymbol{f}_2^{k\xi}_{\eta} \right) \delta(\boldsymbol{R}^k - \boldsymbol{x}) \delta(\Delta \boldsymbol{r}^{k\xi} - \boldsymbol{y}^{\alpha}) \right\rangle.$$

From Equations (2–2)–(2–4), the local densities of kinetic and potential momentum fluxes can be expressed as

$$\bar{\boldsymbol{s}}^{\alpha}_{\text{kin}}(\boldsymbol{x}) = -\left\langle \sum_{k=1}^{n} m^{\alpha} \tilde{\boldsymbol{V}}^{k\alpha} \otimes \tilde{\boldsymbol{V}}^{k\alpha} \delta(\boldsymbol{R}^k - \boldsymbol{x}) \delta(\Delta \boldsymbol{r}^{k\alpha} - \boldsymbol{y}^{\alpha}) \right\rangle,$$

$$\begin{aligned} \bar{\boldsymbol{s}}^{\alpha}_{\text{pot}}(\boldsymbol{x}) = &-\left\langle \frac{1}{2} \sum_{k,l=1}^{n} \sum_{\xi,\eta=1}^{v} (\boldsymbol{R}^{k\xi} - \boldsymbol{R}^{l\eta}) \right. \\ &\left. \otimes \boldsymbol{f}_1^{l\beta\,k\xi} \int_0^1 d\lambda \delta\big(\boldsymbol{R}^k \lambda + \boldsymbol{R}^l (1-\lambda) - \boldsymbol{x}\big) \delta\big(\Delta \boldsymbol{r}^{k\xi} \lambda + \Delta \boldsymbol{r}^{l\eta} (1-\lambda) - \boldsymbol{y}^{\alpha}\big) \right\rangle \\ &-\left\langle \frac{1}{2} \sum_{k=1}^{n} \sum_{\xi,\eta=1}^{v} (\boldsymbol{R}^{k\xi} - \boldsymbol{R}^{k\eta}) \right. \\ &\left. \otimes \boldsymbol{f}_2^{k\xi}_{\eta} \int_0^1 d\lambda \delta(\boldsymbol{R}^k - \boldsymbol{x}) \delta\big(\Delta \boldsymbol{r}^{k\xi} \lambda + \Delta \boldsymbol{r}^{k\eta} (1-\lambda) - \boldsymbol{y}^{\alpha}\big) \right\rangle. \end{aligned}$$

The momentum flux in MD has been considered as the atomistic counterpart of the continuum stress. However, it is seen that

(1) The smallest mathematical infinitesimal volume that does not violate the continuum assumption is the volume ΔV defining the density of lattice points, which is the volume of a primitive unit cell. The vector sum of all the atomic forces within this volume may not pass through the mass center of the ΔV (Figure 4).

(2) The continuum definition of stress is not the momentum flux density. For a crystal with more than one atom in the unit cell, the continuum stress is only the homogenous part of the momentum flux summing over a volume of at least a primitive unit cell, and it may not be symmetric.

The total momentum flux density is, therefore, better represented by the sum of a homogeneous part, $\boldsymbol{t}$, which is due to the motion and deformation of the lattice

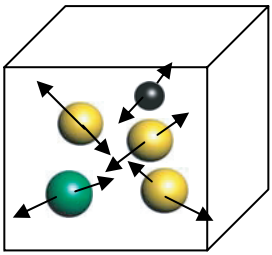

Figure 4. Illustration of atomic forces in a unit cell.

and is related to continuum stress,

$$\bar{\boldsymbol{t}}^{\alpha}_{\text{kin}} = -\left\langle \sum_{k=1}^{n} m^{\alpha} \tilde{\boldsymbol{V}}^{k} \otimes \tilde{\boldsymbol{V}}^{k\alpha} \delta(\boldsymbol{R}^{k} - \boldsymbol{x}) \delta(\Delta \boldsymbol{r}^{k\alpha} - \boldsymbol{y}^{\alpha}) \right\rangle, \tag{3–1}$$

$$\bar{\boldsymbol{t}}^{\alpha}_{\text{pot}} = -\left\langle \frac{1}{2} \int_{0}^{1} d\lambda \sum_{k,l=1}^{n} \sum_{\xi,\eta=1}^{\nu} (\boldsymbol{R}^{k} - \boldsymbol{R}^{l}) \otimes \boldsymbol{f}_{1}^{k\xi\, l\eta} \delta\big(\boldsymbol{R}^{k}\lambda + \boldsymbol{R}^{l}(1-\lambda) - \boldsymbol{x}\big) \delta(\Delta \boldsymbol{r}^{k\xi}\lambda + \Delta \boldsymbol{r}^{l\eta}(1-\lambda) - \boldsymbol{y}^{\alpha}) \right\rangle, \tag{3–2}$$

and an inhomogeneous part, τ, which is due to the internal motion and deformation,

$$\bar{\tau}^{\alpha}_{\text{kin}} = -\left\langle \sum_{k=1}^{n} m^{\alpha} \Delta \tilde{\boldsymbol{v}}^{k\alpha} \otimes \tilde{\boldsymbol{V}}^{k\alpha} \delta(\boldsymbol{R}^{k} - \boldsymbol{x}) \delta(\Delta \boldsymbol{r}^{k\alpha} - \boldsymbol{y}^{\alpha}) \right\rangle, \tag{3–3}$$

$$\begin{aligned} \bar{\tau}^{\alpha}_{\text{pot}} = &-\left\langle \frac{1}{2} \int_{0}^{1} d\lambda \sum_{k,l=1}^{n} \sum_{\xi,\eta=1}^{\nu} (\Delta \boldsymbol{r}^{k\xi} - \Delta \boldsymbol{r}^{l\eta}) \right. \\ &\qquad \left. \otimes \boldsymbol{f}_{1}^{k\xi\, l\beta} \delta\big(\boldsymbol{R}^{k}\lambda + \boldsymbol{R}^{l}(1-\lambda) - \boldsymbol{x}\big) \delta\big(\Delta \boldsymbol{r}^{k\xi}\lambda + \Delta \boldsymbol{r}^{l\eta}(1-\lambda) - \boldsymbol{y}^{\alpha}\big) \right\rangle \\ &-\left\langle \frac{1}{2} \int_{0}^{1} d\lambda \sum_{k=1}^{n} \sum_{\xi,\eta=1}^{\nu} (\Delta \boldsymbol{r}^{k\xi} - \Delta \boldsymbol{r}^{k\eta}) \right. \\ &\qquad \left. \otimes \boldsymbol{f}_{2}^{k\xi\, k\eta} \delta(\boldsymbol{R}^{k} - \boldsymbol{x}) \delta\big(\Delta \boldsymbol{r}^{k\xi}\lambda + \Delta \boldsymbol{r}^{k\eta}(1-\lambda) - \boldsymbol{y}^{\alpha}\big) \right\rangle. \end{aligned} \tag{3–4}$$

Using the identity

$$\frac{d}{d\lambda}\Big(\delta\big(\boldsymbol{R}^k\lambda+\boldsymbol{R}^l(1-\lambda)-\boldsymbol{x}\big)\delta\big(\Delta\boldsymbol{r}^{k\xi}\lambda+\Delta\boldsymbol{r}^{l\eta}(1-\lambda)-\boldsymbol{y}^\alpha\big)\Big)$$
$$=-\nabla_{\boldsymbol{x}}\cdot\Big((\boldsymbol{R}^k-\boldsymbol{R}^l)\delta\big(\boldsymbol{R}^k\lambda+\boldsymbol{R}^l(1-\lambda)-\boldsymbol{x}\big)\delta\big(\Delta\boldsymbol{r}^{k\xi}\lambda+\Delta\boldsymbol{r}^{l\eta}(1-\lambda)-\boldsymbol{y}^\alpha\big)\Big)$$
$$-\nabla_{\boldsymbol{y}^\alpha}\cdot\Big(\big(\Delta\boldsymbol{r}^{k\xi}-\Delta\boldsymbol{r}^{l\eta}\big)\delta\big(\boldsymbol{R}^k\lambda+\boldsymbol{R}^l(1-\lambda)-\boldsymbol{x}\big)\delta\big(\Delta\boldsymbol{r}^{k\xi}\lambda+\Delta\boldsymbol{r}^{l\eta}(1-\lambda)-\boldsymbol{y}^\alpha\big)\Big),$$

the divergences of the potential momentum fluxes can be related to the interatomic forces as

$$\nabla_{\boldsymbol{x}}\cdot\bar{\boldsymbol{t}}^\alpha_{\text{pot}}+\nabla_{\boldsymbol{y}^\alpha}\cdot\bar{\tau}^\alpha_{\text{pot}}=\boldsymbol{f}^\alpha_{\text{pot}}(\boldsymbol{x})$$
$$=\left\langle\sum_{k=1}^{n}\sum_{\eta=1}^{\nu}\left(\sum_{l=1}^{n}\boldsymbol{f}_1^{l\eta,k\alpha}+\boldsymbol{f}_2^{k^\alpha_\eta}\right)\delta(\boldsymbol{R}^k-\boldsymbol{x})\delta(\Delta\boldsymbol{r}^{k\alpha}-\boldsymbol{y}^\alpha)\right\rangle. \quad (3\text{–}5)$$

Note that for cell average $\bar{\boldsymbol{t}}_{\text{pot}}=\sum_{\alpha=1}^{\nu}\bar{\boldsymbol{t}}^\alpha_{\text{pot}}$. Using $\sum_{\alpha,\beta=1}^{\nu}\boldsymbol{f}_2^{k^\alpha_\beta}=0$, one finds

$$\nabla_x\cdot\bar{\boldsymbol{t}}_{\text{pot}}=\left\langle\sum_{k,l=1}^{n}\sum_{\alpha,\beta=1}^{\nu}\boldsymbol{f}_1^{l\beta,k\alpha}\delta(\boldsymbol{R}^k-\boldsymbol{x})\right\rangle \quad (3\text{–}6)$$
$$=\left\langle\sum_{k=1}^{n}\sum_{\alpha,\beta=1}^{\nu}\left(\sum_{l=1}^{n}\boldsymbol{f}_1^{l\beta,k\alpha}+\boldsymbol{f}_2^{k^\alpha_\beta}\right)\delta(\boldsymbol{R}^k-\boldsymbol{x})\right\rangle. \quad (3\text{–}7)$$

This is the well-known stress-force relation in the continuum description.

It is seen from Equations (3–5) and (3–6) that

$$\sum_{\alpha=1}^{\nu}\nabla_{y^\alpha}\cdot\bar{\tau}^\alpha_{\text{pot}}=0.$$

This indicates that the divergence of the inhomogeneous momentum flux density will be averaged out and will not contribute to cell-averaged balance equation of linear momentum. However, note that

$$\sum_{\alpha=1}^{\nu}\bar{\tau}^\alpha_{\text{pot}}\neq 0.$$

The inhomogeneous part of momentum flux does not vanish upon cell averaging. Therefore, as pointed out by Nielsen and Martin [1985], the classical definition of macroscopic stress as "any tensor field which satisfies the condition that its divergence is the vector force field" [Sommerfeld 1950; Nye 1957] cannot give a unique definition of stress, and additional consideration is required to include the

inhomogeneous part of momentum flux in order to uniquely describe the stress field at microscopic scale for inhomogeneous systems.

4. Stress-strain relations in the nano/micro scales

4.1. ***Interatomic forces.*** Results of atomic-level molecular dynamics simulation depend critically on the interatomic forces. A key issue in atomic-level simulations is therefore the choice of a suitable potential energy function or interatomic force. For the sake of simplicity, this paper considers only systems with central force pair potential. Assuming the separation distance of two atoms is d^{ij}, and the total potential energy of the system U is a function of the atomic positions only, one has

$$U = \sum_{i \neq j}^{n} U(d^{ij}).$$

Setting

$$G(d^{ij}) \equiv \frac{1}{d^{ij}} \frac{\partial U}{\partial (d^{ij})},$$

the interatomic force between atoms i and j can be written as

$$\boldsymbol{f}^{ij} = -\frac{\partial U}{\partial (\boldsymbol{d}^{ij})} = -\frac{\partial U}{\partial (d^{ij})} \frac{\boldsymbol{d}^{ij}}{d^{ij}} = -G(d^{ij}) \boldsymbol{d}^{ij}.$$

Here $\boldsymbol{d}^{ij}$ is the separation vector between two atoms i and j.

In our notation the vectorial relative displacement between atom (k, α) and atom (l, β) is

$$\boldsymbol{R}^{k\alpha} - \boldsymbol{R}^{l\beta} = (\boldsymbol{R}_o^{k\alpha} - \boldsymbol{R}_o^{l\beta}) + \boldsymbol{u}(k) - \boldsymbol{u}(l) + \xi(k, \alpha) - \xi(l, \beta).$$

Here $\boldsymbol{R}_o^{k\alpha}$ and $\boldsymbol{R}_o^{l\beta}$ are the position vectors of atoms (k, α) and (l, β) in the ground state, $\boldsymbol{u}(k)$ and $\boldsymbol{u}(l)$ are the displacements of the centers of the k-th and the l-th unit cells, and $\xi(k, \alpha)$ and $\xi(l, \beta)$ are the displacements of atoms (k, α) and (l, β) relative to their unit cell centers, that is, lattice points.

4.2. ***Momentum flux density.*** The temperature in an N-body dynamics systems is generally defined as [Chen and Lee 2006]

$$T^{\alpha} = \left\langle \frac{\Delta V}{3k_B} \sum_{k=1}^{n} m^{\alpha} (\tilde{\boldsymbol{V}}^{k\alpha})^2 \delta(\boldsymbol{R}^k - \boldsymbol{x}) \delta(\Delta \boldsymbol{r}^{k\alpha} - \boldsymbol{y}^{\alpha}) \right\rangle.$$

We see that the kinetic parts of momentum flux in Equations (3–1) and (3–3), caused by the thermal motion of atoms, are related to temperature. They depend only on the magnitude of the fluctuations of atoms. This implies

$$\bar{\boldsymbol{t}}_{\text{kin}}^{\alpha} + \bar{\tau}_{\text{kin}}^{\alpha} = -\gamma T^{\alpha} \boldsymbol{I} \qquad \text{or} \qquad \bar{\boldsymbol{t}}_{\text{kin}}^{\alpha} = -\gamma_1 T^{\alpha} \boldsymbol{I}, \quad \bar{\tau}_{\text{kin}}^{\alpha} = -\gamma_2 T^{\alpha} \boldsymbol{I},$$

with

$$\gamma_1 + \gamma_2 = \gamma, \qquad \gamma = \frac{k_B}{\Delta V}.$$

Using the δ-function identity (see Appendix),

$$\int_0^1 \delta\big(\boldsymbol{R}^k\lambda + \boldsymbol{R}^l(1-\lambda) - \boldsymbol{x}\big)\delta\big(\Delta\boldsymbol{r}^{k\xi}\lambda + \Delta\boldsymbol{r}^{l\eta}(1-\lambda) - \boldsymbol{y}^\alpha\big)d\lambda$$
$$= \sum_{m=1}^{\infty}\frac{1}{m!}\big((\boldsymbol{R}^k - \boldsymbol{R}^l)\cdot\nabla_{\boldsymbol{x}} + (\Delta\boldsymbol{r}^{k\xi} - \Delta\boldsymbol{r}^{l\eta})\cdot\nabla_{\boldsymbol{y}^\alpha}\big)^{m-1}\delta(\boldsymbol{R}^k - \boldsymbol{x})\delta(\Delta\boldsymbol{r}^{k\xi} - \boldsymbol{y}^\alpha),$$

we see that the potential momentum fluxes, Equations (3–2) and (3–4), are functions of a series of high order gradients, with zeroth order terms

$$(\bar{\boldsymbol{t}}^\alpha_{\text{pot}})^0 = -\left\langle\frac{1}{2}\sum_{k,l=1}^{n}\sum_{\xi,\eta=1}^{\upsilon}(\boldsymbol{R}^k - \boldsymbol{R}^l)\otimes\overset{k\xi}{\boldsymbol{f}}{}^{l\eta}_1\delta(\boldsymbol{R}^k - \boldsymbol{x})\delta(\Delta\boldsymbol{r}^{k\xi} - \boldsymbol{y}^\alpha)\right\rangle,$$
$$(\bar{\tau}^\alpha_{\text{pot}})^0 = -\left\langle\frac{1}{2}\sum_{k,l=1}^{n}\sum_{\xi,\eta=1}^{\upsilon}(\Delta\boldsymbol{r}^{k\xi} - \Delta\boldsymbol{r}^{l\eta})\otimes\overset{k\xi}{\boldsymbol{f}}{}^{l\beta}_1\delta(\boldsymbol{R}^k - \boldsymbol{x})\delta(\Delta\boldsymbol{r}^{k\xi} - \boldsymbol{y}^\alpha)\right\rangle$$
$$-\left\langle\frac{1}{2}\sum_{k=1}^{n}\sum_{\xi,\eta=1}^{\upsilon}(\Delta\boldsymbol{r}^{k\xi} - \Delta\boldsymbol{r}^{k\eta})\otimes\overset{k\xi}{\boldsymbol{f}}{}^{k\eta}_2\delta(\boldsymbol{R}^k - \boldsymbol{x})\delta(\Delta\boldsymbol{r}^{k\xi} - \boldsymbol{y}^\alpha)\right\rangle.$$

Note that the sum of zeroth momentum flux, $(\bar{\boldsymbol{t}}^\alpha_{\text{pot}})^0 + (\bar{\tau}^\alpha_{\text{pot}})^0$, is the atomic virial stress. Using the expressions for interatomic forces, $(\bar{\boldsymbol{t}}^\alpha_{\text{pot}})^0$ and $(\bar{\tau}^\alpha_{\text{pot}})^0$ can be expressed as

$$\big(\bar{\boldsymbol{t}}^\alpha_{\text{pot}}(\boldsymbol{x},t)\big)^0 = \frac{1}{2(\Delta V)^2}\int_{V(\boldsymbol{x}')}\sum_{\beta=1}^{\upsilon}G\big(d^{\alpha\beta}\big)(\boldsymbol{x}-\boldsymbol{x}')\otimes\boldsymbol{d}^{\alpha\beta}dV(\boldsymbol{x}'), \tag{4–1}$$

$$\big(\bar{\tau}^\alpha_{\text{pot}}(\boldsymbol{x},t)\big)^0 = \frac{1}{2(\Delta V)^2}\int_{V(\boldsymbol{x}')}\sum_{\beta=1}^{\upsilon}G\big(d^{\alpha\beta}\big)\boldsymbol{y}^{\alpha\beta'}\otimes\boldsymbol{d}^{\alpha\beta}dV(\boldsymbol{x}')$$
$$+\frac{1}{\Delta V}\sum_{\beta=1}^{\upsilon}G\big(y^{\alpha\beta}\big)\boldsymbol{y}^{\alpha\beta}\otimes\boldsymbol{y}^{\alpha\beta}, \tag{4–2}$$

and the first order terms as

$$\left(\bar{\boldsymbol{t}}^{\alpha}_{\text{pot}}(\boldsymbol{x},t)\right)^1 = \frac{1}{4}\nabla_x\cdot\left(\frac{1}{(\Delta V)^2}\int_{V(\boldsymbol{x}')}(\boldsymbol{x}-\boldsymbol{x}')\sum_{\beta=1}^{\upsilon}G(d^{\alpha\beta})(\boldsymbol{x}-\boldsymbol{x}')\otimes\boldsymbol{d}^{\alpha\beta}dV(\boldsymbol{x}')\right)$$
$$+\frac{1}{4}\nabla_{y^\alpha}\cdot\left(\frac{1}{(\Delta V)^2}\int_{V(\boldsymbol{x}')}\sum_{\beta=1}^{\upsilon}\boldsymbol{y}^{\alpha\beta'}G(d^{\alpha\beta})(\boldsymbol{x}-\boldsymbol{x}')\otimes\boldsymbol{d}^{\alpha\beta}dV(\boldsymbol{x}')\right), \quad (4\text{–}3)$$

$$\left(\bar{\tau}^{\alpha}_{\text{pot}}(\boldsymbol{x},t)\right)^1 = \frac{1}{4}\nabla_{\boldsymbol{x}}\cdot\left(\frac{1}{(\Delta V)^2}\int_{V(\boldsymbol{x}')}(\boldsymbol{x}-\boldsymbol{x}')\sum_{\beta=1}^{\upsilon}G(d^{\alpha\beta})\boldsymbol{y}^{\alpha\beta'}\otimes\boldsymbol{d}^{\alpha\beta}dV(\boldsymbol{x}')\right)$$
$$+\frac{1}{4}\nabla_{y^\alpha}\cdot\left(\frac{1}{(\Delta V)^2}\int_{V(\boldsymbol{x}')}\sum_{\beta=1}^{\upsilon}\boldsymbol{y}^{\alpha\beta'}G(d^{\alpha\beta})\boldsymbol{y}^{\alpha\beta'}\otimes\boldsymbol{d}^{\alpha\beta}dV(\boldsymbol{x}')\right)$$
$$+\frac{1}{4}\nabla_{y^\alpha}\cdot\left(\frac{1}{\Delta V}\sum_{\beta=1}^{\upsilon}\boldsymbol{y}^{\alpha\beta}G(y^{\alpha\beta})\boldsymbol{y}^{\alpha\beta}\otimes\boldsymbol{y}^{\alpha\beta}\right), \quad (4\text{–}4)$$

where

$$\boldsymbol{d}^{\alpha\beta}(\boldsymbol{x},\boldsymbol{x}') \equiv \boldsymbol{x}_o+\boldsymbol{u}(\boldsymbol{x})+\boldsymbol{y}^{\alpha}_o+\xi(\boldsymbol{x},\alpha)-\left(\boldsymbol{x}'_o+\boldsymbol{u}(\boldsymbol{x}')+\boldsymbol{y}^{\beta}_o+\xi(\boldsymbol{x}',\beta)\right),$$
$$\boldsymbol{y}^{\alpha\beta} \equiv \boldsymbol{y}^{\alpha}-\boldsymbol{y}^{\beta}=\boldsymbol{y}^{\alpha}_o+\xi^{\alpha}(\boldsymbol{x})-\left(\boldsymbol{y}^{\beta}_o+\xi^{\beta}(\boldsymbol{x})\right),$$
$$\boldsymbol{y}^{\alpha\beta'} \equiv \boldsymbol{y}^{\alpha}-\boldsymbol{y}'^{\beta}=\boldsymbol{y}^{\alpha}_o+\xi^{\alpha}(\boldsymbol{x})-\left(\boldsymbol{y}^{\beta}_o+\xi^{\beta}(\boldsymbol{x}')\right),$$
$$d^{\alpha\beta} \equiv \left|\boldsymbol{d}^{\alpha\beta}\right|,$$
$$y^{\alpha\beta} \equiv \left|\boldsymbol{y}^{\alpha\beta}\right|.$$

Equations (4–1)–(4–4) are the zeroth and the first order *nonlinear nonlocal constitutive relations for the potential momentum flux density*. The independent variables are the lattice displacement $\boldsymbol{u}(\boldsymbol{x},t)$ and the relative atomic displacements $\xi(\boldsymbol{x},\alpha,t)\stackrel{\Delta}{=}\xi^{\alpha}(\boldsymbol{x},t)$.

4.3. ***Linear local momentum flux density.*** To derive the linear constitutive relations for the potential momentum flux density one may make the assumption of infinitesimal deformation, namely, $d^{\alpha\beta}-d^{\alpha\beta}_o\to 0$. Therefore, the internal atomic force density can be written as

$$\boldsymbol{f}^{\alpha}_{\text{int}}(\boldsymbol{x}) \approx \frac{1}{(\Delta V)^2}\int_{V(\boldsymbol{x}')}\sum_{\beta=1}^{\nu}\left(\boldsymbol{c}^{\alpha\beta}_o(\boldsymbol{x}_0,\boldsymbol{x}'_0)+c^{\alpha\beta}_1(\boldsymbol{x}_0,\boldsymbol{x}'_0)\left(\boldsymbol{d}^{\alpha\beta}-\mathbf{d}^{\alpha\beta}_o\right)\right)dV(\boldsymbol{x}'),$$

where $\boldsymbol{d}^{\alpha\beta}_0=\boldsymbol{d}^{\alpha\beta}(\boldsymbol{x}_0,\boldsymbol{x}'_0)$ is the separate vector between two ground-state atoms, and $\boldsymbol{c}^{\alpha\beta}_o(\boldsymbol{x}_0,\boldsymbol{x}'_0)=c^{\alpha\beta}_1\boldsymbol{d}^{\alpha\beta}_o$ and $c^{\alpha\beta}_1$ are the interatomic force constants which can be computed from quantum mechanics and are functions of the type of atoms in

question as well as their separation. For the sake of simplicity, one may write

$$c_{0,1}^{\alpha\beta'} = c_{0,1}^{\alpha\beta}(\boldsymbol{x}_0, \boldsymbol{x}_0'), \qquad c_{0,1}^{\alpha\beta} = c_{0,1}^{\alpha\beta}(\boldsymbol{x}_0, \boldsymbol{x}_0).$$

Using linearized atomic force, Equations (4–1)–(4–4) become

$$\left(\bar{\boldsymbol{t}}_{\text{pot}}^{\alpha}(\boldsymbol{x}, t)\right)^0 = \frac{1}{2(\Delta V)^2}\int_{V(\boldsymbol{x}')}\sum_{\beta=1}^{\upsilon}(\boldsymbol{x}-\boldsymbol{x}')\otimes\left(\boldsymbol{c}_o^{\alpha\beta'} + c_1^{\alpha\beta'}(\boldsymbol{d}^{\alpha\beta} - \boldsymbol{d}_o^{\alpha\beta})\right)dV(\boldsymbol{x}'),$$

$$\begin{aligned}\left(\bar{\boldsymbol{t}}_{\text{pot}}^{\alpha}(\boldsymbol{x}, t)\right)^1 = {}& \frac{1}{4(\Delta V)^2}\nabla_x\cdot\int_{V(\boldsymbol{x}')}\sum_{\beta=1}^{\upsilon}(\boldsymbol{x}-\boldsymbol{x}')(\boldsymbol{x}-\boldsymbol{x}') \\ & \otimes\left(\boldsymbol{c}_o^{\alpha\beta'} + c_1^{\alpha\beta'}(\boldsymbol{d}^{\alpha\beta} - \mathbf{d}_o^{\alpha\beta})\right)dV(\boldsymbol{x}') \\ & + \frac{1}{4(\Delta V)^2}\nabla_{y^\alpha}\cdot\int_{V(\boldsymbol{x}')}\sum_{\beta=1}^{\upsilon}\boldsymbol{y}^{\alpha\beta'}(\boldsymbol{x}-\boldsymbol{x}') \\ & \otimes\left(\boldsymbol{c}_o^{\alpha\beta'} + c_1^{\alpha\beta'}(\boldsymbol{d}^{\alpha\beta} - \mathbf{d}_o^{\alpha\beta})\right)dV(\boldsymbol{x}'),\end{aligned}$$

$$\begin{aligned}\left(\bar{\tau}_{\text{pot}}^{\alpha}(\boldsymbol{x}, t)\right)^0 = {}& \frac{1}{2(\Delta V)^2}\int_{V(\boldsymbol{x}')}\sum_{\beta=1}^{\upsilon}\boldsymbol{y}^{\alpha\beta'}\otimes\left(\boldsymbol{c}_o^{\alpha\beta'} + c_1^{\alpha\beta'}(\boldsymbol{d}^{\alpha\beta} - \mathbf{d}_o^{\alpha\beta})\right)dV(\boldsymbol{x}') \\ & + \frac{1}{2\Delta V}\sum_{\beta=1}^{\upsilon}\boldsymbol{y}^{\alpha\beta}\otimes\left(\boldsymbol{c}_o^{\alpha\beta} + c_1^{\alpha\beta}(\boldsymbol{y}^{\alpha\beta} - \boldsymbol{y}_o^{\alpha\beta})\right),\end{aligned}$$

$$\begin{aligned}\left(\bar{\tau}_{\text{pot}}^{\alpha}(\boldsymbol{x}, t)\right)^1 = {}& \frac{1}{4(\Delta V)^2}\nabla_{\boldsymbol{x}}\cdot\int_{V(\boldsymbol{x}')}(\boldsymbol{x}-\boldsymbol{x}')\sum_{\beta=1}^{\upsilon}\boldsymbol{y}^{\alpha\beta'}\otimes\left(\boldsymbol{c}_o^{\alpha\beta'} + c_1^{\alpha\beta'}(\boldsymbol{d}^{\alpha\beta} - \mathbf{d}_o^{\alpha\beta})\right)dV(\boldsymbol{x}') \\ & + \frac{1}{4(\Delta V)^2}\nabla_{y^\alpha}\cdot\int_{V(\boldsymbol{x}')}\sum_{\beta=1}^{\upsilon}\boldsymbol{y}^{\alpha\beta'}\boldsymbol{y}^{\alpha\beta'}\otimes\left(\boldsymbol{c}_o^{\alpha\beta'} + c_1^{\alpha\beta'}(\boldsymbol{d}^{\alpha\beta} - \mathbf{d}_o^{\alpha\beta})\right)dV(\boldsymbol{x}') \\ & + \frac{1}{4(\Delta V)}\nabla_{y^\alpha}\cdot\sum_{\beta=1}^{\upsilon}\boldsymbol{y}^{\alpha\beta}\boldsymbol{y}^{\alpha\beta}\otimes\left(\boldsymbol{c}_o^{\alpha\beta} + c_1^{\alpha\beta}(\boldsymbol{y}^{\alpha\beta} - \mathbf{y}_o^{\alpha\beta})\right).\end{aligned}$$

Note that material properties should make the ground state stresses vanish: $\bar{\boldsymbol{t}}_{\text{pot}}^{\alpha}(0) = \bar{\tau}_{\text{pot}}^{\alpha}(0) = 0$. Hence, the expressions for potential momentum flux in the ground state

$$\bar{\boldsymbol{t}}_{\text{pot}}^{\alpha}(0) = \frac{1}{2(\Delta V)^2}\int_{V(\boldsymbol{x}')}\sum_{\beta=1}^{\upsilon}\left(\boldsymbol{x}_o - \boldsymbol{x}_o'\right)\otimes\boldsymbol{c}_o^{\alpha\beta'}dV(\boldsymbol{x}'),$$

$$\bar{\tau}_{\text{pot}}^{\alpha}(0) = \frac{1}{2(\Delta V)^2}\int_{V(\boldsymbol{x}')}\sum_{\beta=1}^{\upsilon}\boldsymbol{y}_o^{\alpha\beta}\otimes\boldsymbol{c}_o^{\alpha\beta'}dV(\boldsymbol{x}') + \frac{1}{\Delta V}\sum_{\beta=1}^{\upsilon}\boldsymbol{y}_o^{\alpha\beta}\otimes\boldsymbol{c}_o^{\alpha\beta},$$

can be used for validation once the material parameters $\boldsymbol{c}_0^{\alpha\beta'}$, $\boldsymbol{c}_0^{\alpha\beta}$ and the ground state structural parameters $\boldsymbol{x}_o$ and $\boldsymbol{y}_o^{\alpha\beta}$ are obtained from quantum mechanical calculations.

If one further neglects nonlocal effects considering only the interactions between unit cells in a close neighborhood, one then has

$$\begin{aligned}
\boldsymbol{u}(\boldsymbol{x}) - \boldsymbol{u}(\boldsymbol{x}') &\approx \boldsymbol{u}_{,\boldsymbol{x}} \cdot (\boldsymbol{x}_o - \boldsymbol{x}'_0),\\
\xi(\boldsymbol{x}, \beta) - \xi(\boldsymbol{x}', \beta) &\approx \xi^{\beta}_{,\boldsymbol{x}} \cdot \left(\boldsymbol{x}_o - \boldsymbol{x}'_0\right),\\
\xi(\boldsymbol{x}, \alpha) - \xi(\boldsymbol{x}, \beta) &\triangleq \gamma^{\alpha\beta} \cdot \left(\boldsymbol{y}_o^{\alpha} - \boldsymbol{y}_o^{\beta}\right),
\end{aligned}$$

and hence

$$\left(\boldsymbol{x} - \boldsymbol{x}'\right) - \left(\boldsymbol{x}_o - \boldsymbol{x}'_o\right) = \boldsymbol{u}(\boldsymbol{x}) - \boldsymbol{u}(\boldsymbol{x}') \approx \boldsymbol{u}_{,\boldsymbol{x}} \cdot \left(\boldsymbol{x}_o - \boldsymbol{x}'_0\right), \tag{4–5}$$

$$\left(\boldsymbol{y}^{\alpha} - \boldsymbol{y}^{\beta}\right) - \left(\boldsymbol{y}_0^{\alpha} - \boldsymbol{y}_0^{\beta}\right) = \xi(\boldsymbol{x}, \alpha) - \xi(\boldsymbol{x}, \beta) \triangleq \gamma^{\alpha\beta} \cdot \left(\boldsymbol{y}_o^{\alpha} - \boldsymbol{y}_o^{\beta}\right), \tag{4–6}$$

$$\begin{aligned}
\left(\boldsymbol{y}^{\alpha} - \boldsymbol{y}'^{\beta}\right) - \left(\boldsymbol{y}_0^{\alpha} - \boldsymbol{y}'^{\beta}_0\right) &= \xi(\boldsymbol{x}, \alpha) - \xi(\boldsymbol{x}', \beta)\\
&= \xi(\boldsymbol{x}, \alpha) - \xi(\boldsymbol{x}, \beta) + \xi(\boldsymbol{x}, \beta) - \xi(\boldsymbol{x}', \beta)\\
&\approx \gamma^{\alpha\beta} \cdot \left(\boldsymbol{y}_o^{\alpha} - \boldsymbol{y}_o^{\beta}\right) + \xi^{\beta}_{,\boldsymbol{x}} \cdot \left(\boldsymbol{x}_o - \boldsymbol{x}'_0\right),
\end{aligned} \tag{4–7}$$

$$\boldsymbol{d}^{\alpha\beta} - \boldsymbol{d}_0^{\alpha\beta} \approx \left(\boldsymbol{u}_{,\mathbf{x}} + \xi^{\beta}_{,\boldsymbol{x}}\right) \cdot \left(\boldsymbol{x}_o - \boldsymbol{x}'_0\right) + \gamma^{\alpha\beta} \cdot \left(\boldsymbol{y}_o^{\alpha} - \boldsymbol{y}_o^{\beta}\right). \tag{4–8}$$

The zeroth order linear local potential momentum flux density can be then expressed as

$$\bar{\boldsymbol{t}}^{\alpha}(\boldsymbol{x}, t) = -\gamma_1 T^{\alpha} \boldsymbol{I} + \sum_{\beta=1}^{\upsilon} \left(\boldsymbol{A}^1 : \boldsymbol{u}_{,\boldsymbol{x}} + \boldsymbol{A}^2 : \gamma^{\alpha\beta} + \boldsymbol{A}^3 : \xi^{\beta}_{,\boldsymbol{x}}\right), \tag{4–9}$$

$$\bar{\tau}^{\alpha}(\boldsymbol{x}, t) = -\gamma_2 T^{\alpha} \boldsymbol{I} + \sum_{\beta=1}^{\upsilon} \left(\boldsymbol{B}^1 : \boldsymbol{u}_{,\boldsymbol{x}} + \boldsymbol{B}^2 : \gamma^{\alpha\beta} + \boldsymbol{B}^3 : \xi^{\beta}_{,\boldsymbol{x}}\right). \tag{4–10}$$

Here $(\boldsymbol{A} : \boldsymbol{B})_{ijk\ldots lmn} = A_{ijk\ldots pq} B_{pq\ldots lmn}$.

Note that $\boldsymbol{d}_o^{\alpha\beta}$, $\boldsymbol{x}_o - \boldsymbol{x}'_o$, and $\boldsymbol{y}_o^{\alpha\beta} = \boldsymbol{y}_o^{\alpha} - \boldsymbol{y}_o^{\beta}$ are material constants, while $\boldsymbol{d}^{\alpha\beta}$, $\boldsymbol{x} - \boldsymbol{x}'$ and $\boldsymbol{y}^{\alpha} - \boldsymbol{y}^{\beta}$ are up to first order in $\boldsymbol{u}_{,\boldsymbol{x}}$, $\xi^{\beta}_{,\boldsymbol{x}}$, and $\gamma^{\alpha\beta}$. Using Equations (4–5)–(4–8) one can find that the first order terms of momentum flux density are the strain gradient terms. Therefore, Equations (4–9) and (4–10) represent the linear local form of zeroth order homogeneous and inhomogeneous momentum flux density, and the sum of the two is the field representation of atomic virial

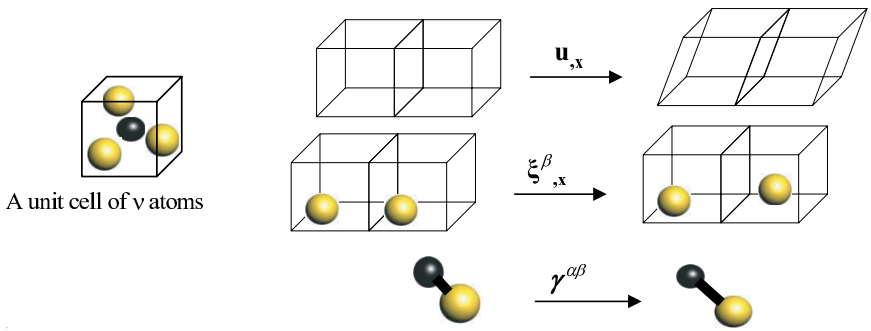

Figure 5. Illustration of strain measures in the formulated field theory.

stress. One can also write them in tensor notation as:

$$\bar{t}^{\alpha}_{mn}(\boldsymbol{x},t) = -\gamma_1^{\delta_{mn}} T^{\alpha} + \sum_{\beta=1}^{\upsilon} \left(A^1_{mnpq}\varepsilon^1_{pq} + A^2_{mnpq}\varepsilon^2_{pq} + A^3_{mnpq}\varepsilon^3_{pq} \right),$$

$$\bar{\tau}^{\alpha}_{mn}(\boldsymbol{x},t) = -\gamma_2^{\delta_{mn}} T^{\alpha} + \sum_{\beta=1}^{\upsilon} \left(B^1_{mnpq}\varepsilon^1_{pq} + B^2_{mnpq}\varepsilon^2_{pq} + B^3_{mnpq}\varepsilon^3_{pq} \right),$$

where

$$\varepsilon^1_{pq} = u_{p,q}, \qquad \varepsilon^2_{pq} = \gamma^{\alpha\beta}_{pq}, \qquad \varepsilon^3_{pq} = \xi^{\beta}_{p,q}, \tag{4–11}$$

and

$$A^{i=1,2,3}_{mnpq}, \qquad B^{i=1,2,3}_{mnpq}$$

are material constants which can be expressed in terms of ground state structural parameters $\boldsymbol{x}_o - \boldsymbol{x}'_0$, $\boldsymbol{y}^{\alpha}_o - \boldsymbol{y}^{\beta}_o$ and a material parameter $c_1^{\alpha\beta}$.

4.4. ***Strain measures.*** The field representation of momentum flux involves temperature, lattice deformation and relative atomic deformation. The linear local forms of momentum flux are expressed in terms of temperature and lattice strain $\boldsymbol{u}_{,\boldsymbol{x}}(\boldsymbol{x})$, relative atomic strain $\xi^{\beta}_{,\boldsymbol{x}}(\boldsymbol{x})$, and atomic-bond strain $\gamma^{\alpha\beta}(\boldsymbol{x})$. They are the lattice deformation gradient, relative atomic deformation gradient and relative atomic-bond stretch, and can be illustrated through Figure 5.

5. Numerical examples

For the purpose of numerical validation, a periodic solid under simple tension is modeled and simulated. Stress and strain relations are computed based on the formulas derived in this paper and by atomic-level molecular dynamics simulation (MD) as well. The general-purpose parallel MD simulation code DL-POLY is employed [Smith and Forester 2001] to perform the simulation. The modeling of simple tension is achieved through NVT ensemble.

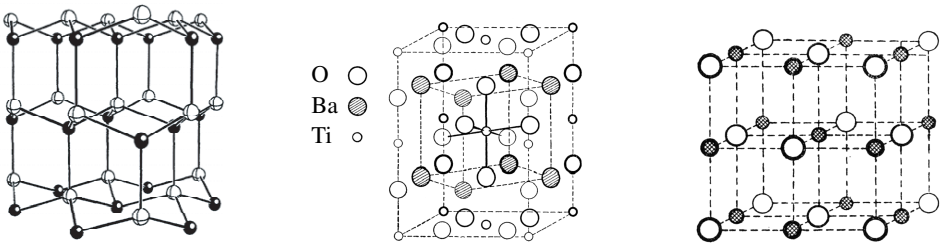

(a) ZnO (wurtzite) (b) $BaTiO_3$ (perovskite, cubic phase) (c) MgO (rock salt)

Figure 6. Crystal structure of zinc oxide, barium titanate, and magnesium oxide.

Three single crystalline materials are considered in this paper. Among them, piezoelectric and semiconductor material Zinc Oxide, ZnO, is wurtzite structured with lattice constants $a = 3.249$ Å and $c = 5.206$ Å, ferroelectric material Barium Titanate, $BaTiO_3$ is in its cubic phase with the lattice constant $a = 3.943$ Å, and MgO, the standard test-bed material for the evaluation of theoretical methods to calculate some mechanical properties, has a rock salt structure with the lattice constant $a = 4.2$ Å. The Coulomb and Buckingham interatomic potentials are employed for the MD simulation, and the material parameters are taken from [Catlow 1986; Grimes 1994; McCoy et al. 1997a; 1997b; Grimes et al. 1995; Chen et al. 1997].

Under uniform simple tension loading, there are no strain gradients, and hence only the zeroth momentum flux exists. Thus, the formula for the total stress reduces to the zeroth order momentum flux, $(\bar{\boldsymbol{t}}^{\alpha}_{\text{pot}})^0 + (\bar{\tau}^{\alpha}_{\text{pot}})^0$, which is identical to the atomic virial stress.

The numerical results of the stress-strain relations before the onset of structure stability (phase transition) by the formulation and DL-POLY are plotted in Figure 7. A good agreement between the results from the formulation and from the DL-POLY simulation is found, while the computational time ratio between these two methods is about 1 to 10^4. Although the analytical stress-strain relation is nonlinear and nonlocal, surprisingly the numerical results indicate that the stress-strain relation is quite linear until structural transformation.

6. Summary and discussion

The field representation of momentum flux density is formulated in this paper within the framework of atomic N-body dynamics. Three strain measures and the momentum flux density–strain relations are obtained. Major considerations and conclusions regarding the formulation may be summarized as follows:

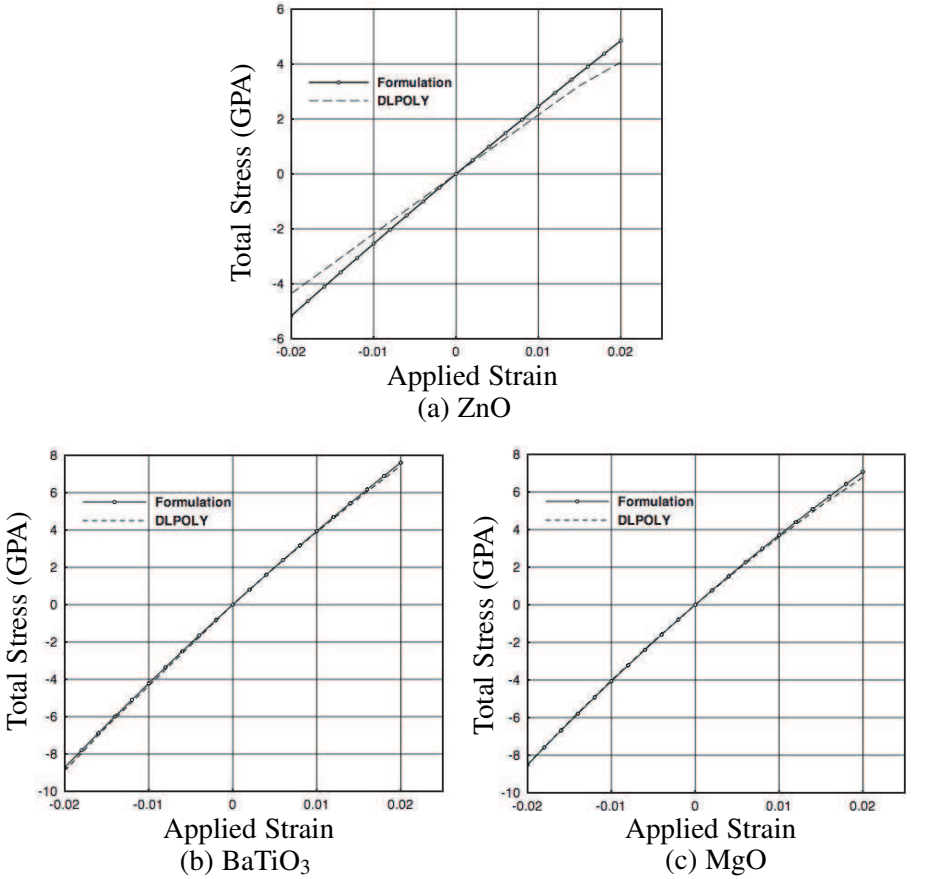

Figure 7. Stress-strain relation of zinc oxide (a), barium titanate (b), and magnesium oxide (c) by the formulation and by molecular dynamics simulation code DL-POLY.

(1) The momentum flux formulated in this paper exactly represents the momentum flux in an atomic N-body dynamics model. Both the atomic-level momentum flux and the atomic displacements can be fully represented in terms of field variables: temperature, lattice deformation and relative atomic deformation. All material constants involved can be obtained through the atomistic formulation.

(2) This paper has shown that the stress in the conventional continuum description is not the momentum flux density in an atomic N-body dynamics model; it is only the homogeneous part of momentum flux density summing over at least the volume of a primitive unit cell. Decomposing the momentum flux into homogeneous and inhomogeneous parts, one can establish the connection

between the atomic momentum flux density and the continuum stress, and obtain the field representation of conservation equations on the atomic scale [Chen and Lee 2006].

(3) The formulations have shown that the momentum flux density-strain relation, which may be referred to as atomic stress-strain relation, is nonlinear and nonlocal in displacements, and involves higher order gradients. In the case of homogeneous strain so that no strain gradients exist, the formula for total stress shall be identical to the virial theorem. Or, if the average stress of a whole specimen is concerned, then the total stress formula shall also be identical to the virial theorem.

(4) The three strain measures are obtained for the linear local constitutive relation. One may prove that the nonlinear nonlocal relation can also be expressed in terms of the temperature and the three strain measures.

(5) The numerical examples in this paper, although quite preliminary, show that the stress-strain relation under uniform loading is linear until structural instability.

Appendix

Define

$$\delta(\lambda; k, l, \xi, \eta, \alpha) \equiv \delta\big(\boldsymbol{R}^k\lambda + \boldsymbol{R}^l(1-\lambda) - \boldsymbol{x}\big)\delta\big(\Delta\boldsymbol{r}^{k\xi}\lambda + \Delta\boldsymbol{r}^{l\eta}(1-\lambda) - \boldsymbol{y}^\alpha\big) \stackrel{\Delta}{=} \delta(\lambda),$$

$$\Delta(k, \xi, \alpha) \equiv \delta\big(\boldsymbol{R}^k - \boldsymbol{x}\big)\delta\big(\Delta\boldsymbol{r}^{k\xi} - \boldsymbol{y}^\alpha\big) \stackrel{\Delta}{=} \Delta = \delta(1),$$

$$A \equiv \big(\boldsymbol{R}^k - \boldsymbol{R}^l\big)\cdot\nabla_{\boldsymbol{x}},$$

$$B \equiv \big(\Delta\boldsymbol{r}^{k\xi} - \Delta\boldsymbol{r}^{l\eta}\big)\cdot\nabla_{\boldsymbol{y}^\alpha}.$$

It is readily verified that

$$\frac{d\delta}{d\lambda} = -(A+B)\delta,$$

$$d\delta = -(A+B)\delta d\lambda,$$

$$\int_0^1 \lambda\frac{d\delta}{d\lambda}d\lambda = \int_0^1 \lambda d\delta = \lambda\delta\big|_0^1 - \int_0^1 \delta d\lambda = \delta(1) - \int_0^1 \delta d\lambda,$$

$$\int_0^1 \delta d\lambda = \Delta + (A+B)\int_0^1 \lambda\delta d\lambda,$$

$$\int_0^1 \lambda^n d\delta = \Delta - n\int_0^1 \lambda^{n-1}\delta d\lambda,$$

which gives

$$\int_0^1 \lambda^{n-1}\delta d\lambda = \frac{\Delta}{n} + \frac{1}{n}(A+B)\int_0^1 \lambda^n \delta d\lambda.$$

One may then prove that

$$\begin{aligned}\int_0^1 \delta d\lambda &= \Delta + (A+B)\int_0^1 \lambda\delta\, d\lambda \\ &= \Delta + (A+B)\left(\frac{\Delta}{2} + \frac{1}{2}(A+B)\int_0^1 \lambda^2\delta\, d\lambda\right) \\ &= \Delta + \frac{1}{2}(A+B)\Delta + \frac{1}{2}(A+B)^2\int_0^1 \lambda^2\delta\, d\lambda \\ &= \cdots = \sum_{n=1}^{\infty}\frac{1}{n!}(A+B)^{n-1}\Delta,\end{aligned}$$

or, in other words,

$$\begin{aligned}&\int_0^1 \delta\big(\boldsymbol{R}^k\lambda+\boldsymbol{R}^l(1-\lambda)-\boldsymbol{x}\big)\delta\big(\Delta\boldsymbol{r}^{k\xi}\lambda+\Delta\boldsymbol{r}^{l\eta}(1-\lambda)-\boldsymbol{y}^{\alpha}\big)d\lambda \\ &\qquad = \sum_{m=1}^{\infty}\frac{1}{m!}\big((\boldsymbol{R}^k-\boldsymbol{R}^l)\cdot\nabla_{\boldsymbol{x}}+(\Delta\boldsymbol{r}^{k\xi}-\Delta\boldsymbol{r}^{l\eta})\cdot\nabla_{\boldsymbol{y}^{\alpha}}\big)^{m-1}\delta(\boldsymbol{R}^k-\boldsymbol{x})\delta(\Delta\boldsymbol{r}^{k\xi}-\boldsymbol{y}^{\alpha}),\end{aligned}$$

$$\int_0^1 \delta\big(\boldsymbol{R}^k\lambda+\boldsymbol{R}^l(1-\lambda)-\boldsymbol{x}\big)d\lambda = \sum_{m=1}^{\infty}\frac{1}{m!}\big((\boldsymbol{R}^k-\boldsymbol{R}^l)\cdot\nabla_{\boldsymbol{x}}\big)^{m-1}\delta(\boldsymbol{R}^k-\boldsymbol{x}).$$

References

[Born et al. 1926] M. Born, W. Heisenberg, and P. Jordan, "On quantum mechanics II", *Z. Phys.* **35**:8–9 (1926), 557–615.

[Catlow 1986] C. R. A. Catlow, "Computer simulation studies of transport in solids", *Annu. Rev. Mater. Sci.* **16** (1986), 517–548.

[Chen and Lee 2003a] Y. Chen and J. D. Lee, "Connecting molecular dynamics to micromorphic theory, I: Instantaneous and averaged mechanical variables", *Physica A* **322** (2003), 359–376.

[Chen and Lee 2003b] Y. Chen and J. D. Lee, "Connecting molecular dynamics to micromorphic theory, II: Balance laws", *Physica A* **322** (2003), 377–392.

[Chen and Lee 2006] Y. Chen and J. D. Lee, "Conservation laws at nano/micro scales", *J. Mech. Mater. Struct.* **1** (2006), 681–704.

[Chen et al. 1997] S. P. Chen, M. Yan, R. W. Grimes, and S. Vyas, "Energies and configurations of defects in Ga, Cr and in doped CoO", *Ceram. Trans.* **69** (1997), 129–134.

[Cosserat and Cosserat 1909] E. Cosserat and F. Cosserat, *Théorie des corps déformables*, Hermann, Paris, 1909.

[Eringen 1967] A. C. Eringen, "Theory of micropolar continua", pp. 23–40 in *Proceedings of the Ninth Midwestern Mechanics Conference* (Madison, WI, 1965), edited by T. C. Huang and J. M. W. Johnson, Developments in Mechanics **III/1**, Wiley, New York, 1967.

[Eringen 1999] A. C. Eringen, *Microcontinuum field theories, I: Foundations and solids*, Springer, New York, 1999. MR 2000i:74007

[Eringen and Suhubi 1964] A. C. Eringen and E. S. Suhubi, "Nonlinear theory of simple micro-elastic solids, I", *Int. J. Eng. Sci.* **2**:2 (1964), 189–203. MR 29 #6672

[Green and Rivlin 1964] A. E. Green and R. S. Rivlin, "Multipolar continuum mechanics", *Arch. Ration. Mech. An.* **17**:2 (1964), 113–147. MR 31 #6415

[Grimes 1994] R. W. Grimes, "Solution of MgO, CaO and TiO_2 in α-Al_2O_3", *J. Am. Ceram. Soc.* **77**:2 (1994), 378–384.

[Grimes et al. 1995] R. W. Grimes, D. J. Binks, and A. B. Lidiard, "The extent of zinc oxide solution in zinc chromate spinel", *Philos. Mag. A* **72** (1995), 651–668.

[Hoover 1986] W. G. Hoover, *Molecular dynamics*, Springer, Berlin, 1986.

[Hoover 1991] W. G. Hoover, *Computational statistical mechanics*, Elsevier, Amsterdam, 1991.

[Horstemeyer and Baskes 1999] M. F. Horstemeyer and M. I. Baskes, "Atomic finite deformation simulations: A discussion on length scale effects in relation to mechanical stresses", *J. Eng. Mater. Technol. (Trans. ASME)* **121** (1999), 114–119.

[McCoy et al. 1997a] M. A. McCoy, R. W. Grimes, and W. E. Lee, "Phase stability and interfacial structures in the SrO-$SrTiO_3$ system", *Philos. Mag. A* **75** (1997), 833–846.

[McCoy et al. 1997b] M. A. McCoy, R. W. Grimes, and W. E. Lee, "Planar intergrowth structures in the ZnO-In_2O_3 system", *Philos. Mag. A* **76** (1997), 1187–1201.

[Mindlin 1964] R. D. Mindlin, "Micro-structure in linear elasticity", *Arch. Ration. Mech. An.* **16**:1 (1964), 51–78. MR 28 #3569

[Nielsen and Martin 1985] O. H. Nielsen and R. M. Martin, "Quantum-mechanical theory of stress and force", *Phys. Rev. B* **32**:6 (1985), 3780–3791.

[Nye 1957] J. F. Nye, *Physical properties of crystals*, Oxford University Press, Oxford, 1957.

[Smith and Forester 2001] W. Smith and T. R. Forester, *The DL-POLY User Manual*, CCLRC, Daresbury Laboratory, Daresbury, Warrington WA4 4AD, England, 2001.

[Sommerfeld 1950] A. Sommerfeld, *Mechanics of deformable bodies*, vol. II, Lectures on Theoretical Physics, Academic Press, New York, 1950. MR 11,700c

[Toupin 1962] R. A. Toupin, "Elastic materials with couple-stresses", *Arch. Ration. Mech. An.* **11**:1 (1962), 385–414. MR 26 #2056

Received 4 Dec 2005.

YOUPING CHEN: ypchen2@gwu.edu
Department of Mechanical and Aerospace Engineering, University of Florida, Gainesville, FL 32611, United States

JAMES LEE: jdlee@gwu.edu
The George Washington University, Academic Center T733, 801 22nd street, NW, Washington, DC 20052, United States

LIMING XIONG: xlm@gwu.edu
Department of Mechanical and Aerospace Engineering, University of Florida, Gainesville, FL 32611, United States

JOURNAL OF MECHANICS OF MATERIALS AND STRUCTURES
Vol. 1, No. 4, 2006

MEASURING IMPACT RESPONSES OF FOAMED POLYMERS

JAMES F. WILSON

A unique dual pendulum system was developed to measure single-impact compression responses of foamed polymers. The data, complemented with a mathematical model of impact, led to measures of the material's energy absorption, compression modulus, and damping. Results are presented for a class of open-celled foamed polymers specifically developed for shock mitigation. The experiments employed such materials of four different densities, with impact times ranging in the 1 to 5 ms range and mean impact stresses up to 160 $\mathrm{kN/m^2}$. The results for these materials showed: (1) energy losses of up to 50% of incident energy, with a peak energy absorption per unit volume of 18 $\mathrm{kJ/m^3}$; (2) peak compression modulus of 880 $\mathrm{kN/m^2}$ with strain rates approaching 200 $\mathrm{s^{-1}}$; (3) a mean damping factor of 0.258 with a standard deviation of 0.029. Such data are of practical importance in many shock-mitigating applications, including prostheses, floor pads and cushions, gloves for hand-held vibrating tools, grips for hockey sticks and tennis rackets, and soles for sports shoes.

Introduction

This design effort and experimental study was motivated by the need for a relatively simple and accurate experimental system to quantify single-impact responses of foamed polymers. Related studies involving repeated specimen loading have employed costly universal testing machines with sensor-controlled stress or strain, and magnetic shakers for forced harmonic motion of the specimen. Studies based on the these methods are presented in the treatise of Gibson and Ashby [2001], who reviewed the open literature up to 1999 on the properties and mathematical modeling of cellular solids, for both man-made foams and naturally occurring materials such as wood and cancerous bone. Measuring techniques and typical data for complex moduli, based on the forced oscillation method, were reviewed by Deverge and Jaouen [2004]. These sources and their extensive bibliographies did not reveal any experimental systems or impact analyses similar to those discussed here. No damping data were found in the open literature for one-time impact on foamed polymers.

Keywords: foamed polymers, impact response.

Specimen type	Specimen geometry		Static modulus	Mass density
	diameter, mm	thickness, mm	E, kN/m^2	kg/m^3
white	38.1	7.00	143.	370.
blue	38.1	6.40	373.	451.
red	38.1	5.30	336.	421.
black	38.1	4.86	377.	481.

Table 1. Geometric and physical properties of the foamed polymer specimens.

The characteristics that typify the foamed polymer studied herein are: linearly elastic behavior for static strains up to about 30%; an after-impact recovery time of about 30 s or less to the state of nearly zero strain (the initial state); and an open-celled microstructure in which there are small holes in the cell walls. This class of foamed polymer was developed in the late 1980s by an orthopedist and a New England material science laboratory. These materials are commercially available through Implus Footcare, Morrisville, NC. The material is particularly characterized by its capacity to absorb high levels of impact energy, and is thus used as padding for artificial limbs and for the insoles of sports shoes. Four different densities of these materials, designated by color, were evaluated in the present study. Some of their physical properties are listed in Table 1, together with the size of the impact specimens used.

Shown in Figure 1 are scanning electron micrographs of the most dense material (black), magnified 16 and 160 times. This foamed polymer has an average cell diameter of about 0.2 mm. The general shape of these cells closely matches those observed in the micrographs of a polyurethane foam for which the average cell diameter was also about 0.2 mm; see [Gibson and Ashby 2001, p. 178, Figure 5.2(g)]. This comparison suggests that the base material was a form of polyurethane. The properties of the base material such as density and chemical composition cannot be disclosed since they are patented and proprietary.

This presentation begins with a description of a unique dual-pendulum measuring system, which is followed by a mathematical model of impact that identifies the key parameters to be measured. The study concludes with extensive experimental results for the foamed polymers of Table 1: determinations of material impact energy loss, and the effects of impact stress level and strain rate on both material stiffness and impact-induced damping.

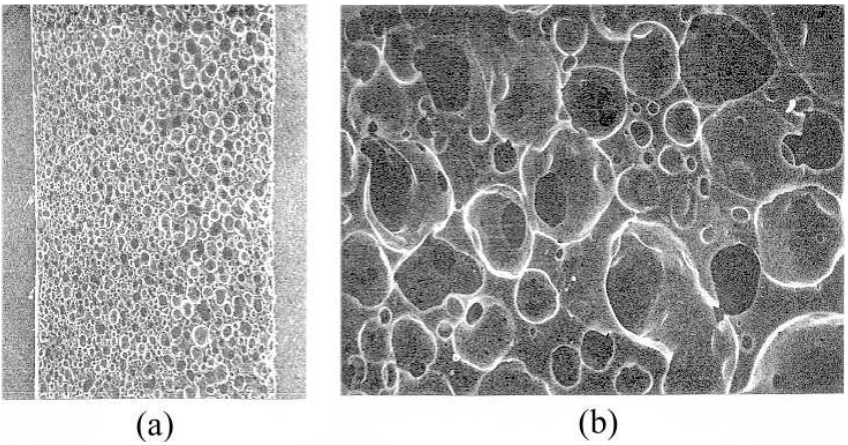

Figure 1. Scanning electron micrographs of the highest density (black) foamed polymer: (a) transverse section through a 4.85 mm thick mat, at 16×; (b) center of mat (a) at 160×. (Courtesy of George W. Pearsall, Duke University.)

Experimental system design

Shown in Figure 2 is the dual pendulum impact system: the driver pendulum and target pendulum, with the foamed polymer specimen of diameter D_0 and thickness h sandwiched between the two impacting die faces. The two pendula are identical. Each consists of a solid steel cylinder of the specimen diameter D_0, with a miniature accelerometer mounted coaxially. The total mass of the steel cylinder and the accelerometer is m, and this assembly is hereafter referred to as a pendulum die. Each steel pendulum arm of length ℓ is rigid or nearly so, and is affixed to the mass center of each die. This arm, together with its bearing shaft, has a mass which is less than one percent of m. The centers of the two arm pivot points are spaced so that the die separation distance is h, the thickness of the test specimen, when the pendula are hanging vertically and at rest. Each pendulum pivot point is the center for a protractor. With a pointer extension to each pendulum arm, the arm angle for a pendulum at rest can be read on its protractor to an accuracy of $\pm 0.1°$.

Shown in Figure 3 are the key positions of the pendula at which the arm angles are measured. The first positions represent the initial static states, in which the driver pendulum arm is hand-held at the visual protractor setting θ_0, and the target pendulum hangs vertically. The second positions are the maximum post-impact rebound angles θ_1 and θ_2 for the driver and target pendulum arms, respectively. These latter extreme rotations are measured either visually or electronically. In the

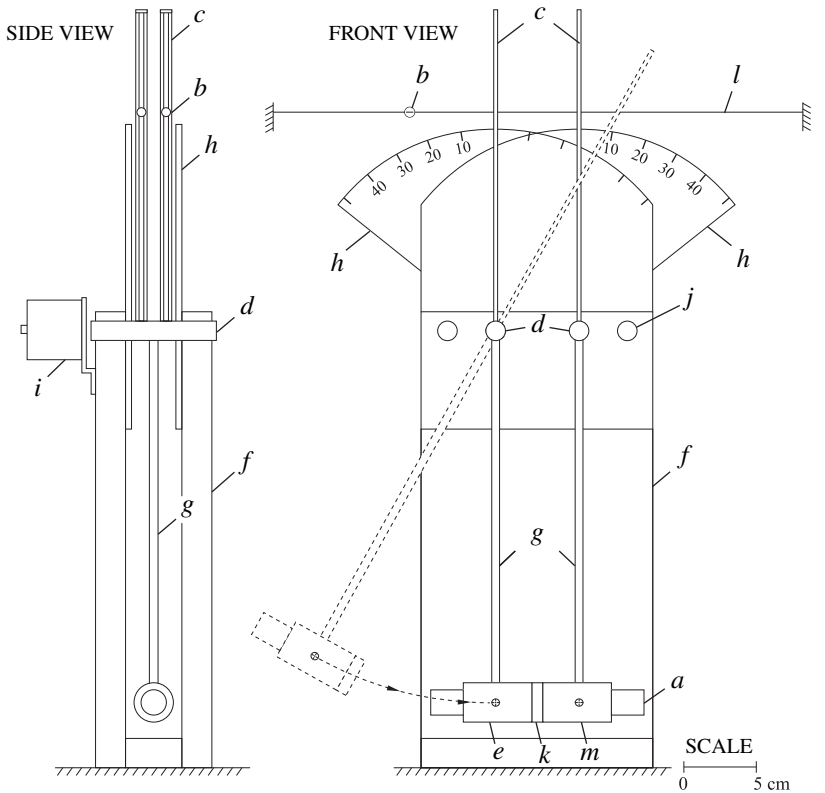

Figure 2. Mechanical design of the dual pendulum system. The components are: a – accelerometer; b – bead; c –steel slotted bead arm; d – steel bearing shaft; e – steel driver die; f – transparent plastic side pannel; g – steel pendulum arm; h – transparent plastic protractor; i – RVDT; j – steel spacer; k – foamed polymer specimen; l – string; m – steel target die.

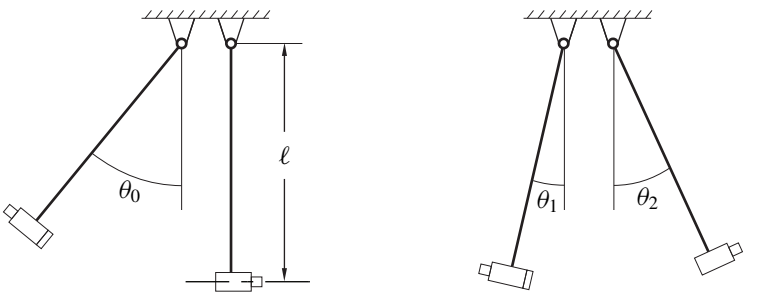

Figure 3. Initial pendulum configuration (left), and maximum rebound configuration (right).

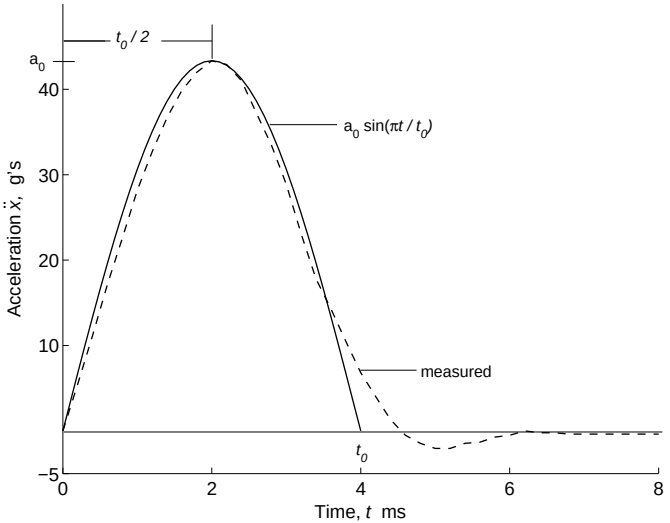

Figure 4. A typical measured acceleration-time history for the impacting driver pendulum, and its best-fit to a half sine curve.

visual method, an extension of the slotted pendulum arm, as shown in Figure 2, pushes a tiny bead along a taut horizontal string, one for each pendulum. There is just enough friction between each relatively weightless bead and string so that the bead does not overshoot its mark corresponding to the maximum arm angle θ_1 or θ_2. Later, when the pendula come to rest, these angles are read on the protractor by aligning the pointer extension with its bead. This visual method for measuring rebound angles gave results that were as accurate and reproducible as the electronic method that used two Schaevitz rotary variable differential transformers (RVDTs) attached to the rotating shafts, as shown in Figure 2. Each RVDT required a 5 volt AC power supply. The voltage output was proportional to rotation, with a sensitivity of 0.01V/degree. At impact, this voltage triggered a digitizing storage oscilloscope, which recorded the time history of rotation for each RVDT.

For each experiment, the driver pendulum was released at a predetermined angle θ_0, its accelerometer output voltage triggered a Hewlett Packard 100 MHz digitizing storage oscilloscope at the instant of impact, and the tangential acceleration-time history $\ddot{x}_1$ of the driver die was recorded and stored for later data processing. The accelerometer was the 25 gram quartz model 353B33 with a 25 volt DC power supply, both manufactured by PCB Piezoelectronics. The sensitivity of this accelerometer was 100 mV/g where $g = 9.81\ \text{m/s}^2$. After numerous preliminary impact experiments using these foamed polymers, it was concluded that a half sine curve of amplitude a_0 and impact time t_0 was a good fit to all measurements $\ddot{x}_1$.

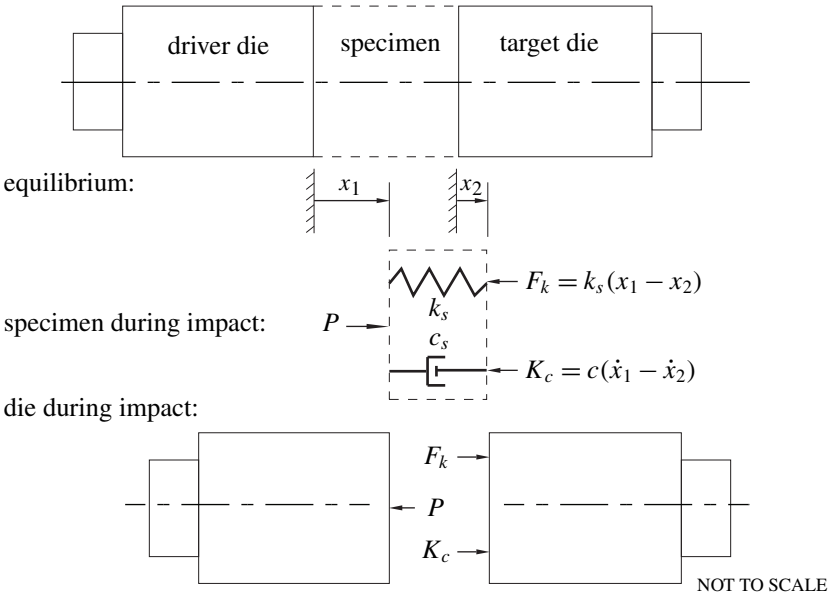

Figure 5. Mathematical models of the two pendulums and the specimen.

That is,

$$\ddot{x}_1 = -a_0 \sin \frac{\pi t}{t_0}, \tag{1}$$

in which the negative sign indicates deceleration. Shown in Figure 4 is a typical experimental trace of $\ddot{x}_1$ and its best-fit half sine curve. Here, the exact time of separation between the specimen and the target die just after impact could not be determined experimentally, and was approximated as t_0.

Given θ_0 and the measured quantities θ_1, θ_2, and $\ddot{x}_1$, the material responses to impact can be computed using the following mathematical model.

Mathematical model of impact

Shown in Figure 5 is the mathematical model of the foamed polymer specimen sandwiched between the two dies. The coordinates x_1 and x_2 are defined as the respective driver and target die face displacements from their static (free hanging) states. The specimen is assumed to behave linearly, or nearly so, to have negligible mass compared to m, and to exhibit damping proportional to the specimen velocity. The representation in Figure 5 reflects these assumptions, in which the specimen's impact force is P and its stiffness and damping parameters are k_s and c_s, respectively. In general, k_s and c_s may vary with time and strain-rate, given an impact time history initiated by θ_0. In these terms, the equations of motion for the

driver pendulum, the specimen, and the target pendulum are, respectively,

$$-P = m\ddot{x}_1, \tag{2}$$

$$P - k_s(x_1 - x_2) - c_s(\dot{x}_1 - \dot{x}_2) = 0, \tag{3}$$

$$k_s(x_1 - x_2) + c_s(\dot{x}_1 - \dot{x}_2) = m\ddot{x}_2. \tag{4}$$

When the first two equations are added to eliminate P,

$$k_s(x_1 - x_2) + c_s(\dot{x}_1 - \dot{x}_2) = -m\ddot{x}_1. \tag{5}$$

The result observed by comparing Equations (4) and (5) is that $\ddot{x}_2 = -\ddot{x}_1$, from which it is concluded that measures of both $\ddot{x}_1$ and $\ddot{x}_2$ would be redundant. The driver die acceleration $\ddot{x}_1$ was the acceleration chosen to be measured.

Kinematics of impact. The kinematics of the compressed specimen are deduced by integrating Equation (1) and using the result that $\ddot{x}_2 = -\ddot{x}_1$. The first integration gives the respective driver and target die velocities as

$$\dot{x}_1 = v_0 - \frac{t_0 a_0}{\pi}\left(1 - \cos\frac{\pi t}{t_0}\right), \qquad \dot{x}_1(0) = v_0, \tag{6}$$

$$\dot{x}_2 = \frac{t_0 a_0}{\pi}\left(1 - \cos\frac{\pi t}{t_0}\right), \qquad \dot{x}_2(0) = 0, \tag{7}$$

which satisfy the stated initial conditions of each die at the instant $t = 0$, or just prior to die impact. The second integration gives the die displacements, subject to zero initial conditions, as

$$x_1 = v_0 t - \frac{t_0 a_0}{\pi}\left(t - \frac{t_0}{\pi}\sin\frac{\pi t}{t_0}\right), \qquad x_1(0) = 0, \tag{8}$$

$$x_2 = \frac{t_0 a_0}{\pi}\left(t - \frac{t_0}{\pi}\sin\frac{\pi t}{t_0}\right), \qquad x_2(0) = 0. \tag{9}$$

The preimpact driver die velocity v_0 in Equations (6) and (8) is deduced by equating the change of potential energy between the driver die's state at θ_0 and the state at first impact ($t = 0$), to the change in kinetic energy between these same states, or

$$mg\ell(1 - \cos\theta_0) = \tfrac{1}{2}mv_0^2, \tag{10}$$

which leads to

$$v_0 = \sqrt{2g\ell(1 - \cos\theta_0)}. \tag{11}$$

The two assumptions inherent in Equation (10) are: energy losses due to bearing and air friction between the two states are negligible, and rotational kinetic energy of the die and arm is negligible in comparison to the to the translational energy of the die. The first assumption was verified by performing free swing tests with the driver arm, in which the specimen and target die were absent. These results showed

that for an initial angular position θ_0, the die arm swung to within one percent of its mirror angle $-\theta_0$. The second assumption was validated by a computation, which showed that the rotational kinetic energy was less than one percent of $mv_0^2/2$ for the dual pendulum apparatus shown in Figure 2.

Energy absorption. The incident energy density, or the energy per volume of the specimen that is available for absorption (Figure 3, left), is defined by

$$W_0 = \frac{4mg\ell}{\pi h D_0^2}(1 - \cos\theta_0). \tag{12}$$

Not absorbed by the specimen is the maximum potential energy per volume of the specimen after rebound (Figure 3, right), or

$$W_r = \frac{4mg\ell}{\pi h D_0^2}\big((1 - \cos\theta_1) + (1 - \cos\theta_2)\big). \tag{13}$$

The specimen's unit energy absorption is the difference of the last two expressions: $W_0 - W_r$. Expressed as a percent of the incident energy density, the unit energy absorption for this nearly frictionless system is thus

$$W = \frac{(1 - \cos\theta_0) - (1 - \cos\theta_1) - (1 - \cos\theta_2)}{(1 - \cos\theta_0)} \times 100\%. \tag{14}$$

Impact stress, strain, and strain rate. Since the specimen's impact force is P, Equations (1) and (2) can be used to calculate the time-dependent impact stress, or

$$\sigma = \frac{4P}{\pi D_0^2} = \frac{4ma_0}{\pi D_0^2} \sin\frac{\pi t}{t_0}. \tag{15}$$

The mean stress $\bar{\sigma}$ up to the time $t_0/2$ of maximum compression, and the peak stress σ_p at this time are deduced from the previous equation as

$$\bar{\sigma} = \frac{2}{t_0}\int_0^{t_0/2} \sigma\, dt = \frac{8ma_0}{\pi^2 D_0^2} \qquad \text{and} \qquad \sigma_p = \frac{4ma_0}{\pi D_0^2}. \tag{16}$$

The impact strain ε is based on the relative displacement $x_1 - x_2$ between the die faces. Using Equations (8) and (9), this strain is thus

$$\varepsilon = \frac{x_1 - x_2}{h} = \frac{v_0 t}{h} - \frac{2t_0 a_0}{\pi h}\left(t - \frac{t_0}{\pi}\sin\frac{\pi t}{t_0}\right), \tag{17}$$

in which v_0 is given by (11). The average strain rate up to maximum compression at $t = t_0/2$, as deduced from Equations (6) and (7), is defined as

$$\dot{\varepsilon}_a = \frac{2}{t_0 h}\int_0^{t_0/2} (\dot{x}_1 - \dot{x}_2)\, dt = \frac{v_0}{h} - \frac{2t_0 a_0}{\pi h}\left(1 - \frac{2}{\pi}\right). \tag{18}$$

Specimen stiffness-damping constraint. A constraint relationship between k_s and c_s can be computed by time averaging (5), using (1). That is,

$$\frac{1}{t_0}\int_0^{t_0}\big(k_s(x_1-x_2)+c_s(\dot{x}_1-\dot{x}_2)\big)\,dt=\frac{ma_0}{t_0}\int_0^{t_0}\sin\frac{\pi t}{t_0}\,dt. \tag{19}$$

Let k_s and c_s be constant, on the average, and integrate (19) after substituting for the displacements and velocities given by Equations (6)–(9). The result is

$$k_s=\frac{4\pi^2 ma_0-2\pi^2(\pi v_0-2t_0a_0)c_s}{\pi^3 t_0 v_0-2\pi^2 t_0^2 a_0+8t_0^2 a_0}, \tag{20}$$

in which v_0 is given by (11).

Impact damping. The nondimensional damping factor ζ, commonly employed in linear dynamic systems, is defined as

$$\zeta=\frac{c_s}{2\sqrt{k_s m}}. \tag{21}$$

Energy methods are now used to predict an explicit equation for ζ. The difference of peak potential energies for the initial and rebound states, depicted in Figure 3, is the energy lost in specimen damping (subject to the assumptions already discussed). This loss is

$$\Delta E=mg\ell(1-\cos\theta_0)-mg\ell(1-\cos\theta_1)-mg\ell(1-\cos\theta_2). \tag{22}$$

A second form for ΔE is based on the damping power, or the product of the damping force $c_s(\dot{x}_1-\dot{x}_2)$ and the relative die velocity $(\dot{x}_1-\dot{x}_2)$. The energy loss is this product integrated over the die-specimen contact time t_0, or

$$\Delta E=c_s\int_0^{t_0}(\dot{x}_1-\dot{x}_2)^2\,dt. \tag{23}$$

When Equations (22) and (23) are equated and the velocities $\dot{x}_1$ and $\dot{x}_2$ of Equations (6) and (7) are substituted, the resulting equation can be solved for ζ. After performing the integrations and regrouping the parameters, this leads to

$$c_s=\frac{\pi^2 mg\ell(\cos\theta_1+\cos\theta_2-\cos\theta_0-1)}{\pi^2 t_0 v_0^2-4\pi t_0^2 a_0 v_0+6t_0^3 a_0^2}. \tag{24}$$

Thus, with c_s and k_s of Equations (24) and (20), the damping factor ζ can be computed from Equation (21).

The results of this impact analysis are summarized as follows. Given the apparatus and specimen parameters (m, ℓ, D_0, h), and imposing the initial angle θ_0, measures of the quantities $(\theta_1, \theta_2, a_0, t_0)$ give measures of the specimen's key responses. These measures are: the percent of the incident energy absorbed, (14);

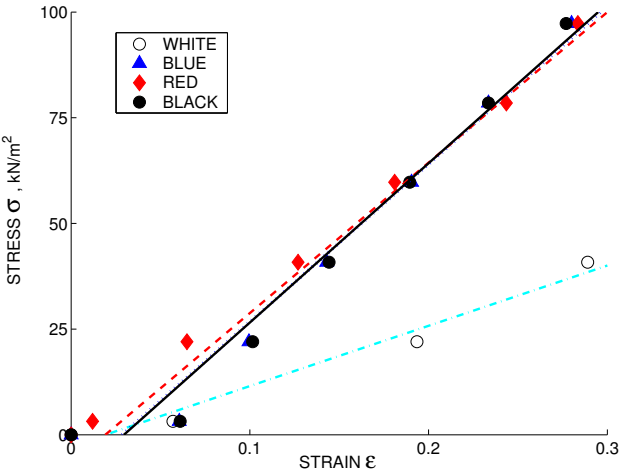

Figure 6. Stress-strain behavior for the four foamed polymers at the low strain rate of about 0.001 s^{-1}.

the stress-strain behavior, Equations (15) and (17); the mean compressive stress and strain rate, Equations (16) and (18); and the stiffness and damping properties, Equations (20), (21), and (24). The experiments to measure $(\theta_1, \theta_2, a_0, t_0)$ are now described.

Experimental protocol and measurements

The foamed polymer specimens described in Table 1 were cut from the as-received sheet material with a sharp steel cookie-cutter die of the same diameter as the impacting die, or 38.1 mm. One set of specimens was used for the standard compression tests, and the other set was used for the impact experiments.

The uniaxial compression tests for each of the four materials were all performed at the rather slow strain rate of about 0.001 s^{-1}. The results are the stress-strain data shown in Figure 6, with a least-squares straight line fit for each material. The slope of each line gives the static modulus E, which is strictly valid only for the stated strain rate. These values of E are listed in Table 1. These results indicate that the four materials behave linearly, or nearly so, up to strains of about 30%, and lend credibility to the hypothesized linear mathematical model.

The protocol for the impact experiments was as follows. The black specimen, defined as the reference specimen, was glued to the die face of the driver pendulum. This pendulum arm was then hand-held at $\theta_0 = 10°$ and released. Then the voltage-time history representing $\ddot{x}_1$ was recorded by the digital storage oscilloscope, which also displayed to four significant figures the peak voltage representing a_0 and the rise time $t_0/2$ to this peak. Using the accelerometer's calibration factor of 100

mV/g, the peak voltage was converted to the peak acceleration a_0, expressed in units of g. Then the first rebound angles θ_1 and θ_2 were measured by one of the two procedures already explained (the bead method was preferred for its simplicity). This same experimental procedure was repeated four more times for $\theta_0 = 10°$. Based on these five trial runs, the arithmetic average (mean value) was computed for each of the four measured quantities $(\theta_1, \theta_2, a_0, t_0)$. This procedure was then repeated for $\theta_0 = 20°$, 30°, and 40° using the same black specimen. A time lapse of at least 60 s was allowed between each impact, so that the specimen could regain its initial thickness.

The sixteen data sets so obtained for the black specimen are listed in Table 2, together with the four incident energy density levels W_0, which were computed from (12) for each respective initial pendulum angle $\theta_0 = 10, 20, 30, 40°$. Here $m = 0.461$ kg (which includes the accelerometer's mass) and $\ell = 0.239$ m. The four incident energy density levels of the black specimens were chosen to be the same as those for the nonblack specimens, as shown in the W_0 column of Table 2. The corresponding values of θ_0 for the nonblack specimens, computed from (12), were all somewhat higher than their black specimen counterparts at $\theta_0 = 10, 20, 30, 40°$,

Specimen type	W_0, kJ/m^3	θ_0, °	Measured mean of five trials θ_1, °	θ_2, °	a_0, g	t_0, ms
white	2.96	12.0	4.42	7.48	7.72	4.62
	11.8	24.1	9.10	17.0	17.0	3.84
	26.1	36.2	15.2	24.8	26.8	3.60
	45.6	48.5	16.8	32.0	35.5	3.44
blue	2.96	11.5	4.44	6.82	14.4	2.43
	11.8	23.0	8.90	15.7	28.5	2.03
	26.1	34.6	12.5	23.8	43.2	1.92
	45.6	46.2	16.7	31.5	56.8	1.87
red	2.96	10.8	4.26	6.52	13.1	2.61
	11.8	20.9	7.26	14.2	25.8	2.19
	26.1	31.4	11.6	22.3	38.6	2.24
	45.6	41.9	14.3	29.6	52.2	2.18
black	2.96	10.0	4.26	6.16	14.8	1.74
	11.8	20.0	7.40	14.1	30.8	1.62
	26.1	30.0	12.5	20.9	47.1	1.41
	45.6	40.0	15.4	27.8	62.5	1.44

Table 2. Dual-pendulum impact measurements.

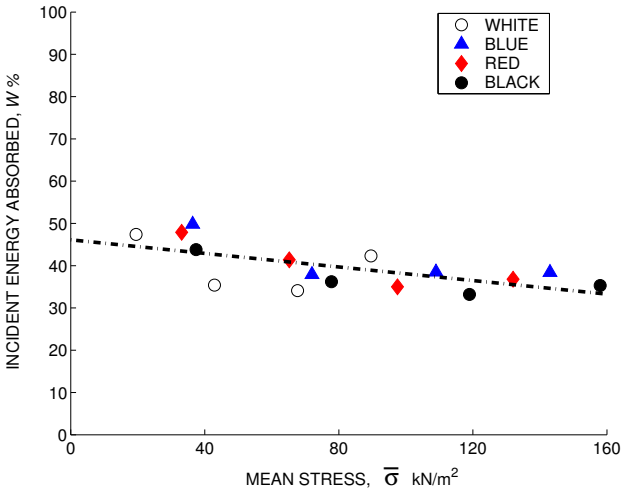

Figure 7. Influence of the mean impact stress on the percent of the incident specimen energy absorbed during impact.

which reflects the differences in specimen thicknesses. The matching of incident energy density levels allows for later comparisons of dynamic responses among specimens of unequal volume.

Using the same experimental protocol as for the black specimen, but with the stated θ_0 values, the sixteen sets of experimental measures $(\theta_1, \theta_2, a_0, t_0)$ for each white, blue, and red specimen were obtained. Again, each numerical entry of each set represents a five-trial average. Such results were reproducible; that is, given θ_0, the deviation of any one measurement of a five-trial run was within 2% of its corresponding mean value.

Computed responses and discussion

Based on the 16 data sets of Table 2, and the two pendulum parameters $m = 0.461\,\text{kg}$ and $\ell = 0.239\,\text{m}$, the material impact responses predicted by the mathematical model were computed. Computational algorithms and graphic displays were developed using Mathematica [Wolfram 1999]. The results are presented in Figures 7–11. In all of these figures, each data point corresponds to a data set $(\theta_0, \theta_1, \theta_2, a_0, t_0)$, or a row in Table 2.

Shown in Figures 7 and 8 are two measures of energy absorption, each as a function of the mean impact stress $\bar{\sigma}$, defined by Equation (16). The dashed straight line in each figure is the least-squares fit to all data. The percent of the incident energy absorbed, based on Equation (14), is shown in Figure 7, which indicates a weakly decreasing energy loss with increasing $\bar{\sigma}$. The best-fit straight line to these

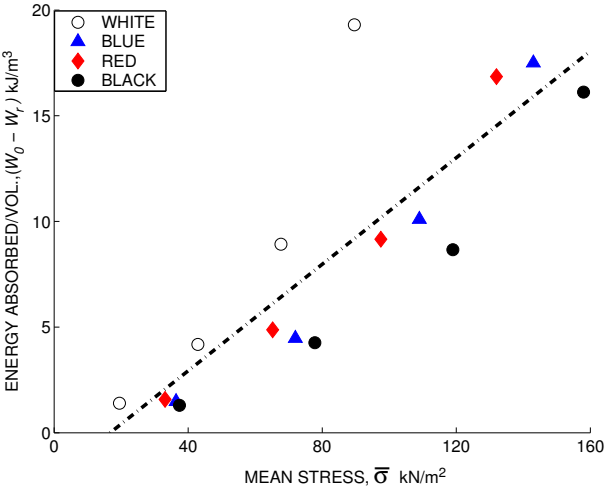

Figure 8. Influence of the mean impact stress on the energy absorbed per unit specimen volume during impact.

data is

$$W(\%) = 46.17 - 0.0803\bar{\sigma}, \tag{25}$$

in which the units of $\bar{\sigma}$ are kN/m^2.

The energy absorbed per unit volume of each specimen, or $W_0 - W_r$ in Equations Equation (12) and Equation (13), is shown in Figure 8. The increase in the unit energy loss W_v is approximately linear with $\bar{\sigma}$, for which the best-fit straight line is

$$W_0 - W_r = 0.126\bar{\sigma} - 2.11, \tag{26}$$

where the units of energy and mean stress are kJ/m^3 and kN/m^2. The data of Figure 8 show that at a given mean stress level $\bar{\sigma}$, the most dense (black) foamed polymer has a consistently lower unit energy loss than the least dense (white) material.

Shown in Figure 9 are the stress-strain curves for all of the specimens, in which each exhibits hysteresis behavior typical of energy-absorbing material. Each curve for each of the four materials has a label a, b, c, or d, which corresponds respectively to the incident unit energy level listed in Table 2, or 2.96, 11.8, 26.1, and 45.6 kJ/m^3. These curves were generated using (15) and (17), which are parametric equations in time t. To each closed curve there corresponds an average strain rate $\dot{\varepsilon}_a$, computed from Equations (18) and (11) for each θ_0. The peak of each closed curve, at $t = t_0/2$, marks the end of increasing compression stress. At the end of impact, assumed to occur at $t = t_0$, the stress is zero. Then each unloaded specimen was observed to recover (along the abscissa to the origin) to nearly its original thickness h in about 30 s. The area enclosed by each of the 16 hysteresis

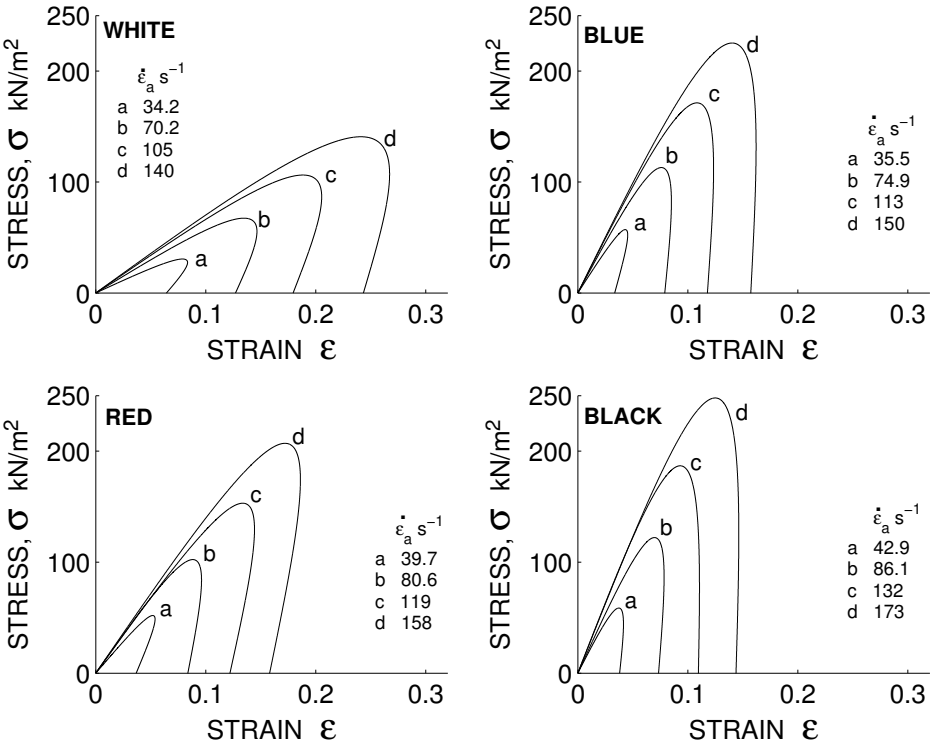

Figure 9. Stress-strain and hysteresis behavior for the foamed polymers, showing the influence of strain rate.

curves in Figure 9 corresponds to the energy absorbed per unit volume, the values of which were also computed using Equation (14) and displayed in Figure 8.

Shown in Figure 10 is a weak dependency of the compression modulus E_c on the average strain rate $\dot{\varepsilon}_a$, for all four materials. This modulus is defined in terms of the elastic stiffness k_s, or

$$E_c = \frac{4hk_s}{\pi D_0^2}. \tag{27}$$

For each material, it appears that E_c approaches a limiting or asymptotic value as $\dot{\varepsilon}_a$ increases. For the highest-density material (black), for instance, $E_c \to 900\,\text{kN/m}^2$ as $\dot{\varepsilon}_a \to 150\,\text{s}^{-1}$. For the two intermediate density materials, the average asymptotic values are nearly the same, or about $700\,\text{kN/m}^2$; and for the least dense material, $E_c \to 300\,\text{kN/m}^2$.

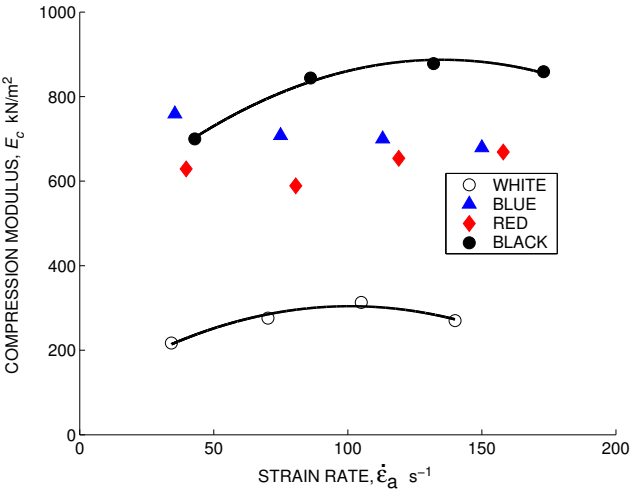

Figure 10. Influence of strain rate on the compression modulus for the four foamed polymers.

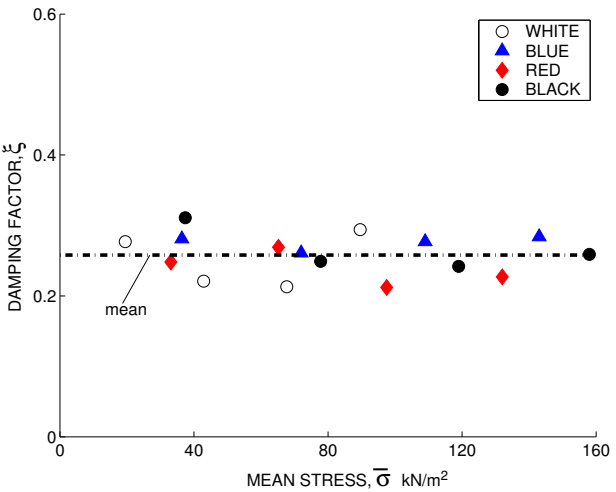

Figure 11. Influence of the mean impact stress on the damping factors for the four foamed polymers.

Shown in Figure 11 is the damping factor ζ, with its weak dependency on the mean level of impact stress $\bar{\sigma}$. The straight line is the least-squares fit (mean value) of data for all four materials, or

$$\zeta = 0.258, \qquad SD = 0.029. \tag{28}$$

Conclusions

This dual-pendulum measuring system is simple in construction and versatile in operation. System bearing-friction was minimized by precision machining and graphite lubrication. The impact energy permanently lost to the apparatus was minimized in two ways: (1) by choosing equal specimen and die diameters, which confined the transmitted acoustic waves to the same diameter cylinders, eliminating most of the energy dispersion in the uniform dies; (2) by assigning more than 99% of a pendulum's mass to the die so that the pendulum's center of percussion was nearly coincident with the die's longitudinal axis of symmetry, thus reducing the horizontal bearing impact reaction force, and its contribution to friction energy loss to nearly zero. Further, by matching each of the four incident energy density levels (a, b, c, d) for the consecutive testing of each specimen type, comparisons of the dynamic responses among specimens of different thicknesses could be made.

That the mathematical model for impact is consistent with the measurements was demonstrated in the following ways:

- For all 16 data sets of Table 2, the following two independent measures for the velocity of the target die just after impact agreed to within about 10%. That is,

$$\dot{x}_1(t{=}t_0) \simeq \sqrt{2gl(1-\cos\theta_1)}. \tag{29}$$

  Here, the left side is the value predicted by Equation (6), and the right side is based on the conservation of energy and the independent measure θ_1.

- The closed area of each of the 16 hysteresis curves of Figure 9 generally agreed within 10% to its counterpart unit energy calculated from Equation (14).

- Consider Figure 9 for a given material. The slope of each stress-strain curve up to about $t = 0.4t_0$ is consistently higher than the slope E of Figure 6 for the same material. Theory predicts that this slope will increase with increasing strain rate, an effect that is due to the accompanying increase in the elastic and damping reaction forces.

Future developments include new and complementary theories of impact for a variety of nonlinear, open or closed-cell materials for which this dual pendulum system can be employed to measure material properties.

Acknowledgements

The author thanks Rhett T. George for his advice on electronic measurements; and the reviewers for their valuable insights.

References

[Deverge and Jaouen 2004] M. Deverge and L. Jaouen, "A review of experimental methods for the elastic and damping characteristics of acoustical porous materials", in *Internoise 2004: The 33rd International Congress and Exposition on Noise Control Engineering*, Prague, Czech Republic, August 22–25 2004, Available at http://www.univ-lemans.fr/~s012782/Deverge_Jaouen_v5.pdf.

[Gibson and Ashby 2001] L. J. Gibson and M. F. Ashby, *Cellular solids: structure and properties*, 2nd ed., Cambridge University Press, Cambridge, 2001.

[Wolfram 1999] S. Wolfram, *The Mathematica book*, 5th ed., Wolfram Media, Champaign, IL, 1999.

Received 11 Dec 2005.

JAMES F. WILSON: jwilson@duke.edu
Pratt School of Engineering, Duke University, 6319 Mimosa Drive, Chapel Hill, NC 27514, United States

JOURNAL OF MECHANICS OF MATERIALS AND STRUCTURES
Vol. 1, No. 4, 2006

SO... IS THIS A SURFACE-BREAKING CRACK?

MILAN POZNIC AND CLAUDIO PECORARI

An inspection technique used to assess the structural integrity of critical components in a nuclear power plant must be able to discern surface-breaking cracks from subsurface cracks. This work proposes an ultrasonic method to provide that information and presents a theoretical investigation into it. The main assumption of the model is that water carried by pressurized pipes infiltrates and fills a surface-breaking crack, while a subsurface crack is dry. The model simulates an inspection in which the modulation technique is employed and the surface hosting the crack is not accessible. A ratio, R, constructed with signals recorded in backscattering configuration during a modulation cycle, is examined and shown to provide a clear criterion allowing subsurface cracks to be distinguished from surface-breaking cracks when a shear vertical wave at 45 degree incidence is employed as a probe.

1. Introduction

Stress corrosion cracks, especially in pipes carrying pressurized water, constitute a serious threat to the structural integrity of nuclear power plants. They are often found in regions proximal to the inner surface of the pipe, and can be either surface-breaking or subsurface. The growth of a subsurface crack is caused mostly by fatigue. However, if a crack reaches the surface of the hosting component, corrosion becomes the main factor affecting crack growth. This is the case because water enters the fracture thanks to the combination of tensile stresses, which cause the crack to remain open while the plant is operating, and the pipe internal pressure, which can reach values of the order of 70 atm.

For this reason, it is of the utmost importance for a nondestructive technique employed in the assessment of a plant's structural integrity to enable not only the detection of stress-corrosion cracks, but also their characterization as surface-breaking or subsurface defects. Indeed, there have been instances in which cracks have been characterized as subsurface during inspection but proved to be surface-breaking upon a destructive metallurgical investigation [Jenssen et al. 2000]. Of relevance to the subject of this work is also the presence of debris resulting from

Keywords: partially closed cracks, modulation, wave scattering stress-corrosion.

corrosion, which tends to bridge the gap between the surfaces, rendering the defect more transparent to an inspecting ultrasonic beam.

This work presents the principles of an ultrasound-based technique designed to discern partially closed cracks that are subsurface from those that are surface-breaking. The proposed method exploits the effects of water confinement within a partially closed, surface-breaking crack on the acoustic response of the defect. The sensitivity of the proposed technique to the presence of fluid trapped between the crack faces, and to compressive stresses acting on the crack, is examined. The emphasis on cracks that are partially closed derives from the near certainty that, following the shut-down of the plant prior to inspection, stresses due to the plant's operating conditions are removed and cracks tend to partially close, at least in vicinity of their tips (see [Newman et al. 2003], for example). This investigation is limited to the worst-case scenario in which the surface hosting the crack is not accessible and the inspection must be carried out from the outer surface of the component.

The article is organized as follows. We first report experimental results which illustrate the characteristic dependence of the stiffness on the pressure applied to dry and fluid-filled interfaces. We then present a model which evaluates the backscattering by partially closed, surface-breaking and subsurface cracks. To simulate the effect of partial closure on backscattering, spring boundary conditions are employed. Experimental results obtained on partially closed interfaces are employed in the theoretical model to describe the effect of water trapped within a surface-breaking fracture. The model is used to simulate experiments in which the partial closure of the crack is modulated by a low-frequency, high-amplitude wave while a probing ultrasonic wave interrogates the defect. We close with a discussion of the significance of these findings for the development of a method allowing water-confining, surface-breaking cracks and dry subsurface cracks to be distinguished from each other.

2. Dry and water-confining interfaces

The interaction between ultrasonic waves and interfaces formed by two rough, nonconforming surfaces in contact under increasing pressure has been investigated extensively both experimentally and theoretically; see for example [Baltazar et al. 2002; Baik and Thompson 1984; Drinkwater et al. 1996; Lavrentyev and Rokhlin 1998; Kim et al. 2004a]. Models have been developed that derive the macroscopic mechanical properties of such interfaces from those of the asperities in contact and from the topographical properties of the surfaces. This considerable effort notwithstanding, several of the outstanding issues concerning this problem still await a solution [Pecorari and Poznic 2006]. In particular, the effect of water

confined between surfaces in partial contact appears not to be accounted for by any available model.

In this section we present experimental results on both dry and water-confining interfaces and use them in the theoretical modeling of ultrasonic wave scattering by surface-breaking and subsurface cracks. The experimental set-up employed in this investigation is discussed in [Pecorari and Poznic 2006] and is not repeated here. The only noteworthy differences from our earlier experimental conditions are:

i. The nominal frequency of the transducer used to generate and receive the waves reflected by the imperfect interface is 2.25 MHz here.

ii. The measurements were carried out also with shear waves.

iii. The rms roughness of the two surfaces employed here was evaluated to be of the order of 0.2 μm. In all the measurements, the inspecting waves insonify the interface at normal incidence.

Among the properties of interest, the stiffness K of the imperfect interface is of primary importance in understanding the interaction between ultrasonic waves and such interfaces. It is defined by the relation $K = \partial P/\partial\delta$, where P is the applied pressure (or the tangential stress) and δ is the relative approach (or the tangential displacement) between the mean planes of the rough surfaces. The values K_N and K_T of the normal and transverse interfacial stiffness can be recovered from the measured reflection coefficients R_L and R_T for longitudinal and shear waves at normal incidence via the well-known relation

$$R_{L,T} = -\frac{1}{1 - 2j\,(K_{N,T}/\omega Z_{L,T})},$$

where ω is the circular frequency of the incident and scattered waves, and Z_L, Z_T are the acoustic longitudinal and shear impedances of the medium. The symbol j represents the imaginary unit. When water is confined by the interface, and the real area over which mechanical contact between the surfaces take place is a small fraction of the nominal area, the normal stiffness of the latter can be written as the sum of two terms: $K_N = (\Lambda/d_0) + \Delta K_N$. The first term describes the effect of a layer of water with thickness d_0, the latter quantity being the distance between the mean planes of the rough surfaces when no pressure is applied to the interface. The symbol Λ represents the only nonzero elastic constant of the liquid medium. The second term, ΔK_N, describes the part of the stiffness which depends on the applied pressure. Since the shear modulus of water is zero, the transverse stiffness does not contain a term analogous to Λ/d_0.

Figure 1 reports experimental results obtained at normal incidence using steel-steel interfaces with rms roughness σ approximately equal to 0.2 microns. They

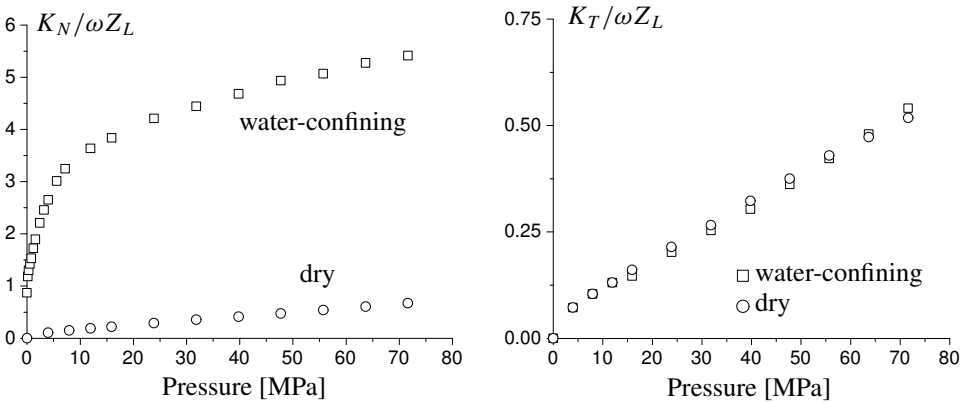

Figure 1. Normalized normal (left) and transverse (right) spring stiffness versus pressure applied to a water-confining and dry steel-steel interface. The symbols represent experimental results.

illustrate the dependence of the normalized normal, $K_N/\omega Z_L$, and transverse, $K_T/\omega Z_L$, interface stiffness components on the applied pressure for both dry and water-confining interfaces, respectively. The pressure is varied from 0 MPa to 80 MPa at which point the reflection coefficient of a longitudinal wave interacting with a water-confining interface is smaller than 0.1. The two most relevant features of Figure 1, left, are the overall larger normal stiffness of the water-confining interface compared to that of the dry one, and the initial fast increase of K_N when pressure not exceeding 5 MPa is applied to the interface. Unpublished numerical simulations by these authors show that the addition of the term accounting for the thin fluid layer, Λ/d, to the stiffness of the dry interface is not sufficient to reproduce the experimental results. A possible explanation for this deficiency of the model may be found in the results of both experimental and theoretical investigations into the interaction between solid surfaces confining water; see [Das et al. 1996; Israelachvili 1992; Grabbe and Horn 1993; Ho et al. 1998; Pashley and Israelachvili 1984]. These works show that repulsive forces between solid surfaces arise when the distance between the latter is comparable to the dimension of the fluid's molecules. The physical origin of such repulsive forces may vary from system to system, but common to all is the increase of structural order caused by the spatial confinement on the molecules of the fluid. These findings suggest that these repulsive forces may also occur between asperities of the system under investigation, opposing their mechanical contact when they are separated by a distance of the order of a nanometer. An alternative interpretation to that just outlined considers the effect of drainage forces which oppose the motion of the solid surfaces in the direction normal to their mean planes. A suitable mathematical model for such a phenomenon should extend the analysis carried out by Chan and Horn [1985] on

cylindrical surfaces with axes oriented normally to each other and to the direction of motion. Essential for the accuracy of the novel model, the extension of Chang and Horn's model should account for the statistical character of the surface profiles. Of importance is also the results concerning the shear stiffness, K_T, which have been obtained with the same two interfaces; see Figure 1, right. They display a dependence on the applied pressure which, for our purposes, can be assumed to be identical. In other words, they show that the viscosity of the fluid does not affect K_T, and thus, a mechanism which does not call upon the viscosity of the fluid appears to offer a more plausible explanation of the experimental observation. In summary, the experimental results of Figure 1 show that water strongly affects the dependence of the interface normal stiffness on the applied pressure, while it does not alter that of the shear stiffness.

3. Theory

Figure 2 illustrates the geometry of the material system and of the defect under consideration. The segment of material of length a separating the crack from the surface in the diagram on the left is also known as the *ligament*. With reference to Figure 2, and following the method developed by Achenbach et al. [1980] and Mendelsohn et al. [1980], the original problem posed by the scattering of an incident bulk wave onto the crack is decomposed into a symmetrical and an antisymmetrical part.

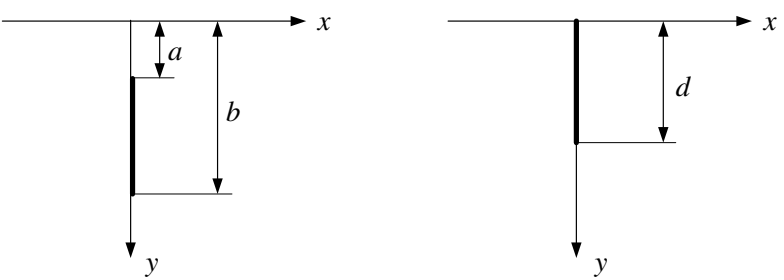

Figure 2. Geometry of the material system and its defect. The material system occupies the half-space $y > 0$. Left: Subsurface crack. Right: surface-breaking crack, with $a = 0$ and $b = d$.

When considering the scattering by a subsurface crack, the boundary conditions along the crack face, which are associated with the symmetrical problem are

$$\left.\begin{aligned} \sigma_{xy}^{+} &= 0, & x &= 0,\ \ 0 \le y < \infty, \\ \sigma_{xx}^{+} &= K_N\, \Delta u, & a &\le y < b, \\ u &= 0, & 0 &\le y < a \ \text{ or } \ b \le y < \infty, \end{aligned}\right\} \tag{3–1}$$

and those associated with the antisymmetrical problem are

$$\left.\begin{aligned} \sigma_{xx}^{+} &= 0, & x &= 0,\ \ 0 \le y < \infty, \\ \sigma_{xy}^{+} &= K_T \Delta v, & a &\le y < b, \\ v &= 0, & 0 &\le y < a \ \text{ or } \ b \le y < \infty. \end{aligned}\right\} \tag{3–2}$$

In these equations, the σ_{ii}^{+} are the total stress components acting on the positive side of the crack, i.e., on the side for which $x = 0^{+}$, while u and v are the displacement components in the x and y direction, respectively. The spring stiffness densities K_N and K_T are generally allowed to be functions of depth, y, so that nonuniform closure can be modeled. The remaining boundary conditions are those used by Achenbach et al. [1980] and Mendelsohn et al. [1980] for an open crack. In particular, the surface $y = 0$ is assumed to be free of traction. The crack closure is simulated by varying the contact pressure between the crack faces according to the next equations, which are given next only for a subsurface crack:

$$\begin{aligned} P(y) &= P_{\text{tip}} \exp \frac{y-b}{\ell}, & (a+b)/2 \le y \le b, \\ P(y) &= P_{\text{tip}} \exp \frac{a-y}{\ell}, & a \le y \le (a+b)/2. \end{aligned} \tag{3–3}$$

Here P_{tip} is the pressure at the crack tips and ℓ is the decay length which controls the spatial extent of the tip closure. The pressure distribution on a surface-breaking crack is obtained from (3–3) by letting $a = 0$ and substituting $(a+b)/2$ with $b = d$. Equations (3–3) are used to assign a local value to the spring stiffness densities by way of the relationships illustrated in Figure 1. The purpose of this feature of the model is twofold. First, the effect of the water on the scattering phenomenon is accounted for within the same mathematical scheme used to treat a dry partially closed crack. Secondly, the boundary conditions in equations (3–1) and (3–2) allow for the simulation of the well documented closure of a crack in the regions proximal to its tips [Newman et al. 2003], the causes of which are varied, still debated, and leading essentially to the same result when considered from the wave scattering point of view.

The equations of motion for the two displacement components are

$$c_L^2 \frac{\partial^2 u}{\partial x^2} + c_T^2 \frac{\partial^2 u}{\partial y^2} + \left(c_L^2 - c_T^2\right) \frac{\partial^2 v}{\partial x \partial y} = \frac{\partial^2 u}{\partial t^2},$$
$$c_L^2 \frac{\partial^2 v}{\partial x^2} + c_T^2 \frac{\partial^2 v}{\partial y^2} + \left(c_L^2 - c_T^2\right) \frac{\partial^2 u}{\partial x \partial y} = \frac{\partial^2 v}{\partial t^2},$$

where t represents time, and c_L and c_T are the phase velocities of longitudinal and shear waves, respectively. The solutions of these are given by the following expressions (see [Achenbach et al. 1980; Mendelsohn et al. 1980]):

$$u^s(\vec{x}) = \frac{2}{\pi} \int_0^\infty \left(\xi k_L A^s e^{-\alpha_L y} - 2\kappa^{-2} \alpha_T k_L C^s e^{-\alpha_T y}\right) \sin(\xi x)\, d\xi + \frac{2}{\pi} \int_0^\infty \left(\alpha_L k_L B^s e^{-\alpha_L x} + 2\kappa^{-2} \xi k_L D^s e^{-\alpha_T x}\right) \cos(\xi y)\, d\xi, \quad (3\text{–}4)$$

$$v^s(\vec{x}) = \frac{2}{\pi} \int_0^\infty \left(\alpha_L k_L A^s e^{-\alpha_L y} - 2\kappa^{-2} \xi k_L C^s e^{-\alpha_T y}\right) \cos(\xi x)\, d\xi + \frac{2}{\pi} \int_0^\infty \left(\xi k_L B^s e^{-\alpha_L x} + 2\kappa^{-2} \alpha_T k_L D^s e^{-\alpha_T x}\right) \sin(\xi y)\, d\xi, \quad (3\text{–}5)$$

for the symmetric field, while those of the antisymmetric are

$$u^a(\vec{x}) = \frac{2}{\pi} \int_0^\infty \left(\xi k_L A^a e^{-\alpha_L y} - 2\kappa^{-2} \alpha_T k_L C^a e^{-\alpha_T y}\right) \cos(\xi x)\, d\xi + \frac{2}{\pi} \int_0^\infty \left(\alpha_L k_L B^a e^{-\alpha_L x} + 2\kappa^{-2} \xi k_L D^a e^{-\alpha_T x}\right) \sin(\xi y)\, d\xi, \quad (3\text{–}6)$$

$$v^a(\vec{x}) = \frac{2}{\pi} \int_0^\infty \left(-\alpha_L k_L A^a e^{-\alpha_L y} + 2\kappa^{-2} \xi k_L C^a e^{-\alpha_T y}\right) \sin(\xi x)\, d\xi - \frac{2}{\pi} \int_0^\infty \left(\xi k_L B^a e^{-\alpha_L x} + 2\kappa^{-2} \alpha_T k_L D^a e^{-\alpha_T x}\right) \cos(\xi y)\, d\xi. \quad (3\text{–}7)$$

The time-dependence of the solution is assumed to be harmonic. In the equations above, $A^{a,s}$, $B^{a,s}$, $C^{a,s}$, and $D^{a,s}$ are functions of the integration variable ξ, and are themselves given in terms of integrals of suitable functions containing the tangential slope of the two components of the crack opening displacement. These are obtained by solving two decoupled singular integral equations derived by enforcing the boundary conditions (3–1) and (3–2) on the solutions of the equations of motion. The symbols k_L and k_T are the wavenumbers of the longitudinal and shear waves, respectively. With the same meaning of the subscripts L and T, the quantities α_L

and α_T are defined by

$$\alpha_L = \begin{cases} \sqrt{\xi^2 - k_L^2} & \text{if } \xi \geq k_L, \\ -j\sqrt{k_L^2 - \xi^2} & \text{if } \xi < k_L, \end{cases} \qquad \alpha_T = \begin{cases} \sqrt{\xi^2 - k_T^2} & \text{if } \xi \geq k_T, \\ -j\sqrt{k_T^2 - \xi^2} & \text{if } \xi < k_T. \end{cases}$$

The branch of the square root function in the complex plane is chosen to satisfy the Sommerfeld radiation condition.

Equations (3–4)–(3–7) concern the field in the quarter-space where both x and y are positive. The field components in the quarter-space where $x < 0$ are obtained from those given by those equations as follows:

$$u^s(x < 0, y) = -u^s(|x|, y), \qquad u^a(x < 0, y) = u^a(|x|, y),$$
$$v^s(x < 0, y) = v^s(|x|, y), \qquad v^a(x < 0, y) = -v^a(|x|, y).$$

In solving the integral equations in the unknown tangential slope of two components of the displacement discontinuity, the condition that their integral over the extent of the crack is null must be enforced. The scattering by an open subsurface crack was solved first by Brind and Achenbach [1981].

The scattering from a partially closed, surface-breaking crack is modeled within the same mathematical framework. The boundary conditions for this problem are obvious extensions of those given for a subsurface crack, and the solutions of the problem are again sought in the form given by equations (3–4)–(3–7).

As described earlier, the real physical system hosting the crack is a steel pipe containing water. Therefore, the boundary conditions stating that the surface $y = 0$ is traction-free are not correct. Enforcing the continuity of traction and normal displacement across the solid-water interface, however, would add considerable mathematical complications without substantially affecting the phenomena of interest in this work. In fact, the algorithm later proposed to characterize the defect as being surface-breaking or internal is designed to measure only the *relative* effect of the applied modulation on the scattering properties of the defect with respect to those displayed by the defect in its unperturbed state. Boundary conditions which amount to a small perturbation of the total field within the solid half-space are not expected to have a significant effect on the results of this algorithm.

4. Numerical results

The experimental results of Section 2 indicate that the most striking difference between the properties of two interfaces under consideration is the rapid increase of the normal stiffness of the water-confining interface as soon as contact between asperities is established. This naturally suggests the use of the parametric modulation technique as a novel method to characterize a crack as being surface-breaking or subsurface. The modulation technique exploits the nonlinear properties of partially

closed cracks, and more specifically the dependence of the crack stiffness on the applied pressure. Xiao and Nagy [1998] employed thermal stresses induced by a laser source to vary the closure of a surface-breaking crack which was simultaneously insonified by a high frequency Rayleigh wave. By means of suitable signal processing of the backscattered ultrasonic pulse acquired during different phases of the thermal modulation, these authors showed that the acoustic signature of the crack can be extracted from the noisy environment (see also [Nagy 1992]). In other words, the modulation technique was shown to be able to selectively detect nonlinear material defects. Rokhlin et al. [2004] adapted this method to increase the sensitivity of ultrasonic inspections to poor adhesive bonds between aluminum plates, while Kim et al. [2004b] (see also references therein) used it to characterize small surface-breaking cracks initiated at surface pits by fatigue. Finally, Kazakov et al. [2002] used the same idea to image the nonlinear properties of a surface-breaking crack. Rokhlin et al. [2004], Kim et al. [2004a; 2004b] and Kazakov et al. [2002] used a low-frequency source of mechanical vibrations to vary the instantaneous properties of the defect of interest.

In this work, an experimental configuration similar to those employed by the previously cited authors is simulated. A crack under investigation is subjected to a sinusoidal, time-dependent pressure field of amplitude ΔP: $P(t) = \Delta P \sin(\Omega t)$, the frequency of the modulation, Ω, being orders of magnitude lower than that of an ultrasonic wave, ω, which is used to monitor the instantaneous state of the crack. This pressure is superposed on the static pressure given in (3–3), which is responsible for the initial partial closure. During a cycle, three backscattered ultrasonic signals are recorded, two at the opposite turning points of each cycle, and one at the mid point when $P(t) = 0$. By using the peak-to-peak amplitude of the back-scattered wave, or any other feature of this signal which reflects the variation of the crack state, the following ratio is constructed:

$$R = \left(B^- - B^+\right)/B_0, \tag{4–1}$$

where $B^{-,+}$ are the features of interest measured when the crack is most open $(-)$ or closed $(+)$, respectively, and B_0 refers to the crack state in its rest condition. Note that the ratio R is independent of the amplitude of the incident wave, and, thus conveys information which depends on the intrinsic properties of the defect and of the modulation, but not on the intensity of the inspecting wave. This work investigates the conditions under which R can possibly serve as an "index of state" to distinguish a fluid filled surface-breaking crack from a dry subsurface crack. The numerical results presented next and the conclusions drawn from them refer to phenomena involving only monochromatic waves. However, given the linearity of the system, their validity can be extended to wave packets formed by linear superposition of harmonic waves.

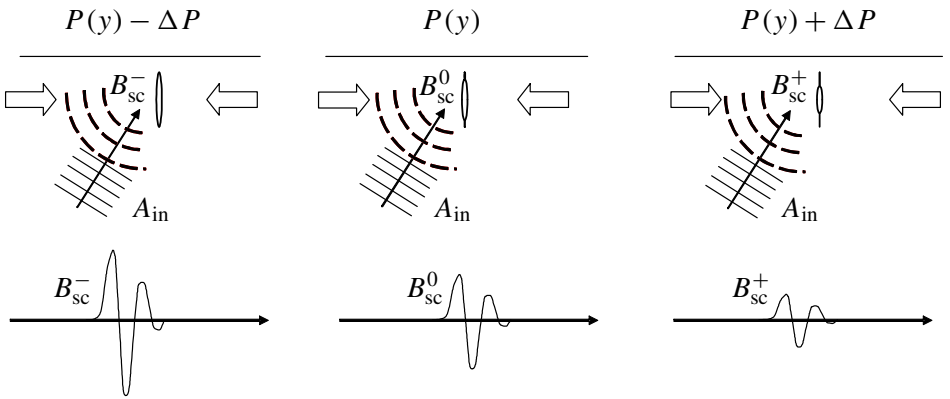

Figure 3. Schematics of the simulated modulation experiment illustrating the relationship between the state of the crack and the signal backscattered by it during a cycle of the modulation. The arrows pointing towards the crack represent the sum of the static pressure and the modulation.

The following numerical investigation considers the scattering by partially closed surface-breaking and subsurface cracks in a steel half-space. The mass density and phase velocity of longitudinal and shear waves in steel are $\rho = 7.8 \times 10^3\,\mathrm{kg\,m^{-3}}$, $c_L = 5900\,\mathrm{ms^{-1}}$, and $c_T = 3200\,\mathrm{ms^{-1}}$. The results presented in all the following figures refer to a configuration in which a shear vertical wave impinges on the defect at 45 degree incidence, unless otherwise stated. The frequency of the wave is $f = 2.25\,\mathrm{MHz}$. The solution of the scattering problem is evaluated in the backscattering direction. The observation point lies at a distance of about 30 shear wavelengths (about 40 mm) from the surface of the half-space.

The residual pressure which determines the closure of the crack (see Equation (3–3)) is chosen to represent three characteristic configurations: one in which the closure is uniform, and two in which it decays with rates equal to 0.1 mm and 1 mm, respectively. The rationale behind the choice of the latter values stems from the assumption that the cracks of interest are detectable by conventional methods, and, thus, their extent is of the order of several millimeters. For such cracks a likely state is one in which their tip(s) are partially closed while throughout the remaining portion of their extent there is no mechanical contact between the surfaces. The pressure at the crack tip, P_{tip}, is chosen to be equal to 5 MPa and 70 MPa to represent two well distinct situations in which the crack tip is nearly open or fairly closed, respectively. The values of the normalized stiffness constants $K_N/(\omega Z_L)$ and $K_T/(\omega Z_L)$ corresponding to these pressure values are 0.2 and 0.07, respectively, if the crack is dry, and 3 and 0.07 if a defect contains water. The amplitude

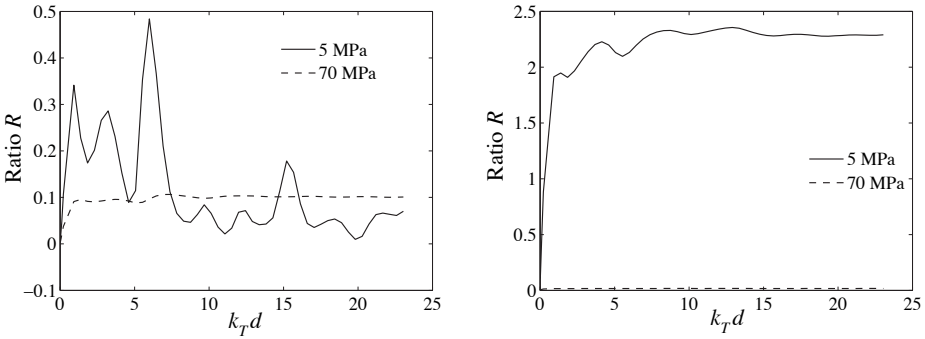

Figure 4. Ratio R versus nondimensional crack size $k_T d$ for values of pressure at the crack tip equal to 5 MPa and 70 MPa. The pressure distribution is constant along the crack extent. Left: dry surface-breaking crack. Right: water-confining surface-breaking crack.

of the modulation is $\Delta P = 5$ MPa in all simulations. For this value of the amplitude ΔP, the modulation causes the crack to open completely when $P_{\text{tip}} = 5$ MPa. The dependence of the ratio R on the nondimensional size of the crack, $k_T d$, is reported over a range which corresponds to cracks with physical dimension reaching values up to 5.36 mm.

In Figure 4, the left panel refers to a dry surface-breaking crack and the right panel to the same crack when it is filled with water. In both figures, the cases in which the crack is subjected to a uniform pressure, P_{tip}, of 5 MPa and 70 MPa are considered. In Figure 4, left, the crack shows a nearly constant response when $P_{\text{tip}} = 70$ MPa, reflecting the modest effect the modulation has on the crack opening, while it displays wide oscillation for the lower value of the applied pressure. In both cases, however, the ratio R does not exceeds values of 0.1 as the size of the crack increases. If water is confined within the crack (Figure 4, right), the value of the ratio for $P_{\text{tip}} = 70$ MPa is even smaller as a consequence of the higher values of the crack stiffness, while for $P_{\text{tip}} = 5$ MPa R reaches values larger than 2 over nearly all the range of values of $k_T d$ considered here. As indicated in Figure 2, right, the depth of the surface-breaking crack is d. This striking contrast is due to the large variation of values spanned by the normal stiffness as the total applied pressure varies between 0 and 10 MPa (see Figure 1, right).

Figure 5 illustrates the dependence of the ratio R for a surface-breaking crack with a closure given by the second equation of (3–3), specified for the case of a surface-breaking crack ($a = 0$, and $b = d$ as upper limit), and with $\ell = 1$ mm. As in the case considered in Figure 4, left, the response of a dry surface-breaking crack

tends to settle around values of the order of 0.1 as the size of the crack increases. However, a water-confining crack subjected to a compressive stress of 70 MPa at its crack tip (Figure 5, right) displays a remarkably different behavior compared to that shown in the corresponding panel of Figure 4. In fact, as the crack size exceeds the decay length, ℓ, corresponding to a value $k_T \ell \approx 5$, the ratio rapidly increases to reach values larger than one. This prediction can be explained as the result of an increasingly larger portion of the crack surface being subjected to a static pressure smaller than the amplitude of the modulation. Since the ratio R measures the relative variation of the backscattered signal caused by the modulation, the larger the portion of the crack, the opening of which is significantly affected by the modulation, the larger R. The extreme example of this situation is provided by the results of the previous figure in which ℓ is infinity. For $P_{\text{tip}} = 70$ MPa, the variation of the opening of the crack produces nearly no modulation of the scattered field since nowhere along the surface the crack opens. On the other hand, for $P_{\text{tip}} = 5$ MPa, the whole surface of the crack completely opens and closes, causing the largest variation of the backscattering considered in this work. The behavior of the curve associated with a pressure of 5 MPa at the crack tip may also be interpreted along the same line. Of interest is also the observation that the two curves appear to converge towards each other as the size of the crack increases. This result is further confirmed by those obtained if the decay length is decreased to become $\ell = 0.1$ mm, as shown in Figure 6, right. On the other hand, the predictions concerning a dry surface-breaking crack, which is partially closed by the same pressure field (Figure 6, left), do not present features which significantly differ from those already shown in the left panels of Figures 4 and 5. Also worthy of attention is the difference between the values of the plateau in the right panels of 5 and 6, the former being slightly larger than the latter (1 versus 0.75). This finding may be expected in virtue of positive correlation between the values of ℓ and the extent of the region over which a significant variation of the local stiffness takes place. That is to say, the wider this region, the stronger the effect of the modulation on the amplitude of the backscattered wave, the extreme case being that considered in Figure 4 for $P_{\text{tip}} = 5$ MPa.

The investigation carried out on a surface-breaking crack was repeated with a subsurface crack. Contrary to the former case, the investigation on the latter yielded results which do not substantially differ from each other. For this reason, only the predictions on the dependence of the ratio R on the size of a crack, $d = (b - a)$, which is subjected to a pressure field decaying with a constant $\ell = 1$ mm are presented in Figure 7, those on the left being obtained for $P_{\text{tip}} = 5$ MPa, while those on the right refer to $P_{\text{tip}} = 70$ MPa. Each figure illustrates the behavior of R for three values of the ligament size: $a/\lambda_T = 0.4$, 1 and 2. The most relevant feature of these results is that, with the exception of a small range of values of $k_T d$

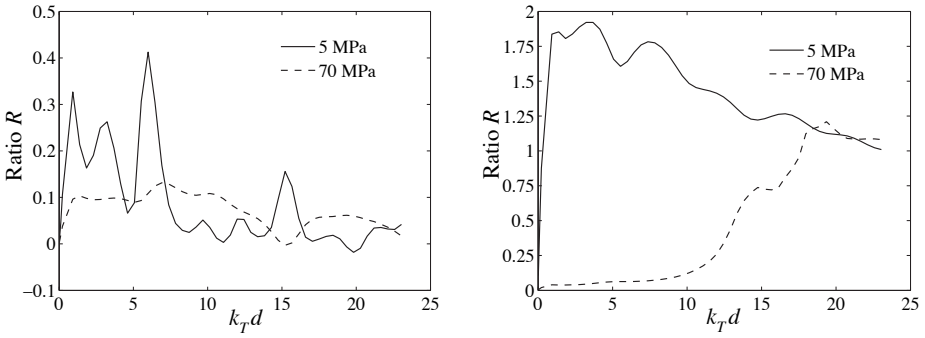

Figure 5. Ratio R versus nondimensional crack size $k_T d$ for values of the pressure at the crack tip equal to 5 MPa and 70 MPa. The pressure distribution decays exponentially from the crack tip with a characteristic length $\ell = 1$ mm. Left: dry surface-breaking crack. Right: water-confining surface-breaking crack.

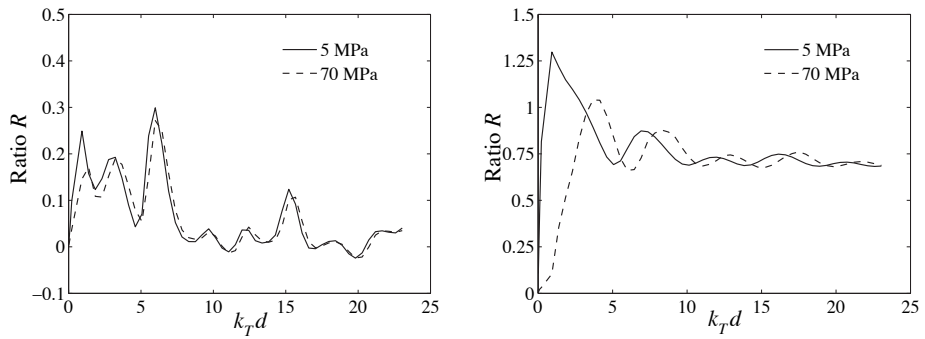

Figure 6. Ratio R versus nondimensional crack size $k_T d$ for values of the pressure at the crack tip equal to 5 MPa and 70 MPa. The pressure distribution decays exponentially from the crack tip with a characteristic length $\ell = 0.1$ mm. Left: dry surface-breaking crack. Right: water-confining surface-breaking crack.

corresponding to cracks smaller than one wavelength of the incident wave, the ratio R always remains below a threshold value of 0.3.

In view of earlier results proving the higher sensitivity of shear waves to small surface breaking cracks when they are insonified at angles of incidence just above the critical angle of longitudinal waves [Pecorari and Poznic 2005; Pecorari 2005], the behavior of the ratio R has been examined also under these conditions, and found to yield no clear criterion to discern subsurface from surface-breaking cracks.

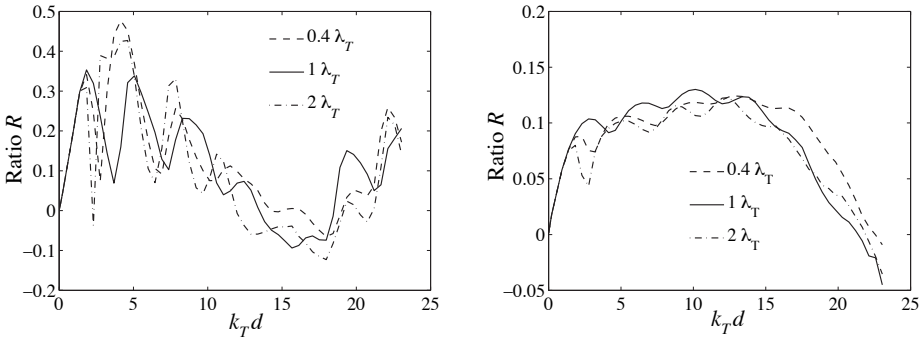

Figure 7. Ratio R versus nondimensional crack size $k_T d = k_T(b-a)$ for values of the ligament, a, equal to $0.4\lambda_T$, $1\lambda_T$, and $2\lambda_T$. The pressure distribution decays exponentially from the crack tip with a characteristic length $\ell = 1$ mm. Left: $P_{\text{tip}} = 5$ MPa. Right: $P_{\text{tip}} = 70$ MPa.

Similar negative results have obtained with longitudinal waves at 45 degrees, 60 degrees and 85 degrees incidence.

Finally, the results in Figure 8 concern the sensitivity of the ratio R to a variation of the angle on incidence from 45 degrees to 40 degrees, both for a surface-breaking crack filled with water (left), and for a dry subsurface crack (right). The pressure closing the crack is characterized by $P_{\text{tip}} = 70$ MPa and $\ell = 0.1$ mm, which is the less favorable of the two cases. Similar results have been obtained for an angle of incidence equal to 50 degrees and by reducing the value of the pressure at the crack tip to 5 MPa. The main conclusion to be drawn from the latter results is that the proposed technique appears to be robust within a variation of the angle of incidence of at least ± 5 degrees, since they confirm the results presented earlier.

5. Summary and concluding remarks

The potential use of the modulation technique to discern surface-breaking from subsurface cracks in components carrying pressurized water has been investigated theoretically. To that end, a model predicting the backscattered signal from dry and water-confining surface-breaking cracks and from subsurface cracks has been developed.

By using the backscattered signals recorded at the two turning points of a modulation cycle, $B^{-,+}$, and when the no modulation is applied, B_0, the ratio

$$R = \frac{B^- - B^+}{B_0}$$

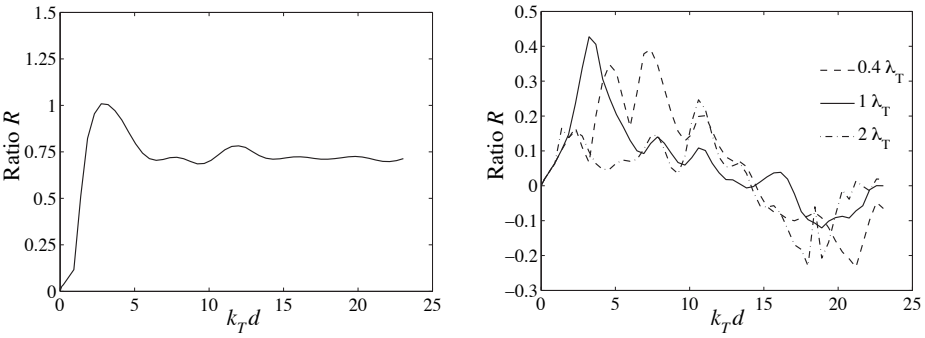

Figure 8. Ratio R versus nondimensional crack size $k_T d = k_T(b-a)$. The pressure distribution decays exponentially from the crack tip with a characteristic length $\ell = 0.1$ mm, and $P_{\text{tip}} = 70$ MPa. The angle of incidence is $\theta_{\text{in}} = 40$ degree. Left: Water-confining, surface-breaking crack. Right: subsurface crack with ligament size a equal to $0.4\lambda_T$, $1\lambda_T$, and $2\lambda_T$.

has been constructed. This ratio does not depend on the amplitude of the incident wave, though it appears to vary with both angle of incidence and wave polarization. For a shear vertical wave at 45 degree incidence, R is predicted to exceeds a threshold limit of 0.5 when a surface-breaking crack is filled with water, while it is always lower than 0.5 if the crack, whether surface-breaking or subsurface, is dry. The difference in the values of the ratio is ascribed to the dramatic variation of the normal stiffness of a partially closed, water-confining crack as the surfaces of the latter come into contact, and it may be used as a criterion for differentiating water-confining surface-breaking from subsurface cracks.

To confirm the validity of the proposed method a deeper investigation into the role of the rms roughness of the composite interface formed by the crack surfaces needs to be carried out. In fact, as illustrated in [Pecorari and Poznic 2005], the variation of the normalized normal stiffness of a water-confining interface is considerably reduced when the rms roughness of the interface increases from 0.1 μm to 1.5 μm. In this context, results by Parisi et al. [2000] (see also references therein) concerning the self-affine nature of the surfaces of fatigue cracks also need be taken into account if the profile of a stress-corrosion crack displays similar properties. Should this be the case, in fact, the extent to which a self-affine profile can be represented by models describing the statistical properties of an infinite interface treated as a stochastic process with spectrum containing components with arbitrarily small wavelengths must be reassessed. Of relevance to the behavior of the partially closed crack tip and to the model used to predict its acoustic response is

also the asymptotic behavior of the normal stiffness in proximity of the crack tip. In this work, the crack is assumed to be either uniformly closed or increasingly open as the observation point moves from the tip toward the mouth or center of the crack. Watanabe et al. [2005] have recently brought to the authors' attention the incompatibility between the asymptotic behavior of the stress ($\propto \sqrt{1/r}$) and of the displacement discontinuity ($\propto \sqrt{r}$) when the crack stiffness is assumed to be constant and finite. This incompatibility would be removed if the self-affine nature of the crack surfaces were considered. In fact, the rms roughness evaluated over an interval shorter than the smaller cut-off wavelength of the profile's power spectrum, and including the crack tip, would be zero. Thus, the crack would be either completely open or completely closed in the neighborhood of its crack tip. In the first case $K_N = 0$, in the second $K_N \to \infty$, and in both the use of the spring boundary conditions would be compatible with the assumed asymptotic behavior of the quantities involved. However, whether either condition would extend far enough from the crack tip to affect the numerical solution of the scattering problem obtained in this work remains a matter to investigate. The limits of the model notwithstanding, it is the authors' opinion that the proposed method deserves the consideration of a working hypothesis for further experimental investigation, and that alone can provide a definite answer to the problem of interest to this communication.

Acknowledgments

This work was carried out as part of the project entitled "Detection of stress-corrosion cracks by means of nonlinear scattering of ultrasonic waves" which is sponsored by the Swedish Centre for Nuclear Technology.

Appendix

In this appendix, the integral equations and the formulas expressing the displacement components of the scattered field in terms of the solutions of the former are given in the case in which the crack is subsurface. The integral equations are found by enforcing the boundary conditions given in equations (3–1) and (3–2) on the general solutions of the equations of motion. These equations are singular and decoupled. Their unknowns, $A(S)$ and $B(S)$, are functions representing the tangents of the tangential and normal crack opening displacement components, respectively.

Let A_{in} be the amplitude of the incident wave and ξ the transform variable used in the integral representation of the general solution of the equations of motion

(3–4)–(3–7). Introduce the normalized quantities and coordinates

$$\bar{A} = A_{\text{in}} k_L,\ \bar{a} = a k_L,\ \bar{b} = b k_L,\ X = x k_L,\ Y = y k_L,$$
$$\zeta = k_L \xi,\ \beta_L = k_L \alpha_L,\ \text{and } \beta_T = k_L \alpha_T,$$

in which k_L is the wave number of the incident wave; also let H be the Heaviside unit step function. The integral equation for the symmetric problem then becomes

$$\int_{\bar{a}}^{\bar{b}} B(S)\left(\frac{1}{S+Y} - \frac{2\pi\kappa^2}{1-\kappa^2}\bar{K}_N(Y)H(S-Y) + \frac{1}{1-\kappa^2}\int_0^\infty (I_1+I_2)\,d\zeta\right) dS + \int_{\bar{a}}^{\bar{b}} \frac{B(S)}{S-Y}\,dS = \frac{\pi\kappa^2}{2(\kappa^2-1)}\frac{\bar{\sigma}^I_{xx}(Y)}{\bar{A}}, \quad \text{(A-1)}$$

where

$$I_1 = \int_0^\infty \frac{(\kappa^2+2\beta_L^2)(\beta_T^2+\zeta^2)e^{-\beta_L Y} - 4\beta_L\beta_T\zeta^2 e^{-\beta_T Y}}{4\zeta^2\beta_L\beta_T - (\zeta^2+\beta_T^2)^2}\left(F_1 e^{\beta_L S} + F_2 e^{\beta_T S}\right) d\zeta,$$

$$I_2 = \int_0^\infty \left(\frac{(\zeta^2+\beta_T^2)^2 - 4\zeta^2\beta_L\beta_T}{\zeta\beta_L} - \left(2-2\kappa^2\right)\right)\sin(\zeta S)\cos(\zeta Y)\,d\zeta,$$

with $F_1 = \left(-\kappa^2(2-\kappa^2) - 4\beta_L^2\zeta^2\right)/\beta_L^2$ and $F_2 = 4\zeta^2$.

The integral equation associated with the antisymmetric problem is

$$\int_{\bar{a}}^{\bar{b}} B(S)\left(\frac{1}{S+Y} + \frac{\pi\kappa^2}{\kappa^2-1}\bar{K}_T(Y)H(S-Y) + \frac{4}{\kappa^2-1}\int_0^\infty (I_3+I_4)\,d\zeta\right) dS + \int_{\bar{a}}^{\bar{b}} \frac{A(S)}{S-Y}\,dS = \frac{\pi}{(1-\kappa^2)}\frac{\bar{\tau}^I_{xy}(Y)}{\bar{A}}, \quad \text{(A-2)}$$

where

$$I_3 = \int_0^\infty \frac{-4\zeta^2\beta_L\beta_T e^{-\beta_L Y} + (2\zeta^2+\kappa^2)^2 e^{-\beta_T Y}}{4\zeta^2\beta_L\beta_T - (\beta_T^2+\zeta^2)^2}\left(E_1 e^{-\beta_L S} + E_2 e^{-\beta_T S}\right) d\zeta,$$

$$I_4 = \int_0^\infty \left(\frac{4\zeta^2\beta_L\beta_T - (\zeta^2+\beta_T^2)^2}{4\zeta\beta_T} - \tfrac{1}{2}\left(\kappa^2-1\right)\right)\sin(\zeta S)\cos(\zeta Y)\,d\zeta,$$

with $E_1 = -\zeta^2$ and $E_2 = (\zeta^4 - \zeta^2\kappa^2 + \kappa^2/4)/\beta_T^2$. If the crack is surface-breaking, additional terms appear in the integrals I_1 and I_3, namely $F_3 = \kappa^2(2-\kappa^2)/\beta_L^2$ and $E_3 = -\kappa^4/4\beta_T^2$, respectively; see also [Mendelsohn et al. 1980]. In all these expressions $\kappa = k_T/k_L$. The right-hand sides of (A-1) and (A-2) are the respective components of the stress field carried by the incident wave.

The components of the displacement field scattered by a subsurface crack, normalized by the amplitude of the incident wave A_{in} and propagating in the positive quarter-space, are given by the following expression:

Symmetric problem.

$$U^S(X,Y)=$$
$$\frac{2}{\pi}\int_0^\infty d\zeta\int_{\bar a}^{\bar b}\left(\frac{(\beta_T^2+\zeta^2)(F_1e^{-\beta_L S}+F_2e^{-\beta_T S})}{\kappa^2\left(4\zeta^2\beta_L\beta_T-(\beta_T^2+\zeta^2)^2\right)}\left(\zeta e^{-\beta_L Y}-\frac{2\zeta\beta_L\beta_T}{\beta_T^2+\zeta^2}e^{-\beta_T Y}\right)\sin(\zeta X)\right.$$
$$\left.+\left(\frac{2\zeta}{\kappa^2}e^{-\beta_T X}-\frac{\beta_T^2+\zeta^2}{\zeta\kappa^2}e^{-\beta_L X}\right)\cos(\zeta Y)\sin(\zeta S)\right)B(S)\,dS,$$

$$V^S(X,Y)=$$
$$\frac{2}{\pi}\int_0^\infty d\zeta\int_{\bar a}^{\bar b}\left(\frac{(\beta_T^2+\zeta^2)(F_1e^{-\beta_L S}+F_2e^{-\beta_T S})}{\kappa^2\left(4\zeta^2\beta_L\beta_T-(\beta_T^2+\zeta^2)^2\right)}\left(\beta_L e^{-\beta_L Y}-\frac{2\zeta^2\beta_L}{\beta_T^2+\zeta^2}e^{-\beta_T Y}\right)\cos(\zeta X)\right.$$
$$\left.+\left(\frac{2\beta_T}{\kappa^2}e^{-\beta_T X}-\frac{(\beta_T^2+\zeta^2)}{\beta_L\kappa^2}e^{-\beta_L X}\right)\sin(\zeta Y)\sin(\zeta S)\right)B(S)\,dS.$$

Antisymmetric problem.

$$U^a(X,Y)=$$
$$\frac{2}{\pi}\int_0^\infty d\zeta\int_{\bar a}^{\bar b}\left(\frac{(E_1e^{-\beta_L S}+E_2e^{-\beta_T S})}{4\zeta^2\beta_L\beta_T-(\beta_T^2+\zeta^2)^2}\left(4\zeta^2\beta_T e^{-\beta_L Y}-2\beta_T(\beta_T^2+\zeta^2)e^{-\beta_T Y}\right)\cos(\zeta X)\right.$$
$$\left.-\left(\beta_L e^{-\beta_L X}-\frac{\beta_T^2+\zeta^2}{2\beta_T}e^{-\beta_T X}\right)\sin(\zeta Y)\sin(\zeta S)\right)A(S)\,dS,$$

$$V^a(X,Y)=$$
$$\frac{2}{\pi}\int_0^\infty d\zeta\int_{\bar a}^{\bar b}\left(\frac{(E_1e^{-\beta_L S}+E_2e^{-\beta_T S})}{4\zeta^2\beta_L\beta_T-(\beta_T^2+\zeta^2)^2}\left(-4\zeta\beta_T\beta_L e^{-\beta_L Y}+2\zeta(\beta_T^2+\zeta^2)e^{-\beta_T Y}\right)\sin(\zeta X)\right.$$
$$\left.-\left(\zeta e^{-\beta_L X}-\frac{\beta_T^2+\zeta^2}{2\zeta}e^{-\beta_T X}\right)\cos(\zeta Y)\sin(\zeta S)\right)A(S)\,dS.$$

Similar expressions for the displacement components scattered by a surface-breaking crack can be found in [Mendelsohn et al. 1980].

References

[Achenbach et al. 1980] J. D. Achenbach, L. M. Keer, and D. A. Mendelsohn, "Elastodynamic analysis of an edge crack", *J. Appl. Mech.* (*Trans. ASME*) **47**:3 (1980), 551–556. MR 81j:73073

[Baik and Thompson 1984] J. M. Baik and R. B. Thompson, "Ultrasonic scattering from imperfect interfaces: a quasi-static model", *J. Nondestr. Eval.* **4**:3–4 (1984), 177–196.

[Baltazar et al. 2002] A. Baltazar, S. I. Rokhlin, and C. Pecorari, "On the relationship between ultrasonic and micromechanical properties of contacting rough surfaces", *J. Mech. Phys. Solids* **50**:7 (2002), 1397–1416.

[Brind and Achenbach 1981] R. J. Brind and J. D. Achenbach, "Scattering of longitudinal and transverse waves by a sub-surface crack", *J. Sound Vib.* **78** (1981), 555–563.

[Chan and Horn 1985] D. Y. C. Chan and R. G. Horn, "The drainage of thin liquid films between solid surfaces", *J. Chem. Phys.* **83**:10 (1985), 5311–5324.

[Das et al. 1996] S. K. Das, M. M. Sharma, and R. S. Schechter, "Solvation force in confined molecular fluids using molecular dynamics simulation", *J. Phys. Chem.* **100**:17 (1996), 7122–7129.

[Drinkwater et al. 1996] B. W. Drinkwater, R. S. Dwyer-Joyce, and P. Cawley, "A study of the interaction between ultrasound and a partially contacting solid-solid interface", *P. Roy. Soc. Lond. A Mat.* **452**:1955 (1996), 2613–2628.

[Grabbe and Horn 1993] A. Grabbe and R. G. Horn, "Double-layer and hydration forces measured between silica sheets subjected to various surface treatments", *J. Colloid Interf. Sci.* **157**:2 (1993), 375–383.

[Ho et al. 1998] R. Ho, J. Y. Yuan, and Z. Shao, "Hydration force in the atomic force microscope: a computational study", *Biophys. J.* **75**:2 (1998), 1076–1083.

[Israelachvili 1992] J. N. Israelachvili, *Intermolecular and surface forces*, 2nd ed., Academic Press, London, 1992.

[Jenssen et al. 2000] A. Jenssen, K. Norrgård, R. Lundström, B. Claesson, and H. Ericsson, "Metallographic examination of cracks in nozzle to safe-end weld of alloy 182 in Ringhals 4", Technical Report N(H)-00/099, Studsvik, 2000.

[Kazakov et al. 2002] V. V. Kazakov, A. Sutin, and P. A. Johnson, "Sensitive imaging of an elastic nonlinear wave-scattering source in a solid", *Appl. Phys. Lett.* **81**:4 (2002), 646–648.

[Kim et al. 2004a] J. Y. Kim, A. Baltazar, and S. I. Rokhlin, "Ultrasonic assessment of rough surface contact between solids from elastoplastic loading-unloading hysteresis cycle", *J. Mech. Phys. Solids* **52**:8 (2004), 1911–1934.

[Kim et al. 2004b] J. Y. Kim, V. A. Yakovlev, and S. I. Rokhlin, "Surface acoustic wave modulation on a partially closed fatigue crack", *J. Acoust. Soc. Am.* **115**:5 (2004), 1961–1972.

[Lavrentyev and Rokhlin 1998] A. I. Lavrentyev and S. I. Rokhlin, "Ultrasonic spectroscopy of imperfect contact interfaces between a layer and two solids", *J. Acoust. Soc. Am.* **103**:2 (1998), 657–664.

[Mendelsohn et al. 1980] D. A. Mendelsohn, J. D. Achenbach, and L. M. Keer, "Scattering of elastic waves by a surface-breaking crack", *Wave Motion* **2**:3 (1980), 277–292.

[Nagy 1992] P. B. Nagy, "Ultrasonic classification of imperfect interfaces", *J. Nondestr. Eval.* **11**:3–4 (1992), 127–140.

[Newman et al. 2003] J. A. Newman, W. T. Riddell, and R. S. Piascik, "Analytical and experimental study of near-threshold interactions between crack closure mechanisms", Technical report TM-2003-211755, ARL-TR-2774, NASA, 2003, Available at http://citeseer.ist.psu.edu/615746.html.

[Parisi et al. 2000] A. Parisi, G. Caldarelli, and L. Pietronero, "Roughness of fracture surfaces", *Europhys. Lett.* **52**:3 (2000), 304–310.

[Pashley and Israelachvili 1984] R. M. Pashley and J. N. Israelachvili, "Molecular layering of water in thin films between mica surfaces and its relation to hydration forces", *J. Colloid Interf. Sci.* **101**:2 (1984), 511–523.

[Pecorari 2005] C. Pecorari, "A note on the sensitivity of *SV* wave scattering to surface-breaking cracks", *Ultrasonics* **43**:7 (2005), 508–511.

[Pecorari and Poznic 2005] C. Pecorari and M. Poznic, "Nonlinear acoustic scattering by a partially closed surface-breaking crack", *J. Acoust. Soc. Am.* **117**:2 (2005), 592–600.

[Pecorari and Poznic 2006] C. Pecorari and M. Poznic, "On the linear and nonlinear acoustic properties of dry and water-confining elasto-plastic interfaces", *P. Roy. Soc. Lond. A Mat.* **462**:2067 (2006), 769–788.

[Rokhlin et al. 2004] S. I. Rokhlin, L. Wang, B. Xie, V. A. Yakovlev, and L. Adler, "Modulated angle beam ultrasonic spectroscopy for evaluation of imperfect interfaces and adhesive bonds", *Ultrasonics* **42**:1–9 (2004), 1037–1047.

[Watanabe et al. 2005] K. Watanabe, S. Ueda, and S. Biwa, 2005. private communication.

[Xiao and Nagy 1998] H. Xiao and P. B. Nagy, "Enhanced ultrasonic detection of fatigue cracks by laser-induced crack closure", *J. Appl. Phys.* **83**:12 (1998), 7453–7460.

Received 15 Dec 2005.

MILAN POZNIC: milan@kth.se
Marcus Wallenberg Laboratory, Department of Aeronautical and Vehicle Engineering, Royal Institute of Technology, SE 10044 Stockholm, Sweden

CLAUDIO PECORARI: pecorari@kth.se
Marcus Wallenberg Laboratory, Department of Aeronautical and Vehicle Engineering, Royal Institute of Technology, SE 10044 Stockholm, Sweden

JOURNAL OF MECHANICS OF MATERIALS AND STRUCTURES
Vol. 1, No. 4, 2006

NANOPARTICLES UNDER THE INFLUENCE OF SURFACE/INTERFACE ELASTICITY

CHANGWEN MI AND DEMITRIS A. KOURIS

We investigate the effect of surface/interface elasticity in the presence of nanoparticles, embedded in a semi-infinite elastic medium. The work is motivated by the technological significance of self-organization of strained islands in multilayered systems. Islands, adatom-clusters, or quantum dots are modeled as inhomogeneities, with properties that differ from the ones of the surrounding material. Within the framework of continuum elasticity theory, the Papkovitch–Neuber displacement methodology coupled with Gurtin's surface elasticity yields an analytical solution. The elastic field is expressed in terms of four sets of spherical and cylindrical harmonics. Surface elasticity introduces an additional length scale and results suggest that local stresses are significantly affected by the size of the nanoparticles.

1. Introduction

Self-assembly presents a promising alternative in fabrication of quantum dots. The main requirements for applications are size uniformity and high spatial density of dots. Currently, uniformity is on the order of 10% and no systematic approach has been proposed for its improvement. Covering of the first generation of islands or dots by a cap layer (say, of a substrate material) and growth of subsequent generations of dots result in the ultimate development of a two-dimensional superlattice. The spatial uniformity of island structures was first addressed by Tersoff et al. [1996]. Their islands were modeled as spherical inclusions (same properties as the surrounding material) in an elastic half-space, a problem that was originally solved by Mindlin and Cheng [1950]. Tersoff et al. [1996] chose to effectively treat the islands as point sources (centers of dilatation) in a semi-infinite matrix. In most material systems used in practice, however, quantum dots and the surrounding material do not have identical material properties.

The presence of inhomogeneities in elastic media has been a well studied subject in applied mechanics for several decades [Mura 1987]. Until recently, however, almost all such studies have been concerned with either an infinite medium or a semi-infinite body without including surface effects, either on the plane boundary,

Keywords: surface/interface effects, inhomogeneity, half-space.

or at the matrix/inhomogeneity interface. Mindlin and Cheng [1950] first studied the thermoelastic stress in a semi-infinite solid containing a spherical inclusion subjected to dilatational thermal expansion. Tsuchida [1970; 1972] derived a three-dimensional solution for displacements and stresses in a half-space having a spherical cavity, for various loading conditions. The classical solution for the elastic state of a spherical inhomogeneity in a semi-infinite elastic body without incorporating surface effects was obtained by Tsutsui et al. [1974].

These problems were solved within the context of classical elasticity, without accounting for size effects. It is well known, however, that under certain circumstances, surface elasticity can be of importance. For material structures with one or more dimensions at the nanometer scale (for example, thin film and nano-sized inhomogeneities), the surface area to volume ratio becomes significant. Consequently, surface effects have a major influence on the local stress-strain field.

The physical origin of the surface stress can be explained by the nature of the chemical bonding of those atoms close to the surface. The loss of the translational symmetry in the direction normal to surface results in a different bonding configuration in the vicinity of the surface, when compared to the one in the bulk. The atoms at and close to the surface lose some of their neighbors or are bonded to some "wrong" neighbors. As a result, the equilibrium interatomic distance for such atoms is different from the bulk atoms. This phenomenon results in an "excess" stress for atoms close to the surface.

The theory of isotropic surface elasticity was established by Gurtin and Murdoch [1975a; 1975b; 1978]. Cahn and Larche [1982] studied the mechanical and chemical equilibrium of a small spherical precipitate in an infinite matrix of a different phase. Recently Sharma et al. [2003] derived closed-form expressions for the displacements and stresses of a strained spherical inhomogeneity by using a variational approach. Sharma and Ganti [2004] also studied the elastic state of spherical and cylindrical inhomogeneities embedded in an infinite elastic medium, by combining the classical Green's function method with linear isotropic surface elasticity theory. Duan et al. [2005b] developed explicit forms of the stress concentration tensor for spherical and circular inhomogeneities with surface effects. While surface/interface effects were incorporated, all of these investigations have been limited to the study of an infinite elastic medium.

In the present work, we model a nanoparticle or island as a spherical inhomogeneity problem inside an elastic half-space. The material properties of the inhomogeneity are different from those of the surrounding material (matrix). The system is subjected to biaxial tension applied at the remote boundary of the matrix, parallel to the free surface. The ensuing three-dimensional problem is solved with the help of the Papkovitch–Neuber displacement potential theory. Section 2 illustrates the formulation of the problem of an embedded inhomogeneity in a half-space including

surface/interface effects. Following [Gurtin et al. 1998], the displacements on the surface/interface boundary are still considered to be continuous. The tractions both on the plane boundary and at the matrix/inhomogeneity interface, however, are discontinuous, as a result of the well known Laplace–Young effects [Adamson 1982, Chapter II]. The problem is solved in Section 3, incorporating the surface/interface stress boundary conditions. Section 4 illustrates the impact of surface/interface effects as the location, size, and material properties of the inhomogeneity change. Finally, a series of conclusions are presented in Section 5. The elaborate and quite tedious mathematical formulation presented in Sections 2 and 3 is the result of a conscious decision to provide a complete, self-contained document, since the detailed methodology cannot be found elsewhere.

2. Displacement formulation

Let us consider a spherical inhomogeneity in a semi-infinite elastic solid, as shown in Figure 1. The center of the inhomogeneity coincides with the center of the coordinate system. Cylindrical (r, θ, z) and spherical (R, θ, φ) coordinates will be used alternatively throughout the manuscript. Following [Gurtin and Murdoch 1978], the plane boundary $(z = -c)$ and the matrix/inhomogeneity interface $(R = a)$ are modeled as thin films of vanishing depth; both "surfaces" adhere to the bulk without slipping. The model is based on the assumption of a linearly elastic and isotropic material system.

The governing equations for the bulk are given by

$$\sigma_{ij,j} = 0, \quad \sigma_{ij} = 2G\left(\frac{\nu}{1-2\nu}\,\varepsilon_{kk}\delta_{ij} + \varepsilon_{ij}\right), \quad \varepsilon_{ij} = \tfrac{1}{2}(u_{i,j} + u_{j,i}),$$

coupled with the equations for surfaces and interfaces derived in [Gurtin and Murdoch 1975a; 1975b]

$$\begin{aligned} \varepsilon^S_{\alpha\beta} &= \tfrac{1}{2}(P_{ij}\varepsilon_{jk}P_{kl} + P_{ij}\bar{\varepsilon}_{jk}P_{kl}), \\ \sigma^S_{\alpha\beta} &= \tau_0\delta_{\alpha\beta} + 2(\mu^S - \tau_0)\varepsilon^S_{\alpha\beta} + (\lambda^S + \tau_0)\varepsilon^S_{\kappa\kappa}\delta_{\alpha\beta} + \tau_0(u^S_\alpha)^S_{,\beta}, \\ [\sigma_{ij}]n_j &= -(\sigma^S_{\alpha\beta})^S_{,\beta}. \end{aligned} \tag{1}$$

By convention, the Roman subscripts denote the quantities belonging to the bulk and assume values from 1 to 3, while the Greek refer to the surface/interface and assume values from 1 to 2. Here u, ε and σ denote displacement, strain and stress fields in bulk; the material properties of the bulk are represented by the shear modulus G and Poisson's ratio ν; λ^S, μ^S and τ_0 refer to the surface Lamé constants, and the residual surface stress when the bulk is unstrained, respectively; $[\sigma_{ij}] = \sigma_{ij}$ (out) $- \sigma_{ij}$ (in) and n is the outward unit normal to the surface; ε^S and σ^S denote the surface strain and surface stress fields on the surface. Since

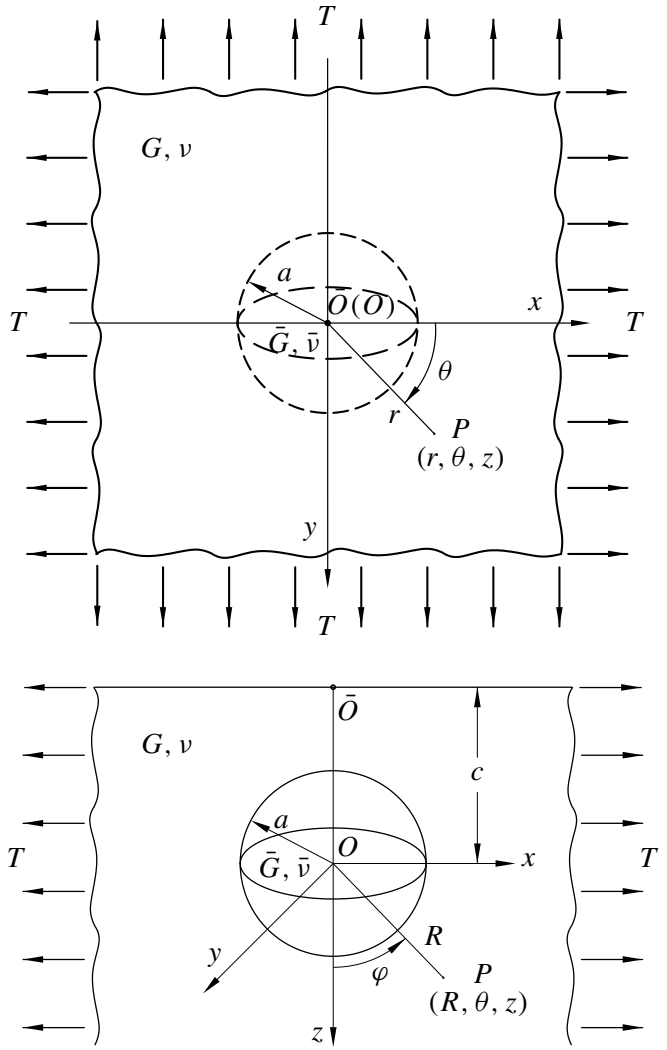

Figure 1. Spherical inhomogeneity in a half-space.

the surface is defined as a two-dimensional continuous space, the components of surface strain and surface stress with direction normal to the surface vanish. $P_{ij} = \delta_{ij} - n_i n_j$ is the projection tensor which allows tensor transformation between the three-dimensional bulk space and the two-dimensional surface space. In terms of the projection tensor, the surface strain is defined as the average value of the bulk strains from both sides projected onto the surface. The notion of surface gradient, surface divergence of a vector, and surface divergence of a superficial tensor can

be clarified by the following identities (see [Gurtin et al. 1998]):

$$(u^S_\alpha)^S_{,\beta} = u_{i,k}P_{kj}, \quad a_\alpha(\alpha^S_{\alpha\beta})^S_{,\beta} = (\sigma^S_{\beta\alpha}\alpha_\beta)^S_{,\alpha} = \mathbf{tr}\big((\sigma^S_{\beta\alpha}\alpha_\beta)^S_{,\gamma}\big), \tag{2}$$

for every constant vector a, where **tr** is the trace. For convenience, the surface divergence of the surface stress tensor will be denoted by γ.

Both in the embedded particle and surrounding matrix, the displacement field satisfies the following Navier's equation (without body forces):

$$\frac{1}{1-2\nu}u_{j,ji} + u_{i,jj} = 0.$$

In the case of axial symmetry without torsion, its solution can be expressed as superposition of two displacement fields due to potentials ϕ_0 and ϕ_3. In cylindrical coordinates, these displacements and the corresponding strains and stresses are given by

$$\begin{aligned}
2Gu_r &= \frac{\partial\phi_0}{\partial r} + z\frac{\partial\phi_3}{\partial r},\\
2Gu_z &= \frac{\partial\phi_0}{\partial z} + z\frac{\partial\phi_3}{\partial z} - (3-4\nu)\phi_3,\\
2G\varepsilon_{rr} &= -\frac{1}{r}\frac{\partial\phi_0}{\partial r} - \frac{\partial^2\phi_0}{\partial z^2} - \frac{z}{r}\frac{\partial\phi_3}{\partial r} - z\frac{\partial^2\phi_3}{\partial z^2},\\
2G\varepsilon_{\theta\theta} &= \frac{1}{r}\frac{\partial\phi_0}{\partial r} + \frac{z}{r}\frac{\partial\phi_3}{\partial r},\\
2G\varepsilon_{zz} &= \frac{\partial^2\phi_0}{\partial z^2} - 2(1-2\nu)\frac{\partial\phi_3}{\partial z} + z\frac{\partial^2\phi_3}{\partial z^2},\\
2G\varepsilon_{rz} &= \frac{\partial^2\phi_0}{\partial r\partial z} - (1-2\nu)\frac{\partial\phi_3}{\partial r} + z\frac{\partial^2\phi_3}{\partial r\partial z},\\
\sigma_{rr} &= -\frac{1}{r}\frac{\partial\phi_0}{\partial r} - \frac{\partial^2\phi_0}{\partial z^2} - \frac{z}{r}\frac{\partial\phi_3}{\partial r} - z\frac{\partial^2\phi_3}{\partial z^2} - 2\nu\frac{\partial\phi_3}{\partial z},\\
\sigma_{\theta\theta} &= \frac{1}{r}\frac{\partial\phi_0}{\partial r} + \frac{z}{r}\frac{\partial\phi_3}{\partial r} - 2\nu\frac{\partial\phi_3}{\partial z},\\
\sigma_{zz} &= \frac{\partial^2\phi_0}{\partial z^2} - 2(1-\nu)\frac{\partial\phi_3}{\partial z} + z\frac{\partial^2\phi_3}{\partial z^2},\\
\sigma_{rz} &= \frac{\partial^2\phi_0}{\partial r\partial z} - (1-2\nu)\frac{\partial\phi_3}{\partial r} + z\frac{\partial^2\phi_3}{\partial r\partial z},\\
u_\theta &= 0, \quad \varepsilon_{r\theta} = \varepsilon_{\theta z} = 0, \quad \sigma_{r\theta} = \sigma_{\theta z} = 0,
\end{aligned} \tag{3}$$

where $\nabla^2\phi_0 = \nabla^2\phi_3 = 0$ and $\nabla^2 = \dfrac{\partial^2}{\partial r^2} + \dfrac{1}{r}\dfrac{\partial}{\partial r} + \dfrac{\partial^2}{\partial z^2}$. Converting these equations to spherical coordinates via

$$z = R\cos\varphi \quad \text{and} \quad r = R\sin\varphi,$$

we get for the spherical components of displacements, strains and stresses

$$2Gu_R = \frac{\partial\phi_0}{\partial R} + \mu\Big(R\frac{\partial\phi_3}{\partial R} - (3-4\nu)\phi_3\Big),$$

$$2Gu_\varphi = \sqrt{1-\mu^2}\Big(-\frac{1}{R}\frac{\partial\phi_0}{\partial\mu} - \mu\frac{\partial\phi_3}{\partial\mu} + (3-4\nu)\phi_3\Big),$$

$$2G\varepsilon_{RR} = \frac{\partial^2\phi_0}{\partial R^2} + \mu\Big(R\frac{\partial^2\phi_3}{\partial R^2} - 2(1-2\nu)\frac{\partial\phi_3}{\partial R}\Big),$$

$$2G\varepsilon_{\theta\theta} = \frac{1}{R}\Big(\frac{\partial\phi_0}{\partial R} - \frac{\mu}{R}\frac{\partial\phi_0}{\partial\mu}\Big) + \mu\Big(\frac{\partial\phi_3}{\partial R} - \frac{\mu}{R}\frac{\partial\phi_3}{\partial\mu}\Big),$$

$$2G\varepsilon_{\varphi\varphi} = -\frac{\partial^2\phi_0}{\partial R^2} - \frac{1}{R}\frac{\partial\phi_0}{\partial R} + \frac{\mu}{R^2}\frac{\partial\phi_0}{\partial\mu} - R\mu\frac{\partial^2\phi_3}{\partial R^2} - \mu\frac{\partial\phi_3}{\partial R} + \frac{\big(-2(1-2\nu)+(3-4\nu)\mu^2\big)}{R}\frac{\partial\phi_3}{\partial\mu},$$

$$2G\varepsilon_{R\varphi} = \sqrt{1-\mu^2} \times \Big(\frac{1}{R^2}\frac{\partial\phi_0}{\partial\mu} - \frac{1}{R}\frac{\partial^2\phi_0}{\partial R\partial\mu} + (1-2\nu)\frac{\partial\phi_3}{\partial R} - \mu\frac{\partial^2\phi_3}{\partial R\partial\mu} + \frac{2(1-\nu)\mu}{R}\frac{\partial\phi_3}{\partial\mu}\Big),$$

$$\sigma_{RR} = \frac{\partial^2\phi_0}{\partial R^2} + R\mu\frac{\partial^2\phi_3}{\partial R^2} - 2(1-\nu)\mu\frac{\partial\phi_3}{\partial R} - \frac{2\nu(1-\mu^2)}{R}\frac{\partial\phi_3}{\partial\mu},$$

$$\sigma_{\theta\theta} = \frac{1}{R}\Big(\frac{\partial\phi_0}{\partial R} - \frac{\mu}{R}\frac{\partial\phi_0}{\partial\mu}\Big) + (1-2\nu)\mu\frac{\partial\phi_3}{\partial R} - \frac{\big(\mu^2(1-2\nu)+2\nu\big)}{R}\frac{\partial\phi_3}{\partial\mu},$$

$$\sigma_{\varphi\varphi} = -\frac{\partial^2\phi_0}{\partial R^2} - \frac{1}{R}\frac{\partial\phi_0}{\partial R} + \frac{\mu}{R^2}\frac{\partial\phi_0}{\partial\mu} - R\mu\frac{\partial^2\phi_3}{\partial R^2} - (1+2\nu)\mu\frac{\partial\phi_3}{\partial R} + \frac{(3-2\nu)\mu^2 - 2(1-\nu)}{R}\frac{\partial\phi_3}{\partial\mu},$$

$$\sigma_{R\varphi} = \sqrt{1-\mu^2}\Big(\frac{1}{R^2}\frac{\partial\phi_0}{\partial\mu} - \frac{1}{R}\frac{\partial^2\phi_0}{\partial R\partial\mu} + (1-2\nu)\frac{\partial\phi_3}{\partial R} - \mu\frac{\partial^2\phi_3}{\partial R\partial\mu} + \frac{2(1-\nu)\mu}{R}\frac{\partial\phi_3}{\partial\mu}\Big),$$

$$u_\theta = 0, \quad 2G\varepsilon_{R\theta} = 2G\varepsilon_{\theta\varphi} = 0, \quad \sigma_{R\theta} = \sigma_{\theta\varphi} = 0, \tag{4}$$

where $\mu = \cos\varphi$, and the harmonic operator now takes the form

$$\nabla^2 = \frac{\partial^2}{\partial R^2} + \frac{2}{R}\frac{\partial}{\partial R} - \frac{2\mu}{R^2}\frac{\partial}{\partial \mu} + \frac{(1-\mu^2)}{R^2}\frac{\partial^2}{\partial \mu^2}.$$

For the purpose of completeness, we now derive general expressions for surface/interface quantities, both on the plane boundary ($z = -c$) and on the matrix/inhomogeneity interface ($R = a$). In cylindrical coordinates, the projection tensor for the plane boundary is given by

$$P_{rr} = P_{\theta\theta} = 1, \quad \text{all other } P_{ij} = 0. \tag{5}$$

Substituting Equations (3) and (5) into the first equation of (1), and the first equation of (2), the surface strain tensor and the surface gradient of the surface displacement on the plane boundary are found to be

$$\varepsilon_{rr}^{fs} = u_{r,r}^{fs} = -\frac{1}{4G}\left(\frac{1}{r}\frac{\partial\phi_0}{\partial r} + \frac{\partial^2\phi_0}{\partial z^2} + \frac{z}{r}\frac{\partial\phi_3}{\partial r} + z\frac{\partial^2\phi_3}{\partial z^2}\right)_{z=-c},$$

$$\varepsilon_{\theta\theta}^{fs} = u_{\theta,\theta}^{fs} = \frac{1}{4G}\left(\frac{1}{r}\frac{\partial\phi_0}{\partial r} + \frac{z}{r}\frac{\partial\phi_3}{\partial r}\right)_{z=-c},$$

$$\varepsilon_{r\theta}^{fs} = u_{r,\theta}^{fs} = 0,$$

where the superscript f denotes the plane boundary. By the use of these relations and the second equation of (1), it is found that

$$\sigma_{rr}^{fs} = \tau_{f0} - \left(\chi_{f2}\frac{1}{r}\frac{\partial\phi_0}{\partial r} + \chi_{f0}\frac{\partial^2\phi_0}{\partial z^2} + \chi_{f2}\frac{z}{r}\frac{\partial\phi_3}{\partial r} + \chi_{f0}z\frac{\partial^2\phi_3}{\partial z^2}\right)_{z=-c}, \tag{6}$$

$$\sigma_{\theta\theta}^{fs} = \tau_{f0} + \left(\chi_{f2}\frac{1}{r}\frac{\partial\phi_0}{\partial r} - \chi_{f1}\frac{\partial^2\phi_0}{\partial z^2} + \chi_{f2}\frac{z}{r}\frac{\partial\phi_3}{\partial r} - \chi_{f1}z\frac{\partial^2\phi_3}{\partial z^2}\right)_{z=-c},$$

$$\sigma_{r\theta}^{fs} = 0,$$

where τ_{f0} denotes the deformation-independent surface stress defined on the plane boundary. The length scale parameters χ_{f0}, χ_{f1}, and χ_{f2} are defined in Equation (28) in the Appendix. The surface divergence of the surface stress tensor can be obtained by transforming the second equation of (2) into cylindrical coordinates. An explicit formula for evaluating this vector can be found in [Duan et al. 2005a, (2.2)]. As a result, the surface divergence of the surface stress γ^f on the plane boundary is given by

$$\gamma_r^f = -\chi_{f0}\left(\frac{\partial^3\phi_0}{\partial r\,\partial z^2} + z\frac{\partial^3\phi_3}{\partial r\,\partial z^2}\right)_{z=-c}, \quad \gamma_\theta^f = \gamma_z^f = 0. \tag{7}$$

For the matrix/inhomogeneity interface ($R = a$), the projection tensor is

$$P_{\theta\theta} = P_{\varphi\varphi} = 1, \quad \text{all other } P_{ij} = 0.$$

The relevant interface quantities can be derived from this equation together with (1), (2) and (4):

$$\varepsilon^s_{\theta\theta} = u^s_{\theta,\theta} = \frac{1}{4G}\left(\frac{1}{R}\frac{\partial\phi_0}{\partial R} - \frac{\mu}{R^2}\frac{\partial\phi_0}{\partial\mu} + \mu\frac{\partial\phi_3}{\partial R} - \frac{\mu^2}{R}\frac{\partial\phi_3}{\partial\mu}\right)_{R=a},$$

$$\varepsilon^s_{\varphi\varphi} = u^s_{\theta,\theta} = \frac{1}{4G}\left(\frac{\mu}{R^2}\frac{\partial\phi_0}{\partial\mu} - \frac{\partial^2\phi_0}{\partial R^2} - \frac{1}{R}\frac{\partial\phi_0}{\partial R} - R\mu\frac{\partial^2\phi_3}{\partial R^2} - \mu\frac{\partial\phi_3}{\partial R} + \frac{-2(1-2\nu)+(3-4\nu)\mu^2}{R}\frac{\partial\phi_3}{\partial\mu}\right)_{R=a},$$

$$\varepsilon^s_{\theta\varphi} = u^s_{\theta,\varphi} = 0,$$

$$\sigma^s_{\theta\theta} = \tau_0 + \left(-\chi_1\frac{\partial^2\phi_0}{\partial R^2} + \chi_2\frac{1}{R}\frac{\partial\phi_0}{\partial R} - \chi_2\frac{\mu}{R^2}\frac{\partial\phi_0}{\partial\mu} - \chi_1 R\mu\frac{\partial^2\phi_3}{\partial R^2} + \chi_2\mu\frac{\partial\phi_3}{\partial R} - \frac{2(1-2\nu)\chi_1 + (\chi_0 - (3-4\nu)\chi_1)\mu^2}{R}\frac{\partial\phi_3}{\partial\mu}\right)_{R=a},$$

$$\sigma^s_{\varphi\varphi} = \tau_0 + \left(-\chi_0\frac{\partial^2\phi_0}{\partial R^2} - \chi_2\frac{1}{R}\frac{\partial\phi_0}{\partial R} + \chi_2\frac{\mu}{R^2}\frac{\partial\phi_0}{\partial\mu} - \chi_0 R\mu\frac{\partial^2\phi_3}{\partial R^2} - \chi_2\mu\frac{\partial\phi_3}{\partial R} + \frac{-2(1-2\nu)\chi_0 + ((3-4\nu)\chi_0 - \chi_1)\mu^2}{R}\frac{\partial\phi_3}{\partial\mu}\right)_{R=a},$$

$$\sigma^s_{\theta\varphi} = 0,$$

$$\gamma_R = \left(-\frac{2\tau_0}{R} + \frac{\chi_3}{R}\frac{\partial^2\phi_0}{\partial R^2} + \chi_3\mu\frac{\partial^2\phi_3}{\partial R^2} + \frac{2(1-\nu)\chi_3(1-\mu^2)}{R^2}\frac{\partial\phi_3}{\partial\mu}\right)_{R=a}, \tag{8}$$

$$\gamma_\theta = 0,$$

$$\gamma_\varphi = \sqrt{1-\mu^2}\left(\frac{\partial}{\partial\mu}\left(\frac{\chi_0}{R}\frac{\partial^2\phi_0}{\partial R^2} + \frac{\chi_2}{R^2}\frac{\partial\phi_0}{\partial R} - \frac{\chi_2}{R^3}\phi_0\right) + \mu\frac{\partial}{\partial\mu}\left(\chi_0\frac{\partial^2\phi_3}{\partial R^2} + \frac{\chi_2}{R}\frac{\partial\phi_3}{\partial R} - \frac{4(1-\nu)\chi_2}{R^2}\phi_3\right) - \left((1-4\nu)\chi_0\frac{\partial^2\phi_3}{\partial R^2} + \frac{(3-8\nu)\chi_0 + \chi_1}{R}\frac{\partial\phi_3}{\partial R}\right)\right)_{R=a},$$

where τ_0 is the deformation-independent interface stress defined at the spherical interface. The interface length scale parameters χ_0, χ_1, χ_2, and χ_3 are defined in Equation (29) of the Appendix.

Given the expressions for the surface divergence of the surface stress (7), the boundary conditions at the free surface can be expressed in cylindrical coordinates

as

$$(\sigma_{rz})_{z=-c} = -\gamma_r^f, \quad (\sigma_{zz})_{z=-c} = 0. \tag{9}$$

At infinity,

$$(\sigma_{rr})_{r\to\infty} = (\sigma_{\theta\theta})_{r\to\infty} = T, \quad (\sigma_{rz})_{r\to\infty} = (\sigma_{zz})_{r\to\infty} = 0, \tag{10}$$

corresponding to the far-field biaxial tension. The boundary conditions at the matrix/inhomogeneity interface consist of the displacement continuity condition and the third equation in (1). These can be rewritten as follows, using Equations (8) for the γ's:

$$\begin{aligned} (u_R)_{R=a} &= (\bar{u}_R)_{R=a}, \quad (u_\varphi)_{R=a} = (\bar{u}_\varphi)_{R=a}, \\ (\sigma_{RR})_{R=a} - (\bar{\sigma}_{RR})_{R=a} &= -\gamma_R, \quad (\sigma_{R\varphi})_{R=a} - (\bar{\sigma}_{R\varphi})_{R=a} = -\gamma_\varphi, \end{aligned} \tag{11}$$

where the quantities denoted by an over bar refer to the inhomogeneity.

In cylindrical and spherical coordinates, the general solution to the harmonic equation can be expressed in terms of cylindrical or spherical harmonics, respectively. Based on these basic solutions, four sets of displacement potentials are selected to represent the solutions to our problem. The first represents the biaxial tension applied at infinity and is given by

$$\frac{\phi_0}{T} = -\frac{(1-\nu)}{(1+\nu)} R^2 P_2(\mu), \qquad \frac{\phi_3}{T} = -\frac{1}{(1+\nu)} R P_1(\mu). \tag{12}$$

Here $P_n(\mu)$ is the Legendre function of the first kind of order n, with $P_0(\mu) = 1$, $P_1(\mu) = \mu$, $P_2(\mu) = (3\mu^2 - 1)/2$, and so forth. In terms of cylindrical coordinates, (12) can be rewritten as

$$\frac{\phi_0}{T} = -\frac{(1-\nu)}{2(1+\nu)}(2z^2 - r^2), \qquad \frac{\phi_3}{T} = -\frac{1}{(1+\nu)} z. \tag{12*}$$

The disturbance due to the presence of the inhomogeneity can be expressed by the following three sets of displacement potentials:

$$\frac{\phi_0}{T} = \sum_{n=0}^{\infty} A_n \frac{P_n(\mu)}{R^{n+1}}, \qquad \frac{\phi_3}{T} = \sum_{n=0}^{\infty} B_n \frac{P_n(\mu)}{R^{n+1}}; \tag{13}$$

$$\frac{\phi_0}{T} = \int_0^\infty \psi_1(\lambda) J_0(\lambda r) e^{-\lambda z}\, d\lambda, \qquad \frac{\phi_3}{T} = \int_0^\infty \lambda \psi_2(\lambda) J_0(\lambda r) e^{-\lambda z}\, d\lambda \tag{14}$$

for the matrix (with $z > -c$, $R > a$), and

$$\frac{\phi_0}{T} = \sum_{n=0}^{\infty} \bar{A}_n R^n P_n(\mu), \qquad \frac{\phi_3}{T} = \sum_{n=0}^{\infty} \bar{B}_n R^n P_n(\mu) \tag{15}$$

for the inhomogeneity ($R < a$). In these expressions, $J_\nu(\lambda r)$ is the Bessel function of the first kind of order ν; A_n, B_n, $\bar{A}_n$ and $\bar{B}_n$ are unknown coefficients of the spherical harmonics; and $\psi_1(\lambda)$ and $\psi_2(\lambda)$ are unknown functions of the integral variable λ. With these choices of the displacement potentials, the boundary condition (10) is satisfied automatically. The unknown constants A_n, B_n, $\bar{A}_n$, $\bar{B}_n$ and the unknown functions $\psi_1(\lambda)$, $\psi_2(\lambda)$ are to be determined by enforcing the boundary conditions (9) and (11).

3. Solution of the problem

The displacement potential (13) is expressed in spherical coordinates. In order to satisfy the boundary condition (9), it must be transformed into cylindrical coordinates. From [Sneddon [1951], p.514], it is found that for $z \geq 0$,

$$\frac{P_n(\mu)}{R^{n+1}} = \frac{1}{n!}\int_0^\infty \lambda^n J_0(\lambda r) e^{-\lambda z}\, d\lambda.$$

Replacing (z) with $(-z)$, (μ) with $(-\mu)$, and with the aid of the parity property of Legendre polynomials, it is found that for $z \leq 0$,

$$\frac{P_n(\mu)}{R^{n+1}} = \frac{(-1)^n}{n!}\int_0^\infty J_0(\lambda r) e^{\lambda z} \lambda^n\, d\lambda.$$

Using this, the displacement potential (13) can be rewritten as

$$\frac{\phi_0}{T} = \int_0^\infty \omega_1(\lambda) J_0(\lambda r) e^{\lambda z}\, d\lambda, \quad \frac{\phi_3}{T} = \int_0^\infty \lambda\omega_2(\lambda) J_0(\lambda r) e^{\lambda z}\, d\lambda, \tag{13*}$$

where

$$\omega_1(\lambda) = \sum_{n=0}^\infty A_n(-1)^n \lambda^n/n!, \quad \omega_2(\lambda) = \sum_{n=0}^\infty B_n(-1)^n \lambda^{n-1}/n!. \tag{16}$$

At this point, the expressions for stress and the surface divergence of the surface stress on the plane boundary can be obtained readily by substituting potentials (12*), (13*), and (14) into (3) and (7) (see Equations (23) and (24)). By satisfying the plane boundary conditions (9), we get the relations

$$\int_0^\infty \lambda^2\Big(\big(\psi_1 + (-c\lambda + 1 - 2\nu)\psi_2\big)e^{c\lambda} - \big(\omega_1 + (-c\lambda - 1 + 2\nu)\omega_2\big)e^{-c\lambda}\Big) J_1(\lambda r)\, d\lambda$$
$$= -\int_0^\infty \chi_0\lambda^3\big((\psi_1 - c\lambda\psi_2)e^{c\lambda} + (\omega_1 - c\lambda\omega_2)e^{-c\lambda}\big) J_1(\lambda r)\, d\lambda,$$

$$\int_0^\infty \lambda^2\Big(\big(\psi_1 + (-c\lambda + 2 - 2\nu)\psi_2\big)e^{c\lambda} + \big(\omega_1 + (-c\lambda - 2 + 2\nu)\omega_2\big)e^{-c\lambda}\Big) J_0(\lambda r)\, d\lambda$$
$$= 0.$$

This is satisfied identically if

$$(\chi_{f0}\lambda+1)\psi_1-(\chi_{f0}c\lambda^2+c\lambda-1+2\nu)\psi_2 = (1-\chi_{f0}\lambda)\omega_1 e^{-2c\lambda}+(\chi_{f0}c\lambda^2-c\lambda-1+2\nu)\omega_2 e^{-2c\lambda},$$

$$\psi_1+(-c\lambda+2-2\nu)\psi_2 = -\omega_1 e^{-2c\lambda}-(-c\lambda-2+2\nu)\omega_2 e^{-2c\lambda}.$$

Solving this for $\psi_1(\lambda)$ and $\psi_2(\lambda)$, we obtain

$$\psi_1(\lambda) = -\big((2(c+b_1)\lambda-(3-4\nu))\omega_1+\big(4(1-2\nu)(1-\nu)-2c(c+2b_1)\lambda^2\big)\omega_2\big) \times e^{-2c\lambda}/(1+2b_1\lambda),$$

$$\psi_2(\lambda) = -\big(2\omega_1-((3-4\nu)+2(c+b_1)\lambda)\omega_2\big)e^{-2c\lambda}/(1+2b_1\lambda), \tag{17}$$

where $b_1=(1-\nu)\chi_{f0}$. These are the conditions necessary to satisfy Equation (9). The stress components on the plane boundary are reduced to (25) by substituting Equations (16) and (17) in (23).

The next task is to satisfy the boundary conditions on the matrix/inhomogeneity interface. For this purpose, we must transform the potential (14) into spherical coordinates. From [Morse and Feshbach 1953, p. 1318], it is found that for $z\geq 0$,

$$e^{\lambda z}J_0(\lambda r)=\sum_{n=0}^{\infty}\frac{(\lambda R)^n}{n!}P_n(\mu).$$

Replacing (z) with $(-z)$, (μ) with $(-\mu)$, and with the aid of the parity property of Legendre polynomials, it is deduced that for $z\leq 0$,

$$e^{-\lambda z}J_0(\lambda r)=\sum_{n=0}^{\infty}(-1)^n\frac{(\lambda R)^n}{n!}P_n(\mu).$$

With the use of this equation, the displacement potential (14) can be expressed in spherical coordinates as

$$\frac{\phi_0}{T}=\sum_{n=0}^{\infty}\alpha_n R^n P_n(\mu), \quad \frac{\phi_3}{T}=\sum_{n=0}^{\infty}\beta_n R^n P_n(\mu), \tag{14*}$$

where

$$\alpha_n=\int_0^{\infty}\frac{(-1)^n\lambda^n}{n!}\psi_1(\lambda)\,d\lambda, \quad \beta_n=\int_0^{\infty}\frac{(-1)^n\lambda^n}{n!}\lambda\psi_2(\lambda)\,d\lambda.$$

Substituting (16) and (17) into these two equations, expanding $1/(1+2b_1\lambda)$ in powers of λ for small b_1, and using Euler's integral of the second kind

$$\int_0^{\infty}\lambda^n e^{-c\lambda}\,d\lambda=n!/c^{n+1} \quad (n,c>0),$$

(see [Gradshteyn and Ryzhik 1994, p. 357]), we can write

$$\alpha_n = \sum_{m=0}^{\infty} (f_m^n A_m + g_m^n B_m), \quad \beta_n = \sum_{m=0}^{\infty} \big(2(m+1)q_{m+1}^n A_m + h_m^n B_m\big), \tag{18}$$

where

$$q_m^n = \frac{(-1)^{m+n}}{m!n!} \int_0^\infty \frac{\lambda^{m+n} e^{-2c\lambda}}{(1+2b_1\lambda)}\, d\lambda$$

$$= \begin{cases} \dfrac{(-1)^{m+n}}{m!n!} \dfrac{(m+n)!}{(2c)^{m+n+1}} & \text{if } b_1 = 0, \\ \displaystyle\sum_{k=0}^{\infty} (-1)^{m+n+k} \frac{(2b_1)^k (m+n+k)!}{m!n!(2c)^{m+n+k+1}} & \text{if } b_1 \neq 0, \end{cases}$$

$$f_m^n = (3-4\nu) q_m^n + 2(c+b_1)(m+1) q_{m+1}^n,$$

$$g_m^n = 4(1-2\nu)(1-\nu) \frac{q_{m-1}^n}{m} - 2c(c+2b_1)(m+1) q_{m+1}^n,$$

$$h_m^n = (3-4\nu) q_m^n - 2(c+b_1)(m+1) q_{m+1}^n.$$

The expressions for displacement, stress, and the interface divergence of the interface stress on the matrix/inhomogeneity interface can be derived by substituting displacement potentials into Equations (4) and (8). The elastic fields in the matrix are obtained by superposing potentials (12), (13), and (14*), while those in inhomogeneity are given by (15). These expressions are listed in the Appendix. To satisfy the boundary condition (11), we must have

$$\sum_{n=0}^{\infty} \begin{pmatrix} s_{A_1} A_n + s_{B_1} B_{n-1} + s_{B_2} B_{n+1} + s_{\alpha_1} \alpha_n + s_{\beta_1} \beta_{n-1} \\ + s_{\beta_2} \beta_{n+1} - \Gamma^{-1} (s_{\bar{A}_1} \bar{A}_n + s_{\bar{B}_1} \bar{B}_{n-1} + s_{\bar{B}_2} \bar{B}_{n+1}) \end{pmatrix} P_n(\mu)$$

$$= -\frac{2(1-2\nu)a}{3(1+\nu)} P_0(\mu) + \frac{2a}{3} P_2(\mu), \tag{19}$$

$$\sum_{n=1}^{\infty} \begin{pmatrix} t_{A_1} A_n + t_{B_1} B_{n-1} + t_{B_2} B_{n+1} + t_{\alpha_1} \alpha_n + t_{\beta_1} \beta_{n-1} \\ + t_{\beta_2} \beta_{n+1} - \Gamma^{-1} (t_{\bar{A}_1} \bar{A}_n + t_{\bar{B}_1} \bar{B}_{n-1} + t_{\bar{B}_2} \bar{B}_{n+1}) \end{pmatrix} P_n'(\mu) = -\frac{a}{3} P_2'(\mu), \tag{20}$$

$$\sum_{n=0}^{\infty} \begin{pmatrix} (i_{s_{A_1}} + i_{A_1}) A_n + (i_{s_{B_1}} + i_{B_1}) B_{n-1} + (i_{s_{B_2}} + i_{B_2}) B_{n+1} \\ + (i_{s_{\alpha_1}} + i_{\alpha_1}) \alpha_n + (i_{s_{\beta_1}} + i_{\beta_1}) \beta_{n-1} + (i_{s_{\beta_2}} + i_{\beta_2}) \beta_{n+1} \\ + (\Gamma^{-1} i_{s_{\bar{A}_1}} - i_{\bar{A}_1}) \bar{A}_n + (\Gamma^{-1} i_{s_{\bar{B}_1}} - i_{\bar{B}_1}) \bar{B}_{n-1} + (\Gamma^{-1} i_{s_{\bar{B}_2}} - i_{\bar{B}_2}) \bar{B}_{n+1} \end{pmatrix} P_n(\mu)$$

$$= \left(\frac{2\tau_0}{aT} + \frac{4(1-2\nu)\chi_3}{3a(1+\nu)} - \frac{2}{3} \right) P_0(\mu) + \left(\frac{2\chi_3}{3a} + \frac{2}{3} \right) P_2(\mu), \tag{21}$$

$$\sum_{n=1}^{\infty}\begin{pmatrix}(l_{s_{A_1}}+l_{A_1})A_n+(l_{s_{B_1}}+l_{B_1})B_{n-1}+(l_{s_{B_2}}+l_{B_2})B_{n+1}\\ +(l_{s_{\alpha_1}}+l_{\alpha_1})\alpha_n+(l_{s_{\beta_1}}+l_{\beta_1})\beta_{n-1}+(l_{s_{\beta_2}}+l_{\beta_2})\beta_{n+1}\\ +(\Gamma^{-1}l_{s_{\bar{A}_1}}-l_{\bar{A}_1})\bar{A}_n+(\Gamma^{-1}l_{s_{\bar{B}_1}}-l_{\bar{B}_1})\bar{B}_{n-1}+(\Gamma^{-1}l_{s_{\bar{B}_2}}-l_{\bar{B}_2})\bar{B}_{n+1}\end{pmatrix}P_n'(\mu)$$

$$=\left(\frac{3\chi_0-\chi_1}{3a}-\frac{1}{3}\right)P_2'(\mu), \quad (22)$$

where $P_n'(\mu)=dP_n(\mu)/d\mu$, $\Gamma=\bar{G}/G$, and the coefficients s, t, i, l are defined in the Appendix (page 788). In Equations (19) and (20), the displacement containing α_1, β_0 represents the rigid body motion of the matrix. We set $\alpha_1=\beta_0=0$ by viewing the matrix as a reference state. The displacement containing $\bar{A}_1$, $\bar{B}_0$ corresponds to the rigid body motion of the inhomogeneity. As a result, one of the two coefficients can be set to zero, so we set $\bar{A}_1\neq 0$, $\bar{B}_0=0$. Equating the coefficients of $P_n(\mu)$, $P_n'(\mu)$ on both sides of Equations (19)–(22), and with the aid of Equation (18), we obtain a set of linear algebraic equations leading to the unknown coefficients $\{A_n, B_n, \bar{A}_n, \bar{B}_n\}$.

4. Results and discussion

Results were obtained in order to illustrate the impact of surface and interface effects on the elastic field in the vicinity of the inhomogeneity (nanoparticle). The key parameters are the shear moduli ratio Γ and the inhomogeneity position and size, denoted by c and a, respectively. The shear modulus of the matrix is set to $G=26\,\text{GPa}$, while Γ ranges over different values of the nanoparticle's stiffness. The limiting value $\Gamma=0$ represents a spherical void while $\Gamma\to\infty$ corresponds to a rigid particle. Poisson's ratios are kept equal ($\nu=\bar{\nu}=0.25$) for the matrix and the inhomogeneity. The far-field biaxial tension is set at $T=100\,\text{MPa}$. Numerical computations indicate that the coefficients A_n, B_n, $\bar{A}_n$, and $\bar{B}_n$ decay monotonically with increasing n. These coefficients converge more rapidly for small ratios a/c. As a result, for all ratios a/c, less than 20 terms are necessary to obtain the elastic field, with an accuracy of five significant figures.

When surface and interface effects are ignored, the results are compared with the classical solution of a semi-infinite elastic body having a spherical cavity or a spherical inhomogeneity [Tsuchida and Nakahara 1970; Tsutsui et al. 1974], and were found to be in perfect agreement.

The impacts of interface and free-surface elasticity were studied separately. First, only the effects of interface elasticity were considered. The interface elastic constants were selected as $\lambda^s=6.85107\,\text{N/m}$, $\mu^s=-0.83145\,\text{N/m}$, and $\tau_0=0.91084\,\text{N/m}$. These quantities can be deduced from the manipulation of the surface properties of an aluminum [111] free surface in [Miller and Shenoy 2000].

4.1. ***Interface elasticity only: stress distribution.*** Normalized stress components with and without interface elasticity are shown in Figures 2–4. Stresses at three specific points of the matrix/inhomogeneity interface vary with the ratio a/c (radius of the particle normalized by the distance from the free surface). The particle position is fixed at $c = 50$ nm. It is clear that the stress changes significantly when the particle size is small, for both soft ($\Gamma = 0.5$) and hard ($\Gamma = 2$) particles. In some cases, the interface effects even change the sign of the stress for small ratios of a/c. As expected, the stress fields converge to the classical solutions when the inhomogeneity size increases.

Numerical calculations are also performed to study the impact of interface elasticity on the stress distribution at $R = a$ when a spherical particle of fixed size approaches the plane boundary. Results were similar to the ones illustrated in Figures 2–4. As long as the particle size is of nanometer size, interface elasticity significantly changes the particle/matrix interface stresses, even if the particle is pretty far from the plane boundary (free surface).

To examine the stress distribution along the interface, calculations were carried out for various shear moduli ratios (Figures 5–6). For the matrix, softer particles ($\Gamma < 1$) are affected more than harder particles ($\Gamma > 1$). As seen in Figure 6, top, the maximum shear stress τ_1 converges to the classical solution as Γ increases when the inhomogeneity is hard ($\Gamma > 1$), while it deviates greatly from the classical solution when the inhomogeneity is soft ($\Gamma < 1$).

The maximum principal stress $\bar{\sigma}_1$ is compressive, while its classical counterpart is tensile everywhere. The sign of $\bar{\sigma}_1$ has been altered by the interface effects. Unlike σ_1, $\bar{\sigma}_1$ is more sensitive to harder particles than to softer ones. Compared to $\bar{\sigma}_1$, $\bar{\tau}_1$ is only slightly affected by interface elasticity. It remains tensile at every point around the interface. The maximum variation of $\bar{\tau}_1$ from the classical solution occurs at $\varphi = \pi$ for soft inhomogeneity ($\Gamma < 1$).

Figure 7 illustrates the variation of stresses σ_{rr} and $\sigma_{\theta\theta}$ with r/c, at the plane boundary. The impact of interface elasticity on σ_{rr} and $\sigma_{\theta\theta}$ is analogous to that on σ_1 and τ_1: the softer the particle, the more significant the interface elasticity becomes. However, for large values of r/c (≥ 3), σ_{rr} and $\sigma_{\theta\theta}$ converge to the classical solution.

By limit analysis, the solutions of the present problem with only the interface effects should approach those of a spherical inhomogeneity with interface effects in an infinite medium when $a \ll c$. With the ratio $a/c \leq 0.01$, the elastic field at the spherical interface is in agreement with the one obtained for the infinite medium, with an accuracy of at least five significant figures.

4.2. ***Free-surface elasticity only: stress distribution.*** Calculations were performed to determine the free-surface elasticity effects on the stress distribution at $z = -c$

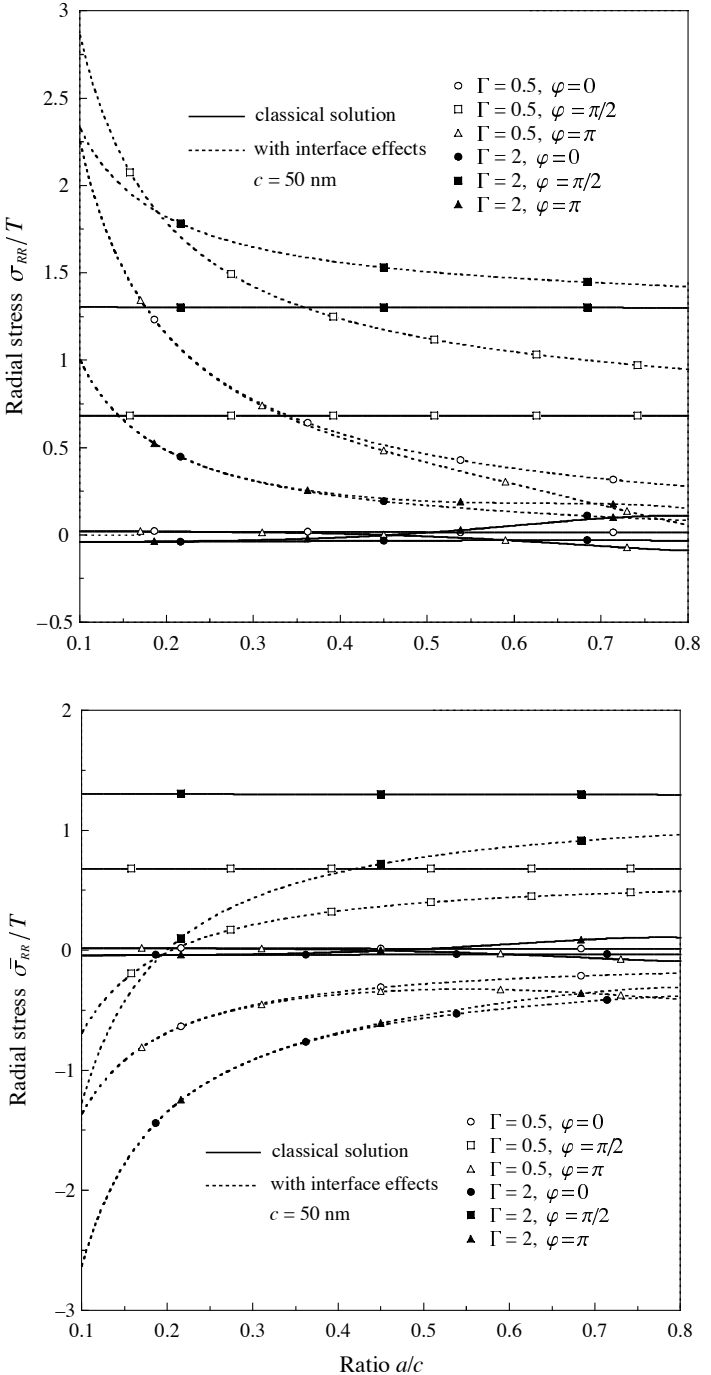

Figure 2. Variation of σ_{RR} (top) and $\bar{\sigma}_{RR}$ (bottom) versus a/c around the spherical interface at $\varphi = 0, \pi/2, \pi$.

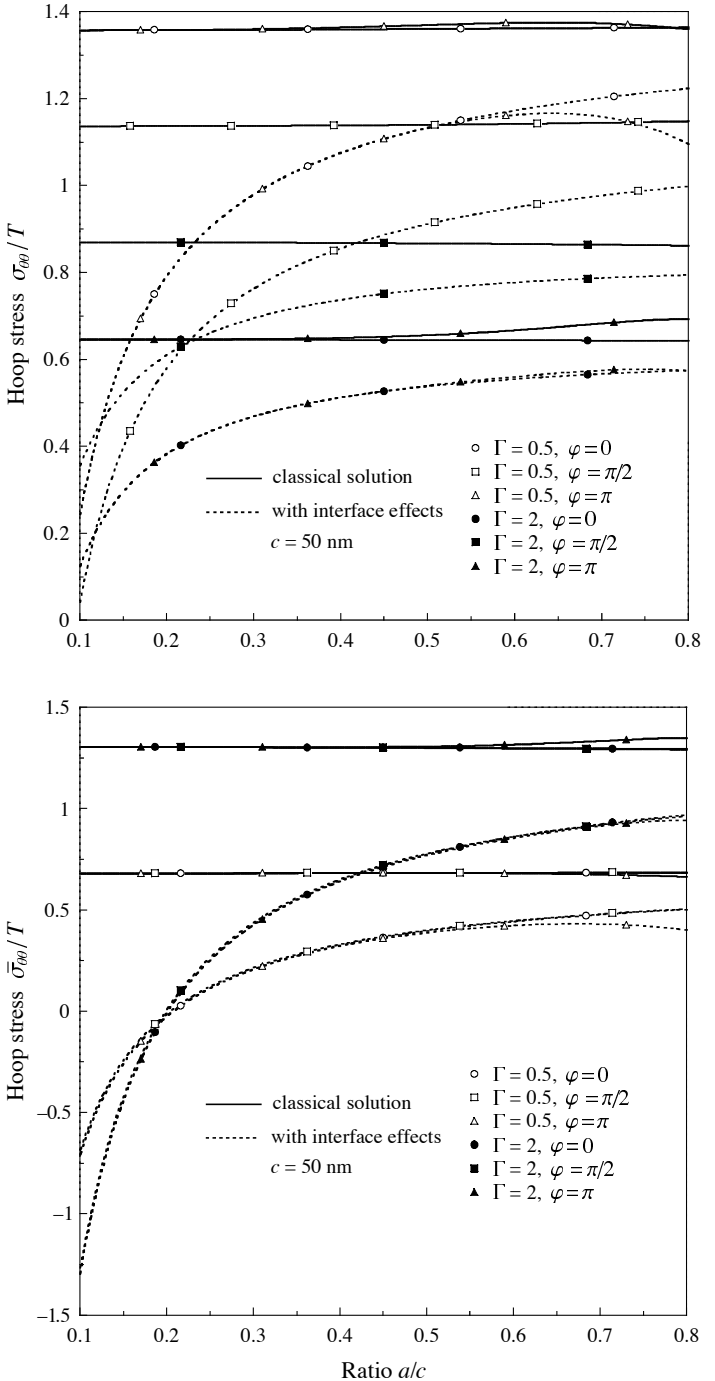

Figure 3. Variation of $\sigma_{\theta\theta}$ (top) and $\bar{\sigma}_{\theta\theta}$ (bottom) versus a/c around the spherical interface at $\varphi = 0, \pi/2, \pi$.

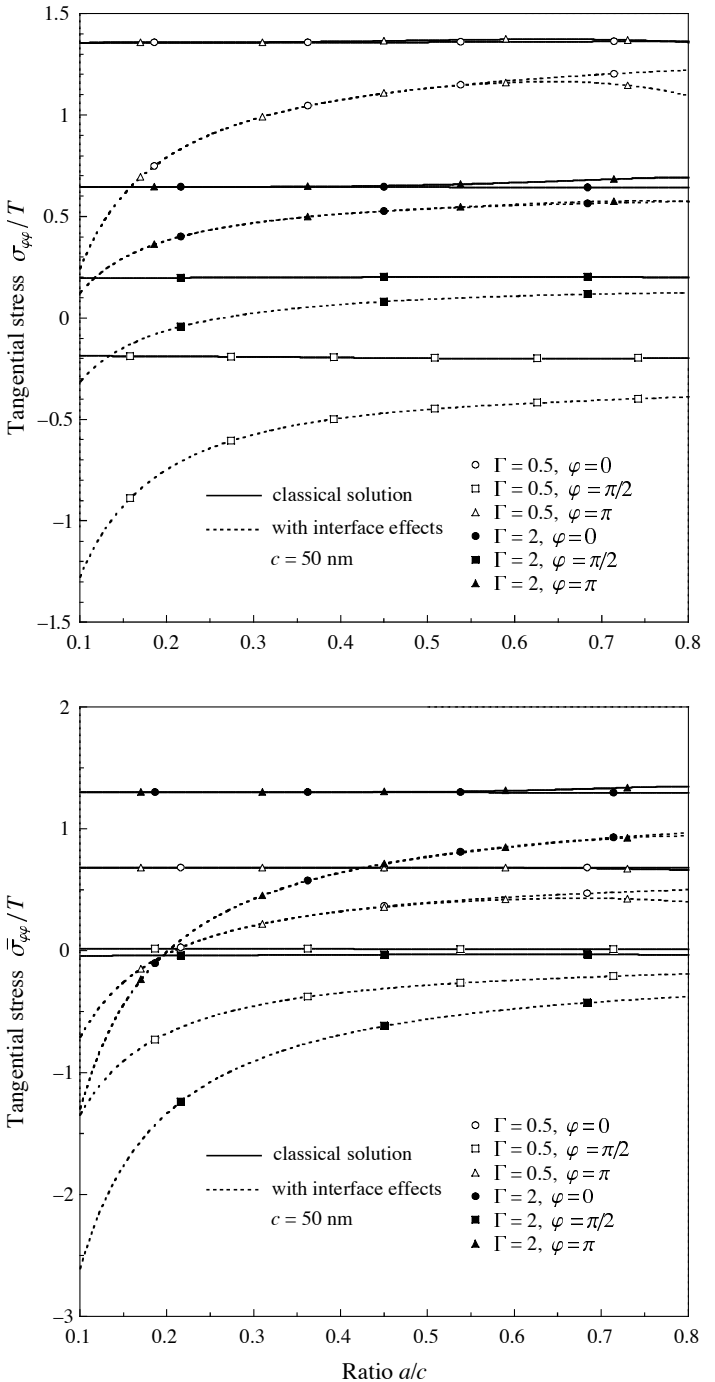

Figure 4. Variation of $\sigma_{\varphi\varphi}$ (top) and $\bar{\sigma}_{\varphi\varphi}$ (bottom) versus a/c around the spherical interface at $\varphi = 0, \pi/2, \pi$.

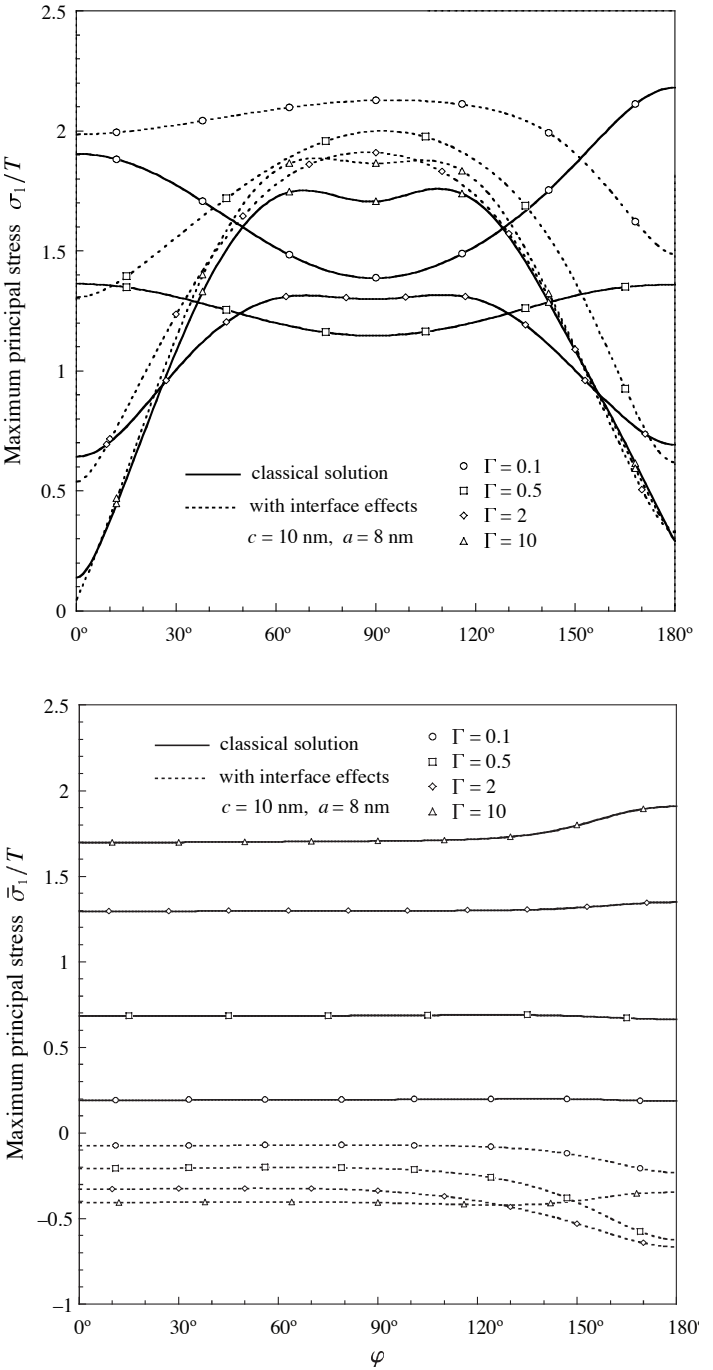

Figure 5. Variation of maximum principal stress σ_1 (top) and $\bar{\sigma}_1$ (bottom) with φ at the spherical interface.

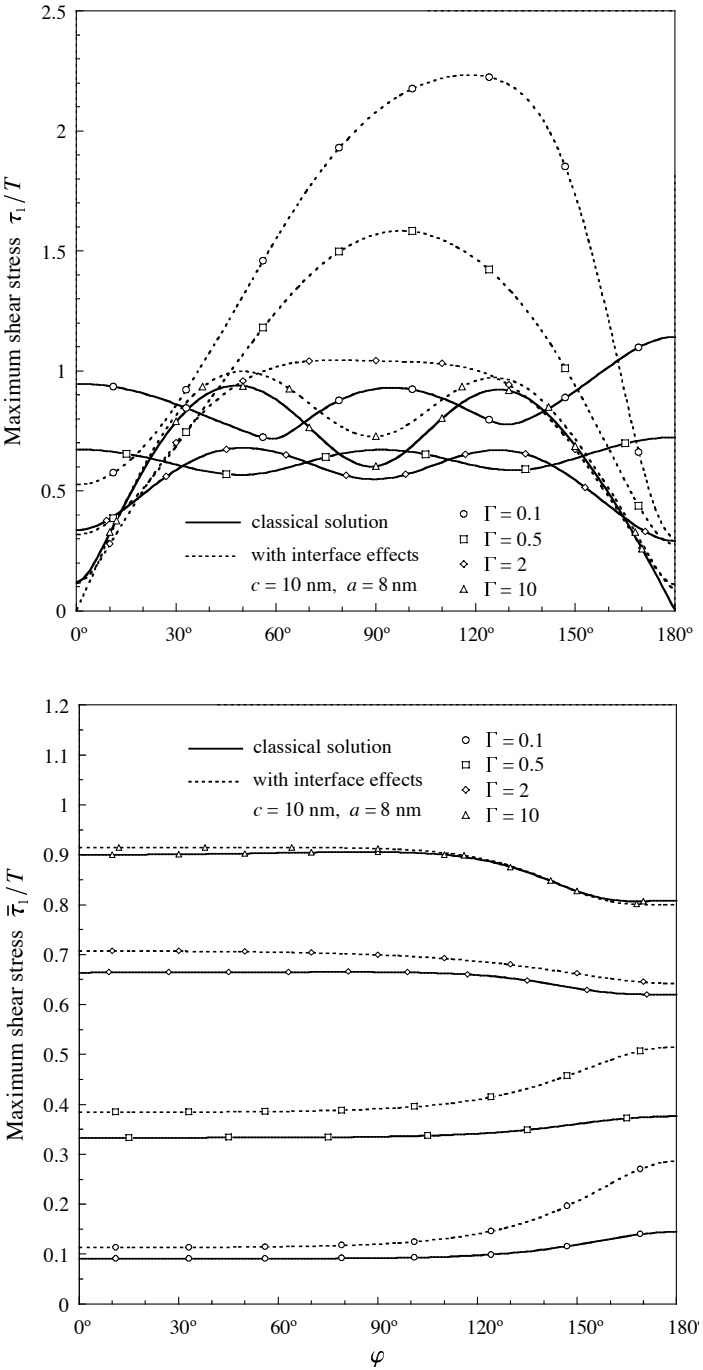

Figure 6. Variation of maximum shear stress τ_1 (top) and $\bar{\tau}_1$ (bottom) with φ at the spherical interface.

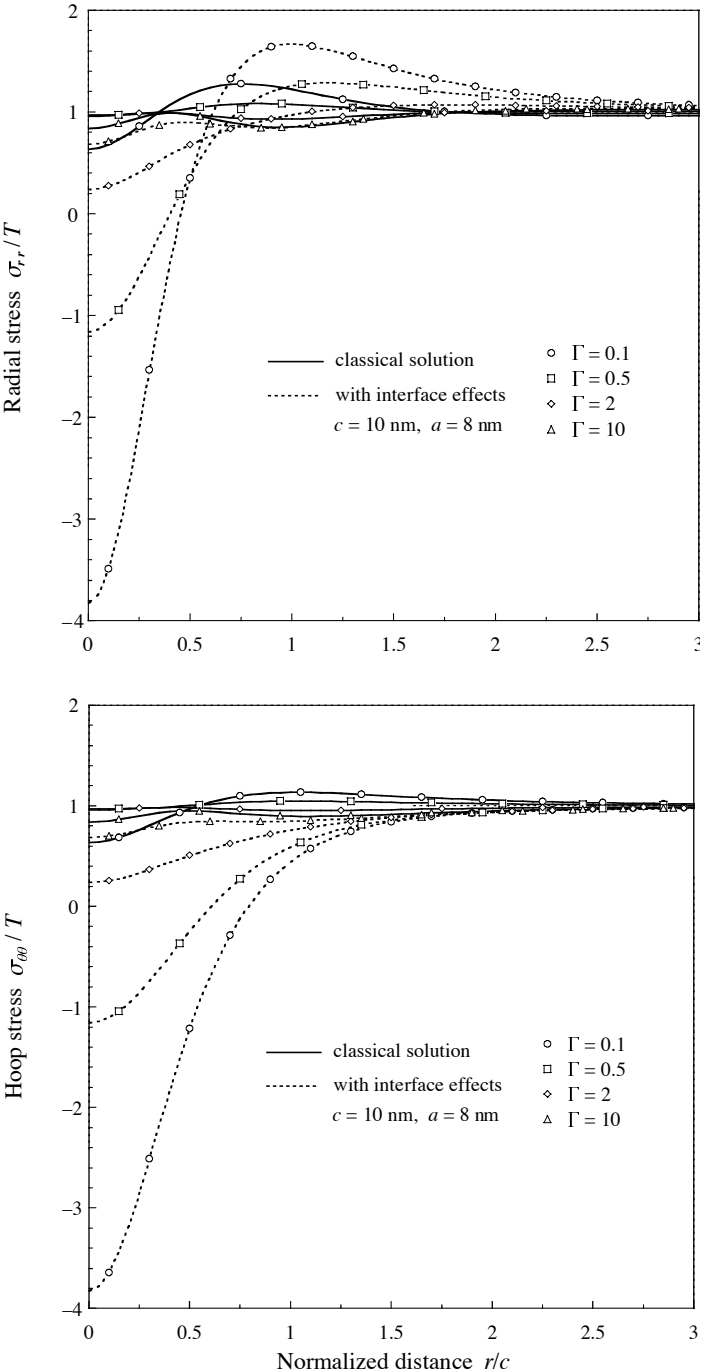

Figure 7. Variation of σ_{rr} (top) and $\sigma_{\theta\theta}$ (bottom) with r/c at the plane boundary.

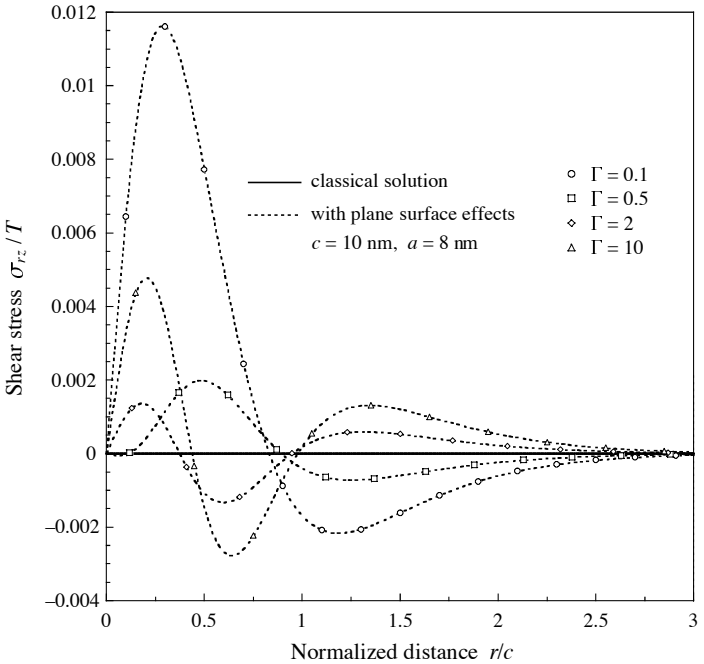

Figure 8. Variation of σ_{rz} with r/c at the plane boundary.

and $R = a$. We consider an aluminum [100] free surface with properties $\lambda^{fs} = 3.49387\,\text{N/m}$, $\mu^{fs} = -5.70915\,\text{N/m}$, and $\tau_{f0} = 0.56893\,\text{N/m}$ [Miller and Shenoy 2000]. The most important character of the plane surface effects is the nonvanishing shear stress σ_{rz} at the plane boundary, as shown analytically in (25). In the classical solution, the conditions of zero traction at the plane boundary force σ_{rz} to vanish. Figure 8 shows the distribution of σ_{rz} with the normalized radial coordinate r/c, for $c = 10$ nm, $a = 8$ nm, and various shear moduli ratios. When the particle stiffness is not too different from the surrounding material ($\Gamma = 0.5 - 2$), surface elasticity is not important. Otherwise ($\Gamma = 0.1, 10$), its influence is significant. Nevertheless, the magnitude of σ_{rz} is small ($\leq 2\%\, T$). The impact of the free surface effects on σ_{rr} and $\sigma_{\theta\theta}$ is found to be of the same order as that of σ_{rz}. The influence on the stress fields at the matrix/inhomogeneity interface is even smaller. One can safely conclude that compared to the applied tension at infinity, the free surface elasticity may be neglected.

5. Summary and conclusions

The axisymmetric problem of a spherical particle near the surface of a semi-infinite elastic body was solved, incorporating the effects of surface/interface elasticity.

The solution was obtained within the framework of linear elasticity, through a displacement potential formulation.

The free surface and the interface were modeled as two-dimensional continuous spaces with vanishing thickness. Aside from the bulk material properties, the surface and interface boundaries have their own material constants (for example, the residual surface stress and surface Lamé constants). Numerical calculations indicate that the stress distribution along the plane boundary and the matrix/particle interface is significantly affected by surface/interface elasticity.

Following the analysis, one can make a few important observations:

- The impact of interface elasticity is a function of the particle size: the smaller the particle, the more important interface elasticity becomes. The elastic fields converge to the classical solution as the particle size increases (typically for $a \geq 100$ nm).

- The influence of interface elasticity depends on the softness or rigidity of the particles. For the matrix, the interface effects on the stress distribution are more pronounced when the particles are soft. However, the opposite is true for the particles themselves.

- In contrast with the zero traction requirement along the free surface in the classical solution, plane elasticity yields a nonvanishing shear stress, as shown in (25) and Figure 8. The plane surface effects become more important when the particle approaches the plane boundary. However, for distances where continuum theory is considered valid (typically ≥ 5 nm), the magnitude of the disturbance due to the plane surface elasticity is small, when compared to the applied load.

- Due to the presence of the residual interface stress (see [He and Li in press]), superposition will not be valid when one considers interface elasticity. This is critical, because it significantly complicates the problem when multiple loads (say, misfit strain and mechanical load) are applied separately.

The study presented here illustrates that models incorporating nanoparticles near surfaces cannot ignore surface and particularly, interface elasticity effects. This is especially true when one models self-organized adatom clusters and islands, since most of these structures are of nanoscale size. The important problem of strained islands due to misfit strains will be addressed in a separate communication.

Appendix

Elastic fields at the plane boundary. The stresses along the plane boundary are given below in terms of potentials (12*), (13*), and (14):

$$
\begin{aligned}
\left(\frac{\sigma_{rr}}{T}\right)_{z=-c} &= 1 - \int_0^\infty \lambda(\omega_1 - c\lambda\omega_2)\left(\lambda J_0(\lambda r) - \tfrac{1}{r}J_1(\lambda r)\right)e^{-c\lambda}\,d\lambda \\
&\quad - \int_0^\infty 2\nu\lambda^2\omega_2 J_0(\lambda r)\,e^{-c\lambda}\,d\lambda \\
&\quad - \int_0^\infty \lambda(\psi_1 - c\lambda\psi_2)\left(\lambda J_0(\lambda r) - \tfrac{1}{r}J_1(\lambda r)\right)e^{c\lambda}\,d\lambda \\
&\quad + \int_0^\infty 2\nu\lambda^2\psi_2 J_0(\lambda r)\,e^{c\lambda}\,d\lambda, \\
\left(\frac{\sigma_{\theta\theta}}{T}\right)_{z=-c} &= 1 - \int_0^\infty \lambda\left(\tfrac{1}{r}(\omega_1 - c\lambda\omega_2)J_1(\lambda r) + 2\nu\lambda\omega_2 J_0(\lambda r)\right)e^{-c\lambda}\,d\lambda \\
&\quad - \int_0^\infty \lambda\left(\tfrac{1}{r}(\psi_1 - c\lambda\psi_2)J_1(\lambda r) - 2\nu\lambda\psi_2 J_0(\lambda r)\right)e^{c\lambda}\,d\lambda, \\
\left(\frac{\sigma_{zz}}{T}\right)_{z=-c} &= \int_0^\infty \lambda^2\left(\omega_1 - (c\lambda + 2 - 2\nu)\omega_2\right)J_0(\lambda r)\,e^{-c\lambda}\,d\lambda \\
&\quad + \int_0^\infty \lambda^2\left(\psi_1 + (-c\lambda + 2 - 2\nu)\psi_2\right)J_0(\lambda r)\,e^{c\lambda}\,d\lambda, \\
\left(\frac{\sigma_{rz}}{T}\right)_{z=-c} &= -\int_0^\infty \lambda^2\left(\omega_1 - (c\lambda + 1 - 2\nu)\omega_2\right)J_1(\lambda r)\,e^{-c\lambda}\,d\lambda \\
&\quad + \int_0^\infty \lambda^2\left(\psi_1 + (-c\lambda + 1 - 2\nu)\psi_2\right)J_1(\lambda r)\,e^{c\lambda}\,d\lambda.
\end{aligned}
\tag{23}
$$

The surface divergence of the surface stress on the plane boundary is

$$
\begin{aligned}
\gamma_r^f = \chi_{f0}T\Big(&\int_0^\infty \lambda^3(\omega_1 - c\lambda\omega_2)J_1(\lambda r)e^{-c\lambda}\,d\lambda \\
&+ \int_0^\infty \lambda^3(\psi_1 - c\lambda\psi_2)J_1(\lambda r)e^{c\lambda}\,\partial\lambda\Big).
\end{aligned}
\tag{24}
$$

With Equations (16) and (17), Equation (23) is reduced to

$$
\begin{aligned}
\left(\frac{\sigma_{rr}}{T}\right)_{z=-c} &= 1 + \sum_{n=0}^{\infty}(-1)^n A_n\left(-4\frac{F_0^{n+2}}{n!} + 4(1-\nu)\frac{1}{r}\frac{F_1^{n+1}}{n!}\right) \\
&\quad + \sum_{n=0}^{\infty}(-1)^n B_n\left(4(1-2\nu)\frac{F_0^{n+1}}{n!} + 4c\frac{F_0^{n+2}}{n!}\right. \\
&\qquad \left. -4(1-2\nu)(1-\nu)\frac{1}{r}\frac{F_1^n}{n!} - 4(1-\nu)c\frac{1}{r}\frac{F_1^{n+1}}{n!}\right), \\
\left(\frac{\sigma_{\theta\theta}}{T}\right)_{z=-c} &= 1 + \sum_{n=0}^{\infty}(-1)^n A_n\left(-4\nu\frac{F_0^{n+2}}{n!} - \frac{4(1-\nu)}{r}\frac{F_1^{n+1}}{n!}\right) \\
&\quad + \sum_{n=0}^{\infty}(-1)^n B_n\left(4\nu(1-2\nu)\frac{F_0^{n+1}}{n!} + 4\nu c\frac{F_0^{n+2}}{n!}\right. \\
&\qquad \left. + \frac{4(1-2\nu)(1-\nu)}{r}\frac{F_1^n}{n!} + \frac{4c(1-\nu)}{r}\frac{F_1^{n+1}}{n!}\right),
\end{aligned}
\tag{25}
$$

$$\left(\frac{\sigma_{rz}}{T}\right)_{z=-c} = \sum_{n=0}^{\infty} 4b_1(-1)^n \left(-A_n \frac{F_1^{n+3}}{n!} + B_n\left((1-2\nu)\frac{F_1^{n+2}}{n!} + c\frac{F_1^{n+3}}{n!}\right)\right),$$

$$(\sigma_{zz})_{z=-c} = 0, \tag{26}$$

where

$$F_\nu^n = \int_0^\infty \frac{J_\nu(\lambda r)e^{-c\lambda}\lambda^n}{1+2b_1\lambda}\, d\lambda. \tag{27}$$

With the aid of the Taylor's series expansion of $1/(1+2b_1\lambda)$ for small parameter b_1, and the relation

$$\int_0^\infty J_\nu(\lambda r)e^{-c\lambda}\lambda^n\, d\lambda = \frac{(n-\nu)!}{(r^2+c^2)^{(n+1)/2}} P_n^\nu\left(\frac{c}{\sqrt{r^2+c^2}}\right) \quad (c>0,\, \nu+n>-1)$$

from [Gradshteyn and Ryzhik 1994, p. 732–733], Equation (27) can be approximated as

$$F_\nu^n \approx \sum_{m=0}^{\infty} (-1)^m (2b_1)^m \frac{(m+n+\nu)!}{(r^2+c^2)^{(m+n+1)/2}} P_{m+n}^\nu\left(\frac{c}{\sqrt{r^2+c^2}}\right),$$

where $P_n^\nu(\mu)$ is the associated Legendre function of order n and degree ν.

The length parameters in (6) are defined as

$$\chi_{f0} = (\lambda^{fs} + 2\mu^{fs})/4G, \quad \chi_{f1} = (\lambda^{fs} + \tau_{f0})/4G, \quad \chi_{f2} = \chi_{f0} - \chi_{f1}, \tag{28}$$

where λ^{fs}, μ^{fs} denote the surface Lamé moduli for the plane boundary ($z=-c$).

Elastic fields at the spherical interface. The displacements and stresses in the matrix at $R=a$ are given by

$$\left(\frac{2Gu_R}{T}\right)_{R=a} = \sum_{n=0}^{\infty}\left(\frac{2}{3}a\left(\frac{1-2\nu}{1+\nu}\delta_{0n} - \delta_{2n}\right) + s_{A_1}A_n + s_{B_1}B_{n-1} + s_{B_2}B_{n+1} + s_{\alpha_1}\alpha_n + s_{\beta_1}\beta_{n-1} + s_{\beta_2}\beta_{n+1}\right) P_n(\mu),$$

$$\left(\frac{2Gu_\varphi}{T}\right)_{R=a} = \sqrt{1-\mu^2}\sum_{n=1}^{\infty}\left(\frac{1}{3}a\delta_{2n} + t_{A_1}A_n + t_{B_1}B_{n-1} + t_{B_2}B_{n+1} + t_{\alpha_1}\alpha_n + t_{\beta_1}\beta_{n-1} + t_{\beta_2}\beta_{n+1}\right) P_n'(\mu),$$

$$\left(\frac{\sigma_{RR}}{T}\right)_{R=a} = \sum_{n=0}^{\infty}\left(\frac{2}{3}(\delta_{0n} - \delta_{2n}) + i_{A_1}A_n + i_{B_1}B_{n-1} + i_{B_2}B_{n+1} + i_{\alpha_1}\alpha_n + i_{\beta_1}\beta_{n-1} + i_{\beta_2}\beta_{n+1}\right) P_n(\mu),$$

$$\left(\frac{\sigma_{R\varphi}}{T}\right)_{R=a} = \sqrt{1-\mu^2}\sum_{n=1}^{\infty}\left(\frac{1}{3}\delta_{2n} + l_{A_1}A_n + l_{B_1}B_{n-1} + l_{B_2}B_{n+1} + l_{\alpha_1}\alpha_n + l_{\beta_1}\beta_{n-1} + l_{\beta_2}\beta_{n+1}\right) P_n'(\mu),$$

$$\left(\frac{\sigma_{\theta\theta}}{T}\right)_{R=a}=\sum_{n=1}^{\infty}\Bigg(-\frac{A_n}{a^{n+3}}-\frac{B_{n-1}(n-1)(1-2\nu)}{(2n-1)a^{n+1}}-\frac{\beta_{n-1}a^{n-2}(n-1)(1-2\nu)}{(2n-1)}$$
$$-\frac{B_{n+1}\big((n+2)(1-2\nu)+2(2n+3)\nu\big)}{(2n+3)a^{n+3}}-\alpha_n a^{n-2}$$
$$-\frac{\beta_{n+1}a^{n}\big(2(2n+3)\nu+(n+2)(1-2\nu)\big)}{(2n+3)}\Bigg)\mu P_n'(\mu)$$
$$+\sum_{n=0}^{\infty}\Bigg(\delta_{0n}-\frac{A_n(n+1)}{a^{n+3}}-\frac{B_{n-1}n^2(1-2\nu)}{(2n-1)a^{n+1}}+\frac{\beta_{n-1}a^{n-2}n(n-1)(1-2\nu)}{(2n-1)}$$
$$-\frac{B_{n+1}(n+1)\big((n+2)(1-2\nu)+2(2n+3)\nu\big)}{(2n+3)a^{n+3}}+\alpha_n a^{n-2}n$$
$$+\frac{\beta_{n+1}a^{n}(n+1)\big((n+1)(1-2\nu)-2(2n+3)\nu\big)}{(2n+3)}\Bigg)P_n(\mu),$$

$$\left(\frac{\sigma_{\varphi\varphi}}{T}\right)_{R=a}=\sum_{n=1}^{\infty}\Bigg(\frac{A_n}{a^{n+3}}+\frac{B_{n-1}(n-1)(3-2\nu)}{(2n-1)a^{n+1}}+\frac{\beta_{n-1}a^{n-2}(n-1)(3-2\nu)}{(2n-1)}$$
$$-\frac{B_{n+1}\big(2(2n+3)(1-\nu)-(n+2)(3-2\nu)\big)}{(2n+3)a^{n+3}}+\alpha_n a^{n-2}$$
$$-\frac{\beta_{n+1}a^{n}\big(2(2n+3)(1-\nu)-(n+2)(3-2\nu)\big)}{(2n+3)}\Bigg)\mu P_n'(\mu)$$
$$+\sum_{n=0}^{\infty}\Bigg(\frac{1}{3}(\delta_{0n}+2\delta_{2n})-\frac{A_n(n+1)^2}{a^{n+3}}-\frac{B_{n-1}n^2(n-2\nu)}{(2n-1)a^{n+1}}$$
$$-\frac{B_{n+1}(n+1)\big((n+2)(n+2-2\nu)+2(2n+3)(1-\nu)\big)}{(2n+3)a^{n+3}}$$
$$-\alpha_n a^{n-2}n^2-\frac{\beta_{n-1}a^{n-2}(n-1)n(n-1+2\nu)}{(2n-1)}$$
$$-\frac{\beta_{n+1}a^{n}(n+1)\big((n+1)(n+1+2\nu)+2(2n+3)(1-\nu)\big)}{(2n+3)}\Bigg)P_n(\mu).$$

The displacements and stresses in the inhomogeneity at $R=a$ are given by

$$\left(\frac{2\bar{G}\bar{u}_R}{T}\right)_{R=a}=\sum_{n=0}^{\infty}(s_{\bar{A}_1}\bar{A}_n+s_{\bar{B}_1}\bar{B}_{n-1}+s_{\bar{B}_2}\bar{B}_{n+1})P_n(\mu),$$

$$\left(\frac{2\bar{G}\bar{u}_\varphi}{T}\right)_{R=a} = \sqrt{1-\mu^2}\sum_{n=1}^{\infty}(t_{\bar{A}_1}\bar{A}_n + t_{\bar{B}_1}\bar{B}_{n-1} + t_{\bar{B}_2}\bar{B}_{n+1})P_n'(\mu),$$

$$\left(\frac{\bar{\sigma}_{RR}}{T}\right)_{R=a} = \sum_{n=0}^{\infty}(i_{\bar{A}_1}\bar{A}_n + i_{\bar{B}_1}\bar{B}_{n-1} + i_{\bar{B}_2}\bar{B}_{n+1})P_n(\mu),$$

$$\left(\frac{\bar{\sigma}_{R\varphi}}{T}\right)_{R=a} = \sqrt{1-\mu^2}\sum_{n=1}^{\infty}(l_{\bar{A}_1}\bar{A}_n + l_{\bar{B}_1}\bar{B}_{n-1} + l_{\bar{B}_2}\bar{B}_{n+1})P_n'(\mu),$$

$$\begin{aligned}\left(\frac{\bar{\sigma}_{\theta\theta}}{T}\right)_{R=a} = &-\sum_{n=1}^{\infty}\Bigg(\bar{A}_n a^{n-2} + \frac{\bar{B}_{n-1}a^{n-2}(n-1)(1-2\bar{\nu})}{(2n-1)} \\ &\qquad + \frac{\bar{B}_{n+1}a^n\big(2(2n+3)\bar{\nu} + (n+2)(1-2\bar{\nu})\big)}{(2n+3)}\Bigg)\mu P_n'(\mu) \\ &+\sum_{n=0}^{\infty}\Bigg(\bar{A}_n a^{n-2}n + \frac{\bar{B}_{n-1}a^{n-2}n(n-1)(1-2\bar{\nu})}{(2n-1)} \\ &\qquad + \frac{\bar{B}_{n+1}a^n(n+1)\big((n+1)(1-2\bar{\nu}) - 2(2n+3)\bar{\nu}\big)}{(2n+3)}\Bigg)P_n(\mu),\end{aligned}$$

$$\begin{aligned}\left(\frac{\bar{\sigma}_{\varphi\varphi}}{T}\right)_{R=a} = &\sum_{n=1}^{\infty}\Bigg(\bar{A}_n a^{n-2} + \frac{\bar{B}_{n-1}a^{n-2}(n-1)(3-2\bar{\nu})}{(2n-1)} \\ &\qquad - \frac{\bar{B}_{n+1}a^n\big(2(2n+3)(1-\bar{\nu}) - (n+2)(3-2\bar{\nu})\big)}{(2n+3)}\Bigg)\mu P_n'(\mu) \\ &-\sum_{n=0}^{\infty}\Bigg(\bar{A}_n a^{n-2}n^2 + \frac{\bar{B}_{n-1}a^{n-2}(n-1)n(n-1+2\bar{\nu})}{(2n-1)} \\ &\qquad + \frac{\bar{B}_{n+1}a^n(n+1)\big((n+1)(n+1+2\bar{\nu}) + 2(2n+3)(1-\bar{\nu})\big)}{(2n+3)}\Bigg)P_n(\mu).\end{aligned}$$

The interface divergence of the interface stress at $R=a$ is given by

$$\begin{aligned}\gamma_R = T\sum_{n=0}^{\infty}\Bigg(&-\Big(\frac{2}{aT}\tau_0 + \frac{4(1-2\nu)\chi_3}{3a(1+\nu)}\Big)\delta_{0n} - \frac{2\chi_3}{3a}\delta_{2n} + i_{S_{A_1}}A_n + i_{S_{B_1}}B_{n-1} + i_{S_{B_2}}B_{n+1} \\ &+ i_{S_{\alpha_1}}\alpha_n + i_{S_{\beta_1}}\beta_{n-1} + i_{S_{\beta_2}}\beta_{n+1} + \Gamma^{-1}\big(i_{S_{\bar{A}_1}}\bar{A}_n + i_{S_{\bar{B}_1}}\bar{B}_{n-1} + i_{S_{\bar{B}_2}}\bar{B}_{n+1}\big)\Bigg)P_n(\mu),\end{aligned}$$

$$\begin{aligned}\gamma_\varphi = T\sqrt{1-\mu^2}\sum_{n=1}^{\infty}\Bigg(&-\frac{(3\chi_0-\chi_1)}{3a}\delta_{2n} + l_{S_{A_1}}A_n + l_{S_{B_1}}B_{n-1} + l_{S_{B_2}}B_{n+1} + l_{S_{\alpha_1}}\alpha_n \\ &+ l_{S_{\beta_1}}\beta_{n-1} + l_{S_{\beta_2}}\beta_{n+1} + \Gamma^{-1}\big(l_{S_{\bar{A}_1}}\bar{A}_n + l_{S_{\bar{B}_1}}\bar{B}_{n-1} + l_{S_{\bar{B}_2}}\bar{B}_{n+1}\big)\Bigg)P_n'(\mu).\end{aligned}$$

In these equations, the coefficients are defined as

$$s_{A_1} = -\frac{(n+1)}{a^{n+2}}, \qquad t_{A_1} = -\frac{1}{a^{n+2}},$$

$$s_{B_1} = -\frac{n(n+3-4\nu)}{(2n-1)a^n}, \qquad t_{B_1} = -\frac{(n-4+4\nu)}{(2n-1)a^n},$$

$$s_{B_2} = -\frac{(n+1)(n+5-4\nu)}{(2n+3)a^{n+2}}, \qquad t_{B_2} = -\frac{(n+5-4\nu)}{(2n+3)a^{n+2}},$$

$$s_{\alpha_1} = na^{n-1}(1-\delta_{1n}), \qquad t_{\alpha_1} = -a^{n-1}(1-\delta_{1n}),$$

$$s_{\beta_1} = \frac{n(n-4+4\nu)a^{n-1}(1-\delta_{1n})}{(2n-1)}, \qquad t_{\beta_1} = -\frac{(n-4+4\nu)a^{n-1}(1-\delta_{1n})}{(2n-1)},$$

$$s_{\beta_2} = \frac{(n+1)(n-2+4\nu)a^{n+1}}{(2n+3)}, \qquad t_{\beta_2} = -\frac{(n+5-4\nu)a^{n+1}}{(2n+3)},$$

$$s_{\bar{A}_1} = na^{n-1}, \qquad t_{\bar{A}_1} = -a^{n-1},$$

$$s_{\bar{B}_1} = \frac{n(n-4+4\bar{\nu})a^{n-1}(1-\delta_{1n})}{(2n-1)}, \qquad t_{\bar{B}_1} = -\frac{(n-4+4\bar{\nu})a^{n-1}(1-\delta_{1n})}{(2n-1)},$$

$$s_{\bar{B}_2} = \frac{(n+1)(n-2+4\bar{\nu})a^{n+1}}{(2n+3)}, \qquad t_{\bar{B}_2} = -\frac{(n+5-4\bar{\nu})a^{n+1}}{(2n+3)},$$

$$i_{A_1} = \frac{(n+1)(n+2)}{a^{n+3}}, \qquad i_{S_{A_1}} = \frac{(n+1)(n+2)\chi_3}{a^{n+4}},$$

$$i_{B_1} = \frac{n(n^2+3n-2\nu)}{(2n-1)a^{n+1}}, \qquad i_{S_{B_1}} = \frac{n\big(n(n+1)-2(1-2\nu)(n-1)\big)\chi_3}{(2n-1)a^{n+2}},$$

$$i_{B_2} = \frac{(n+1)(n+2)(n+5-4\nu)}{(2n+3)a^{n+3}}, \qquad i_{S_{B_2}} = \frac{(n+1)(n+2)(n+5-4\nu)\chi_3}{(2n+3)a^{n+4}},$$

$$i_{\alpha_1} = (n-1)na^{n-2}, \qquad i_{S_{\alpha_1}} = (n-1)n\chi_3 a^{n-3},$$

$$i_{\beta_1} = \frac{(n-1)n(n-4+4\nu)a^{n-2}}{(2n-1)}, \qquad i_{S_{\beta_1}} = \frac{(n-1)n(n-4+4\nu)\chi_3 a^{n-3}}{(2n-1)},$$

$$i_{\beta_2} = \frac{(n+1)(n^2-n-2-2\nu)a^n}{(2n+3)}, \qquad i_{S_{\beta_2}} = \frac{(n+1)\big(n(n+1)+2(1-2\nu)(n+2)\big)\chi_3 a^{n-1}}{(2n+3)},$$

$$i_{\bar{A}_1} = (n-1)na^{n-2}, \qquad i_{S_{\bar{A}_1}} = (n-1)n\chi_3 a^{n-3},$$

$$i_{\bar{B}_1} = \frac{(n-1)n(n-4+4\bar{\nu})a^{n-2}}{(2n-1)}, \qquad i_{S_{\bar{B}_1}} = \frac{(n-1)n(n-4+4\bar{\nu})\chi_3 a^{n-3}}{(2n-1)},$$

$$i_{\bar{B}_2} = \frac{(n+1)(n^2-n-2-2\bar{\nu})a^n}{(2n+3)}, \qquad i_{S_{\bar{B}_2}} = \frac{(n+1)\big(n(n+1)+2(1-2\bar{\nu})(n+2)\big)\chi_3 a^{n-1}}{(2n+3)},$$

$$l_{A_1}=\frac{(n+2)}{a^{n+3}},\qquad l_{S_{A_1}}=\frac{(n+2)(n\chi_0+\chi_1)}{a^{n+4}},$$

$$l_{B_1}=\frac{(n^2-2+2\nu)}{(2n-1)a^{n+1}},\qquad l_{S_{B_1}}=\frac{\big(n^3-2n^2(1-2\nu)-2n+4(1-\nu)\big)\chi_0+\big(n^2+4(1-\nu)(n-1)\big)\chi_1}{(2n-1)a^{n+2}},$$

$$l_{B_2}=\frac{(n+2)(n+5-4\nu)}{(2n+3)a^{n+3}},\qquad l_{S_{B_2}}=\frac{(n+2)(n+5-4\nu)(n\chi_0+\chi_1)}{(2n+3)a^{n+4}},$$

$$l_{\alpha_1}=-(n-1)a^{n-2},\qquad l_{S_{\alpha_1}}=(n-1)\big((n+1)\chi_0-\chi_1\big)a^{n-3},$$

$$l_{\beta_1}=-\frac{(n-1)(n-4+4\nu)a^{n-2}}{(2n-1)},\qquad l_{S_{\beta_1}}=\frac{(n-1)(n-4+4\nu)\big((n+1)\chi_0-\chi_1\big)a^{n-3}}{(2n-1)},$$

$$l_{\beta_2}=-\frac{(n^2+2n-1+2\nu)a^n}{(2n+3)},\qquad l_{S_{\beta_2}}=\frac{\big(\big(n^3+n^2(5-4\nu)+n(5-8\nu)-3\big)\chi_0-\big((n+1)^2-4(1-\nu)(n+2)\big)\chi_1\big)a^{n-1}}{(2n+3)},$$

$$l_{\bar{A}_1}=-(n-1)a^{n-2},\qquad l_{S_{\bar{A}_1}}=(n-1)\big((n+1)\chi_0-\chi_1\big)a^{n-3},$$

$$l_{\bar{B}_1}=-\frac{(n-1)(n-4+4\bar{\nu})a^{n-2}}{(2n-1)},\qquad l_{S_{\bar{B}_1}}=\frac{(n-1)(n-4+4\bar{\nu})\big((n+1)\chi_0-\chi_1\big)a^{n-3}}{(2n-1)},$$

$$l_{\bar{B}_2}=-\frac{(n^2+2n-1+2\bar{\nu})a^n}{(2n+3)},\qquad l_{S_{\bar{B}_2}}=\frac{\big(\big(n^3+n^2(5-4\bar{\nu})+n(5-8\bar{\nu})-3\big)\chi_0-\big((n+1)^2-4(1-\bar{\nu})(n+2)\big)\chi_1\big)a^{n-1}}{(2n+3)}.$$

The length scale parameters are defined as

$$\chi_0=\frac{1}{4G}(\lambda^S+2\mu^S),\quad \chi_1=\frac{1}{4G}(\lambda^S+\tau_0),\qquad \chi_2=\chi_0-\chi_1,\quad \chi_3=\chi_0+\chi_1, \tag{29}$$

where λ^S, μ^S are the interface Lamé moduli for spherical interface ($R=a$).

References

[Adamson 1982] A. W. Adamson, *Physical chemistry of surfaces*, Wiley, New York, 1982.

[Cahn and Larche 1982] J. W. Cahn and F. Larche, "Surface stress and the chemical equilibrium of small crystals. II. solid particles embedded in a solid matrix", *Acta Metall.* **30**:1 (1982), 51–56.

[Duan et al. 2005a] H. L. Duan, J. Wang, Z. P. Huang, and B. L. Karihaloo, "Eshelby formalism for nano-inhomogeneities", *P. Roy. Soc. Lond. A Mat.* **461**:2062 (2005), 3335–3353.

[Duan et al. 2005b] H. L. Duan, J. Wang, Z. P. Huang, and Z. Y. Luo, "Stress concentration tensors of inhomogeneities with interface effects", *Mech. Mater.* **37**:7 (2005), 723–736.

[Gradshteyn and Ryzhik 1994] I. S. Gradshteyn and I. M. Ryzhik, *Table of integrals, series and products*, 5th ed., Academic Press, San Diego, 1994.

[Gurtin and Murdoch 1975a] M. E. Gurtin and A. I. Murdoch, "A continuum theory of elastic material surfaces", *Arch. Ration. Mech. An.* **57**:4 (1975), 291–323.

[Gurtin and Murdoch 1975b] M. E. Gurtin and A. I. Murdoch, "A continuum theory of elastic material surfaces", *Arch. Ration. Mech. An.* **59**:4 (1975), 389–390.

[Gurtin and Murdoch 1978] M. E. Gurtin and A. I. Murdoch, "Surface stress in solids", *Int. J. Solids Struct.* **14**:6 (1978), 431–440.

[Gurtin et al. 1998] M. E. Gurtin, J. Weissmuller, and F. Larche, "A general theory of curved deformable interfaces in solids at equilibrium", *Philos. Mag. A* **78**:5 (1998), 1093–1109.

[Miller and Shenoy 2000] R. E. Miller and V. B. Shenoy, "Size-dependent elastic properties of nanosized structural elements", *Nanotechnology* **11**:3 (2000), 139–147.

[Mindlin and Cheng 1950] R. D. Mindlin and D. H. Cheng, "Thermoelastic stress in the semi-infinite solid", *J. Appl. Phys.* **21**:9 (1950), 931–933.

[Morse and Feshbach 1953] P. M. Morse and H. Feshbach, *Methods of theoretical physics*, vol. II, McGraw-Hill, New York, 1953.

[Mura 1987] T. Mura, *Micromechanics of defects in solids*, Martinus Nijhoff, The Hague, 1987.

[Sharma and Ganti 2004] P. Sharma and S. Ganti, "Size-dependent Eshelby's tensor for embedded nano-inclusions incorporating surface/interface energies", *J. Appl. Mech. (Trans. ASME)* **71**:5 (2004), 663–671.

[Sharma et al. 2003] P. Sharma, S. Ganti, and N. Bhate, "Effect of surfaces on the size-dependent elastic state of nano-inhomogeneities", *Appl. Phys. Lett.* **82**:4 (2003), 535–537.

[Sneddon 1951] I. N. Sneddon, *Fourier transforms*, McGraw-Hill, New York, 1951.

[Tersoff et al. 1996] J. Tersoff, C. Teichert, and M. G. Lagally, "Self-organization in growth of quantum dot superlattices", *Phys. Rev. Lett.* **76**:10 (1996), 1675–1678.

[Tsuchida and Nakahara 1970] E. Tsuchida and I. Nakahara, "Three-dimensional stress concentration around a spherical cavity in a semi-infinite elastic body", *Bull. Jpn. Soc. Mech. Eng.* **13**:58 (1970), 499–508.

[Tsuchida and Nakahara 1972] E. Tsuchida and I. Nakahara, "Stresses in a semi-infinite body subjected to uniform pressure on the surface of a cavity and the plane boundary", *Bull. Jpn. Soc. Mech. Eng.* **15**:79 (1972), 1–10.

[Tsutsui et al. 1974] S. Tsutsui, S. Chikamatsu, and K. Saito, "Stress field of the semi-infinite medium containing a spherical inclusion under all-around tension", *Trans. Jpn. Soc. Mech. Eng.* **40**:337 (1974), 2484–2493.

Received 23 Dec 2005.

CHANGWEN MI: mi@uwyo.edu
Department of Mechanical Engineering, University of Wyoming, Laramie WY 82071, United States

DEMITRIS A. KOURIS: kouris@uwyo.edu
Department of Mechanical Engineering, University of Wyoming, Laramie WY 82071, United States

JOURNAL OF MECHANICS OF MATERIALS AND STRUCTURES
Vol. 1, No. 4, 2006

EXTREME VALUES OF POISSON'S RATIO AND OTHER ENGINEERING MODULI IN ANISOTROPIC MATERIALS

ANDREW N. NORRIS

Conditions for a maximum or minimum of Poisson's ratio of anisotropic elastic materials are derived. For a uniaxial stress in the 1-direction and Poisson's ratio ν defined by the contraction in the 2-direction, the following three quantities vanish at a stationary value: s_{14}, $[2\nu s_{15} + s_{25}]$ and $[(2\nu - 1)s_{16} + s_{26}]$, where s_{IJ} are the components of the compliance tensor. Analogous conditions for stationary values of Young's modulus and the shear modulus are obtained, along with second derivatives of the three engineering moduli at the stationary values. The stationary conditions and the hessian matrices are presented in forms that are independent of the coordinates, which lead to simple search algorithms for extreme values. In each case the global extremes can be found by a simple search over the stretch direction **n** only. Simplifications for stretch directions in a plane of orthotropic symmetry are also presented, along with numerical examples for the extreme values of the three engineering constants in crystals of monoclinic symmetry.

1. Introduction

Poisson's ratio ν, Young's modulus E and the shear modulus G, collectively called the engineering moduli, are of fixed value in isotropic materials and related by $2G(1 + \nu) = E$. No such connection holds in anisotropic elastic solids, and all three become dependent upon the directions of stretch, lateral strain, and the shear directions. Hayes [1972] derived some universal relations between values for certain pairs of orthogonal directions. However, apart from cubic symmetry [Norris 2006b], there is no general formula for the directions and values associated with the largest and smallest values of the engineering moduli. The purpose of this paper is to provide systematic methods which can be used to find the extreme values of the engineering moduli in any type of anisotropy.

The problem of finding the extreme values of Young's modulus is the simplest since E depends only on a single direction of stretch. Numerical searching is practical and straightforward; thus Cazzani and Rovati provide a detailed analysis of the extrema of Young's modulus for cubic and transversely isotropic materials

Keywords: Poisson's ratio, Young's modulus, shear modulus, anisotropic.

[Cazzani and Rovati 2003] and for materials with tetragonal symmetry [Cazzani and Rovati 2005], with extensive illustrative examples. Boulanger and Hayes [1995] obtained analytic expressions related to extrema of Young's modulus. For stretch in the 1-direction, they showed that $E = 1/s_{11}$ achieves a stationary value if the two conditions $s_{15} = 0$ and $s_{16} = 0$ are satisfied. In a pair of complementary papers, Ting derived explicit expressions for the stress directions and the stationary values of Young's modulus for triclinic and monoclinic [Ting 2005b], orthotropic, tetragonal, trigonal, hexagonal and cubic materials [Ting 2005a]. We will rederive the stationary conditions for E below, along with conditions required for a local maximum or minimum.

Poisson's ratio and the shear modulus depend upon pairs of orthogonal directions, which makes their classification far more complicated than for E. At the same time, there is considerable interest in anisotropic materials which exhibit negative values of Poisson's ratio, also called auxetic materials [Yang et al. 2004]. In sharp contrast to isotropic solids for which $-1 < \nu < 1/2$, the value of ν is unrestricted in anisotropic materials and may achieve arbitrarily large positive and negative values in the same material. The first hint of this surprising possibility was given by Boulanger and Hayes [1998] who presented a theoretical set of elastic moduli for a material with orthorhombic symmetry which satisfy the positivity requirements, but exhibit simultaneous arbitrarily large positive and negative values of ν. Ting and Chen [2005] and Ting [2004] subsequently demonstrated that the same remarkable phenomenon can be obtained in any nonisotropic material symmetry, including cubic symmetry and transverse isotropy. Further explanation of the effect in cubic symmetry is provided in Section 6 below and in [Norris 2006b]. We note that Rovati presented extensive numerical examples of auxetic behavior in orthorhombic [Rovati 2003] and monoclinic materials [Rovati 2004], while Ting and Barnett [2005] derived general conditions required for the occurrence of negative values of ν.

The purpose of this paper is to provide a general framework for finding the maximum and minimum values of ν and G in anisotropic materials. Some progress in this regard is due to Ting [2005a] who discusses the conditions for extreme values of the shear modulus with particular attention to shear in planes of material symmetry. As far as I know, there are no results reported to date on conditions necessary for extreme values of the Poisson's ratio. Particular attention is given in this paper to the Poisson's ratio, with the emphasis on deriving conditions that are independent of the coordinate system used. It will become evident that there is a strong analogy between the problems for the shear modulus and the Poisson's ratio. In particular, by formulating the problems in a coordinate free manner, the task of searching for extreme values of both is similar.

The outline of the paper is as follows. The three engineering moduli are introduced in Section 2, along with the equations for the transformation of elastic moduli under rotation. These are used in Section 3 to derive the conditions required for stationary values of ν, E and G, and the values of the second derivatives (Hessian) at the stationary points are determined in Section 4. The various results are all cast in terms of stretch, strain and shearing along coordinate axes. The more general format for stationary conditions in general directions, independent of the coordinates, are presented in Section 5. The specific application to Poisson's ratio is considered in Section 6. The stationary conditions for stretch in a plane of orthotropic symmetry are derived, and it is shown that at most four stationary values of ν can occur, two for in-plane lateral strain, and two out-of-plane. These results are applied to the specific case of extreme values of ν in materials with cubic symmetry, recovering results of [Norris 2006b]. Applications to generally anisotropic materials are also discussed, and a fast procedure for searching for extreme values of ν is derived and demonstrated for some materials of monoclinic symmetry. Finally, in Section 7 we present a similar procedure for finding the global extreme values of G in generally anisotropic media, with numerical examples.

2. Definition of the engineering moduli and preliminary equations

Poisson's ratio measures lateral strain in the presence of uniaxial stress. For any orthonormal pair of vectors $\{\mathbf{n}, \mathbf{m}\}$, the Poisson's ratio $\nu_{nm} = \nu(\mathbf{n}, \mathbf{m})$ is defined by the ratio of the strains in the two directions for a uniaxial state of stress along one of them [Rovati 2004]:

$$\nu_{nm} = -\frac{\boldsymbol{\varepsilon} : \mathbf{mm}}{\boldsymbol{\varepsilon} : \mathbf{nn}} \qquad \text{for } \boldsymbol{\sigma} = \sigma\, \mathbf{nn},$$

where $\boldsymbol{\varepsilon}$ and $\boldsymbol{\sigma}$ are the symmetric tensors of strain and stress, respectively, and $\mathbf{ab}$ is the tensor product, sometimes denoted $\mathbf{a} \otimes \mathbf{b}$. The Young's modulus $E_n = E(\mathbf{n})$ relates the axial strain and stress,

$$E_n = \frac{\sigma}{\boldsymbol{\varepsilon} : \mathbf{nn}} \qquad \text{for } \boldsymbol{\sigma} = \sigma\, \mathbf{nn}.$$

The third engineering modulus is the shear modulus $G_{nm} = G(\mathbf{n}, \mathbf{m})$,

$$G_{nm} = \frac{\sigma}{\boldsymbol{\varepsilon} : (\mathbf{nm} + \mathbf{mn})} \qquad \text{for } \boldsymbol{\sigma} = \sigma\, (\mathbf{nm} + \mathbf{mn}).$$

Tensor components are defined relative to the fixed orthonormal basis $\{\mathbf{e}_1, \mathbf{e}_2, \mathbf{e}_3\}$,

$$\boldsymbol{\sigma} = \sigma_{ij}\, \mathbf{e}_i \mathbf{e}_j, \qquad \boldsymbol{\varepsilon} = \varepsilon_{ij}\, \mathbf{e}_i \mathbf{e}_j.$$

The stress σ_{ij} and strain ε_{ij} are related by

$$\varepsilon_{ij} = s_{ijkl} \sigma_{kl}.$$

(Lower case Latin suffixes take on the values 1, 2, and 3, and the summation convention on repeated indices is assumed unless noted otherwise.) Here s_{ijkl} denote the components of the fourth order compliance tensor. We use the Voigt notation for conciseness; compliance is $\mathbf{S} = [s_{IJ}]$, $I, J = 1, 2, \ldots, 6$, with $I = 1, 2, 3, 4, 5, 6$ corresponding to $ij = 11, 22, 33, 23, 31, 12$, and $s_{JI} = s_{IJ}$.

The goal is to find conditions for a maximum or minimum of the engineering moduli, with emphasis on Poisson's ratio. With no loss in generality assume that $\mathbf{n}$ is in the $\mathbf{e}_1$ direction, and $\mathbf{m}$ is in the $\mathbf{e}_2$ direction. Thus, we consider $\nu \equiv \nu_{12}$, $E \equiv E_1$ and $G \equiv G_{12}$, that is,

$$\nu = -\frac{s_{12}}{s_{11}}, \qquad E = \frac{1}{s_{11}}, \qquad G = \frac{1}{4s_{66}}. \tag{1}$$

(We take $s_{66} = s_{1212}$ although it is common to subsume the factor of 4 in the definition of s_{66} in eq. $(1)_3$.) Our objective is then to find conditions for a maximum or minimum of each engineering modulus under the assumption that the material is assumed to be free to orient in arbitrary directions with oriented moduli while the stress remains of fixed orientation. This is equivalent to stationarity conditions for ν_{nm}, E_n and G_{nm} for a fixed orientation material while $\{\mathbf{n}, \mathbf{m}\}$ range over all possible orthonormal pairs.

We therefore need to consider how ν, E and G of (1) vary under general rotation of the material. Define the rotation by angle θ about an arbitrary direction $\mathbf{q}$, $|\mathbf{q}| = 1$, as $\mathbf{Q}(\mathbf{q}, \theta) \in O(3)$, such that vectors (including the basis vectors) transform as $\mathbf{r} \to \mathbf{r}' = \mathbf{Q}\mathbf{r}$. Under the change of basis associated with $\mathbf{Q}(\mathbf{q}, \theta)$, second order tensors (including stress and strain) transform as $\boldsymbol{\sigma} \to \boldsymbol{\sigma}'$, where $\sigma'_{ij} = Q_{ir}Q_{js}\sigma_{rs}$, or

$$\sigma'_{ij} = \mathbb{Q}_{ijrs}\sigma_{rs}, \qquad \text{where} \quad \mathbb{Q}_{ijrs} = \tfrac{1}{2}\big(Q_{ir}Q_{js} + Q_{is}Q_{jr}\big).$$

In order to simplify the algebra we use the connection between fourth order elasticity tensors in 3 dimensions and second order symmetric tensor of 6 dimensions [Mehrabadi and Cowin 1990]. Accordingly, the 6×6 matrix $\widehat{\mathbf{S}}$ with elements $\widehat{S}_{IJ}$ is defined as

$$\widehat{\mathbf{S}} = \mathbf{T}\mathbf{S}\mathbf{T}, \qquad \text{where } \mathbf{T} \equiv \operatorname{diag}\big(1,\ 1,\ 1,\ \sqrt{2},\ \sqrt{2},\ \sqrt{2}\big).$$

Rotation of second and fourth order tensors is most simply presented in terms of the 6×6 rotation matrix $\widehat{\mathbf{Q}}$ which is the 6-dimensional version of the fourth order tensor $\mathbb{Q}_{ijrs}$, introduced by Mehrabadi et al. [1995]. Fourth order tensors transform as $\widehat{\mathbf{S}} \to \widehat{\mathbf{S}}' = \widehat{\mathbf{Q}}\widehat{\mathbf{S}}\widehat{\mathbf{Q}}^T$, where $\widehat{\mathbf{Q}}(\mathbf{q}, \theta)$ is an orthogonal second order tensor of six dimensions, satisfying $\widehat{\mathbf{Q}}\widehat{\mathbf{Q}}^T = \widehat{\mathbf{Q}}^T\widehat{\mathbf{Q}} = \widehat{\mathbf{I}} = \operatorname{diag}(1, 1, 1, 1, 1, 1)$. It satisfies

$$\frac{\partial \widehat{\mathbf{Q}}}{\partial \theta}(\mathbf{q}, \theta) = \widehat{\mathbf{R}}(\mathbf{q})\widehat{\mathbf{Q}}, \qquad \widehat{\mathbf{Q}}(\mathbf{q}, 0) = \widehat{\mathbf{I}}, \tag{2}$$

where $\widehat{\mathbf{R}}$ is a skew symmetric six dimensional tensor linear in $\mathbf{q}$,

$$\widehat{\mathbf{R}}(\mathbf{q}) = \begin{pmatrix} 0 & 0 & 0 & 0 & \sqrt{2}q_2 & -\sqrt{2}q_3 \\ 0 & 0 & 0 & -\sqrt{2}q_1 & 0 & \sqrt{2}q_3 \\ 0 & 0 & 0 & \sqrt{2}q_1 & -\sqrt{2}q_2 & 0 \\ 0 & \sqrt{2}q_1 & -\sqrt{2}q_1 & 0 & q_3 & -q_2 \\ -\sqrt{2}q_2 & 0 & \sqrt{2}q_2 & -q_3 & 0 & q_1 \\ \sqrt{2}q_3 & -\sqrt{2}q_3 & 0 & q_2 & -q_1 & 0 \end{pmatrix}.$$

Further details can be found in [Mehrabadi et al. 1995; Norris 2006a].

3. Extremal conditions

Consider any one of the engineering moduli, say f, as a function of both the underlying compliance and of the rotation $\widehat{\mathbf{Q}}$. A stationary value is obtained if f is unchanged with respect to additional small rotations. In order to formulate this more precisely, assume f is at a stationary point, and define

$$\widehat{\mathbf{S}}(\mathbf{q}, \theta) = \widehat{\mathbf{Q}}(\mathbf{q}, \theta)\widehat{\mathbf{S}}\widehat{\mathbf{Q}}^T(\mathbf{q}, \theta). \tag{3}$$

Define the rotational derivative,

$$f'(\mathbf{q}) \equiv \frac{\partial f}{\partial \theta}\big(\widehat{\mathbf{S}}(\mathbf{q}, \theta)\big)\Big|_{\theta=0} = \frac{\partial f}{\partial s_{IJ}} s'_{IJ}(\mathbf{q}). \tag{4}$$

The elements $s'_{IJ}(\mathbf{q})$ of the the rotational derivative of the compliance can be expressed by using the representation (2) with (3),

$$\widehat{\mathbf{S}}' = \widehat{\mathbf{R}}(\mathbf{q})\widehat{\mathbf{S}} + \widehat{\mathbf{S}}\widehat{\mathbf{R}}^T(\mathbf{q}). \tag{5}$$

Thus, we have the equality given on top of page 798, where the s_{IJ} are the values at $\theta = 0$ (which are independent of $\mathbf{q}$) and the derivatives are linear functions of the coordinates of $\mathbf{q}$. We may write

$$f'(\mathbf{q}) = \mathbf{d}^{(f)} \cdot \mathbf{q}, \tag{6}$$

where the vector $\mathbf{d}^{(f)}$ is independent of $\mathbf{q}$ and depends only on the compliances.

The engineering modulus f is stationary with respect to the direction $\mathbf{n}$, and the direction $\mathbf{m}$ where applicable, if $f'(\mathbf{q})$ vanishes for *all* axes of rotation $\mathbf{q}$. This is equivalent to requiring that all possible deviations in $\mathbf{n}$ and $\mathbf{m}$ leave f unchanged to first order in the rotation. The stipulation that this hold for all rotation axes covers all permissible transformations. The general condition for stationarity is therefore that the vector $\mathbf{d}^{(f)}$ must vanish, that is,

$$\mathbf{d}^{(f)} = 0 \quad \text{at a stationary point of } f.$$

$$\begin{pmatrix} s'_{11} \\ s'_{22} \\ s'_{33} \\ s'_{12} \\ s'_{23} \\ s'_{13} \\ s'_{14} \\ s'_{25} \\ s'_{36} \\ s'_{15} \\ s'_{16} \\ s'_{24} \\ s'_{26} \\ s'_{34} \\ s'_{35} \\ s'_{44} \\ s'_{55} \\ s'_{66} \\ s'_{45} \\ s'_{46} \\ s'_{56} \end{pmatrix} = \begin{pmatrix} 0 & 4s_{15} & -4s_{16} \\ -4s_{24} & 0 & 4s_{26} \\ 4s_{34} & -4s_{35} & 0 \\ -2s_{14} & 2s_{25} & 2s_{16}-2s_{26} \\ 2s_{24}-2s_{34} & -2s_{25} & 2s_{36} \\ 2s_{14} & 2s_{35}-2s_{15} & -2s_{36} \\ s_{12}-s_{13} & -s_{16}+2s_{45} & s_{15}-2s_{46} \\ s_{26}-2s_{45} & s_{23}-s_{12} & -s_{24}+2s_{56} \\ -s_{35}+2s_{46} & s_{34}-2s_{56} & s_{13}-s_{23} \\ s_{16} & -s_{11}+s_{13}+2s_{55} & -s_{14}-2s_{56} \\ -s_{15} & s_{14}+2s_{56} & s_{11}-s_{12}-2s_{66} \\ s_{22}-s_{23}-2s_{44} & -s_{26} & s_{25}+2s_{46} \\ -s_{25}-2s_{46} & s_{24} & -s_{22}+s_{12}+2s_{66} \\ -s_{33}+s_{23}+2s_{44} & -s_{36}-2s_{45} & s_{35} \\ s_{36}+2s_{45} & s_{33}-s_{13}-2s_{55} & -s_{34} \\ 2s_{24}-2s_{34} & -2s_{46} & 2s_{45} \\ 2s_{56} & 2s_{35}-2s_{15} & -2s_{45} \\ -2s_{56} & 2s_{46} & 2s_{16}-2s_{26} \\ s_{25}-s_{35}+s_{46} & -s_{14}+s_{34}-s_{56} & s_{55}-s_{44} \\ -s_{36}+s_{26}-s_{45} & s_{44}-s_{66} & s_{14}-s_{24}+s_{56} \\ s_{66}-s_{55} & s_{36}-s_{16}+s_{45} & -s_{25}+s_{15}-s_{46} \end{pmatrix} \begin{pmatrix} q_1 \\ q_2 \\ q_3 \end{pmatrix}.$$

We now apply this formalism to the three engineering moduli and derive $\mathbf{d}^{(\nu)}$, $\mathbf{d}^{(E)}$ and $\mathbf{d}^{(G)}$ in turn.

3.1. ***Poisson's ratio.*** For Poisson's ratio, Equation (4) becomes

$$\nu'(\mathbf{q}) = (s_{11})^{-2}\left[s_{12}\, s'_{11}(\mathbf{q}) - s_{11}\, s'_{12}(\mathbf{q})\right]. \tag{7}$$

Thus, from the display above and Equations (6) and (7), we have

$$\mathbf{d}^{(\nu)} = \frac{2}{s_{11}^2}\left[s_{11}s_{14}\mathbf{e}_1 + \left(2s_{12}s_{15} - s_{11}s_{25}\right)\mathbf{e}_2 + \left(s_{11}s_{26} - s_{11}s_{16} - 2s_{12}s_{16}\right)\mathbf{e}_3\right]. \tag{8}$$

Setting this to zero and using the definition of ν in (1), and the fact that $s_{11} > 0$, we obtain three conditions for a stationary value of Poisson's ratio:

$$s_{14} = 0, \qquad 2\nu s_{15} + s_{25} = 0, \qquad (2\nu - 1)s_{16} + s_{26} = 0. \tag{9}$$

These must be simultaneously satisfied at a maximum or minimum of ν. Note that the compliance elements appearing in (9) are all zero in isotropic materials.

3.2. ***Young's modulus.*** Proceeding in the same manner as for the Poisson's ratio, and using $E'(\mathbf{q}) = -(s_{11})^{-2} s'_{11}(\mathbf{q})$, gives

$$\mathbf{d}^{(E)} = 4(s_{11})^{-2}\,(-s_{15}\mathbf{e}_2 + s_{16}\mathbf{e}_3).$$

Setting this to zero implies the conditions for an extremum in Young's modulus

$$s_{15} = 0, \qquad s_{16} = 0. \tag{10}$$

These agree with two conditions determined by Boulanger and Hayes [1995] and by Ting [2005b].

3.3. ***Shear modulus.*** The rotational derivative of the shear modulus is

$$G'(\mathbf{q}) = -\tfrac{1}{4}(s_{66})^{-2} s'_{66}(\mathbf{q}),$$

and the gradient vector is

$$\mathbf{d}^{(G)} = \tfrac{1}{2}(s_{66})^{-2}\left[s_{56}\mathbf{e}_1 - s_{46}\mathbf{e}_2 + (s_{26} - s_{16})\mathbf{e}_3\right].$$

Hence, the shear modulus has an extreme value if the following conditions hold:

$$s_{56} = 0, \qquad s_{46} = 0, \qquad s_{16} - s_{26} = 0. \tag{11}$$

4. Second derivatives

The nature of a stationary value of the general engineering modulus f can be discerned, at least locally, by the second derivative. By analogy with Equation (4), we define the rotational second derivative,

$$f''(\mathbf{q}) \equiv \frac{\partial^2 f}{\partial s_{IJ}\,\partial s_{KL}}\, s'_{IJ}(\mathbf{q}) s'_{KL}(\mathbf{q}) + \frac{\partial f}{\partial s_{IJ}}\, s''_{IJ}(\mathbf{q}). \tag{12}$$

The elements $s''_{IJ}(\mathbf{q})$ of the rotational second derivative of the compliance follow from

$$\widehat{\mathbf{S}}''(\mathbf{q}) = \widehat{\mathbf{R}}^2\widehat{\mathbf{S}} + \widehat{\mathbf{S}}\widehat{\mathbf{R}}^{2T} + 2\widehat{\mathbf{R}}\widehat{\mathbf{S}}\widehat{\mathbf{R}}^{T}.$$

This is a direct consequence of Equation (5). We do not need all 21 elements, and for brevity only present the following three values which are necessary to evaluate the second derivatives of the engineering moduli,

$$s''_{11} = 4\big[(s_{13}-s_{11}+2s_{55})q_2^2+(s_{12}-s_{11}+2s_{66})q_3^2-2(s_{14}+2s_{56})q_2q_3 \\ +s_{15}q_3q_1+s_{16}q_1q_2\big],$$

$$s''_{12} = 2\big[(s_{13}-s_{12})q_1^2+(s_{23}-s_{12})q_2^2+(s_{11}+s_{22}-2s_{12}-4s_{66})q_3^2 \\ +(s_{14}-2s_{24}+4s_{56})q_2q_3+(s_{25}-2s_{15}+4s_{46})q_3q_1+(s_{16}+s_{26}-4s_{45})q_1q_2\big],$$

$$s''_{66} = 2\big[(s_{55}-s_{66})q_1^2+(s_{44}-s_{66})q_2^2+(s_{16}+s_{26}-2s_{36}-2s_{45})q_1q_2 \\ +(s_{11}+s_{22}-2s_{12}-4s_{66})q_3^2+(2s_{25}-2s_{15}+3s_{46})q_1q_3+(2s_{14}-2s_{24}+3s_{56})q_2q_3\big].$$

Before applying these to the three engineering moduli $f = \nu$, E and G, we note that in each case that f is a homogeneous function of degree 0 or -1 in the compliance elements. Consequently the second derivative f'' evaluated at the stationary point where $f' = 0$ simplifies because the first term in (12) vanishes, leaving

$$f''(\mathbf{q}) = \frac{\partial f}{\partial s_{IJ}}\, s''_{IJ}(\mathbf{q}) \qquad \text{at } f'(\mathbf{q}) = 0. \tag{13}$$

The terms $s''_{IJ}(\mathbf{q})$ are second order in $\mathbf{q}$, and we can write

$$f''(\mathbf{q}) = \mathbf{D}^{(f)} : \mathbf{qq} \qquad \text{at } f'(\mathbf{q}) = 0,$$

where $\mathbf{D}^{(f)} = \mathbf{D}^{(f)T}$ is a nondimensional symmetric 3×3 matrix which is independent of $\mathbf{q}$. Thus, $\mathbf{D}^{(f)}$ is positive (negative) semidefinite at a local minimum (maximum) of f. The condition for a local minimum (maximum) is therefore that the three eigenvalues of $\mathbf{D}^{(f)}$ are positive (negative). If the matrix is not definite and has eigenvalues of opposite sign, then the modulus has a locally saddle shaped behavior.

4.1. ***Poisson's ratio.*** The second derivative of the Poisson's ratio at a stationary point is, using (13),

$$\nu''(\mathbf{q}) = -(s_{11})^{-1}\left(s''_{12} + \nu s''_{11}\right) \qquad \text{at } \nu'(\mathbf{q}) = 0. \tag{14}$$

Thus, when $\nu'(\mathbf{q}) = 0$, Equation (14) gives

$$\nu''(\mathbf{q}) = \frac{2}{s_{11}^2}\Big\{s_{11}(s_{12}-s_{13})q_1^2+\big[s_{11}(s_{12}-s_{13})+2s_{12}(s_{13}-s_{11}+2s_{55})\big]q_2^2 \\ +\big[s_{11}(2s_{12}+4s_{66}-s_{11}-s_{22})+2s_{12}(s_{12}-s_{11}+2s_{66})\big]q_3^2 \\ +2\big[s_{11}(s_{24}-2s_{56}-\tfrac{1}{2}s_{14})-2s_{12}(s_{14}+2s_{56})\big]q_2q_3 \\ +2\big[s_{11}(s_{15}-2s_{46}-\tfrac{1}{2}s_{25})+s_{12}s_{15}\big]q_3q_1 \\ +2\big[s_{11}(2s_{45}-\tfrac{1}{2}s_{16}-\tfrac{1}{2}s_{26})+s_{12}s_{16}\big]q_1q_2\Big\}.$$

Since this is evaluated at the stationary value, we may use (9) to simplify and obtain

$$\mathbf{D}^{(\nu)} = \frac{2}{s_{11}} \begin{pmatrix} s_{12}-s_{13} & 2s_{45}-s_{16} & s_{15}-2s_{46} \\ 2s_{45}-s_{16} & s_{12}-s_{13}- \\ & 2\nu(s_{13}-s_{11}+2s_{55}) & s_{24}-2(1-2\nu)s_{56} \\ s_{15}-2s_{46} & s_{24}-2(1-2\nu)s_{56} & s_{12}-s_{22}+2s_{66}+ \\ & & (1-2\nu)(s_{12}-s_{11}+2s_{66}) \end{pmatrix}, \quad (15)$$

where we have used the definition of ν to simplify the elements.

4.2. ***Young's modulus.*** At a stationary point we have $E''(\mathbf{q}) = -(s_{11})^{-2}\, s''_{11}$ and $E'(\mathbf{q}) = 0$. Using the extremal (10), we find

$$\mathbf{D}^{(E)} = \frac{1}{s_{11}^2} \begin{pmatrix} 0 & 0 & 0 \\ 0 & s_{11}-s_{13}-2s_{55} & s_{14}+2s_{56} \\ 0 & s_{14}+2s_{56} & s_{11}-s_{12}-2s_{66} \end{pmatrix}.$$

Note that $\mathbf{D}^{(E)}$ is rank deficient (of rank 2), which is a consequence of the fact that E is invariant under rotation about the $\mathbf{e}_1$ stretch axis. The local nature of the stationary value depends upon the two nonzero eigenvalues of the matrix.

4.3. ***Shear modulus.*** The shear modulus satisfies

$$G''(\mathbf{q}) = -\tfrac{1}{4}(s_{66})^{-2}\, s''_{66} \qquad \text{at } G'(\mathbf{q}) = 0,$$

and hence,

$$\mathbf{D}^{(G)} = \frac{1}{2s_{66}^2} \begin{pmatrix} s_{66}-s_{55} & s_{36}-s_{16}+s_{45} & s_{15}-s_{25} \\ s_{36}-s_{16}+s_{45} & s_{66}-s_{44} & s_{24}-s_{14} \\ s_{15}-s_{25} & s_{24}-s_{14} & 2s_{12}+4s_{66}-s_{11}-s_{22} \end{pmatrix}.$$

5. Coordinate invariant formulation

In this section we rephrase the results for the stationary conditions and for the second derivatives at the stationary conditions in coordinate invariant form. Let $\{\mathbf{n}, \mathbf{m}, \mathbf{p}\}$ be an orthonormal triad analogous to $\{\mathbf{e}_1, \mathbf{e}_2, \mathbf{e}_3\}$ before. Define the nondimensional symmetric second order tensors $\mathbf{A}$, $\mathbf{B}$, $\mathbf{C}$, $\mathbf{N}$, $\mathbf{M}$ and $\mathbf{P}$ by

$$A_{ij} = s_{nn}^{-1} s_{ijkl} n_k n_l, \qquad B_{ij} = s_{nn}^{-1} s_{ijkl} m_k m_l, \qquad C_{ij} = s_{nn}^{-1} s_{ijkl} p_k p_l,$$
$$N_{ij} = s_{nn}^{-1} s_{ikjl} n_k n_l, \qquad M_{ij} = s_{nn}^{-1} s_{ikjl} m_k m_l, \qquad P_{ij} = s_{nn}^{-1} s_{ikjl} p_k p_l,$$

where $s_{nn} = s_{ijkl} n_i n_j n_k n_l$. Thus,

$$\nu(\mathbf{n}, \mathbf{m}) = -\mathbf{A} : \mathbf{mm}, \qquad E(\mathbf{n}) = \frac{1}{s_{nn}}, \qquad G(\mathbf{n}, \mathbf{m}) = \frac{E(\mathbf{n})}{4\mathbf{N} : \mathbf{mm}}.$$

5.1. ***Poisson's ratio.*** The derivative of Poisson's ratio can be expressed in general form as

$$\mathbf{d}^{(\nu)} = \big[\mathbf{A} : (\mathbf{mp}+\mathbf{pm})\big]\mathbf{n} - \big[(2\nu\mathbf{A}+\mathbf{B}) : (\mathbf{pn}+\mathbf{np})\big]\mathbf{m} + \big\{\big[(2\nu-1)\mathbf{A}+\mathbf{B}\big] : (\mathbf{nm}+\mathbf{mn})\big\}\mathbf{p}, \quad (16)$$

which follows from (8), and may be checked by the substitutions $\mathbf{n}\to\mathbf{e}_1$, $\mathbf{m}\to\mathbf{e}_2$ and $\mathbf{p}\to\mathbf{e}_3$. This provides a local expansion of the Poisson's ratio for small rotation about the axis $\mathbf{q}$:

$$\nu(\mathbf{q},\theta) = \nu(\mathbf{q},0) + \mathbf{d}^{(\nu)}\cdot\mathbf{q}\,\theta + \mathrm{O}(\theta^2).$$

In particular, $\mathbf{d}^{(\nu)} = 0$ at a stationary point.

The second order tensor $\mathbf{D}^{(\nu)}$ of (15) becomes, in general format,

$$\begin{aligned}\mathbf{D}^{(\nu)} = {}& \big[\mathbf{A} : (\mathbf{mm}-\mathbf{pp})\big]\mathbf{nn} + \big\{\nu - [(1+2\nu)\mathbf{A}+4\nu\mathbf{N}] : \mathbf{pp}\big\}\mathbf{mm}\\ &+ \big\{2\nu^2 - 1 + [4(1-\nu)\mathbf{N}-\mathbf{M}] : \mathbf{mm}\big\}\mathbf{pp}\\ &+ \big[(2\mathbf{P}-\mathbf{N}) : (\mathbf{nm}+\mathbf{mn})\big]\tfrac{1}{2}(\mathbf{nm}+\mathbf{mn})\\ &+ \big[(\mathbf{N}-2\mathbf{M}) : (\mathbf{pn}+\mathbf{np})\big]\tfrac{1}{2}(\mathbf{pn}+\mathbf{np})\\ &+ \big\{\big[\mathbf{M}-2(1-2\nu)\mathbf{N}\big] : (\mathbf{mp}+\mathbf{pm})\big\}\tfrac{1}{2}(\mathbf{mp}+\mathbf{pm}). \quad (17)\end{aligned}$$

Hence, the local expansion near a stationary point is

$$\nu(\mathbf{q},\theta) = \nu(\mathbf{q},0) + \tfrac{1}{2}\mathbf{D}^{(\nu)} : \mathbf{qq}\,\theta^2 + \mathrm{O}(\theta^3).$$

5.2. ***Young's modulus.*** In the same way as before we find that

$$\mathbf{d}^{(E)} = 2E(\mathbf{n})\big[-\mathbf{A} : (\mathbf{pn}+\mathbf{np})\,\mathbf{m} + \mathbf{B} : (\mathbf{nm}+\mathbf{mn})\,\mathbf{p}\big], \quad (18)$$

$$\mathbf{D}^{(E)} = E(\mathbf{n})\big\{\big[\mathbf{A} : (\mathbf{nn}-\mathbf{pp}) - 2\mathbf{P} : \mathbf{nn}\big]\mathbf{mm} + \big[\mathbf{A} : (\mathbf{nn}-\mathbf{mm}) - 2\mathbf{M} : \mathbf{nn}\big]\mathbf{pp} + (\mathbf{A}+2\mathbf{N}) : (\mathbf{mp}+\mathbf{pm})\tfrac{1}{2}(\mathbf{mp}+\mathbf{pm})\big\}. \quad (19)$$

5.3. ***Shear modulus.*** Similarly, for the shear modulus

$$\mathbf{d}^{(G)} = 4\frac{G^2(\mathbf{n})}{E(\mathbf{n})}\big[\mathbf{N} : (\mathbf{mp}+\mathbf{pm})\,\mathbf{n} - \mathbf{M} : (\mathbf{pn}+\mathbf{np})\,\mathbf{m} + (\mathbf{B}-\mathbf{A}) : (\mathbf{nm}+\mathbf{mn})\,\mathbf{p}\big] \quad (20)$$

$$\begin{aligned}\mathbf{D}^{(G)} = {}& 8\frac{G^2(\mathbf{n})}{E(\mathbf{n})}\big\{\mathbf{N} : (\mathbf{mm}-\mathbf{pp})\,\mathbf{nn} + \mathbf{M} : (\mathbf{nn}-\mathbf{pp})\,\mathbf{mm} + 4\mathbf{N} : \mathbf{mm}\,\mathbf{pp} \quad (21)\\ &+ (\mathbf{P}+\mathbf{C}-\mathbf{A}) : (\mathbf{nm}+\mathbf{mn})\tfrac{1}{2}(\mathbf{nm}+\mathbf{mn})\\ &+ (\mathbf{A}-\mathbf{B}) : \big[(\mathbf{mm}-\mathbf{nn})\,\mathbf{pp} - (\mathbf{mp}+\mathbf{pm})\tfrac{1}{2}(\mathbf{mp}+\mathbf{pm}) + (\mathbf{pn}+\mathbf{np})\tfrac{1}{2}(\mathbf{pn}+\mathbf{np})\big]\big\}.\end{aligned}$$

6. Applications to Poisson's ratio

We now concentrate on general properties of the Poisson's ratio, applying the formalism for the stationary value to different situations. We begin with the general case of a plane of material symmetry in an orthotropic material.

6.1. ***Plane of symmetry in orthotropic material.*** We assume the stretch direction $\mathbf{n}$ lies in a plane of symmetry of an orthotropic material, and the direction of contraction $\mathbf{m}$ lies (a) perpendicular to the plane or (b) in the plane. This configuration includes all planes in hexagonal materials that contain the axis of symmetry, and therefore provides the stationary values of ν in materials with hexagonal symmetry (transverse isotropy).

With no loss in generality, let $\mathbf{e}_3^{(0)}$ be the normal to the plane of symmetry and let case (a) correspond to $\mathbf{m} = \mathbf{e}_3$ and case (b) corresponds to $\mathbf{m}$ in the plane of $\mathbf{e}_1^{(0)}, \mathbf{e}_2^{(0)}$. In both (a) and (b) $\mathbf{n}$ lies in the plane of $\mathbf{e}_1^{(0)}, \mathbf{e}_2^{(0)}$. Define the rotated axes

$$\mathbf{e}_1 = \cos\theta\, \mathbf{e}_1^{(0)} + \sin\theta\, \mathbf{e}_2^{(0)}, \qquad \mathbf{e}_2 = -\sin\theta\, \mathbf{e}_1^{(0)} + \cos\theta\, \mathbf{e}_2^{(0)}, \qquad \mathbf{e}_3 = \mathbf{e}_3^{(0)}.$$

Let S_{IJ} denote the compliances relative to the fixed set of axes $\{\mathbf{e}_1^{(0)}, \mathbf{e}_2^{(0)}, \mathbf{e}_3^{(0)}\}$, and s_{IJ} the compliances in the coordinates of the rotated axes. By definition of a symmetry plane, all coefficients s_{ijkl} with index 3 appearing once or thrice are zero. Then,

$$s_{11} = \frac{S_{11}S_{22} - S_0^2}{S_{11} + S_{22} - 2S_0} + \tfrac{1}{4}(S_{11} + S_{22} - 2S_0)\Big(\frac{S_{22} - S_{11}}{S_{11} + S_{22} - 2S_0} - \cos 2\theta\Big)^2, \quad (22)$$

$$s_{12} = S_{12} + \tfrac{1}{4}(S_{11} + S_{22} - 2S_0)\, \sin^2 2\theta, \quad (23)$$

$$s_{13} = \tfrac{1}{2}(S_{13} + S_{23}) - \tfrac{1}{2}(S_{23} - S_{13})\, \cos 2\theta, \quad (24)$$

$$s_{16} = \tfrac{1}{4}(S_{11} + S_{22} - 2S_0)\Big(\frac{S_{22} - S_{11}}{S_{11} + S_{22} - 2S_0} - \cos 2\theta\Big)\, \sin 2\theta, \quad (25)$$

$$s_{26} = \tfrac{1}{4}(S_{11} + S_{22} - 2S_0)\Big(\frac{S_{22} - S_{11}}{S_{11} + S_{22} - 2S_0} + \cos 2\theta\Big)\, \sin 2\theta, \quad (26)$$

$$s_{36} = \tfrac{1}{2}(S_{23} - S_{13})\, \sin 2\theta, \quad (27)$$

where $S_0 \equiv S_{12} + 2S_{66}$. Thus, in the two cases to be considered, we have $\mathbf{n} = \mathbf{e}_1$ and $s_{11} = 1/E(\theta)$.

Case (a): $\mathbf{m} = \mathbf{e}_3$ *perpendicular to the plane of symmetry.* We now consider stationary values of $\nu = \nu_{13}$, for which the three conditions for stationary ν are, instead of (9),

$$s_{14} = 0, \qquad 2\nu s_{16} + s_{36} = 0, \qquad (2\nu - 1)s_{15} + s_{35} = 0. \quad (28)$$

The first and last of these are automatically satisfied, based on the assumed material symmetry. Using s_{16} and s_{36} from (22)–(27), the second of (28) implies that

$\sin 2\theta = 0$, which is the exceptional case of prior symmetry, or that θ satisfies

$$\cos 2\theta = \frac{S_{22} - S_{11}}{S_{11} + S_{22} - 2S_0} + \frac{1}{\nu}\Big(\frac{S_{23} - S_{13}}{S_{11} + S_{22} - 2S_0}\Big).$$

Using this to eliminate $\cos 2\theta$ from the expression for $\nu = \nu_{13} = -s_{13}/s_{11}$ yields a quadratic equation for ν,

$$\nu^2 - \nu_a \nu - \tfrac{1}{4}\rho_a = 0,$$

where

$$\nu_a = \frac{(S_0 - S_{22})S_{13} + (S_0 - S_{11})S_{23}}{S_{11}S_{22} - S_0^2}, \qquad \rho_a = \frac{(S_{23} - S_{13})^2}{S_{11}S_{22} - S_0^2}.$$

Define E^* and θ^* by

$$E^* = \frac{S_{11} + S_{22} - 2S_0}{S_{11}S_{22} - S_0^2},$$

then we may identify E^* as the value of $E(\theta)$ when the second term on the RHS of (22) vanishes, that is, $E^* = E(\theta^*)$, where θ^* satisfies

$$\cos 2\theta^* = \frac{S_{22} - S_{11}}{S_{11} + S_{22} - 2S_0}. \tag{29}$$

The angle θ^* defines the direction at which E is stationary (maximum or minimum). It exists iff the RHS of (29) lies between -1 and 1. Regardless of whether or not the angle exists, it can be checked, $\nu_a = \nu_{13}(\theta^*) = -E^* s_{13}(\theta^*)$. The value of Young's modulus in the stretch direction θ for the stationary value of ν satisfies

$$\frac{E^*}{E} + \frac{\nu_a}{\nu} = 2.$$

In summary, the possible stationary values for stretch in the plane of symmetry and the strain measured in the direction perpendicular to the plane are

$$\nu_{a\pm} = \tfrac{1}{2}\nu_a \pm \tfrac{1}{2}(\nu_a^2 + \rho_a)^{1/2}, \tag{30}$$

and the stationary values occur if $-1 < \gamma_{a\pm} < 1$, where

$$\gamma_{a\pm} = \frac{S_{22} - S_{11}}{S_{11} + S_{22} - 2S_0} + \frac{1}{\nu_{a\pm}}\Big(\frac{S_{23} - S_{13}}{S_{11} + S_{22} - 2S_0}\Big),$$

in which case the direction of stretch is given by $\theta = \frac{1}{2}\cos^{-1}\gamma_{a\pm}$. Otherwise the stationary values occur at $\theta = 0$ and $\pi/2$.

Case (b): $\mathbf{m} = \mathbf{e}_2$ *in the plane of symmetry.* With $\mathbf{n} = \mathbf{e}_1$ again, conditions $(9)_1$ and $(9)_2$ are met and only $(9)_3$ is not automatically satisfied. Substituting the expressions for s_{16} and s_{26} from (22)–(27) into equation $(9)_3$ implies that either $\sin 2\theta = 0$, which is simply the axial case, or

$$\cos 2\theta = \frac{S_{22} - S_{11}}{S_{11} + S_{22} - 2S_0} + \frac{1}{\nu - 1}\Big(\frac{S_{22} - S_{11}}{S_{11} + S_{22} - 2S_0}\Big).$$

Substituting this into the relation for $\nu = \nu_{12}$, namely $\nu s_{nn} + s_{12} = 0$, and eliminating $\cos 2\theta$ produces a quadratic equation in ν. The equation is most simply expressed as a quadratic in the shifted Poisson's ratio $(\nu - 1)$:

$$(\nu - 1)^2 - (\nu_b - 1)(\nu - 1) - \tfrac{1}{4}\rho_b = 0,$$

where

$$\nu_b = -1 - E^*\big(S_{12} - S_0\big), \qquad \rho_b = \frac{(S_{11} - S_{22})^2}{S_{11}S_{22} - S_0^2}.$$

That is, $\nu_b = \nu_{12}(\theta^*) = -E^* s_{12}(\theta^*)$. Note that the value of Young's modulus E in the stretch direction θ satisfies

$$\frac{E^*}{E} + \frac{\nu_b - 1}{\nu - 1} = 2.$$

In summary, the possible stationary values for stretch and strain both in the plane of symmetry are

$$\nu_{b\pm} = \tfrac{1}{2}(\nu_b + 1) \pm \tfrac{1}{2}\big((\nu_b - 1)^2 + \rho_b\big)^{1/2}, \tag{31}$$

and the stationary values occur if $-1 < \gamma_{b\pm} < 1$, where

$$\gamma_{b\pm} = \frac{S_{22} - S_{11}}{S_{11} + S_{22} - 2S_0} + \frac{1}{\nu_{b\pm} - 1}\Big(\frac{S_{22} - S_{11}}{S_{11} + S_{22} - 2S_0}\Big),$$

in which case the direction of stretch is given by $\theta = \frac{1}{2}\cos^{-1}\gamma_{b\pm}$.

6.2. ***Example: cubic materials.*** The general coordinate invariant form of the compliance of a cubic material is [Walpole 1984]

$$\mathbf{S} = \Big(\frac{1}{3\kappa} - \frac{1}{2\mu_2}\Big)\mathbf{J} + \frac{1}{2\mu_1}\mathbf{I} + \Big(\frac{1}{2\mu_2} - \frac{1}{2\mu_1}\Big)\mathbf{D}, \tag{32}$$

where $\mathbf{I}$ and $\mathbf{J}$ are fourth order isotropic tensors, $I_{ijkl} = \frac{1}{2}(\delta_{ik}\delta_{jl} + \delta_{il}\delta_{jk})$, $J_{ijkl} = \frac{1}{3}\delta_{ij}\delta_{kl}$, and

$$\mathbf{D} = \mathbf{aaaa} + \mathbf{bbbb} + \mathbf{cccc}.$$

Here, the orthonormal triad $\{\mathbf{a}, \mathbf{b}, \mathbf{c}\}$ is coaxial with the cube axes. The condition that the elastic strain energy is always positive definite is that the three moduli κ, μ_1 and μ_2 are positive. We use, for simplicity, crystallographic-type notation for

unit vectors, e.g., $pq\bar{r}$ where p, q and r are positive numbers, indicates the unit vector $(p\mathbf{a}+q\mathbf{b}-r\mathbf{c})/\sqrt{p^2+q^2+r^2}$.

We consider the stationary conditions (9) for stretch in the $\mathbf{e}_1$ direction and lateral strain in the $\mathbf{e}_2$ direction. Since s_{14}, s_{15}, s_{16}, s_{25} and s_{26} vanish for isotropic media, it follows that the only contribution to these quantities is from the tensor $\mathbf{D}$. We may therefore rewrite the stationary conditions (9) as

$$D_{14}=0, \qquad 2\nu D_{15}+D_{25}=0, \qquad (2\nu-1)D_{16}-D_{26}=0, \tag{33}$$

where $D_{14}=D_{1123}$, etc. The realm of stretch directions that needs to be considered may be reduced to those defining the irreducible $\frac{1}{48}$th of the surface of the unit sphere. This in turn is defined by $\frac{1}{48}$th of the surface of the cube (see figure), where the vertices of the triangle correspond to the directions 001, 110, and 111. In a separate paper [Norris 2006b] it is shown that the extreme values of ν do not occur within the interior of the triangle. It turns out that the extreme values are only possible for stretch direction $\mathbf{e}_1$ along 001, 110, or in certain cases, for $\mathbf{e}_1$ located along the edge between 110 and 111. In the case that $\mathbf{e}_1=001$, the lateral direction $\mathbf{e}_2$ may be any orthogonal direction, and when $\mathbf{e}_1=110$ the lateral directions are 001 or $1\bar{1}0$, each of which can correspond to the minimum or maximum for ν, depending on the elastic parameters κ, μ_1 and μ_2. It is clear from the symmetry of the situation that the quantities D_{14}, D_{15}, D_{16}, D_{25} and D_{26} vanish identically for $\mathbf{e}_1$ along 001 or 110 with $\mathbf{e}_2$ as described. A full description of the possible extreme values of ν in cubic materials is involved but complete, and we refer to [Norris 2006b] for details.

To summarize the findings of Norris [2006b] regarding solutions of Equations (33): all possible stretch directions which solve the three stationary conditions are confined to the symmetry plane with normal 110, and equivalent planes of

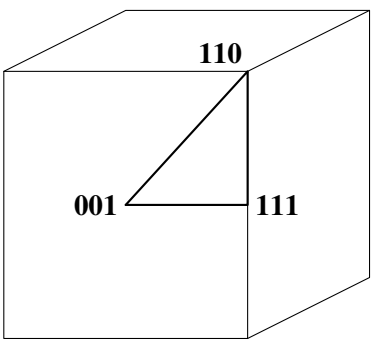

Figure 1. The irreducible $\frac{1}{48}$th of the cube surface is defined by the isosceles triangle with vertices as shown.

symmetry. We can therefore apply the results for a plane of orthotropic symmetry. Explicit calculation from (32) gives $S_{66} = (4\mu_1)^{-1}$, $S_{12} = S_{23} = (9\kappa)^{-1} - (6\mu_2)^{-1}$, $S_{13} = S_{12} + \chi/4$, $S_0 = S_{12} + 2S_{66}$, $S_{11} = S_0 + \chi/4$, $S_{22} = S_0 + \chi/2$, where $\chi = (\mu_2)^{-1} - (\mu_1)^{-1}$. Thus,

$$\nu_a = \nu_b = \nu_{111} \equiv \frac{3\kappa - 2\mu_1}{6\kappa + 2\mu_1}, \qquad \rho_a = \rho_b = \rho \equiv \tfrac{1}{6}(\nu_{111} + 1)\Big(\frac{\mu_1}{\mu_2} - 1\Big), \tag{34}$$

where $\nu_{111} = \nu(111, \mathbf{m})$ is the Poisson's ratio for stretch in the 111 direction, and is independent of the lateral direction $\mathbf{m}$.

The actual values of the possible extrema for ν can be obtained from equations and (30), (31) and (34). Skipping over the unedifying details, see [Norris 2006b], it can be shown that only the stationary values ν_{a-} and ν_{b+} are possible global extrema,

$$\nu_{a-} = \tfrac{1}{2}\nu_{111} - \tfrac{1}{2}\sqrt{\nu_{111}^2 + \rho}, \qquad \nu_{b+} = \tfrac{1}{2}(\nu_{111} + 1) + \tfrac{1}{2}\sqrt{(\nu_{111} - 1)^2 + \rho}.$$

Note that ν_{111} is independent of μ_2, which only enters these expressions via the term ρ. The extremely large values of Poisson's ratio discovered by Ting and Chen [2005] correspond to $\rho \gg 1$, which can occur if $\mu_2/\mu_1 \ll 1$. Under this circumstance ν_{a-} is large and negative, ν_{b+} is large and positive, and the magnitudes are, in principle, unbounded [Ting and Chen 2005; Ting and Barnett 2005; Norris 2006b].

The directions associated with the global extrema are given by

$$\cos 2\theta_{a-} = \tfrac{1}{3} - \frac{1}{3\nu_{a-}}, \qquad \cos 2\theta_{b+} = \tfrac{1}{3} + \frac{1}{3(\nu_{b+} - 1)}.$$

Both directions bifurcate from $\theta = 0$ [Norris 2006b], and therefore these extreme values only occur if $\nu < -\frac{1}{2}$ or $\nu > \frac{3}{2}$, respectively. A complete description of the extrema for all possible values of the elastic moduli is given by Norris [2006b].

6.3. ***Application to generally anisotropic materials.*** We first present a result that suggests a simple algorithm for searching for global extreme values of ν in generally anisotropic materials.

6.3.1. *A local min-max result for Poisson's ratio.* The tensor of second derivatives of $\nu(\mathbf{n}, \mathbf{m})$ at the stationary point $\mathbf{D}^{(\nu)}$ must be positive or negative definite in order that the stationary point be a minimum or a maximum, respectively. Consider a possible minimum, then a necessary although not sufficient condition is that the three diagonal elements of $\mathbf{D}^{(\nu)}$ are positive. In particular, Equation (17) gives

$$\mathbf{D}^{(\nu)} : \mathbf{nn} = \nu_{np} - \nu_{nm} \geq 0.$$

This implies that $\nu = \nu_{nm}$ must be strictly less than ν_{np}. At the same time, the stationary condition $\mathbf{d}^{(\nu)} = 0$ must hold, and in particular,

$$\mathbf{d}^{(\nu)} \cdot \mathbf{n} = 0 \qquad \Rightarrow \qquad \boldsymbol{\varepsilon} : \mathbf{mp} = 0 \qquad \text{for } \boldsymbol{\sigma} = \sigma\, \mathbf{nn}. \tag{35}$$

This implies that the shear strain ε_{mp} in the $\mathbf{m}$, $\mathbf{p}$-plane is zero. Hence, for any unit vector $\mathbf{r} \perp \mathbf{n}$, we have

$$\boldsymbol{\varepsilon} : \mathbf{rr} = (\mathbf{r} \cdot \mathbf{m})^2\, \varepsilon_{mm} + (\mathbf{r} \cdot \mathbf{p})^2\, \varepsilon_{pp},$$

or

$$\nu_{nr} = (\mathbf{r} \cdot \mathbf{m})^2\, \nu_{nm} + (\mathbf{r} \cdot \mathbf{p})^2\, \nu_{np} = \nu_{nm} + (\mathbf{r} \cdot \mathbf{p})^2 \left(\nu_{np} - \nu_{nm}\right) \geq \nu_{nm},$$

with equality only for $\mathbf{r} = \mathbf{m}$. Thus:

Lemma 1. *If ν_{nm} is a minimum (maximum) value, then it is also a minimum (maximum) among all possible ν_{nr} for $\mathbf{r}$ in the plane perpendicular to $\mathbf{n}$.*

This result is a direct consequence of the general expression for $\mathbf{D}^{(\nu)}$. It implies that if we can satisfy (35) then the values of ν_{nm} and ν_{np} are the extreme values for the given stretch direction $\mathbf{n}$. We next show how this single condition can be achieved.

6.3.2. *Satisfaction of one extremal condition.* The stationary values of Poisson's ratio occur, in general, for stretch directions at which the vector $\mathbf{d}^{(\nu)}$ of Equation (16) vanishes. We now show that one of the three components can be made to vanish; specifically, $\mathbf{d}^{(\nu)} \cdot \mathbf{n} = \mathbf{A} : (\mathbf{mp} + \mathbf{pm})$ is zero for an appropriate choice of the orthogonal directions $\mathbf{m}$ and $\mathbf{p}$.

We use the fact that the appropriate pair $\mathbf{m}$ and $\mathbf{p}$ correspond to stationary values of $\mathbf{A} : \mathbf{mm}$ and $\mathbf{A} : \mathbf{pp}$. These satisfy $\mathbf{A} : \mathbf{mm} + \mathbf{A} : \mathbf{pp} = \mathrm{tr}\mathbf{A} - 1$, so a maximum in one implies a minimum for the other. In order to find these directions for a given $\mathbf{n}$, consider the function of $\mathbf{m}$:

$$g(\mathbf{m}) \equiv \mathbf{A} : \mathbf{mm} - \lambda \mathbf{m} \cdot \mathbf{m} - 2\alpha \mathbf{m} \cdot \mathbf{n}.$$

Setting to zero the gradient with respect to $\mathbf{m}$ implies that $\mathbf{m}$ satisfies

$$\mathbf{m} = \alpha \left(\mathbf{A} - \lambda \mathbf{I}\right)^{-1} \mathbf{n}.$$

The scalars λ and α follow by requiring that $\mathbf{m} \cdot \mathbf{n} = 0$ and $\mathbf{m} \cdot \mathbf{m} = 1$, respectively. The former implies that λ satisfies

$$\mathbf{n} \cdot \left(\mathbf{A} - \lambda \mathbf{I}\right)^{-1} \mathbf{n} = 0.$$

This condition can be rewritten by expanding the inverse in terms of the cofactor matrix of $\left(\mathbf{A} - \lambda \mathbf{I}\right)$, and using the property $\mathbf{A} : \mathbf{nn} = 1$, which yields a quadratic in λ:

$$\lambda^2 + \lambda \left(1 - \mathrm{tr}\, \mathbf{A}\right) + \mathrm{adj}(\mathbf{A}) : \mathbf{nn} = 0. \tag{36}$$

Here adj($\mathbf{A}$) is the adjoint matrix. If $\mathbf{A}$ is invertible, then adj($\mathbf{A}$) = (det$\mathbf{A}$)$\mathbf{A}^{-1}$, and more generally the adjoint is the transpose of the cofactor matrix. Thus for any type of anisotropy, and for any direction $\mathbf{n}$, it is a straightforward to determine the appropriate orthogonal pair $\mathbf{m}$, $\mathbf{p}$, which automatically give $\mathbf{d}^{(\nu)} \cdot \mathbf{n} = 0$. Finding the right axes requires solving the quadratic (36) for λ. The associated values of Poisson's ratio are the maximum and minimum for the given direction $\mathbf{n}$. In this way, finding extremal values of Poisson's ratio for all possible $\mathbf{n}$ is reduced to seeking values which satisfy the remaining two conditions:

$$(2\nu\mathbf{A} + \mathbf{B}) : \mathbf{np} = 0, \qquad \big[(2\nu - 1)\mathbf{A} + \mathbf{B}\big] : \mathbf{nm} = 0,$$

or equivalently, $2\nu s_{15} + s_{25} = 0$ and $(2\nu - 1)s_{16} + s_{26} = 0$, respectively. This is the strategy used to determine the global extrema of ν in materials with cubic symmetry [Norris 2006b].

6.3.3. *Algorithm for finding global extreme values of* ν. Rather than searching for directions $\mathbf{n}$ which satisfy the three stationary conditions on ν, Lemma 1 suggests that a simple search for maximum and minimum values of Poisson's ratio can be effected as follows. For a given $\mathbf{n}$ define the pair $\nu_\pm(\mathbf{n})$ by

$$\begin{aligned}
\nu_\pm(\mathbf{n}) &= -\mathbf{A} : \mathbf{m}_\pm^{(A)}\mathbf{m}_\pm^{(A)}, \\
\mathbf{m}_\pm^{(A)} &= \|\big(\mathbf{A} - \lambda_\pm^{(A)}\mathbf{I}\big)^{-1}\mathbf{n}\|^{-1}\,\big(\mathbf{A} - \lambda_\pm^{(A)}\mathbf{I}\big)^{-1}\mathbf{n}, \\
\lambda_\pm^{(A)} &= \tfrac{1}{2}\big(\operatorname{tr}\mathbf{A} - 1\big) \pm \tfrac{1}{2}\big[\big(\operatorname{tr}\mathbf{A} - 1\big)^2 - 4\,\operatorname{adj}(\mathbf{A}) : \mathbf{nn}\big]^{1/2}.
\end{aligned}$$

The search for global extrema is then a matter of finding the largest and smallest values of $\nu_\pm(\mathbf{n})$ by searching over all possible directions $\mathbf{n}$. In practice, even for triclinic materials with no symmetry, the search only has to be performed over half of the unit sphere $\|\mathbf{n}\| = 1$, such as $\mathbf{n} \cdot \mathbf{e} \geq 0$ for some fixed direction $\mathbf{e}$. In this way, the numerical search is equivalent in complexity to that of finding the global extrema of Young's modulus.

This algorithm was applied to data for two crystals of monoclinic symmetry: Cesium dihydrogen phosphate and Lanthanum niobate, with the results in Table 1. The numerical results were obtained by using a 100×100 mesh for the hemisphere $\|\mathbf{n}\| = 1$, $\mathbf{n} \cdot \mathbf{e}_2 \geq 0$. It was found that the extreme values of the engineering moduli are not sensitive to the mesh size, although the values of the directions do change slightly.

7. Applications to the shear modulus

If we compare the vector derivative function for the shear modulus, $\mathbf{d}^{(G)}$ of (20), with $\mathbf{d}^{(\nu)}$ of (16), we note that the components in the $\mathbf{n}$ direction have a similar form, but with different matrices involved. Thus, it is $\mathbf{N}$ for $\mathbf{d}^{(G)} \cdot \mathbf{n}$, while for

Material	quantity	value	n_1	n_2	n_3
Cesium dihydrogen phosphate (CsH_2PO_4)	$E_{\max}$	19.3	0.44	0.76	0.47
	$E_{\min}$	0.53	0.99	0.00	0.06
	$G_{\max}$	12.2	0.42	0.71	−0.56
	$G_{\min}$	0.20	0.68	0.00	0.73
	$\nu_{\max}$	2.70	−0.23	0.82	0.52
	$\nu_{\min}$	−1.93	−0.49	0.85	−0.20
Lanthanum niobate ($LaNbO_4$)	$E_{\max}$	154.8	0.45	0.87	−0.21
	$E_{\min}$	2.27	−0.50	0.00	0.87
	$G_{\max}$	72.57	−0.28	0.71	−0.64
	$G_{\min}$	0.70	−0.96	0.00	0.27
	$\nu_{\max}$	3.95	0.00	1.00	0.00
	$\nu_{\min}$	-3.01	0.00	1.00	0.00

Table 2. Extreme values of E, G and ν for two materials of monoclinic symmetry with symmetry plane $n_2 = 0$. Units of E and G are GPa. Cesium dihydrogen phosphate: $s_{11} = 1820.0$, $s_{22} = 103.0$, $s_{33} = 772.0$, $s_{44} = 33.25$, $s_{55} = 112.5$, $s_{66} = 29.25$, $s_{12} = -219.0$, $s_{13} = -1170.0$, $s_{23} = 138.0$, $s_{15} = 124.5$, $s_{25} = -75.0$, $s_{35} = -90.5$, $s_{46} = 8.25$. Lanthanum niobate: $s_{11} = 66.8$, $s_{22} = 14.8$, $s_{33} = 146.0$, $s_{44} = 5.7$, $s_{55} = 265.0$, $s_{66} = 4.675$, $s_{12} = 16.9$, $s_{13} = -94.8$, $s_{23} = -30.8$, $s_{15} = 118.0$, $s_{25} = 45.6$, $s_{35} = -186.5$, $s_{46} = 0.95$. Units in $(\text{TPa})^{-1}$. (Data from Every and McCurdy [1992]).

$\mathbf{d}^{(\nu)} \cdot \mathbf{n}$ it is $\mathbf{A}$. The properties of the second derivatives $\mathbf{D}^{(G)} : \mathbf{nn}$ and $\mathbf{D}^{(\nu)} : \mathbf{nn}$ are similarly related. Proceeding with the same arguments as for the Poisson's ratio, we deduce:

Lemma 2. *If G_{nm} is a minimum (maximum) value, then it is also a minimum (maximum) among all possible G_{nr} for $\mathbf{r}$ in the plane perpendicular to $\mathbf{n}$.*

This in turn leads to a similar method for finding the global extrema of G.

7.1. ***Algorithm for finding global extreme values of G.*** Define the pair $G_\pm(\mathbf{n})$ by

$$G_\pm(\mathbf{n}) = \frac{E(\mathbf{n})}{\mathbf{N} : \mathbf{m}_\pm^{(N)}\mathbf{m}_\pm^{(N)}},$$

$$\mathbf{m}_\pm^{(N)} = \left\| \left(\mathbf{N} - \lambda_\pm^{(N)}\mathbf{I}\right)^{-1}\mathbf{n} \right\|^{-1} \left(\mathbf{N} - \lambda_\pm^{(N)}\mathbf{I}\right)^{-1}\mathbf{n},$$

$$\lambda_\pm^{(N)} = \tfrac{1}{2}\left(\operatorname{tr}\mathbf{N} - 1\right) \pm \tfrac{1}{2}\left[\left(\operatorname{tr}\mathbf{N} - 1\right)^2 - 4\operatorname{adj}(\mathbf{N}) : \mathbf{nn}\right]^{1/2}.$$

Then the global extreme values of G can be found by searching over $\mathbf{n}$ only. Thus, the problem of finding the global extrema of the shear modulus is reduced to the same level of complexity as searching for the maximum and minimum Young's modulus. Table 1 summarizes the extreme values of G found using this algorithm for two crystals of monoclinic symmetry.

8. Conclusions

The results of this paper provide a consistent framework for determining the extreme values of the three engineering moduli in materials of any crystal symmetry or none. General conditions have been derived which must be satisfied at stationary values of ν, E and G. These are equations (9), (10) and (11), which have also been cast in forms that are independent of the coordinates used, in equations (16), (18) and (20), respectively. The associated three hessian matrices which determine the local nature of the stationary value, maximum, minimum or saddle, are given in equations (17), (19) and (21). The stationary conditions for Poisson's ratio simplify for stretch in a plane of orthotropic symmetry, for which there are at most 4 stationary values of ν. Two can occur for in-plane stretch and strain, and the other two for out-of-plane strain. This implies that transversely isotropic materials have at most four stationary values of Poisson's ratio. The results for the plane of symmetry also reproduce known results for cubic materials [Norris 2006b]. The hessian matrices for ν and G lead to algorithms for finding the extreme values. The key is to remove the dependence on the $\mathbf{m}$ direction by explicit representation of the maximum and minimum for a given $\mathbf{n}$ direction. The algorithms have been demonstrated by application to materials of low symmetry.

References

[Boulanger and Hayes 1995] P. Boulanger and M. Hayes, "On Young's modulus for anisotropic media", *J. Appl. Mech.* (*Trans. ASME*) **62** (1995), 819–820.

[Boulanger and Hayes 1998] P. Boulanger and M. Hayes, "Poisson's ratio for orthorhombic materials", *J. Elasticity* **50**:1 (1998), 87–89.

[Cazzani and Rovati 2003] A. Cazzani and M. Rovati, "Extrema of Young's modulus for cubic and transversely isotropic solids", *Int. J. Solids Struct.* **40**:7 (2003), 1713–1744.

[Cazzani and Rovati 2005] A. Cazzani and M. Rovati, "Extrema of Young's modulus for elastic solids with tetragonal symmetry", *Int. J. Solids Struct.* **42**:18–19 (2005), 5057–5096.

[Every and McCurdy 1992] A. G. Every and A. K. McCurdy, *Second and higher order elastic constants*, vol. III/29A, Landolt–Bornstein, Springer, Berlin, 1992.

[Hayes 1972] M. A. Hayes, "Connexions between the moduli for anisotropic elastic materials", *J. Elasticity* **2**:2 (1972), 135–141.

[Mehrabadi and Cowin 1990] M. M. Mehrabadi and S. C. Cowin, "Eigentensors of linear anisotropic elastic materials", *Q. J. Mech. Appl. Math.* **43**:1 (1990), 15–41.

[Mehrabadi et al. 1995] M. M. Mehrabadi, S. C. Cowin, and J. Jaric, "Six-dimensional orthogonal tensor representation of the rotation about an axis in three dimensions", *Int. J. Solids Struct.* **32**:3–4 (1995), 439–449.

[Norris 2006a] A. N. Norris, "Optimal orientation of anisotropic solids", *Q. J. Mech. Appl. Math.* **59**:1 (2006), 29–53.

[Norris 2006b] A. N. Norris, "Poisson's ratio in cubic materials", 2006. P. Roy. Soc. Lond. A Mat.

[Rovati 2003] M. Rovati, "On the negative Poisson's ratio of an orthorhombic alloy", *Scr. Mater.* **48**:3 (2003), 235–240.

[Rovati 2004] M. Rovati, "Directions of auxeticity for monoclinic crystals", *Scr. Mater.* **51**:11 (2004), 1087–1091.

[Ting 2004] T. C. T. Ting, "Very large Poisson's ratio with a bounded transverse strain in anisotropic elastic materials", *J. Elasticity* **77**:2 (2004), 163–176.

[Ting 2005a] T. C. T. Ting, "Explicit expression of the stationary values of Young's modulus and the shear modulus for anisotropic elastic materials", *J. Mech.* **21**:4 (2005), 255–266.

[Ting 2005b] T. C. T. Ting, "The stationary values of Young's modulus for monoclinic and triclinic materials", *J. Mech.* **21**:4 (2005), 249–253.

[Ting and Barnett 2005] T. C. T. Ting and D. M. Barnett, "Negative Poisson's ratios in anisotropic linear elastic media", *J. Appl. Mech. (Trans. ASME)* **72**:6 (2005), 929–931.

[Ting and Chen 2005] T. C. T. Ting and T. Chen, "Poisson's ratio for anisotropic elastic materials can have no bounds", *Q. J. Mech. Appl. Math.* **58**:1 (2005), 73–82.

[Walpole 1984] L. J. Walpole, "Fourth rank tensors of the thirty-two crystal classes: multiplication tables", *P. Roy. Soc. Lond. A Mat.* **A391**:1800 (1984), 149–179.

[Yang et al. 2004] W. Yang, Z. Li, W. Shi, B. Xie, and M. Yang, "Review on auxetic materials", *J. Mater. Sci.* **39**:10 (2004), 3269–3279.

Received 12 Apr 2006.

ANDREW N. NORRIS: norris@rutgers.edu
Mechanical and Aerospace Engineering, Rutgers University, 98 Brett Road, Piscataway, NJ 08854-8058, United States
http://mechanical.rutgers.edu/norris

SUBMISSION GUIDELINES

ORIGINALITY

Authors may submit manuscripts in PDF format on-line. Submission of a manuscript acknowledges that the manuscript is *original and has neither previously, nor simultaneously, in whole or in part, been submitted elsewhere.* Information regarding the preparation of manuscripts is provided below. Correspondence by email is requested for convenience and speed. For further information, write to:

Marie-Louise Steele
Division of Mechanics and Computation
Durand Building, Room 262
Stanford University
Stanford CA 94305

LANGUAGE

Manuscripts must be in English. A brief abstract of about 150 words or less must be included. The abstract should be self-contained and not make any reference to the bibliography. Also required are keywords and subject classification for the article, and, for each author, postal address, affiliation (if appropriate), and email address if available. A home-page URL is optional.

FORMAT

Authors are encouraged to use LaTeX and the standard article class, but submissions in other varieties of TeX, and, exceptionally in other formats, are acceptable. Electronic submissions are strongly encouraged in PDF format only; after the refereeing process we will ask you to submit all source material.

REFERENCES

Bibliographical references should be listed alphabetically at the end of the paper and include the title of the article. All references in the bibliography should be cited in the text. The use of BibTeX is preferred but not required. Tags will be converted to the house format (see a current issue for examples), however, in the manuscript, the citation should be by first author's last name and year of publication, e.g. "as shown by Kramer, et al. (1994)". Links will be provided to all literature with known web locations and authors are encoraged to provide their own links on top of the ones provided by the editorial process.

FIGURES

Figures prepared electronically should be submitted in Encapsulated PostScript (EPS) or in a form that can be converted to EPS, such as GnuPlot, Maple, or Mathematica. Many drawing tools such as Adobe Illustrator and Aldus FreeHand can produce EPS output. Figures containing bitmaps should be generated at the highest possible resolution. If there is doubt whether a particular figure is in an acceptable format, the authors should check with production by sending an email to:

production@mathscipub.org

Each figure should be captioned and numbered so that it can float. Small figures occupying no more than three lines of vertical space can be kept in the text ("the curve looks like this:"). It is acceptable to submit a manuscript with all figures at the end, if their placement is specified in the text by means of comments such as "Place Figure 1 here". The same considerations apply to tables.

WHITE SPACE

Forced line breaks or page breaks should not be inserted in the document. There is no point in your trying to optimize line and page breaks in the original manuscript. The manuscript will be reformatted to use the journal's preferred fonts and layout.

PROOFS

Page proofs will be made available to authors (or to the designated corresponding author) at a web site in PDF format. Failure to acknowledge the receipt of proofs or to return corrections within the requested deadline may cause publication to be postponed.

JOURNAL OF MECHANICS OF MATERIALS AND STRUCTURES

Volume 1 No. 4 April 2006